One-dimensional Titanium Dioxide Nanomaterial based Memristive Device and its Neuromorphic Computing Applications

by

Ming Xiao

A thesis
presented to the University of Waterloo
in fulfillment of the
thesis requirement for the degree of
Doctor of Philosophy

in

Mechanical Engineering (Nanotechnology)

Waterloo, Ontario, Canada, 2019

©Ming Xiao 2019

Examining Committee Membership

The following served on the Examining Committee for this thesis. The decision of the Examining Committee is by majority vote.

External Examiner	Professor Shimeng Yu, School of Electrical and Computer Engineering, Georgia Institute of Technology, USA
Supervisors	Professor Norman Y. Zhou, Department of Mechanical & Mechatronics Engineering, University of Waterloo, Canada and, Professor Walter W. Duley, Department of Physics & Astronomy, University of Waterloo, Canada
Internal Member	Professor Kevin Musselman, Department of Mechanical & Mechatronics Engineering, University of Waterloo, Canada
Internal Member	Professor Michael Mayer, Department of Mechanical & Mechatronics Engineering, University of Waterloo, Canada
Internal-external Member	Professor Irene Goldthorpe, Department of Electrical and Computer Engineering, University of Waterloo, Canada

Author’s declaration

This thesis consists of material all of which I authored or co-authored: see Statement of Contributions included in the thesis. This is a true copy of the thesis, including any required final revisions, as accepted by my examiners.

I understand that my thesis may be made electronically available to the public.

Statement of Contributions

This thesis comprises of a literature review (Chapter 2) and a series of four data chapters each written in a manuscript format (Chapters 3-6). At the time of submission ten papers were published, one manuscript was submitted for review in refereed journals. The manuscripts have been modified to fit the style of the thesis. I am the primary author in all manuscript. Dr. Norman Zhou and Dr. Walter Duley are the anchor authors and have reviewed each chapter. There are several co-authors on these manuscripts that have contributed to the work and their contributions are described, below.

Chapter 3

Ming Xiao, Kevin, P. Musselman, Walter W. Duley, Y. Norman Zhou, "Resistive Switching Memory of TiO_2 Nanowire Networks Grown on Ti Foil by a Single Hydrothermal Method". Nano-Micro Letters 2017, 9 (15), 1-9.

Dr. Kevin Musselman provided editorial support and guidance. I synthesized the nanomaterials, designed and fabricated the devices, conducted the electrical characterization and wrote the manuscript.

Chapter 4

Ming Xiao, Kevin P. Musselman, Walter W. Duley, Y. Norman Zhou, "Reliable and Low-Power Multilevel Resistive Switching in TiO_2 Nanorod Arrays Structured with a TiO_x Seed Layer". ACS Applied Materials & Interfaces, 2017, 9 (5), 4808-4817.

Dr. Kevin Musselman provided editorial support and guidance. I synthesized the nanomaterials, designed and fabricated the devices, conducted the electrical characterization and wrote the manuscript.

Chapter 5

Ming Xiao, Daozhi Shen, Kevin P. Musselman, Walter W. Duley, Y. Norman Zhou, "Oxygen Vacancies Migration/Diffusion Induced Synaptic Plasticity in a Single Titanate Nanobelt". Nanoscale, 2018, 10 (*13*), 6069-6079.

Dr. Daozhi Shen provided support on the nanomaterial synthesis and discussion about the device characterization. Dr. Kevin Musselman provided editorial support and guidance. I synthesized the nanomaterials, designed and fabricated the devices, conducted the electrical characterization and wrote the manuscript.

Chapter 6

Ming Xiao, Daozhi Shen, Moritz H. Futscher, Bruno Ehrler, Kevin P. Musselman, Walter W. Duley, Y. Norman Zhou, "Threshold Switching in Single TiO_2 Nanobelt Devices Emulating an Artificial Nociceptor". Submitted to Advanced Electronic Materials (No. aelm.20190595)

Dr. Daozhi Shen provided support on the nanomaterial synthesis and discussion about the device characterization. Moritz H. Futscher and Dr. Bruno Ehrler provided support on the thermal admittance spectroscopy characterization of the samples and discussion about the data. Dr. Kevin Musselman provided editorial support and guidance. I synthesized the nanomaterials, designed and fabricated the devices, conducted the electrical characterization and wrote the manuscript.

Abstract

Memristor devices as the alternative to the next-generation non-volatile memory devices has been widely studied recently due to its advantages of simple structure, fast switching speed, low power consumption. Among all the different materials that demonstrate the potential of resistive switching behavior, memristor devices based on TiO_2 has attracted particular attention considering its richness in switching mechanism associated with wide range of phases. Furthermore, one-dimensional (1D) nanomaterial based memristor devices demonstrate promising potential considering about its advantages of confinement of electron transport in individual nanowires, enabling precision engineering of electrical performance for stable and reliable memristor devices, high integration density potential, etc.

In this research, we propose the use of facile hydrothermal methods to synthesize TiO_2 nanowires for the fabrication of memristor devices. Three different types of devices were fabricated, i.e., based on TiO_2 nanowire networks on Ti foil, TiO_2 nanorod arrays grown on fluorine-doped tin oxide (FTO) substrate, and single TiO_2 and titanate nanowire directly synthesized from TiO_2 nanoparticles. The corresponding devices demonstrated promising resistive switching performance respectively and were further used for multilevel memory storage and more importantly, the emulation of artificial synapses for the application of neuromorphic computing. The corresponding switching mechanisms were explored and it was found that the oxygen vacancies in TiO_2 nanowires during the hydrothermal process play an important role in the switching and charge transport mechanism. This work will improve the understanding of engineering the electrical performance of TiO_2 based memristive devices and provide insights into the switching mechanism in 1D nanomaterial based memristive devices.

Keywords: memristor, TiO_2, one-dimensional nanomaterial, hydrothermal method, synapse emulation

Acknowledgements

Throughout this four-year long PhD journey, I have received tremendous help from different people, without whom it is impossible to finish this PhD program.

I would like to thank my supervisors Prof. Norman Y. Zhou and Prof. Walter W. Duley for their guidance, instructions, encouragement, motivations and support throughout the whole PhD program. Great thanks are also given to Prof. Kevin Musselman for his fruitful discussion, helpful suggestions and introduction to other research groups for collaboration on my research. I want to express my appreciation to all my colleagues and friends who supported me in my research and life in different ways in different phases of this journey: Dr. Paola Russo, Dr. Ehsan Marzbanrad, Dr. Dulal Saha, Dr. Peng Peng, Dr. Robert Liang, Dr. Zhen Jiao, Dr. Luchan Lin, Dr. Daozhi Shen, Dr. Boyd Panton, Dr. Andrew Michael, Dr. Ran Peng, Dr. Joyce Koo, Dr. Lifang Hu, Dr. Bo Zhao, Dr. Di Xu, Brett Sherren, Pablo Enrique, Amirali Shamsolhodael, Viet Huong Nguyen, Dr. David Muñoz-Rojas, Moritz Futscher, Dr. Bruno Ehrler, Jiayun Feng, Zhuang Hui, Shubham Ranjan, Dr. Sumei Wang, Dr. Bai Sun, Dr. Xiaonan Wang and Qian Sun.

I would like to thank all of my colleagues in the Centre for Advanced Materials Joining (CAMJ) with whom I have a pleasant time during my doctoral studies. I would like to thank Richard Barber and Dr. Czang-Ho Lee for their support in Giga-to-Nanoelectronics (G2N) Lab for the access to different instruments that are essential for my research. I also would like to thank the Waterloo Institute of Nanotechnology (WIN) for supporting my work. I am grateful for Carmen Andrei and Travis Casagrande at the Canadian Center for Electron Microscopy (CCEM) in McMaster University for the support with transmission electron microscopy and focused-ion-beam characterization.

My warmest thanks to my wife Xunyan Yan, who, although 12,600 km apart, always supports, encourages and loves me in my daily life. Particular thanks to Jiajia, our first kid, who gives me great strength to overcome all difficulties throughout my life.

I also want to thank my family (father, parents-in-law, brother, sister-in-law) for their endless love and encouragement throughout my life in University of Waterloo.

Dedication

To my family

Table of Contents

Examining Committee Membership ii

Author's declaration iii

Statement of Contributions i

Abstract iii

Acknowledgements iv

Dedication v

List of Figures x

List of Tables xxiv

List of Abbreviations, Symbols and Nomenclature xxv

Chapter 1. Introduction 1

1.1. Background 1

1.2. Objectives 2

1.3. Organization of the thesis 2

Chapter 2. Literature Review 4

2.1. Memristive devices and ReRAM devices 4

2.1.1. What are memristor/memristive devices? 4

2.1.2. What are ReRAM devices? 4

2.1.3. Characteristic parameters of ReRAM devices 7

2.1.4. Summary of resistive switching mechanism 9

2.1.4.1. Cation migration---Electrochemical Metallization Memory (ECM) 9

2.1.4.2. Anion migration---Valence Change Memory (VCM) 12

2.1.4.3. Charge trapping and Detrapping 17

2.1.4.4. Thermochemical reaction (TCM) 17

2.1.5 Applications of memristive devices 19

2.1.5.1. Multilevel memory for data storage ... 19

2.1.5.2. Logic calculation ... 20

2.1.5.3. Neuromorphic computing ... 21

2.2. 1D TiO_2 nanomaterial based memristive devices ... 28

2.2.1. TiO_2 based memristive devices ... 28

2.2.2. 1D TiO_2 nanomaterial based memristive devices ... 29

2.2.2.1 1D nanomaterial based memristive devices ... 29

2.2.2.2 1D TiO_2 nanomaterials based memristive devices ... 32

2.3. Hydrothermal synthesized TiO_2 nanowires and memristive devices ... 33

2.4. Summary ... 35

Chapter 3. Resistive Switching Memory of TiO_2 Nanowire Networks Grown on Ti Foil by a Single Hydrothermal Method[195] ... 37

3.1. Overview ... 37

3.2. Introduction ... 37

3.3. Materials and Methods ... 38

3.4. Results and Discussion ... 39

3.4.1. Characterization of TiO_2 nanowire networks ... 39

3.4.2. Electrical performance evaluation ... 41

3.4.2.1. Resistive switching characteristics ... 41

3.4.2.2. Switching Mechanism Analysis ... 44

3.4.2.3. Endurance and Retention Study ... 48

3.5. Conclusions ... 49

Chapter 4. Reliable and Low-Power Multilevel Resistive Switching in TiO_2 Nanorod Arrays Structured with a TiO_x Seed Layer[217] ... 50

4.1. Overview ... 50

4.2. Introduction ... 50

4.3. Experimental Section 52
4.3.1. TiO_2 NRA synthesis and device fabrication 52
4.3.2. Characterization 53
4.4. Results and Discussion 54
4.4.1. Materials Characterization 54
4.4.1.1. SEM and TEM 54
4.4.1.2. GIXRD 56
4.4.1.3. XPS 57
4.4.2. Electrical Characterization 59
4.4.2.1. Resistive switching behavior 59
4.4.2.2. Endurance and retention Study 63
4.4.2.3. Switching mechanism study 64
4.4.2.4. Multilevel memory behavior 68
4.5. Conclusions 71
Chapter 5. Oxygen Vacancy Migration/Diffusion Induced Synaptic Plasticity in a Single Titanate Nanobelt[246] 73
5.1. Overview 73
5.2. Introduction 73
5.3. Experimental Section 75
5.3.1. Synthesis of sodium and hydrogen titanate nanobelts 75
5.3.2. Device fabrication and characterization 76
5.3.3. Material characterization 76
5.4. Results and Discussion 76
5.4.1. Material Characterization 76
5.4.2. Synaptic performance 79

5.4.2.1. Excitatory postsynaptic current 79
5.4.2.2. Short term plasticity 82
5.4.2.3. Potentiation and depression 85
5.4.2.4. Learning and forgetting response 89
5.4.3. Kinetic mechanism 94
5.5. Conclusions 98
Chapter 6. Threshold Switching in Single TiO_2 Nanobelt Device Emulating an Artificial Nociceptor 99
6.1. Overview 99
6.2. Introduction 99
6.3. Experimental Section 102
6.3.1. Synthesis of TiO_2 nanobelts 102
6.3.2. Device fabrication and characterization 102
6.3.3. Material characterization 103
6.4. Results and Discussion 103
6.4.1. I-V sweeping performance and mechanism study 103
6.4.1.1 I-V sweeping performance 103
6.4.1.2 Charge transport mechanism 113
6.4.2. Artificial nociceptor performance 119
6.4.2.1. Threshold dynamics 119
6.4.2.2. Nociceptor features 122
6.5. Conclusions 124
Chapter 7. Conclusions and Outlook 126
Letters of Copyright permission 130
Reference 154

List of Figures

Figure 1. Schematic diagram of MIM structure in ReRAM devices, in which M' and M'' denote the metal electrode and I denote the insulator (switching layer). 6

Figure 2. An example of the non-volatile Pt/Ta_2O_{5-x}/TaO_{2-x}/Pt ReRAM devices, (a) Scanning electron microscopy image of a 30-nm crossbar arrays of devices with the inset showing a magnified single device, (b) Transmission electron microscopy cross-section of a 30-nm crossbar cell. The insulating Ta_2O_{5-x} layer can be seen along with the TaO_{2-x} base layer, with a total thickness of 30 nm. Adapted with permission[52]. Copyright 2011, Nature Publishing Group........ 6

Figure 3. Sketches for classification of resistive switching, (a) Unipolar switching, and (b) bipolar switching. (CC: compliance current). Adapted with permission[51]. Copyright 2007, Nature Publishing Group. 7

Figure 4. Schematic current-voltage characteristic of ECM devices and corresponding mechanism, in which active electrode (Ag, Cu, etc.) contributes to the resistive switching. Voltage is applied to the Ag electrode while Pt electrode is grounded. In the initial stage, no Ag ions is in the insulator layer (A); when under positive applied voltage to the active electrode, an oxidation reaction occurs at the active electrode/insulating layer interface. Then, the injected Cu or Ag ions migrate within the electric field through the insulating layer (B), At the inert electrode/insulating layer interface another electron-transfer reaction occurs. The Cu/Ag ions are reduced, and a Cu/Ag filament starts to grow towards the anode after having formed a stable Cu/Ag nucleus (C). The bridging between the anode and cathode with Cu/Ag filament switches the device from HRS to LRS. While the rupture of the filament with a negative voltage switches the device from HRS to LRS. Adapted with permission[37]. Copyright 2015, Wiley-VCH. 10

Figure 5. Demonstration of the switching mechanism in ECM devices. (a) Schematic design of the in-situ experiment set-up. (b) In-situ current-voltage (*I-V*) response. (c)-(f), Cross-sectional STEM images obtained after the voltage applications of 0, -0.4, -0.8, and +0.4 V, respectively. (g)-(j) Black-and-white images converted from the raw STEM images of (c)-(f), respectively. Adapted with permission[59]. Copyright, 2011, Wiley-VCH. 11

Figure 6. In-situ TEM observation of conductive filament growth in vertical Ag/a-Si/W memories. (a) Experiment set-up. The Ag/a-Si/W resistive memory device was fabricated on a W probe in TEM, scale bar, 100 nm. (b) *I-t* characteristic recorded during the forming process at a voltage of 12 V. (c-g) TEM images of the devices corresponding to data points c-g in (b) recorded during the

forming process. Scale bar, 20 nm. It could be seen the filament formation in (g) from the top Ag towards W electrode. Adapted with permission[60]. Copyright 2012, Nature Publishing Group. .. 12
Figure 7. Schematic current-voltage characteristic of VCM devices and corresponding mechanisms, in which the defects of insulating layer (vacancies, interstitials, etc.) are responsible for the resistive switching. Both active and bottom (right) electrode are inert. When a negative voltage is applied to left electrode, oxygen vacancies migrate towards this electrode (B). Hence, the insulating region between the sub-stoichiometric well-conducting filament and the active electrode becomes conducting and the VCM cell switches to the LRS (C). By reversing the voltage-polarity oxygen vacancies are pushed back from the active electrode (D) and finally the HRS is reestablished (A). Adapted with permission[37]. Copyright 2015, Wiley-VCH. 13
Figure 8. Schematic diagram of the experimental scanning probe set-up in the TEM chamber, (b) High resolution TEM image of structure after the electroforming process. (c) Selected area electron diffraction and (d) fast Fourier transformed micrograph of the Magnéli phase. Adapted with permission[61]. Copyright 2010, Nature Publishing Group. 14
Figure 9. Voltage-induced morphology evolution in the TaO_{2-x} layer. (a-c) Cross-sectional HAADF-STEM images showing the structural evolution after the set (a), reset (b) and breakdown (c) operations. Bright area: Ta-rich phase (conducting paths) and dark area: non-conducting clusters. Inset shows the atomic resolution STEM images exhibiting the individual Ta atoms (green circles). (d-f) Pseudocolour maps converted from the raw images of a-c, respectively. Yellow: Ta-rich phase (conducting paths), blue: non-conducting clusters. Bright and yellow regions in (a-f) are regarded as conductive percolation paths. Scale bar, 3 nm. Adapted with permission[63]. Copyright 2013, Nature Publishing Group. 15
Figure 10. Schematic diagram of for the transport mechanism of charge trapping and detrapping process. (a) Nearly empty traps, (b) thermally generated carrier conduction, (c) traps partially filled and (d) fully filled traps, the device is transitioned from HRS to LRS at (d). The CeO_2 quantum dots function as the trap centers. Reprinted with permission[76]. Copyright 2013) American Chemical Society. 17
Figure 11. Schematic diagram for filamentary channels in TCM devices and corresponding unipolar resistive switching characteristics. RS: resistive switching, TE, top electrode. BE, bottom electrode. Adapted from Reference[82]... 18

Figure 12. In-situ TEM observation of the evolution of the conductive filaments during forming the subsequent reset process of a Pt/ZnO/Pt cell. (a-d) A series of TEM images corresponding to the data points a-d in (f). The white dashed lines in (b-d) highlight the filament. (e) TEM image obtained after the reset process. (f) The corresponding *I-V* curve of forming (blue) and subsequent reset (red) process. Adapted with permission[83]. Copyright 2013, American Chemical Society. . 19

Figure 13. Multilevel memory storage of a WO_x resistive switching memory device with high endurance performance, adapted from Reference[84]. 20

Figure 14. Illustration of material implication logic operation by a memristor device. Adapted with permission[7]. Copyright 2010, Nature Publishing Group. 21

Figure 15. The interaction between presynaptic neuron and postsynaptic neuron. Adapted from Reference[104]. 23

Figure 16. Ag_2S based devices showing short-term plasticity and long-term potentiation, depending on the input-pulse repetition time. (a) Schematic diagram of a Ag_2S synapse and the signal transmission of a biological synapse. Application of input pulses causes the precipitation of Ag atoms from the Ag_2S electrode, resulting in the formation of a Ag atomic bridge between the Ag_2S electrode and a counter metal electrode. When the precipitated Ag atoms do not form a bridge, the synapses work as the STP. After an atomic bridge is formed, it works as LTP. (b) Experimental demonstration of the STP and LTP by recording the change in conductance of the synapse when the input pulses were applied with a relative long intervals of T=20 s and (c) T=2 s. Adapted with permission[11]. Copyright 2011, Nature Publishing Group. 25

Figure 17. Summary of configuration and devices for the heterosynaptic emulation based on memristive devices. (a) Schematic illustration of two-terminal plasticity (homosynaptic) and (b) heterosynaptic plasticity. (c) SEM image of the device on the substrate, in which the Ag clusters between the pre and post electrodes can be modulated by the application of bias on the MOD electrode. (a)-(c) are adapted with permission[115]. Copyright 2015, Wiley-VCH. (d) A schematic illustration of a different device based on the metal oxide sandwich memristor devices with a side electrode functioning as the modulatory electrodes. Adapted with permission[116]. Copyright 2017, Wiley-VCH. (e) Schematic diagram showing the synaptic interactions enabled by the diffusion of plasticity-related proteins (PRP) among multiple synapse. Specifically, PRPs are generated in the postsynaptic terminal of synapse 1 and can diffuse to the synapses 2, 3, 4 through the dendrite. Depending on the difference among diffusion, synaptic behavior among these synapses can be

different. (f) five terminal MoS_2 devices, in which the distribution of conductive ions at the terminals such as Electrode A, B, C and D can be controlled separately and lead to the potential heterosynaptic emulation possibilities, inset, SEM image of the fabricated MoS_2 devices. (e) and (f) are adapted with permission[120]. Copyright 2018, Nature Publishing Group. (g) Six terminal MoS_2 devices, in which any two of the inner electrodes (1, 2, 3, 4) can be controlled by the outside electrodes (5 and 6). Adapted with permission[118]. Copyright 2018, Nature Publishing Group. .. 26

Figure 18. Natural image processing using the memristor crossbar structures. (a) SEM image of the fabricated memristor array. Upper right inset: magnified SEM image of the crossbar. Scale bar, 3 μm. Lower left inset: memristor chip integrated on the test board after wire-bonding process. (b) A 32×32 chequerboard pattern programmed into the memristor array and subsequently read back using the hardware system in (a). (c) Original 120×120 image. The image is divided into non-overlapping 4×4 patches for processing. (d) A 4×4 patch from the original image. (e) The experimentally reconstructed patch from the 16×32 memristor crossbar using the locally competitive algorithm and an offline-learned dictionary based on "winner-take-all" approach. (f) Membrane potentials of the neurons as a function of iteration number during the locally competitive algorithm analysis. The red horizontal line marks the threshold parameter λ. (g) Experimentally reconstructed image based on the reconstructed patches. Adapted with permission[126]. Copyright 2017, Nature Publishing Group. 27

Figure 19. (a) Typical I-V sweeping results of individual MgO/Co_3O_4 nanowire device, inset, SEM image of the nanowire device. (b) Switching endurance performance up to 10^8 cycles. Adapted with permission[146]. Copyright 2010, American Chemical Society. 30

Figure 20. (a) SEM image of $Cu/Zn_2SnO_4/Pd$ device, (b) *I-V* characteristic bipolar resistive switching behavior, and (c) EDX Cu elemental mapping results for the device in the ON (LRS) state of (a) which demonstrated uniform Cu distribution on the nanowire. Adapted with permission[178]. Copyright 2012, Royal Society of Chemistry. 31

Figure 21. Schematic illustration of conducting paths and the transport mechanism that explain the properties of invariant set and reset voltages against different distances between electrodes. (a) Demonstration that oxygen vacancy filament connects to the gold core in the center of nanowire because the distance between two electrodes is much larger than the thickness of the Ga_2O_3 shell thickness. (b) Indication that the oxygen vacancy channel can link to the gold core due to the smaller diameter compared to the distance. (c) *I-V* characteristic of a single gold-in Ga_2O_3 core-

shell nanowire with different distances between electrode and the inset is the SET chip image. Theses set and reset voltages are almost the same with different distances. Adapted with permission[179]. Copyright 2012, American Chemical Society. 31

Figure 22. Simulation of electric field distribution around the femtosecond laser irradiated TiO_2 nanowire-Au electrode bridging structure at a polarized laser wavelength of 800 nm. The color scale indicates the magnitude of the generated electric field. (b) SEM images of bridged TiO_2-Au structure after fs laser irradiation. Inset shows magnified joints and the presence of spot welding. (c) Memory level profiles for femtosecond laser irradiated TiO_2-Au memory units. Repeatable memory behavior with selectable levels is displayed. Adapted with permission[148]. Copyright 2016, Wiley-VCH. 33

Figure 23. Hydrothermal grown TiO_2 nanowire (nanorod) arrays on different substrates, (a) Ti foil, adapted with permission[192]. Copyright 2008, American Institute of Physics. (b) Si substrate, adapted with permission[193]. Copyright 2010, AIP Publishing LLC. (c) graphene nanosheets (inset, cross-sectional view of the as-grown TiO_2-graphene-TiO_2 heterostructures), adapted with permission[194]. Copyright 2011, Wiley-VCH. (d) FTO glass substrate. Adapted with permission[191]. Copyright 2009, American Chemical Society. 35

Figure 24. Schematic diagram of the fabrication process for TiO_2 nanowire network based device on Ti foil. 39

Figure 25. Characterization of TiO_2 nanowires, (a) Top view SEM image (inset, statistical summary of diameters of ~100 nanowires), (b) HRTEM image, yellow arrows indicate the crystalline defects (inset, TEM image of TiO_2 nanowires), (c) Raman spectrum, (d) XRD results, (e) Ti 2p XPS spectrum and (f) O 1s XPS spectrum 41

Figure 26. *I-V* characteristic curve of the Al/TiO_2 nanowire networks/Ti device (left inset, schematic diagram of interfaces in the device in the pristine state. Right inset, optical photo of an actual fabricated device on Ti foil) 42

Figure 27. *I-V* characteristic curve of the Al/TiO_2 nanowire networks/Ti device under different voltages 44

Figure 28. Schematic illustration of (a) SET and (b) RESET process of the Al/TiO_2 nanowire networks/Ti device 45

Figure 29. *I-V* characteristic curves of the Al/TiO_2 nanowire networks/Ti device with different thicknesses of the nanowire layers via the control of the hydrothermal growth time, (a) 4 h growth time, (b) 12 h growth time, (c) 16 h growth time and (d) 24 h growth time................................ 46
Figure 30. *I-V* characteristic curves under positive (a) and negative (b) sweeping voltages on a double-logarithmic scale 47
Figure 31. (a) Endurance and (b) retention performance of the Al/TiO_2 nanowire networks/Ti device 48
Figure 32. Schematic diagram of the fabrication process of TiO_2 NRA with seed layer, top right: optical photo for a fabricated TiO_2 NRA based device with Al top electrode. 53
Figure 33. Morphology of TiO_2 NRAs prepared with a seed layer (a) low magnification top-view SEM image, (b) high magnification top-view SEM image (inset: 70° tilted cross-sectional view), (c) TEM image of a single TiO_2 nanorod, (d) HRTEM image of a TiO_2 nanorod (inset: SAED pattern of the same nanorod)... 55
Figure 34. SEM images of TiO_2 NRA prepared without a seed layer, (a) Low magnification, (b) High magnification (inset, 70° cross-sectional view). Even though there seems a thin continuous layer at the base of the nanorod arrays, this thin layer did not engineer the orientation compared with the pre-applied seed layer on the surface of FTO substrate... 55
Figure 35. GIXRD characterization of the seed layer, TiO_2 NRAs prepared with and without a seed layer 56
Figure 36. XPS spectra of TiO_2 NRA prepared with a seed layer: (a) survey, (b) Ti 2p and (c) O 1s... 58
Figure 37. XPS spectra of TiO_x seed layer: (a) survey, (b) Ti 2p and (c) O 1s 58
Figure 38. XPS spectra of TiO_2 NRA prepared without a seed layer: (a) survey, (b) Ti 2p and (c) O 1s 59
Figure 39. *I-V* curves of (a) Al/TiO_2 NRA/TiO_x layer/FTO device and (b) Al/TiO_2 NRA/FTO device for 100 successive cycles (for each figure, left inset: *I-V* curve for a typical cycle and right inset: schematic design of the device) 60
Figure 40. Endurance study of Al/TiO_2 NRA/FTO device under voltage sweeping.................. 62
Figure 41. Cell uniformity performance check by examining the current response at specific read voltage for different cells (a) Al/TiO_2 NRA/FTO devices and (b) Al/TiO_2 NRA/TiO_x layer/FTO device. (The standard deviations are from the summary of 10 repeated *I-V* sweeping cycles). For

the Al/TiO_2 NRA/FTO devices, the ON/OFF ratio is relatively small, which is difficult to distinguish between two different resistance states in the application of ReRAM devices. Furthermore, the big variation in current response among different cells (for example, the LRS current response for cell No.2 is in the same range of the HRS current response for cell Nos. 8-10) also make the Al/TiO_2 NRA/FTO devices not suitable for the ReRAM devices in the electronic industry. Comparatively speaking, the Al/TiO_2 NRA/TiO_x layer/FTO devices displayed a better cell uniformity of the electrical performance in terms of the relatively stable and low HRS current and larger ON/OFF ratios. Even though there is a variation in the LRS current response among different cells, all the ON/OFF ratios are big enough for distinguishing from two different states. 62

Figure 42. (a) Endurance and (b) retention performance of Al/TiO_2 NRA/TiO_x layer/FTO device 63

Figure 43. Cumulative probability curve for LRS and HRS resistances of Al/TiO_2 NRA/TiO_x layer/FTO device for ~550 cycles........ 64

Figure 44. Log-log *I-V* response for the Al/TiO_2 NRA/TiO_x layer/FTO device, (a) Positive region and (b) Negative region 66

Figure 45. Log-log *I-V* curves of (a) LRS and (b) HRS at different temperatures, (c) ON/OFF ratio vs. temperature, (d) Linear fit for LRS resistance, (e) ln(*I*) vs. 1000/*T* and corresponding fits at specific read voltages and (f) activation energy $\Delta E = E_c - E_{trap}$ calculated from the slopes in (e) plotted as a function of *V*. The standard deviations for (c), (d) and (e) are from the statistical average of 15 repeatable cycles. All measurements were carried out under ambient atmospheric conditions. 67

Figure 46. Schematic representation of the switching mechanism in fabricated Al/TiO_2 NRA/TiO_x layer/FTO device, (a) cross-sectional design, (b) pristine state, (c) positive bias, $0 \rightarrow V_{TFL}$, traps are partially filled, (d) positive bias, $V_{TFL} \rightarrow 4$ V $\rightarrow 0$ V, traps are fully filled, the device has transitioned from HRS to LRS........ 68

Figure 47. (a) *I-V* curve for Al/TiO_2 NRA/TiO_x layer/FTO device under different SET voltages and (b) demonstration of 4-level memory performance under cyclic voltage sweeping........ 69

Figure 48. (a) *I-V* curves of Al/TiO_2 NRA/TiO_x layer/FTO device at different SET voltages and (b) demonstration of 6-level memory response in cyclic voltage sweeping........ 69

Figure 49. Log-log *I-V* curves for Al/TiO_2 NRA/TiO_x layer/FTO device at different SET voltages (a) V_{set}=2 V, (b)V_{set}=3 V, (c) V_{set}=4 V, (d)V_{set}=5 V, (e) V_{set}=6 V 70
Figure 50. Slope of *I-V* curve of Al/TiO_2 NRA/TiO_x layer/FTO devices in the region with $V>V_{TFL}$ for different SET voltages (average of 10 cycles at each SET voltage). The *I-V* curve in this region is found to have a slope of $1/\theta$ based on SCLC theory where θ is $\theta=1/(1+N_t/N_c(exp(-q(V_a-V_{TFL})/KT))$. Then $ln(1/\theta)-1$ is inversely proportional to the applied SET voltage. For our device, the V_{TFL} is small and nearly constant (~1 V) for different SET voltages (V_a), so different SET voltages all result in sharply increasing current with the slope decreasing at higher SET voltage. These properties confirm that current flow in fabricated Al/TiO_2 NRA/TiO_x layer/FTO devices is controlled by a SCLC mechanism. 71
Figure 51. Material characterization of $H_2Ti_3O_7$ nanobelts, (a) SEM image, inset shows a magnified view of the selected region. These images reveal that the nanobelts have a rectangular cross-section with a width of 50-200 nm and a length of several μm. (b) TEM image, (c) HRTEM image (arrows point out defects in the crystalline structure), (d) O1s XPS spectra. The peak at 532.5 eV is attributed to oxygen vacancies (concentration ~26.33%), while the small shoulder at 534.2 eV is attributed to the OH^- group in the $H_2Ti_3O_7$ nanobelts (concentration ~ 2.95%). The strongest peak arises from oxygen in the lattice. (e) Ti 2p XPS spectra, (f) XRD characterization of $H_2Ti_3O_7$ nanobelts and their characteristic peaks indexed from the JCPDS database (No. 47-0561). Some characteristic peaks of $H_2Ti_3O_7$ are indicated with arrows. 77
Figure 52. Comparison of contact geometry for nanowire vs. nanobelt. (a) Scanning TEM (STEM) image of a representative nanobelt and (b) its corresponding line-scan obtained from electron energy loss spectroscopy. This indicates that the nanobelt has a width of ~230 nm and a height of ~55 nm, with a width-to-height ratio of 4.2:1. These dimensions are consistent with a quasi-rectangular cross-section. (c) Schematic diagram showing the contact morphology at the Au electrodes for nanowire vs. nanobelt structures. 78
Figure 53. EPSC response, (a) schematic of a synapse, (b) schematic of the nanobelt device for the synaptic response study and SEM image of nanobelt device, (c) EPSC performance for a series of 50 ms pulses with amplitudes 8, 10, 12, 15, 18 and 20 V, respectively, (d) summary of EPSCs and the corresponding calculated energy consumption, where the average currents and corresponding standard deviation are calculated from the current responses over 2000 cycles as

shown in (f), (e) EPSC during 10 cycles of EPSC excited as in (c), the interval period among adjacent cycles is 20 s. (f) EPSC evolution over 2000 cycles with pulse amplitudes as in (c). ... 81

Figure 54. Short-term plasticity response. (a) Current enhancement for 10 consecutive, identical 8 V pulses. PPF and PTP are defined as shown, (b-c) Relationship between gained weight (%) for PPF and PTP vs. the time interval between two consecutive pulses. The fitted exponential curves $y=A_1\times\exp(-x/t_1)+y_0$ are shown. For the PPF, $A_1=0.625$, $t_1=0.499$ s, $y_0=0.053$ while for PTP, $A_1=4.722$, $t_1=0.707$ s, $y_0=0.124$, (d-f) Accumulating current response on excitation with 100 identical consecutive pulses plotted vs. (d) time interval between pulses (50 ms duration, 20 V pulse), (e) pulse duration (50 ms interval, 20 V pulse), and (f) pulse amplitude (pulse duration and interval are 50 ms). 84

Figure 55. Current accumulation vs. number of identical consecutive 10 V pulses. The pulse duration, T, is as shown. 84

Figure 56. Evolution of the potentiation response on application of up to 2200 identical pulses. The pulse duration for each pulse is as indicated. Pulse amplitude is 10 V. 85

Figure 57. Potentiation and depression response. (a) 100, +20 V 100 ms pulses followed by 100, −10 V 100 ms pulses. The test was repeated for 10 cycles. Current was measured by a 2 V, 100 ms read pulse immediately after each potentiation and depression pulse. (b) Expanded view of the highlighted segment in (a). (c) Test over 50, 000 pulses with 50 potentiation and 50 depression pulses as before. The response in the last 5 cycles is shown. (d) Test carried out to illustrate the large number of potentiation and depression states. Each cycle involved 2200, +10 V, 100 ms pulses followed by 2200, −6 V, 100 ms pulses. P and D indicate potentiation and depression, respectively. 86

Figure 58. Potentiation and depression response. (a) 10 cycles of potentiation and depression response for 100 consecutive, 100 ms, +20 V pulses followed by 100 consecutive, 100 ms, −10 V pulses. A 2 V read voltage was applied after each pulse to obtain the current, (b) Expanded view of the area (A) in (a) demonstrating current potentiation. (c) Expanded view of the area (B) in (a) demonstrating current depression. 87

Figure 59. Potentiation/depression characteristics and current response for up to 50,000 pulses illustrating the robustness of the system and (b-f) demonstrated expanded view in selected region (B-F) in (a). P and D in (b-f) indicate potentiation and depression, respectively. 87

Figure 60. Current response for 2200 positive (+10 V) and negative (−6 V) pulses with identical durations of 100 ms, respectively. 88

Figure 61. Nonlinear transmission characteristic of single positive and negative sweeping behavior. (a) *I-V* characteristics of the single nanobelt device at positive sweeping voltages (0 to 10 V then back to 0 V). (b) *I-V* characteristics of the single nanobelt device at negative sweeping voltages (0 to −5 V then back to 0 V). (c) The curve of current response from (a) and (b) versus time. 4 cycles of potentiation and depression by sweeping voltage is demonstrated. (d) The conductance variation of the device with the sweeping cycles in (c). Reproducible potentiation (P) and depression (D) can be observed. 88

Figure 62. Potentiation and quasi-depression response for different negative pulse amplitudes (a-c) 100 consecutive 20 V, 100 ms pulses followed by 100 consecutive −15 V, 100 ms pulses. (d-e) 100 consecutive 20 V 100 ms pulses followed by 100 consecutive −20 V, 100 ms pulses. All the pulses have a duty cycle of 50%. The current responses in (b) (c) (e) and (f) are extracted after each pulse at a 2 V read voltage.. 89

Figure 63. Learning and forgetting response and STP-to-LTP transition induced by repeated stimulation. (a) Learning and forgetting curve with 50, 500 ms, 20 V pulses. Current during relaxation was read at 2 V. (b) Current decay curve and its fit to the equation of $I=I_0+Ae^{-t/\tau}$, where I_0=1.16 nA, A=20.9 nA and τ is 25.64 s. (c) Current decay behavior with the number of pulses up to 400 and (d) time constant summary up to 400 pulses.. 91

Figure 64. Material characterization of $Na_2Ti_3O_7$ nanobelts. (a) SEM image, (b) TEM image, (c) HRTEM image (arrows point out defects in the crystalline structure), (d) Ti 2p XPS spectrum (e) O1s XPS spectrum. The peak at 532.52 eV is attributed to oxygen vacancies (concentration ~ 25.00%), while the small shoulder at 535.3 eV is attributed to the OH- group in the $Na_2Ti_3O_7$ nanobelts (concentration ~ 8.12%). The strongest peak arises from oxygen in the lattice (concentration ~ 66.89%). (f) Na 1s XPS spectrum. 92

Figure 65. EPSC performance in a single $Na_2Ti_3O_7$ nanobelt device. (a) SEM image of the device. (b) EPSC response with a series of 12, 16, 18 and 20 V pulses 100 ms long pulses. (c) The current response for different pulse amplitudes and calculated energy consumption. The calculated energy consumption is 630 pJ at a voltage of 12 V. (d) Summary of EPSC over more than 150 cycles with different pulse amplitudes. Variation in the current response for the 12 V pulse can be attributed to a low signal-to-noise ratio in the low current measurement.. 92

Figure 66. Current accumulation and potentiation/depression response in a single $Na_2Ti_3O_7$ nanobelt device. (a) Current obtained under excitation with consecutive, identical, +20 V, 300 ms pulses. The total number of pulses is 75. (b) Potentiation and depression response over 5 cycles. Each cycle consists of 100 identical +20 V, 300 ms, pulses followed by 100 identical −10 V, 300 ms, pulses. (c) Detailed view for the selected region (A) for the current potentiation in (b). (d) Detailed view for the selected region (B) for the current depression in (b). 93

Figure 67. Spike rate-dependent synaptic plasticity of single $Na_2Ti_3O_7$ nanobelt devices under excitation with positive/negative pulses. (a) Evolution of current accumulation during 10 consecutive, +20 V, 400 ms, pulses, (b) current response vs. number of pulses with different positive pulse durations.. 94

Figure 68. Synaptic mechanism study. (a) Temperature dependence of the current decay following excitation with 50 consecutive +20 V, 500 ms, pulses. The current was read at 2 V, (b) Plot of ln(1/τ) vs. 1000/T showing exponential dependence. The linear fit from Equation 3 is shown and implies that the diffusion activation energy is *E*=0.33 eV.. 96

Figure 69. *I-V* curve for the electrical contact at the interfaces between Au electrodes and the $H_2Ti_3O_7$ nanobelt. 96

Figure 70. *I-V* curves for the volatile rectification behavior of single $H_2Ti_3O_7$ nanobelt device. The original *I-V* curve is obtained by sweeping from −5 to +5 V. The positive rectification curve is obtained by sweeping from −5 V to +5 V immediately after the positive sweeping from 0 to 10 V. Similarly, the negative rectification curve is obtained by sweeping from −5 V to +5 V immediately after the negative sweeping from 0 to −10 V. The sweeping speed is 50 mV s^{-1}........................ 97

Figure 71. Plot of ln(1/τ) vs. 1000/T and linear fit from Equation 3 in main text for (a) single $Na_2Ti_3O_7$ and (b) single TiO_2 nanobelt devices from temperature dependence of current decay behavior following excitation with 100 consecutive +20 V, 500 ms, pulses. The calculated diffusion activation energy are E=0.41 eV and E=0.42 eV, respectively.................................... 97

Figure 72. Schematic of the synaptic response mechanism. (a) In the initial state oxygen vacancies are distributed randomly throughout the nanobelt, and a Schottky barrier is formed at each Au/nanobelt interface. (b) With applied positive electric field, the accumulation of oxygen vacancies at the left interface of the Au/nanobelt leads to a reduction in the strength of the Schottky barrier, increasing the conductivity of the device. Back diffusion of these defects in response to

the concentration gradient would recover the Schottky barrier, leading to a decrease in the current response... 98

Figure 73. Material characterization of TiO_2 nanobelts and the architecture of a TiO_2 nanobelt device (a) SEM image, (b) HRTEM image with void defects highlighted in red, (c) O 1s XPS spectrum, (d) Low-magnification SEM image of Pt-Pt electrodes fabricated on the SiO_2 wafer, (e) High magnification SEM image for a typical pair of interdigitated Pt-Pt electrodes, (f) SEM image of a typical TiO_2 nanobelt device on paired electrodes. 104

Figure 74. Threshold switching sweeping performance for single TiO_2 nanobelt devices. (a) Sweeping performance at 20 V at a constant sweeping rate of 0.1 V/s plotted on a linear scale, (b) corresponding I-V curve plotted on a semi-logarithmic scale. (c) LRS/HRS ratio for the device at the reading voltage of 3 V over 80 sweeping cycles in (b). (d) Sweeping voltage dependent performance and summary of LRS/HRS ratio at the reading voltage of 3V. (e) Statistical summary for the LRS/HRS ratio among 26 devices having identical geometries. (f) Endurance performance for 10,000 cycles at room temperature. The inset shows one cycle of the applied pulses, where the 2 V, 50 ms and -2 V, 50 ms pulses are used as read pulses. The device did not fail during the measurement, showing a high degree of robustness. 106

Figure 75. I-V sweeping performance for the single TiO_2 nanobelt device at different sweeping voltages. At low sweeping range such as 2 V ((a) and (d)), the device demonstrated a typical charging and discharging cyclic voltammetry curves of a capacitor with a series resistor. However, at higher bias such as 6 V ((b) and (e)) and 10V ((c) and (f)), the volatile threshold switching performance is observed with the capacitive contribution from low bias. Inset of each figure shows the equivalent circuit of the devices at different sweeping voltages. 108

Figure 76. Sweeping behavior for Pt-TiO_2 nanobelt-Pt device under sweeping voltages at (a) 2 V, (b) 3 V, (c) 4 V, (d) 5 V, (e) 6 V. (f) 8 V, (g) 10 V, (h) 15 V and (i) 20 V in a linear scale. 109

Figure 77. Sweeping behavior for Pt-TiO_2 nanobelt-Pt device under sweeping voltages at (a) 2 V, (b) 3 V, (c) 4 V, (d) 5 V, (e) 6 V. (f) 8 V, (g) 10 V, (h) 15 V and (i) 20 V in a semi-logarithmic scale... 110

Figure 78. I-V sweeping performance for TiO_2 nanobelt on paired Au-Au electrode, (a) line scale and (b) semi-logarithm sale, and on paired Ti-Ti electrodes, (c) line scale and (d) semi-logarithm sale. The sweeping rate is 0.1 V/s for both measurement.. 111

Figure 79. Transition from a capacitor behavior to a memristor with a capacitive contribution for single TiO_2 nanobelt device on paired Au-Au electrodes.. 112
Figure 80. I-V sweeping performance for TiO_2 nanobelt on paired Pt-Pt electrodes with different concentration of defect by further annealing the obtained TiO_2 nanobelts at 700 ^oC for 2 h. (a) TEM and (b) HRTEM characterization of nanobelts, (c) I-V sweeping performance, a highly insulating capacitive performance is obtained for the TiO_2 nanobelt device with very few defects 112
Figure 81. Charge transport mechanism for a single TiO_2 nanobelt device. (a) Temperature dependent sweeping performance at temperatures from 293 K to 353 K. A constant sweeping rate of 0.1 V/s is used for all the measurements. Four stages associated with application of a bias are highlighted for fitting with different equations. (b) $ln(J/T^2)$ as a function of inverse temperature ($1/T$) for voltages in Stage I. (c) $ln(R)$ as a function of temperature $(T^{-1/4})$ at different low voltages in Stage I. (d) $ln(J)$ as a function of inverse electric field $(1/E)$ at different temperatures for voltages in Stage II. (e) $ln(J)$ as a function of inverse electric field $(1/E)$ at different temperatures for different voltages in Stage III. (f) $ln(J/T^2)$ as a function of inverse temperature ($1/T$) in Stage IV at different temperature. Five sweeping cycles were obtained at each temperature and average values and standard deviations were calculated correspondingly. (g) Schematic diagram of DOS distribution of pure TiO_2 vs TiO_2 containing defects. (h) Schematic band diagram for the TiO_2 nanobelt device at zero bias. (i-l) Schematic band diagram for the TiO_2 nanobelt device in Stage I, II, III and IV, respectively.. 117
Figure 82. Charge transport mechanism study for a single TiO_2 nanobelt device. (a) $ln(J/T^2)$ as a function of square root of the electric field ($E^{1/2}$) at various temperatures in Stage I. (b) $ln(J/T^2)$ as a function of square root of the electric field ($E^{1/2}$) at various temperatures in Stage IV. All the measurement is the same as described in Figure 81. 118
Figure 83. Thermal admittance spectroscopy characterization for TiO_2 nanobelt devices. (a) Capacitance and (b) loss spectra measured in the dark at 0 V with an AC perturbation of 50 mV. (c) Arrhenius plot of the observed thermal emission rates as a function of temperature. The linear fit shown in red reveals the activation energy and the attempt-to-escape frequency. (d) Density of trap states (DOS) at different temperatures as a function of the demarcation energy E_ω.......... 118
Figure 84. Sweeping rate dependent I-V performance for single TiO_2 nanobelt device on paired Au-Au electrodes. 119

Figure 85. Threshold dynamics of the single TiO_2 nanobelt devices emulating a nociceptor. (a) Schematic of neuron transmission for a nociceptor. (b) Schematic diagram for threshold switching in the device. The threshold value will determine the output current response, below which, no or insignificant current response is detected. (c) Response of the single TiO_2 nanobelt device to single pulses with different amplitudes from 3 V to 10 V. (d) Response of the single TiO_2 nanobelt device to number of pulses at various pulse amplitude. 121

Figure 86. Response of the single TiO_2 nanobelt device to a single 5 V pulse with different durations. 122

Figure 87. Nociceptive behavior. (a) No adaptation response, different voltage amplitudes for the devices to reach the saturation state. (b) Relaxation response, 50 ms 10 V EPSC transient current over 4 cycles, current is read at 2 V, (c) Temperature dependent current transient behavior read at 2 V after the 50 ms 10 V was applied, inset, activation energy from analysis of transient current at different temperatures. (d) Schematic diagram of the allodynia and hyperalgesia features with increasing stimuli intensity in normal (uninjured) and damaged (injured) conditions. (e) Current response for a train of pulses from 3 V to 7 V (50 ms) after the stimulation of high amplitude pulses (15 V and 20 V pulse, 50 ms), showing allodynia and hyperalgesia characteristics. (f) Current response to a train of pulses from 3 V to 7 V (50 ms) after the stimulation of high amplitude pulse (15 V 50 ms pulse) with different time interval, showing allodynia and hyperalgesia characteristics. 124

Figure 88. Proposed nanowire crossbar structure for the integration of nanowire devices for the practical application in neuromorphic computing 129

List of Tables

Table 1. Fractional percentage of oxygen (O 1s) states in samples (%) 59

List of Abbreviations, Symbols and Nomenclature

1D	One-dimensional
E_c, E_v	Energy level at the conduction band minima and valence band maximum,
E_{trap}	Energy level of electron traps
E_F	Fermi level
V_a, V_{set}, V_{TFL}	Applied voltage, SET voltage, Trap-filled limited voltage
DOS	Density of states
ECM	Electrochemical Metallization Memory
EDS	Energy disperse X-ray spectroscopy
EELS	Electron energy loss spectroscopy
EPSC	Excitatory Current Response
(FE)SEM	(Field-emission) scanning electron microscopy
FRAM	Ferroelectric Random-Access Memory
FTO	Fluorine doped tin oxide
HRS	High resistance state
(HR)TEM	(High-resolution) Transmission Electron Microscopy
(GI)XRD	(Grazing Incidence) X-ray diffraction
I-V curves	Current-voltage curves
LRS	Low resistance state
LTP	Long-term potentiation
MIM	Metal-Insulator-Metal structure
MRAM	Magnetic Random-Access Memory
NRA	Nanorod arrays
PPF	Paired-pulse potentiation
PRAM	Phase-change Random Access Memory
PTP	Post-tetanic potentiation
RAM	Random Access Memory
ReRAM	Resistive switching Random Access Memory

SAED	Selected-area electron diffraction
SCLC	Space-Charge-Limited Current
STP	Short-term potentiation
TAT	Trap-Assisted Tunneling
TCM	Thermochemical Reaction Memory
VCM	Valence Change Memory
VRH	Variable Range Hopping
XPS	X-ray photoelectron spectroscopy
XRD	X-ray diffraction

Chapter 1. Introduction

1.1. Background

In recent years, memristive or resistive switching random access memory (ReRAM) devices based on metal-semiconductor or insulator-metal structures are gaining wide attention for the applications of non-volatile memory devices[1-4], logic circuits[5-8] and neuromorphic computing[9-13] due to the advantages of simple two-terminal structure, fast switching speed, high density and low power consumption, etc[14-19]. During the last decade, a wide range of materials have been proposed for the potential applications of non-volatile memory devices, such as binary transition metal oxides, perovskite-type complex transition metal oxides, large band gap high-*k* dielectrics, carbon based materials, organic materials, etc[18]. However, despite great efforts in exploring the nature of the switching mechanism, many details and the contribution of different factors in memristive devices are still completely unknown[20].

Furthermore, compared with the commonly used thin film nanomaterials, memristive devices based on one-dimensional (1D) nanomaterials demonstrate promising advantages such as confined structure for conductive filament formation and rupture, potential of being integrated into high-density devices, etc. High-quality electrical performance of fabricated memristive devices together with good stability and reproducibility can be realized[21]. In terms of the applications of non-volatile memory, to compete with complementary metal oxide semiconductor field effect transistors in conventional memory and logic circuits, the newly proposed memristive devices should satisfy the requirements of electroforming-free, low-power consumption, good retention and endurance performance, distinguishable resistance states and the potential to display multilevel memory performance[22]. However, a cost-effective way to fabricate 1D nanomaterial based memristive devices that satisfy the requirements for the applications is still lacking. Hydrothermal synthesis of metal oxide nanowires has been widely used in the application of sensing[23-25], dye-sensitized solar cells[26, 27], supercapacitor[28], field emission[29], etc. But research on memristive devices fabricated using hydrothermal-grown nanowires and their corresponding switching mechanisms are still lacking. Furthermore, considering the surface to volume ratio of 1D nanomaterial, the defects on the surface would have a crucial effect on the electrical performance. It would therefore be interesting to study the effect of the surface defects on the resistive switching behavior for 1D nanomaterial based memristive devices via different ways.

1.2. Objectives

The objective of the research program to date has been to examine the resistive switching performance, application in memory and artificial synapse applications and corresponding switching mechanism based on 1D TiO_2 nanomaterials synthesized by hydrothermal methods. Three different of nanowire configuration are explored for the memristor device fabrication and characterization, i.e., TiO_2 nanowire networks, TiO_2 nanorod arrays, and a single TiO_2 nanowire. The main objectives are:

(1) Synthesis and characterization of TiO_2 nanowire networks on Ti foil by a single hydrothermal process, characterization of obtained Al/TiO_2 nanowire networks/Ti foil ReRAM devices and study its corresponding switching mechanism,

(2) Resistive switching performance study of TiO_2 nanorod arrays (NRAs) based ReRAM devices on fluorine doped tin oxide (FTO) glass substrate by a hydrothermal method. Improvement of the resistive switching performance of TiO_2 NRA based ReRAM device via the introduction of a seed layer and exploring its corresponding switching mechanism,

(3) Study the feasibility of using a single TiO_2 nanobelt and its precursors during the hydrothermal process for the application of memory device and artificial synapse emulation for the application of neuromorphic computing.

(4) Explore and propose the switching mechanism of 1D nanomaterial based memristive devices, rational design investigation of 1D nanomaterial based memristive devices that could be used as resistive switching memories and artificial synapse that satisfy different requirements.

1.3. Organization of the thesis

The research focused on 1D TiO_2 nanomaterial based memristive devices for the applications of non-volatile memory devices and artificial synapse and the corresponding switching mechanism. The proposal is organized as follows:

- **Chapter 1** is an introduction describing the background and objectives of this work.
- **Chapter 2** covers the literature review of memristive devices focusing on its main electrical characterization parameters and a brief summary of switching mechanism. Furthermore, previous studies of memristive devices based 1D nanomaterial with different methods including hydrothermal methods would be discussed as well.

- **Chapter 3** presents the study of low-power resistive switching memory based on TiO_2 nanowire networks on a Ti foil by a single hydrothermal method. A switching mechanism based on the migration of oxygen vacancies is proposed.
- **Chapter 4** presents the study of the resistive switching memory performance based on TiO_2 NRAs on FTO substrate. The study proposed that the introduction of a seed layer on the surface of FTO substrate would significantly improve the electrical performance of the obtained ReRAM devices which demonstrated low-power bipolar multilevel memory behavior. The switching mechanism of the obtained devices is controlled by space-charge-limited current (SCLC) in which the oxygen vacancies in the seed layer and the individual nanorods function as trap centers.
- **Chapter 5** presents the study of the precursors of the TiO_2 nanobelts during the hydrothermal process, that are $Na_2Ti_3O_7$ and $H_2Ti_3O_7$ nanobelts for the memristive performance and the potential artificial synapse emulation for the neuromorphic computing applications.
- **Chapter 6** further study the charge transport mechanism in the single TiO_2 nanobelt device and propose a unique voltage-dependent threshold switching mechanism for the emulation of artificial nociceptor devices.
- **Chapter 7** summarizes the research conclusion based on the above chapters and proposes the future work.

Chapter 2. Literature Review

The focus of this chapter is to provide the literature review of the recent development of memristive devices, resistive switching random access memory (ReRAM) and the summary of switching mechanisms. Electrical performance and characterization of TiO_2 nanomaterial based memristive devices are also summarized.

2.1. Memristive devices and ReRAM devices

2.1.1. What are memristor/memristive devices?

Memristor, or memristive device was suggested as the fourth elemental circuit unit theoretically by Chua in 1970s[30, 31]. Even though its experimental history can go back two centuries[32], it has not received much attention afterwards until the link between the experimental resistive switching device base on nanoscale TiO_2 and the memristor concept was established in 2008 by Strukov *et al.* in Hwelett Packard[33]. Ever since, the interest in resistive switching devices dramatically increased in recent years. The research in the past decade has demonstrated that memristors promise to be disruptive in electronics for the high speed, high scalability, low power consumption, and compatibility with complementary metal-oxide semiconductor. Therefore, memristor devices can be exploited for the next generation of non-volatile memory devices[1-4], logic operations or analog circuits[5-8] and the emulation of synaptic dynamics by functioning as the fundamental element for the realization of artificial neural networks, promising for neuromorphic computing applications[9-13]. A class of memristor devices used in memory application is often called resistive random access memory (ReRAM).

2.1.2. What are ReRAM devices?

With the critical dimension downscaling to 5 nm to 2021 in the semiconductor industry as demonstrated by the latest International Roadmap for Devices and Systems (IRDS 2018), the memory devices are faced with great opportunities and challenges. Conventional silicon-based flash memories, consisting of a metal-oxide-semiconductor field-effect transistor with an additional floating gate in each cell are reaching their miniaturization limit in the near future, not only for technical reasons, but also for physical limitations such as large leakage currents[16]. Furthermore, the silicon-based memories are also suffering from their own disadvantages. Therefore, novel types of non-volatile memories which could satisfy the requirement of fast

operation speed, good endurance and retention performance, and low power consumption are greatly demanded. In recent years, mainly four types of random access memories (RAM) have been proposed: ferroelectric RAMs (FRAMs)[34], magnetic RAMs (MRAMs)[35], phase-change RAMs (PRAMs)[36] and resistive switching RAMs (ReRAMs)[20]. Among these different types, ReRAM has been gaining a wide attention as the next-generation non-volatile memory devices due to its advantages of simple metal-insulator-metal (MIM) structure, fast operation speed, robust retention and endurance performance, promising scalability potentials and multilevel data storage capability[15, 20, 37]. Furthermore, resistive switching in thin film devices may enable functional scaling of logic and memory circuits beyond the limits of complementary metal-oxide-semiconductors. A resistive switching memory cell in a ReRAM is generally built by a capacitor-like MIM structure, in which an insulating or resistive layer 'I' is sandwiched between two conductors 'M', as demonstrated in Figure 1. Resistive switching occurs when the device could be electrically switched between at least two different resistance states: a high resistance state (HRS) and a low resistance state (LRS). The resistance values at a certain reading voltage is different when the resistive switching occurs, and HRS, by definition, refers to the state with the high resistance values. Similarly, LRS refers to the state with the low resistance values. By applying either a voltage or a current to a cell, reversible switching between the LRS and HRS can be achieved. Once switched, the cell retains the particular resistance state level for a long time. One example of the nanoscale crossbar for non-volatile memory devices can be seen in Figure 2[38]. The I-V sweeping performance of ReRAM devices is a typical characteristic feature of memristor devices, i.e., its I-V sweeping performance is pinched to zero when the voltage drop across the origin point [39, 40] It should be noted that ReRAM devices is only a typical example of memristive devices.

The materials used for ReRAM devices can be classified into five types[18]: (1) binary transition metal oxides, e.g., TiO_2, Cr_2O_3, CuO_x, FeO_x, WO_3, Ta_2O_5, NiO, etc., (2) Perovskite-type complex transition metal oxides, e.g., (Ba, Sr)TiO_3, Pb(Zr_xTi_{1-x})O_3, $BiFeO_3$, etc., (3) Large band gap high-k dielectrics, e.g. Al_2O_3, SiO_2, and Gd_2O_3, (4) Carbon based materials, e.g., graphene oxide[41-43], amorphous carbon materials[44], etc., (5) emerging organic and bio-materials, such as poly(methyl methacrylate) (PMMA)[45] and silk protein[46]. Combination of these materials is also used for different functional devices[47-50].

Two schemes of resistive switching types in ReRAM devices are generally observed, unipolar and bipolar with respect to the electrically polarity required for the resistive switching to occur [51]. Switching is unipolar when the procedure does not depend on the polarity of the voltage and current signal. A system in its HRS (OFF state) is switched by a threshold voltage into the LRS (ON state) as sketched in Figure 3(a). In contrast, the characteristic is called bipolar when the set to an ON state occurs at one voltage polarity and then reset to the OFF state on reversed voltage polarity, as demonstrated in Figure 3(b).

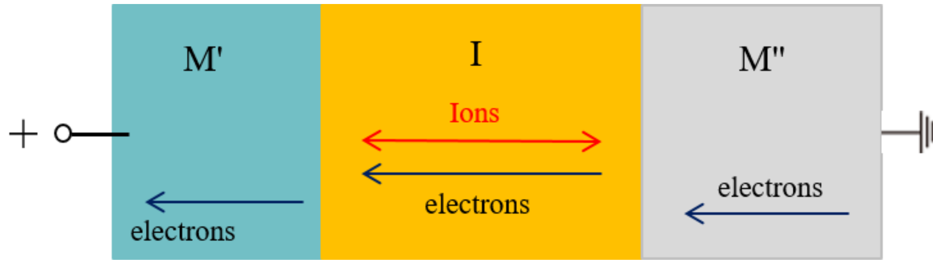

Figure 1. Schematic diagram of MIM structure in ReRAM devices, in which M' and M" denote the metal electrode and I denote the insulator (switching layer).

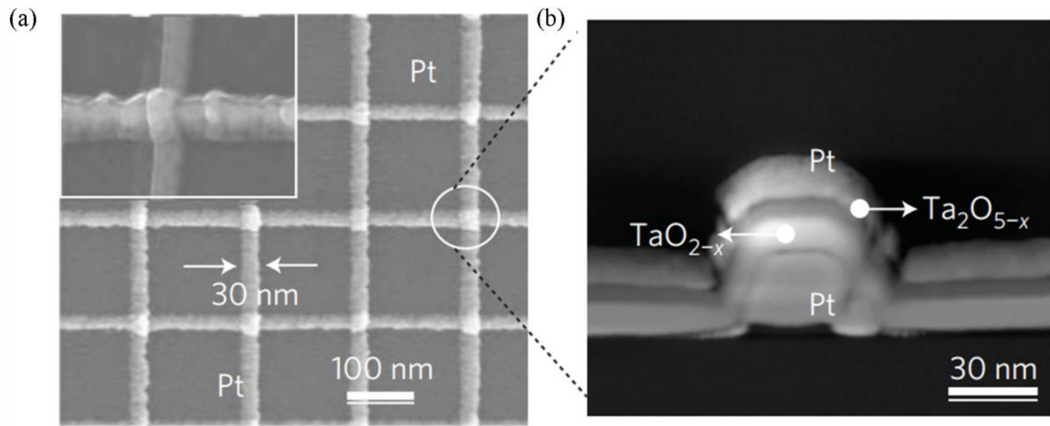

Figure 2. An example of the non-volatile Pt/Ta_2O_{5-x}/TaO_{2-x}/Pt ReRAM devices, (a) Scanning electron microscopy image of a 30-nm crossbar arrays of devices with the inset showing a magnified single device, (b) Transmission electron microscopy cross-section of a 30-nm crossbar cell. The insulating Ta_2O_{5-x} layer can be seen along with the TaO_{2-x} base layer, with a total thickness of 30 nm. Adapted with permission[52]. Copyright 2011, Nature Publishing Group.

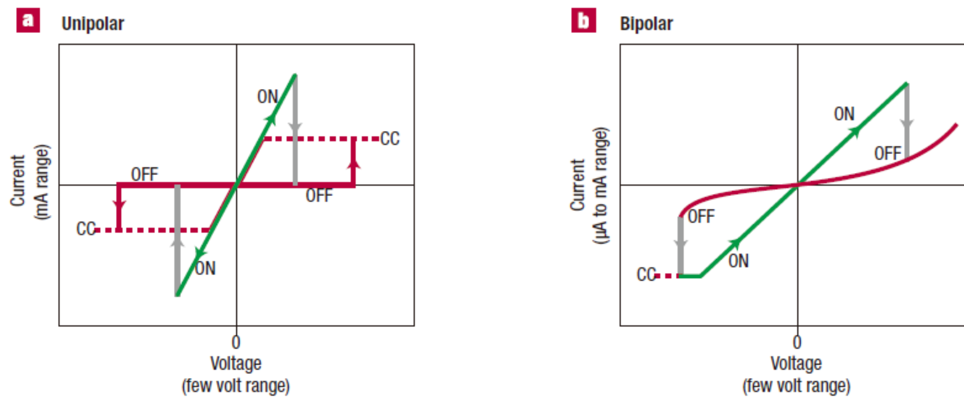

Figure 3. Sketches for classification of resistive switching, (a) Unipolar switching, and (b) bipolar switching. (CC: compliance current). Adapted with permission[51]. Copyright 2007, Nature Publishing Group.

2.1.3. Characteristic parameters of ReRAM devices

As a future candidate for the next-generation non-volatile memory devices, the ReRAM devices should satisfy several performance requirements to replace Flash memory and dynamic RAM (DRAM) devices. There are a number of characteristic parameters and requirements for ReRAM devices:

(1) Resistance ratio: A typical large ON/OFF ratio>10 is generally required for ReRAM devices to distinguish from different states and allow for small and highly efficient sense amplifiers and, hence, reasonably cost-effective ReRAM chips. Furthermore, to realize the high-density data storage, the multi-level memory performance of ReRAM devices is highly demanded. This would require distinguishable ratios at the read voltage among different states[53].

(2) Endurance: Endurance denotes how many write cycles with alternating SET and RESET process can be performed until the ON or OFF states falls out of the predefined acceptance window. Contemporary Flash memory show a maximum number of write cycles between 10^3 and 10^7, depending on the type. Through careful design, a high endurance up to 10^{12} cycles is achieved in Ta_2O_{5-x}/TaO_{2-x} devices[52].

(3) Retention: Retention is the ability of a memory cell to keep stored information if the cell is not addressed. A data retention time of >10 years is demanded for universal non-volatile memories devices. Furthermore, the retention time should be checked under elevated temperature condition (85°C). Normally, the retention of the current proposed ReRAM devices is in the

range of 10^3 to 10^6 s. Further extrapolated retention for different states in actual studies has demonstrated to satisfy this requirement.

(4) Write and read operation: write voltage should be in the range of a few hundred mV (not lower, in order to be compatible with scaled CMOS) to a few V. The length of the write voltage pulses is typically <30ns. This allows for a competition with DRAM devices and outperforms Flash, which has a programming speed of some 10 μs. Currently, a 5 ns switching speed has already been achieved in Ag/Mn:ZnO/Pt memory devices[54]. An even faster switching speed as low as ~100 ps has also been demonstrated for tantalum pentoxide based ReRAM devices, which is very promising for non-volatile memory devices as well as other high speed circuit applications[55]. In terms of read operation, read voltages need to be significantly smaller than write voltages in order to prevent an unintentional write during the read operation.

(5) Multilevel memory potential: The potential of multilevel memory performance of ReRAM memory devices is highly demanded for high-density information data storage. Furthermore, distinguishable resistance states among each level is also required. Typically, four or five level memory performance could be generally achieved for most of the proposed devices[56, 57]. Further increasing the number of the levels poses great difficulties[58].

(6) Scalability and power consumption: To realize the high-density non-volatile memory as well as emerging applications in logic operation and neuromorphic devices, the power consumption of the ReRAM devices should be very low to compete with the complementary metal oxide memory and logic circuits[22]. But this is very challenging to achieve currently. Furthermore, the high-density storage for the future development of memory devices would require a small feature size as well as eliminating the sneak current. All these requirements are very challenging for current ReRAM devices to achieve simultaneously. With the development of e-beam lithography, a 10×10 nm^2 crossbar structure has already been achieved in Hf/HfO_x devices with a low energy consumption[4]. Furthermore, a low power consumption with the programming current as low as 10^{-10} A and $<10^{-12}$ A for SET and RESET switching, respectively has also been achieved in Pt/NbO_x/TiO_y/NbO_x/TiN stack devices[22].

It should be noted even though one or several above-mentioned requirements have already been achieved for some devices, there is still lacking realizations of devices to achieve all of the requirements. Further studies are highly demanded for the achievement of excellent low power consumption, good uniformity and reliability, high scalability prospects, robust retention and

endurance, distinguishable resistance states and potential to demonstrate multilevel memory performance for the next-generation non-volatile memory devices.

2.1.4. Summary of resistive switching mechanism

2.1.4.1. Cation migration---Electrochemical Metallization Memory (ECM)

Depending on the driving force, interface reaction, ionic transport for the resistive switching, the switching mechanism of memristive devices can be primarily divided into thermal, electrical and ion-migration induced resistive switching. Ion migration mechanism could be further subdivided into cation-migration cells, which are based on the electrochemical growth and dissolution of metallic filaments, and anion-migration cells, in which electronically conducting paths of sub-oxides are formed and removed by local redox processes[51]. However, the mechanism of memristive devices, for example the nature of filament formation and their growth dynamics are still under debate nowadays and the following paragraphs provide a brief summary of current research status.

In cation-based memristive devices, active electrodes, such as Ag and Cu are responsible for the resistive switching process. This kind of switching mechanism of memristive devices is called electrochemical metallization memory (ECM). As demonstrated in Figure 4, the initial stage of the device is HRS, with no reaction of Ag (Figure 4(A)). When the positive voltage is applied to the top Ag electrode, an oxidation reaction occurs at the Ag/insulating layer interface (Figure 4(B)). The obtained Ag ions (cations) would migrate towards to the bottom inert electrode (Pt in our case) and reduce to Ag atoms (Figure 4(C)). The accumulation of the Ag atoms from the bottom towards top electrode would finally bridge the two electrodes, switching the device from HRS to LRS. It should be noted that the corresponding current response is very steep and quickly reaches the compliance current, which is used for preventing the device from permanent breakdown (Figure 4(D)). The negative voltage would induce the rupture of the filament by repelling the Ag atoms back to Pt electrode and switches the device from LRS to HRS again (Figure 4(E)).

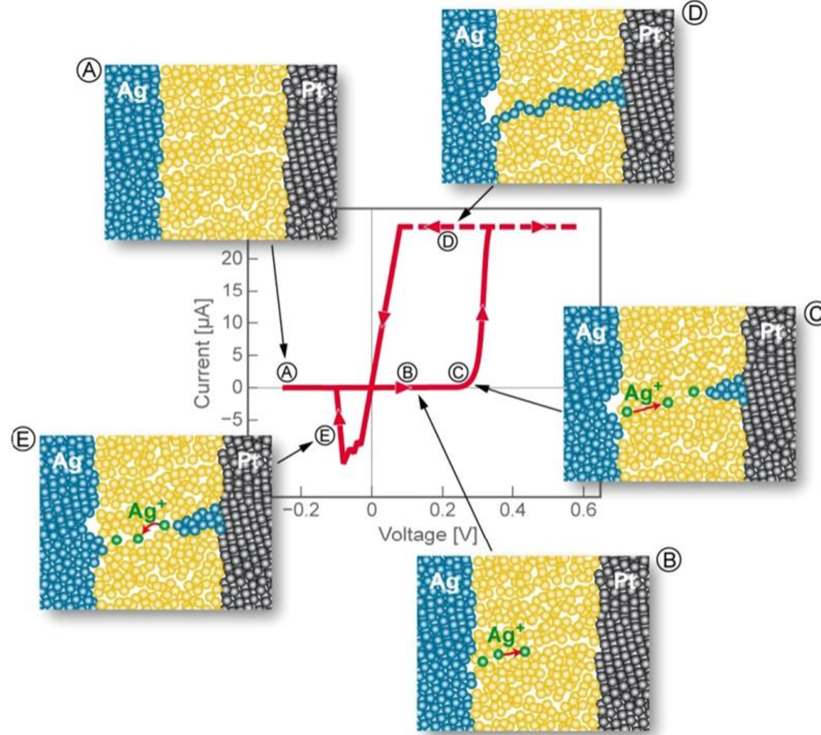

Figure 4. Schematic current-voltage characteristic of ECM devices and corresponding mechanism, in which active electrode (Ag, Cu, etc.) contributes to the resistive switching. Voltage is applied to the Ag electrode while Pt electrode is grounded. In the initial stage, no Ag ions is in the insulator layer (A); when under positive applied voltage to the active electrode, an oxidation reaction occurs at the active electrode/insulating layer interface. Then, the injected Cu or Ag ions migrate within the electric field through the insulating layer (B), At the inert electrode/insulating layer interface another electron-transfer reaction occurs. The Cu/Ag ions are reduced, and a Cu/Ag filament starts to grow towards the anode after having formed a stable Cu/Ag nucleus (C). The bridging between the anode and cathode with Cu/Ag filament switches the device from HRS to LRS. While the rupture of the filament with a negative voltage switches the device from HRS to LRS. Adapted with permission[37]. Copyright 2015, Wiley-VCH.

To investigate the resistive switching mechanism of ECM device, Choi *et al.* investigated the current response and the microstructure morphology change of Cu/GeTe layer/Pt-Ir device by in-situ transmission electron microscopy (TEM), as demonstrated in Figure 5[59]. It could be observed that multiple nano-filaments (with a diameter of ~5 nm) formed under the negative voltage (Figure 5(d), and these filaments become strengthened when a further -0.8 V voltage was applied (Figure 5(e)). The current response increased with the increase of the negative voltage, suggesting that these filaments serve as conducting paths. The observation of the filament formation and rupture is in agreement with the proposed ECM mechanism as demonstrated in Figure 4.

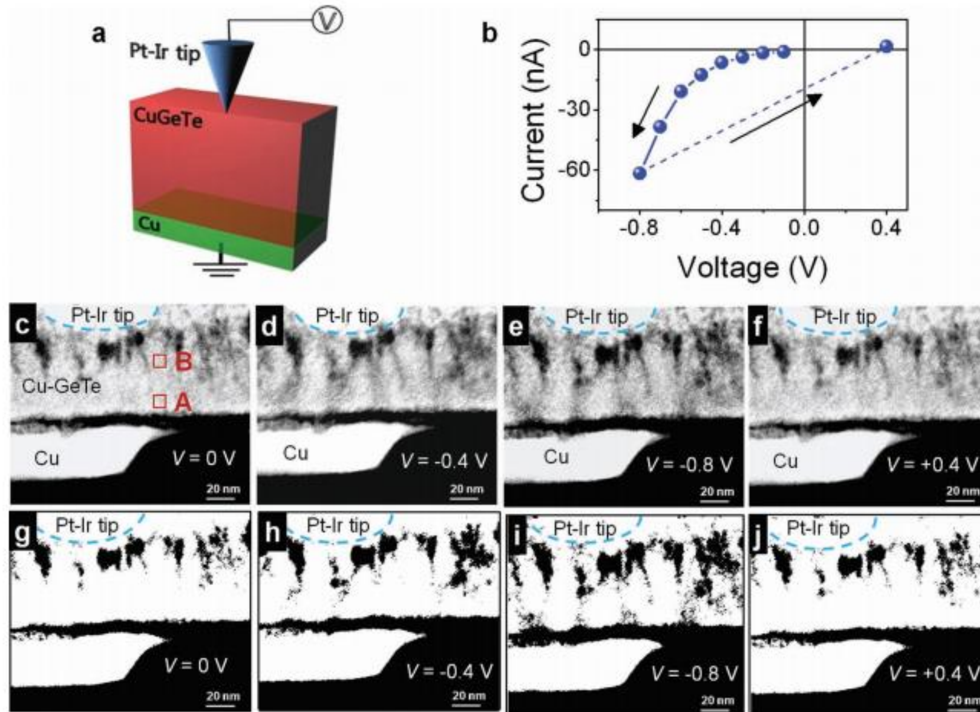

Figure 5. Demonstration of the switching mechanism in ECM devices. (a) Schematic design of the in-situ experiment set-up. (b) In-situ current-voltage (*I-V*) response. (c)-(f), Cross-sectional STEM images obtained after the voltage applications of 0, -0.4, -0.8, and +0.4 V, respectively. (g)-(j) Black-and-white images converted from the raw STEM images of (c)-(f), respectively. Adapted with permission[59]. Copyright, 2011, Wiley-VCH.

However, the migration of active ions in the insulating layer highly depends on mobility of cations in the dielectric layer. Yang *et al.* demonstrated an in-situ measurement of the Ag/amorphous Si/W structure in which the Ag ions migrate towards the W electrode at a much slower rate, which leads to the reduction of the Ag atoms inside of the dielectric layer in contrast to the W/dielectric interface[60]. The result would be the filament formation from the Ag electrode towards the W electrode, as shown in Figure 6. This process will lead to a dramatic current response increase as demonstrated in Figure 6(b). In comparison, Yang *et al.* also showed that the filament formation agrees with the demonstration in Figures 4 and 5 (bottom W electrode towards Ag top electrode) when the dielectric layer changed from amorphous Si to SiO_2.

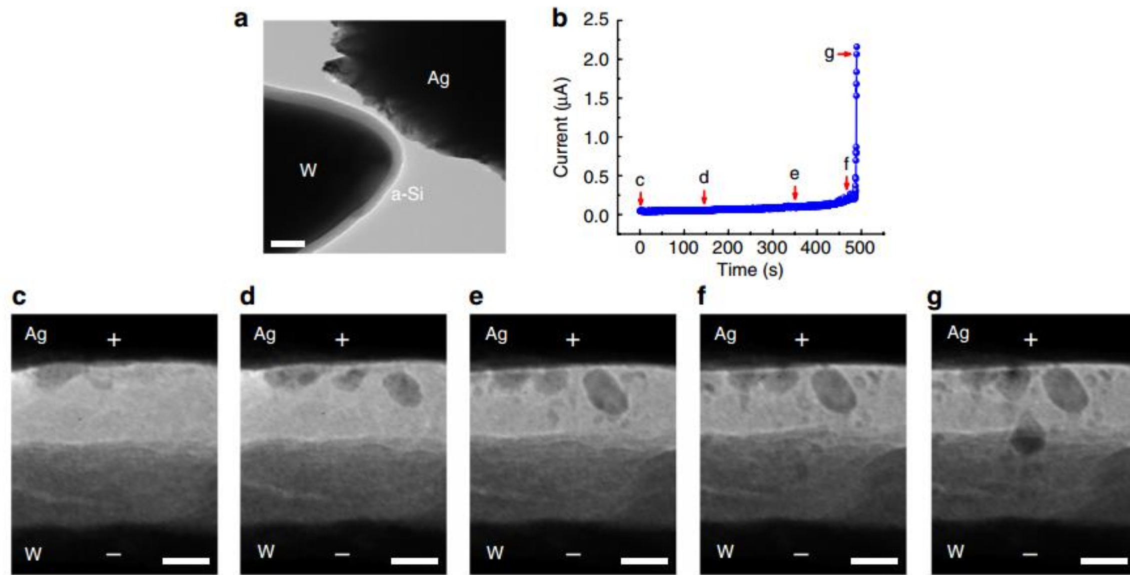

Figure 6. In-situ TEM observation of conductive filament growth in vertical Ag/a-Si/W memories. (a) Experiment set-up. The Ag/a-Si/W resistive memory device was fabricated on a W probe in TEM, scale bar, 100 nm. (b) *I-t* characteristic recorded during the forming process at a voltage of 12 V. (c-g) TEM images of the devices corresponding to data points c-g in (b) recorded during the forming process. Scale bar, 20 nm. It could be seen the filament formation in (g) from the top Ag towards W electrode. Adapted with permission[60]. Copyright 2012, Nature Publishing Group.

2.1.4.2. Anion migration---Valence Change Memory (VCM)

In anion-migration based memristive devices, the resistive switching mechanism is mostly based on the migration of anions (defects in the insulating layer). Typically, oxygen vacancies in N-type metal oxide material (such as TiO_2, ZnO, etc.) and metal vacancies or interstitials in P-type metal oxide materials (such as NiO, CuO, etc.) are generated or rearranged in the switching layer. Correspondingly, the material of the filament is different from the original switching layer in terms of the electronic properties, the so-called valence change memory. Take ZrO_2 as an example, as shown in Figure 7. Positive charged oxygen vacancies would rearrange into a filament (or a plug). In the OFF state (Figure 7(A)), the filament consists of n-type oxide and a potential barrier in front of the left electrode. By applying a negative voltage, oxygen vacancies from the plug part of the filament are attracted into the barrier (Figure 7(B)), which results in a significant decrease of the barrier height and width due to a local reduction process, which turns the cell into the ON-state (LRS) (Figure 7(C)). For the RESET process, a positive voltage is applied to the active interface which repels the oxygen vacancies (Figure 7(D)), leading to a local re-oxidation, and turns the cell into the OFF state (HRS) again.

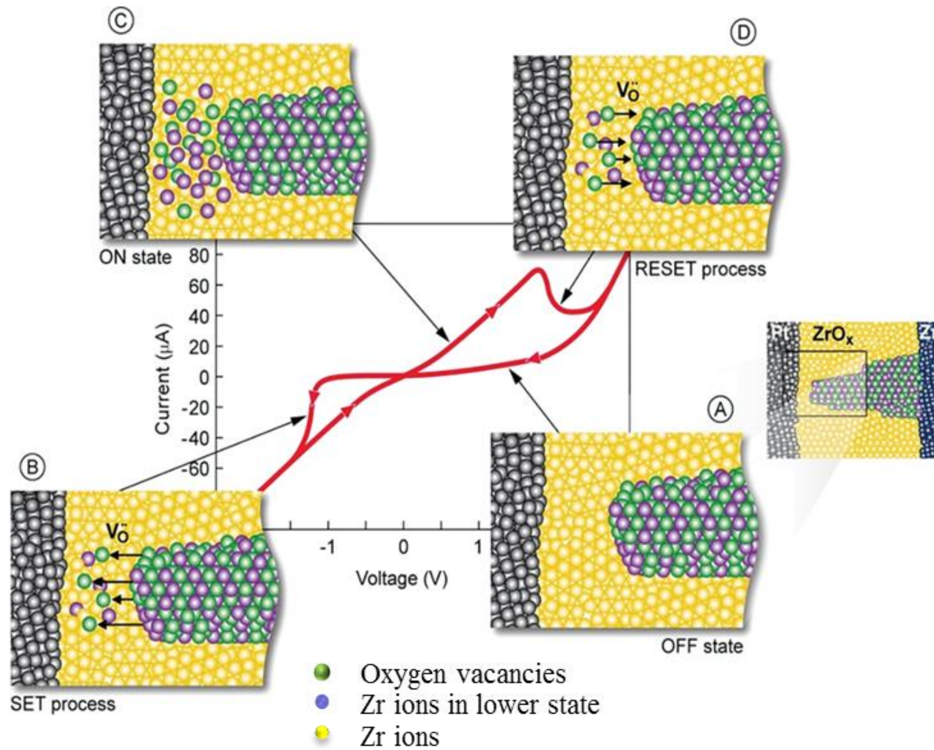

Figure 7. Schematic current-voltage characteristic of VCM devices and corresponding mechanisms, in which the defects of insulating layer (vacancies, interstitials, etc.) are responsible for the resistive switching. Both active and bottom (right) electrode are inert. When a negative voltage is applied to left electrode, oxygen vacancies migrate towards this electrode (B). Hence, the insulating region between the sub-stoichiometric well-conducting filament and the active electrode becomes conducting and the VCM cell switches to the LRS (C). By reversing the voltage-polarity oxygen vacancies are pushed back from the active electrode (D) and finally the HRS is reestablished (A). Adapted with permission[37]. Copyright 2015, Wiley-VCH.

The conducting channels in metal oxide responsible for the resistive switching behavior were first demonstrated by Kwon, D.H. *et al.,* in which the Magnéli phase of TiO_2 was identified from cross-sectional high resolution TEM in combination with its corresponding selected area electron diffraction pattern and fast Fourier transformed images (Figure 8)[61]. The conical structure of Ti_4O_7 nano-filament with the diameter of 15 and 3 nm at the cathode and anode interfaces respectively is bridging top and bottom electrodes. Due to its high conductivity nature, the bridged Ti_4O_7 nano-filament would switch the device to ON state. The formation of the Magnéli phase in TiO_2 under electric field is believed to be the generation of oxygen vacancies as the first step, following by the rearrangement of these oxygen vacancies until a certain critical density reached, leading to the formation of the ordered structure (Magnéli phase). In theory, surpassing the limit that sustains the

original crystal structure would result in the local phase transformation into the metallic Magnéli phase in the Ti-O system[62].

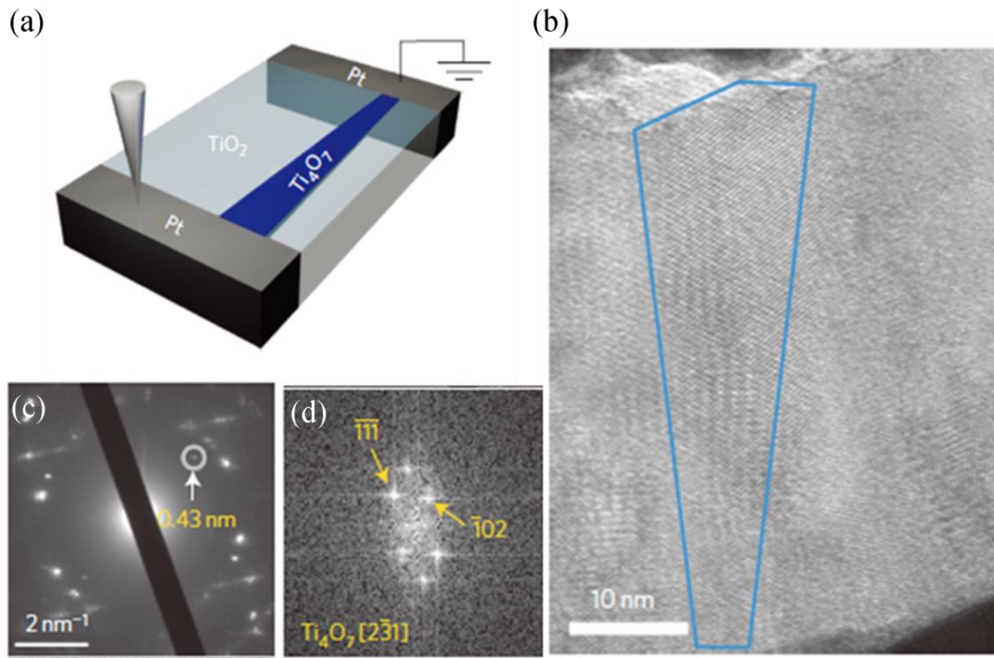

Figure 8. Schematic diagram of the experimental scanning probe set-up in the TEM chamber, (b) High resolution TEM image of structure after the electroforming process. (c) Selected area electron diffraction and (d) fast Fourier transformed micrograph of the Magnéli phase. Adapted with permission[61]. Copyright 2010, Nature Publishing Group.

Park *et al.* further demonstrated the observation and identification of conductive channels in the tantalum oxide based memristive devices ($Pt/SiO_2/Ta_2O_{5-x}/TaO_{2-x}/Pt$) via in-situ TEM characterization techniques[63]. Each resistance state (set, reset and breakdown) was confirmed with the in-situ current-voltage measurement. Figure 9 demonstrated the microstructure morphology evolution of the switching TaO_{2-x} layer under different states of the resistive devices. The cross-sectional high-angle annular dark-field (HAADF) scanning TEM (STEM) images clearly demonstrated the voltage–induced variations in Ta-rich areas during SET (Figure 9a), RESET (Figure 9b) and breakdown (Figure 9c) operations. The converted color images from the Figure 9a-c further displayed the conductive paths in the switching layer in Figure 9d-f. The metallic TaO_{1-x} phase (yellow region) was confirmed by electron energy loss spectroscopy (EELS) analyses. At the SET state, we could observe large conductive clusters that were clearly percolated into the switching TaO_{2-x} layer, as demonstrated in Figure 9a and 9d. After RESET switching, the conductive clusters in the TaO_{2-x} layer became smaller and their percolation paths were partially

interrupted (Figure 9b and 9e). After the breakdown operations, the areas of conductive clusters significantly increased because of almost-filled Ta-rich clusters (Figure 9c and 9f).

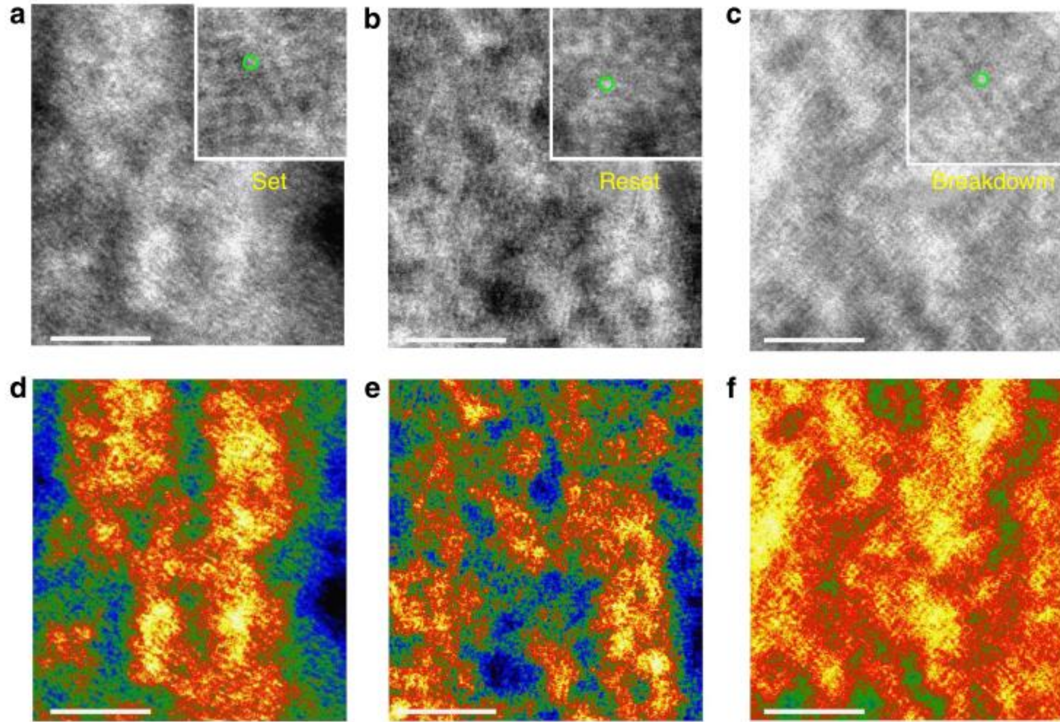

Figure 9. Voltage-induced morphology evolution in the TaO_{2-x} layer. (a-c) Cross-sectional HAADF-STEM images showing the structural evolution after the set (a), reset (b) and breakdown (c) operations. Bright area: Ta-rich phase (conducting paths) and dark area: non-conducting clusters. Inset shows the atomic resolution STEM images exhibiting the individual Ta atoms (green circles). (d-f) Pseudocolour maps converted from the raw images of a-c, respectively. Yellow: Ta-rich phase (conducting paths), blue: non-conducting clusters. Bright and yellow regions in (a-f) are regarded as conductive percolation paths. Scale bar, 3 nm. Adapted with permission[63]. Copyright 2013, Nature Publishing Group.

Moreover, for metal oxides which contain different types of defects, the involvement of theses defects in resistive switching performance has not been excluded. Wedig A. *et al.* demonstrated that there is a bridge between ECM and VCM in HfO_2, TiO_2 and Ta_2O_5 materials considering the migration of both cations and anions. Cations such as Hf, Ti and Ta ions would form metallic filaments and participate in the resistive switching process[64, 65]. These cations are mobile under electric field and can participate in the resistive switching process in competition with the commonly thought migration of oxygen vacancies in VCM devices. This suggests that the migration of metallic cations (ECM) and migration of anions (oxygen vacancies) can be possible to occur simultaneously in some resistive switching systems considering that both cations and

anions are mobile. A complete transition from VCM to ECM is also realized by interface engineering[64, 66]. The dual effects of anions and cations is also reported theoretically to be crucial in resistive switching behavior of p-type metal oxides[67].

However, in spite of the various materials with similar structures demonstrating similar *I-V* response, the exact nature of the filament formation and rupture and its driving forces are still now under discussion and differs from material-to-material. The reason for the rupture of the filament is still unknown as different researchers proposed different models for their explanations. Other factors, such as concentration of defects in the switching layer, the effect of Joule heating, and crystallinity of the switching layer make resistive switching mechanism of VCM ReRAM devices even more complicated. The direct evidences of the identity of the mobile species in the switching oxides are still lacking[17]. These factors severely hinder the optimization of the performance of the devices and further applications.

Besides these factors, two other factors should also be considered in terms of the electrical performance of VCM based ReRAM devices: work function and oxygen affinity of the active electrode[18]. In theory, the difference between the work function of the electrode and the Fermi level of the metal oxide to a large extent would determine the contact resistance, which could display a rectifying characteristic (Schottky contact) when the difference is big while displaying a linear response when the different is negligible (Ohmic contact). In reality, the surface states at the metal/semiconductor interface will play an important role in determining the contact state behavior. The analysis of the meta/metal oxide interface by taking into consideration of the work function as well as the effect of the surface states should be carefully combined to lead to a convincing conclusion of the contact property. Furthermore, the oxygen affinity of the active electrode also plays a crucial role in the switching mechanism. Interface engineering of the metal/metal oxide was shown to engineer the resistive switching performance of obtained devices[68]. The metal electrode that has a high oxygen affinity would lead to an additional depletion of oxygen ions in the adjacent oxide near the interface and hence, an additional decrease of the barrier supporting the low contact resistance. The interface between electrode and metal oxide should be taken into consideration for the engineering of the performance[69]. The typical example is the Ti electrode on the surface of TiO_2 to generate more oxygen vacancies[70]. In contrast, some other types of metal electrode such as Al would generate an interfacial insulating layer on the surface of the metal oxide,

which would function as reservoir of oxygen vacancies and engineer the resistive switching performance[71, 72].

2.1.4.3. Charge trapping and Detrapping

Another model for the resistive switching performance is based on the physical perspective of electron transport process. In the switching process, the electric field induced the trapping and detrapping of carriers, mostly electrons in the system are responsible for the resistive switching behavior of the devices. Compared with the migration of oxygen vacancies which need higher current (over ~μA), the charge trapping and detrapping could be more likely to happen for the low current resistive switching[22]. The sources of the trap centers can be the defects of the switching materials (mostly, oxygen vacanices[47, 73-75]), additional charge traps such as quantum dots[76], imbedded nanoparticle layer[77] and stacked graphene layers[49]. Typical examples of the *I-V* curves can be fit by a Poole-Frenkel (P-F) conduction mechanism[78], hopping, and a space-charge limited conduction (SCLC) mechanism[79-81]. A schematic illustration of the charge trapping induced resistive switching performance is shown in Figure 10[76].

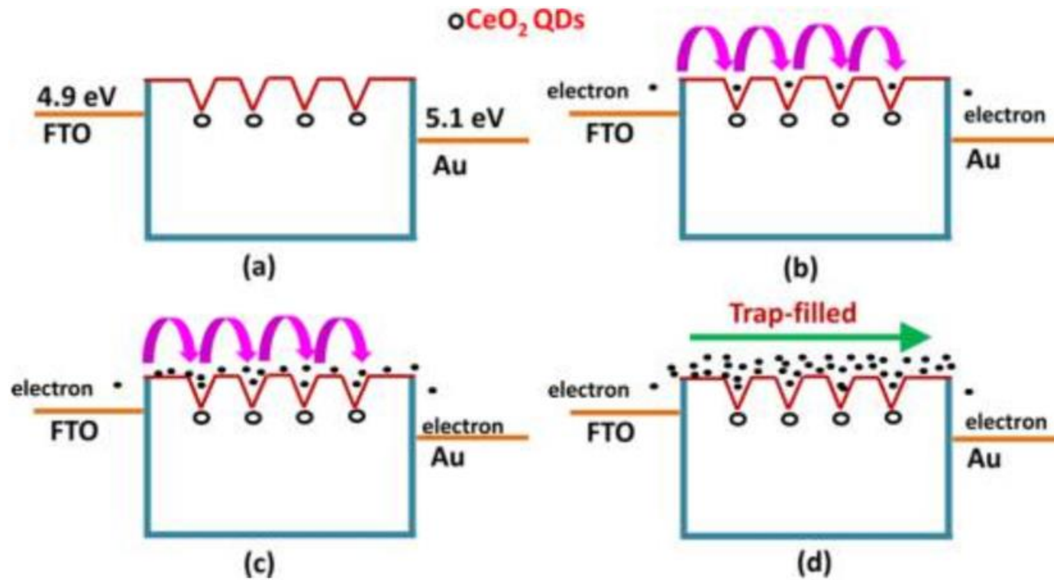

Figure 10. Schematic diagram of for the transport mechanism of charge trapping and detrapping process. (a) Nearly empty traps, (b) thermally generated carrier conduction, (c) traps partially filled and (d) fully filled traps, the device is transitioned from HRS to LRS at (d). The CeO_2 quantum dots function as the trap centers. Reprinted with permission[76]. Copyright 2013) American Chemical Society.

2.1.4.4. Thermochemical reaction (TCM)

In thermochemical reaction-dominated memristive devices, the forming and set process correspond to the thermal decomposition of the storage media and consequent formation of the

conductive filaments. This corresponds to the large voltage that is applied to the pristine devices and switches the device from HRS to LRS. The reset process is triggered by thermal melting of the existing conductive filaments by sweeping the relatively lower voltage. The schematic design is shown in Figure 11.

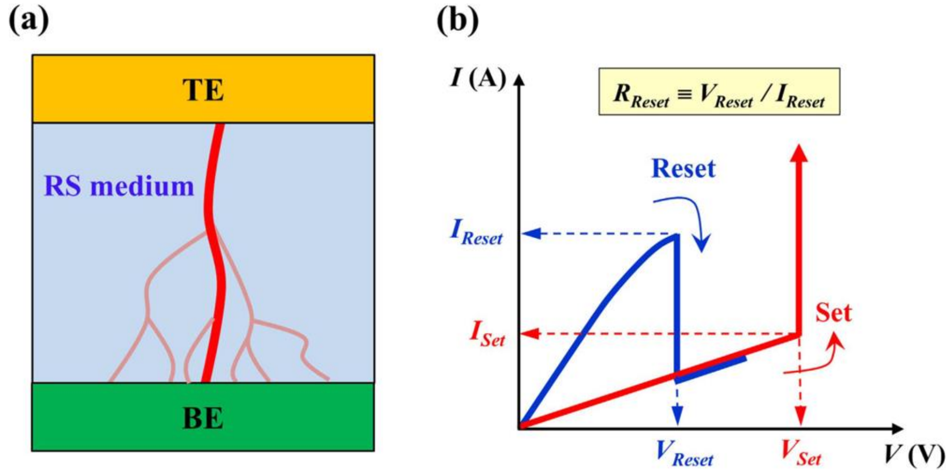

Figure 11. Schematic diagram for filamentary channels in TCM devices and corresponding unipolar resistive switching characteristics. RS: resistive switching, TE, top electrode. BE, bottom electrode. Adapted from Reference[82].

Chen *et al.* demonstrated that the conductive filament in a Pt/ZnO/Pt device is composed of Zn-dominated ZnO_{1-x} by in-situ TEM as shown in Figure 12[83]. Figure 12(a)-(d) displayed the evolution of the conductive filament, growing from the cathode to the anode during the forming process. When large concentrations of oxygen vacancies gather at the cathode, the zinc atoms rearrange their position/structure from ZnO to crystalline Zn-dominated ZnO_{1-x}. Meanwhile the reset process would rupture the filament by migration of the neighboring oxygen ions (Figure 12(e)). The migration of oxygen ions leads to the conversion between Zn-dominated ZnO_{1-x} and ZnO, which result in the resistive switching behavior. The corresponding unipolar *I-V* curve is shown in Figure 12(f)[83].

It should be noted that although different switching mechanisms have been proposed for the ReRAM devices, there is still controversy about the nature of the switching performance. Even for the same type of switching material, the electrical performance of the device also is interpreted differently by different researchers. Our understanding of the nature of the resistive switching is still far from comprehensive. Further study of the mechanism of the switching performance of memristive devices is highly required for the engineering and optimization of the performance and future applications.

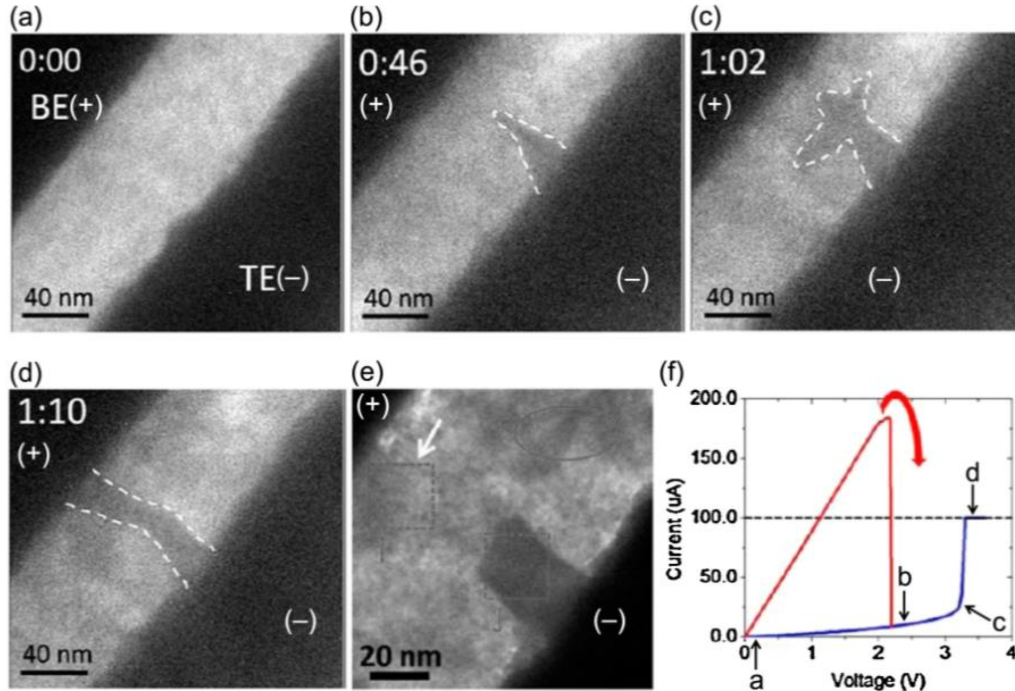

Figure 12. In-situ TEM observation of the evolution of the conductive filaments during forming the subsequent reset process of a Pt/ZnO/Pt cell. (a-d) A series of TEM images corresponding to the data points a-d in (f). The white dashed lines in (b-d) highlight the filament. (e) TEM image obtained after the reset process. (f) The corresponding *I-V* curve of forming (blue) and subsequent reset (red) process. Adapted with permission[83]. Copyright 2013, American Chemical Society.

2.1.5 Applications of memristive devices

2.1.5.1. Multilevel memory for data storage

A multilevel operation is highly desired for next-generation non-volatile memory devices for the application of data storage, and device scalability. Resistive switching devices utilizing the resistance change rather than charge storage have attracted consideration as potential alternatives to conventional charge-based memory devices such as flash memory. Unlike binary state devices, multilevel resistive switching requires relatively well defined and distinguishable resistive states, as well as long retention behavior for each state. In practice it is really challenging to achieve a high number of resistance states. A wide range of materials have demonstrated stable multilevel memory operation performance[49, 58, 84-87]. For example, a 3 bit/cell operation is achieved by WO_x resistive switching devices with high endurance performance[84] as shown in Figure 13. Another research of a graphene oxide thin film device with Ti top electrode demonstrated 4-level storage capabilities, with ultrafast switching speed and high flexibility property[85].

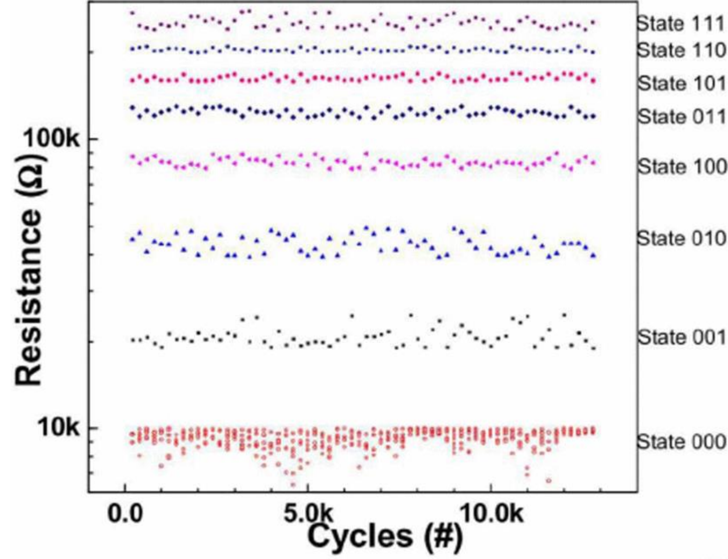

Figure 13. Multilevel memory storage of a WO_x resistive switching memory device with high endurance performance, adapted from Reference[84].

2.1.5.2. Logic calculation

By utilizing the resistance change and its nonvolatile characteristic, memristor devices have also been used for the Boolean operation[7] and further logic computing[6, 88, 89]. Moreover, a memristor device provides the unique characteristic of logic-in-memory operation, capable of constructing an in-memory computation system by merging the function of memory and arithmetic logic unit, which are separated in the conventional von Neumann architecture[89]. J Borgehetti *et al.* firstly demonstrated that the memristive device can enable material implication, a fundamental Boolean logic operation on two variables *p* and *q*, as shown in Figure 14[7]. Linn E. et al. further demonstrated that the passive crossbar memristor devices could demonstrate 14 of 16 Boolean functions in a single bipolar resistive switching or complementary resistive switching cell unit[90]. Xu *et al.* further demonstrated that all the 16 Boolean logic functions can be achieved by diode-integrated single unipolar memristor devices[89]. Furthermore, to eliminate the effect of sneaking current path for the crossbar memristor devices, some other types of memristive structures such as complementary resistive switching performance[5], or connected with a transistor to form a 1T1R[91], a selector device to form a 1S1R[92 1, 93] and a diode device to form a 1D1R[94, 95] structures are also proposed for the logic computing operation.

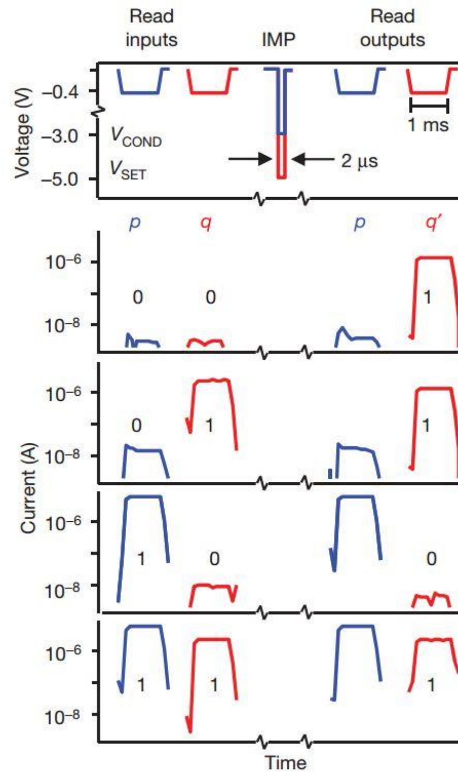

Figure 14. Illustration of material implication logic operation by a memristor device. Adapted with permission[7]. Copyright 2010, Nature Publishing Group.

2.1.5.3. Neuromorphic computing

The development of artificial neural networks that could rival their biological counterparts is very promising and highly desired, especially for the era of Big Data. Compared to conventional digital computers designed from the von Neumann configuration in which the arithmetic/logic units and memory units are separated, the configuration of brain outperform digital computers due to its dramatically different configuration, which could simultaneously operate the arithmetic calculation and memory without the burden of data transmission. The key to the high efficiency of biological systems is the mass connectivity between neurons that offers parallel processing power[10]. The mammalian including human brains outperforms computers in many computational tasks, such as recognizing a complex image much faster and with better fidelity, and yet consumes a tiny fraction of energy used by computers to do this.[96] Indeed, the research on artificial neural networks could be dated back to the 1950s[97-99], where small networks of neurons and functional properties were explored. However, the progress of artificial neural networks has been less remarkable compared with the progress on digital computers due to (1) the difficulty in realizing the device limited by the computer fabrication and (2) the difficulty in accurately modeling the

neural networks[100]. In recently years, driven by the advanced integration electronics fabrication process with nanometer scaling being feasible and highly desired demand to process huge data and information, the research on the neural networks or artificial intelligence, both theoretically and experimentally, are gaining a wide attention around the world.

Implementing neuromorphic computing in hardware would be a great boost for applications involving complex processes such as image processing and pattern recognition. The key component for the neural networks is the artificial neurons and the synapses where the synapses connect the pre-neurons and the post neurons, as shown in Figure 15. Synapses are elemental to information propagation in the central nervous system in the brain as well as body. In most neurons, the presynaptic sites are located either on a dendrite or on the cell body and the human brain is estimated to contain ~10^{14}-10^{15} synapses[100]. Synapses dominate the architecture of the brain and are responsible for massive parallelism, structure plasticity and robustness of the brain. They are also biological computations that underlie perception and learning. The signal transmission in the chemical synapses is mediated by endogenous messenger chemicals, known as neurotransmitters. In brief, the information flow arrives at the axon terminal as an action potential. This action potential triggers the release of a neurotransmitter from a vesicle, whereupon the neurotransmitter binds to a receptor on ion channels, and ions cross the membrane through open channels. This influx of ion produces a synaptic potential in the postsynaptic neuron. When the integrated or total sum of the synaptic potential channels exceeds its threshold, the postsynaptic neuron will fire an action potential, i.e. the neuron responds or conveys information to its connecting neurons and the process continues. After the transmission, the subsequent spontaneous decay of ion concentration at the axon terminal will lead to the presynaptic neuron returning to the previous state.[101, 102] The synaptic weight between two neurons can therefore be precisely adjusted by the ionic flow through them. This dynamic process is at the root of information processing and memory in the brain. A solid state device that can accurately emulate the functions and plasticity of biological synapses in a chemical synapse will therefore be the most important building block of brain-inspired computation systems[103].

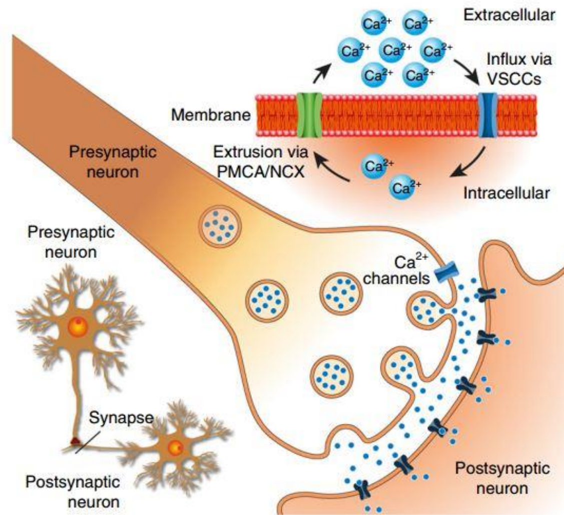

Figure 15. The interaction between presynaptic neuron and postsynaptic neuron. Adapted from Reference[104].

Due to the impressive development of integrated circuits, researchers firstly used traditional semiconductor devices, mostly transistors to emulate the biosynaptic behaviors, which comes at the expense of requiring massively parallel logic cells and switching cells to be constructed, leading to large areas circuits, low efficiency and low speed operation, and high costs.[105] Furthermore, the down-scaling of semiconductor transistors is approaching its physical limits, which push researchers to seek for alternative devices that can emulate the behaviors of biosynapse.

A memristor, as a two-terminal device, bears striking resemblance to the synapse. Indeed, the resistance change of a memristor device can be adjusted by the flow of charge through it, making the device perfect to mimic the dynamics of a biological synapse and also is far more advantageous than transistors due to its simple structures, high switching speed and ability to allow the integrated network to develop complex emergent behaviors. The research of making use of memristor devices for the emulation of biosynapses has seen great progress in the past decade. The research of memristor for the application of neuromorphic computing can be classified as two different aspects: (1) examining new materials, configuration of memristor devices for the emulation of multifunction for the artificial synapse and (2) integration of memristor devices to artificial neural networks for practical applications.

As to the first aspect, great progress has been achieved for the emulation of biosynapses. For example, the formation of Ag conductive filaments controlled by the applied bias in the Ag_2S atomic switches can emulate the learning behavior of the human brain.[106] Furthermore, the same research group demonstrated that the precise control of the Ag filament in the Ag_2S system

resembles the short-term plasticity (STP) and long-term potentiation (LTP), key features for the biological synapses, as shown in Figure 16.[11] Similar behavior is also observed for the valence change memory, where the oxygen vacancies based filaments can also be precisely adjusted by the repeated pulses, leading to the transition from short-term memory to long-term memory[107]. Furthermore, the inner mechanism of the conductive filament formation and rupture is controlled by the ionic migration and diffusion, which can further be used for mimicking the learning and forgetting, relearning, and reinforcement learning behavior[105, 108]. Kuzum et al. demonstrated firstly the memristors devices can undergo Hebbian learning, a fundamental learning rule in the human brain[10]. It was further theoretically demonstrated that the second-order memristor, which take into consideration of not only the conductance of the memristor device, but also the internal dynamics such as accumulated heat, is required to emulate the timing-controlled Ca^{2+} dynamics including frequency-dependent plasticity and timing-based plasiticy[109]. Therefore, by the inner timing mechanism of the memristor devices, the performance of the device can be controlled by the history of the previous performance, this can lead to the paired pulse potentiation (PPF) and paired pulse depression (PPD)[110] and metaplasticity[111-114] . Based on the controlled ion migration by electric field and inner diffusion mechanism, researchers used external or multiterminal electrodes to modulate the synaptic behavior, leading to the emulation of heterosynaptic behavior, providing great potential for the emulation of biosynapses in the human brain[115-120]. A summary of the configuration for the heterosynaptic emulation is shown in Figure 17. Furthermore, for mimicking the human brain, the energy consumption per synaptic event should be in the sub-pJ or even in the fJ energy range, which were achieved by metal oxide thin film based memristor devices[121] and also in an organic nanowire based memristive device[122].

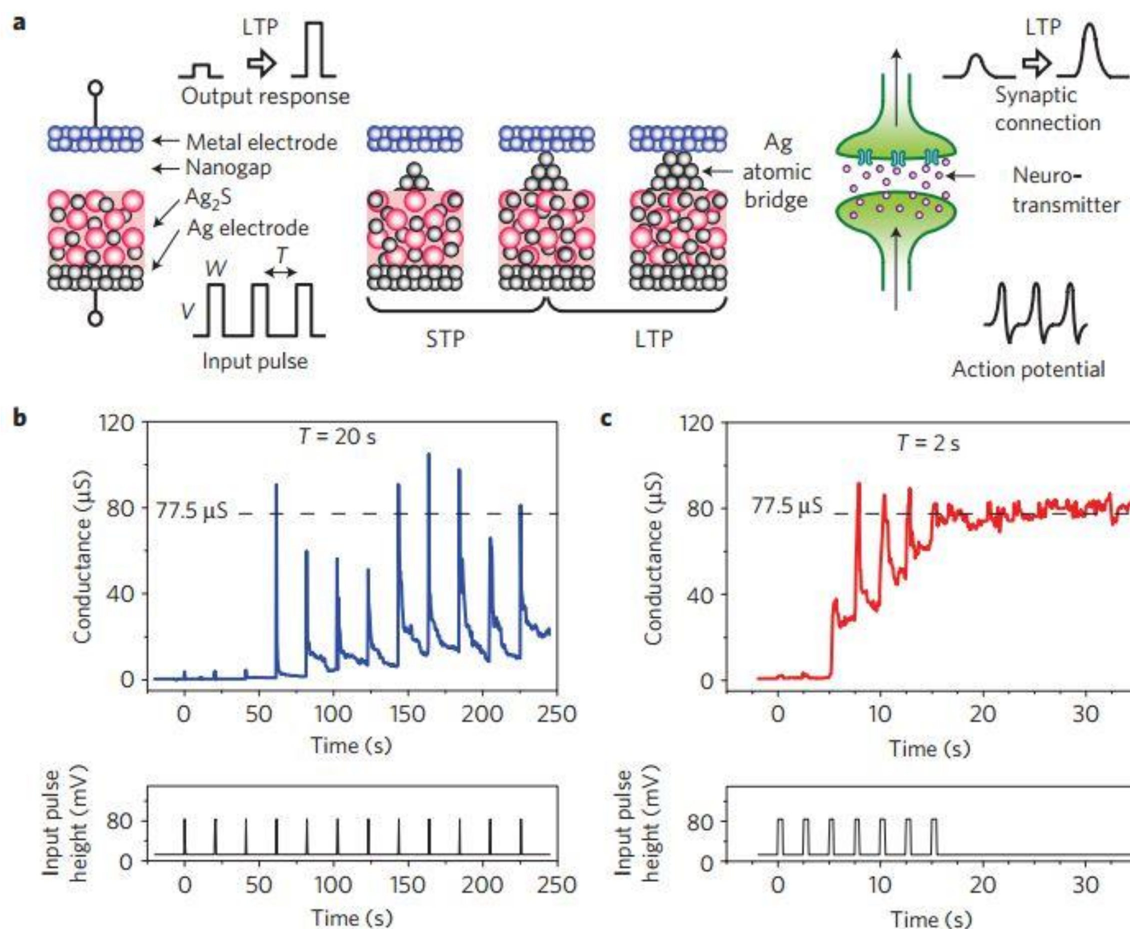

Figure 16. Ag_2S based devices showing short-term plasticity and long-term potentiation, depending on the input-pulse repetition time. (a) Schematic diagram of a Ag_2S synapse and the signal transmission of a biological synapse. Application of input pulses causes the precipitation of Ag atoms from the Ag_2S electrode, resulting in the formation of a Ag atomic bridge between the Ag_2S electrode and a counter metal electrode. When the precipitated Ag atoms do not form a bridge, the synapses work as the STP. After an atomic bridge is formed, it works as LTP. (b) Experimental demonstration of the STP and LTP by recording the change in conductance of the synapse when the input pulses were applied with a relative long intervals of T=20 s and (c) T=2 s. Adapted with permission[11]. Copyright 2011, Nature Publishing Group.

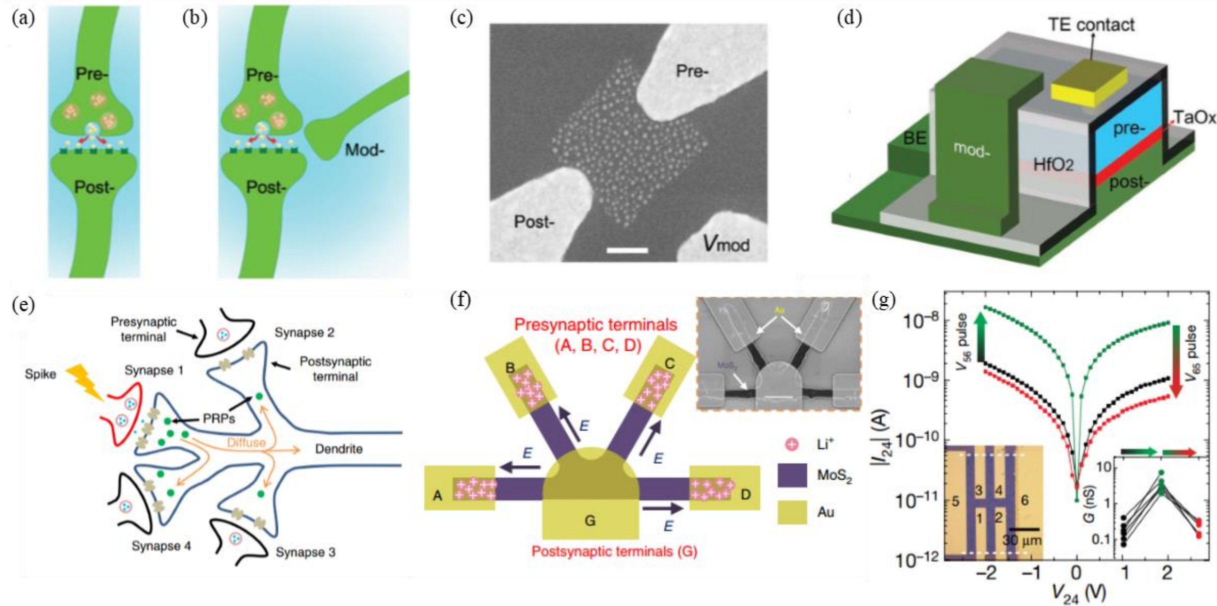

Figure 17. Summary of configuration and devices for the heterosynaptic emulation based on memristive devices. (a) Schematic illustration of two-terminal plasticity (homosynaptic) and (b) heterosynaptic plasticity. (c) SEM image of the device on the substrate, in which the Ag clusters between the pre and post electrodes can be modulated by the application of bias on the MOD electrode. (a)-(c) are adapted with permission[115]. Copyright 2015, Wiley-VCH. (d) A schematic illustration of a different device based on the metal oxide sandwich memristor devices with a side electrode functioning as the modulatory electrodes. Adapted with permission[116]. Copyright 2017, Wiley-VCH. (e) Schematic diagram showing the synaptic interactions enabled by the diffusion of plasticity-related proteins (PRP) among multiple synapse. Specifically, PRPs are generated in the postsynaptic terminal of synapse 1 and can diffuse to the synapses 2, 3, 4 through the dendrite. Depending on the difference among diffusion, synaptic behavior among these synapses can be different. (f) five terminal MoS_2 devices, in which the distribution of conductive ions at the terminals such as Electrode A, B, C and D can be controlled separately and lead to the potential heterosynaptic emulation possibilities, inset, SEM image of the fabricated MoS_2 devices. (e) and (f) are adapted with permission[120]. Copyright 2018, Nature Publishing Group. (g) Six terminal MoS_2 devices, in which any two of the inner electrodes (1, 2, 3, 4) can be controlled by the outside electrodes (5 and 6). Adapted with permission[118]. Copyright 2018, Nature Publishing Group.

As to the second aspect, the practical application of memristive devices are used for certain artificial neural networks. These applications are normally based on mature materials and process such as the widely studied TiO_2 based memristive devices. By the fabrication of crossbar memristive devices, certain functions have been reported, including pattern and face classification,[123-125] sparse coding[126], multilayer perceptron network,[127] coincidence detection[128], different learning behavior such as unsupervised learning[129, 130], self-adaptive learning[131], etc. A

typical example for the use of crossbar memristive device for the application of face classification is shown in Figure 18.

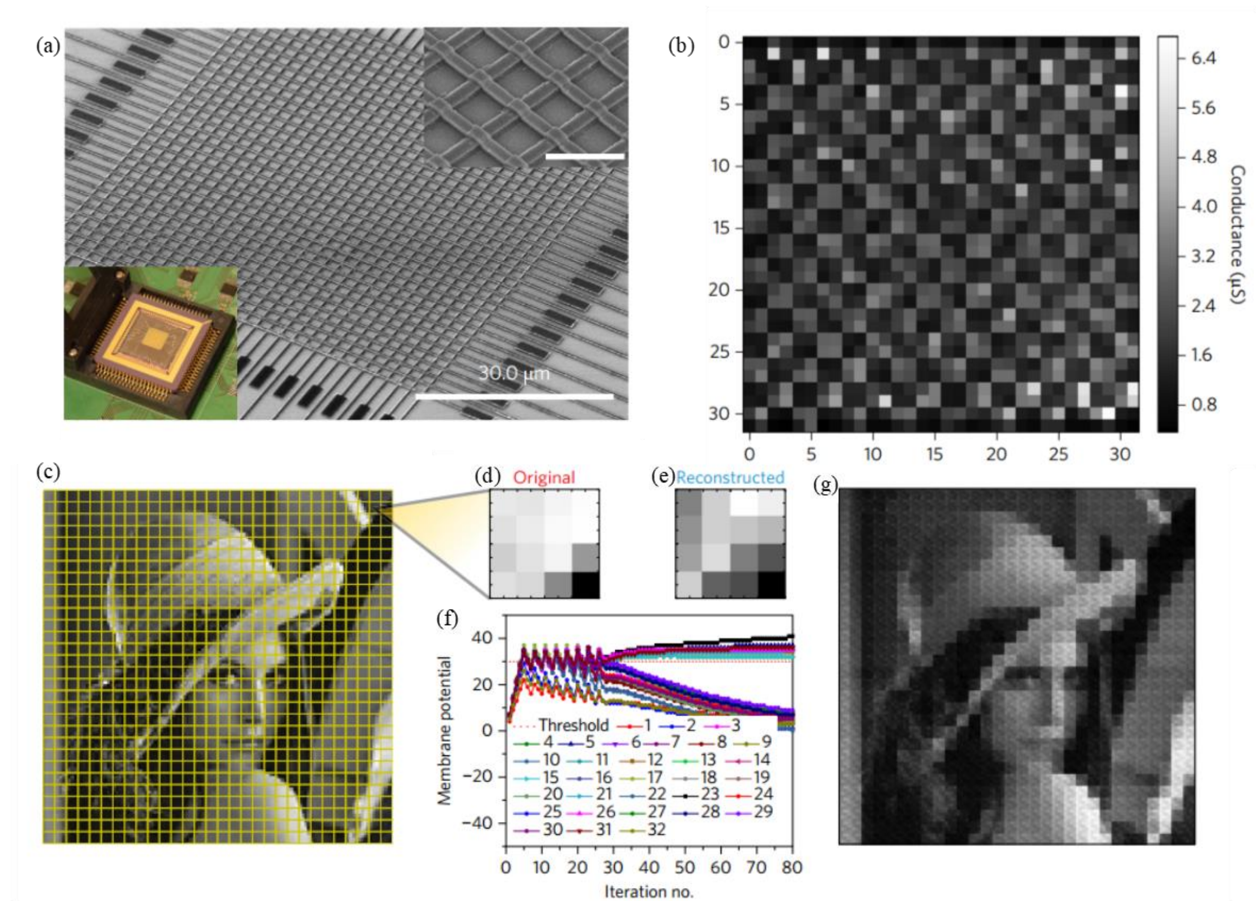

Figure 18. Natural image processing using the memristor crossbar structures. (a) SEM image of the fabricated memristor array. Upper right inset: magnified SEM image of the crossbar. Scale bar, 3 μm. Lower left inset: memristor chip integrated on the test board after wire-bonding process. (b) A 32×32 chequerboard pattern programmed into the memristor array and subsequently read back using the hardware system in (a). (c) Original 120×120 image. The image is divided into non-overlapping 4×4 patches for processing. (d) A 4×4 patch from the original image. (e) The experimentally reconstructed patch from the 16×32 memristor crossbar using the locally competitive algorithm and an offline-learned dictionary based on "winner-take-all" approach. (f) Membrane potentials of the neurons as a function of iteration number during the locally competitive algorithm analysis. The red horizontal line marks the threshold parameter λ. (g) Experimentally reconstructed image based on the reconstructed patches. Adapted with permission[126]. Copyright 2017, Nature Publishing Group.

2.2. 1D TiO_2 nanomaterial based memristive devices

2.2.1. TiO_2 based memristive devices

Among different nanomaterials that display resistive switching performance, TiO_2 nanomaterial-based memristive devices have been widely studied due to its ease of fabrication[68, 132] and its ability to demonstrate both unipolar[133, 134] and bipolar[73, 135, 136] resistive switching behavior. Furthermore, realization of the first memristor based on TiO_2 further promoted the wide study in different types of TiO_2 material based resistive switching behavior[33]. However, as to the switching mechanism based on TiO_2 materials, various experimental and theoretical mechanisms are observed and proposed. Both unipolar resistive switching[61] and bipolar[137] resistive switching performance in VCM device have been observed in in-situ TEM studies, which suggest the migration of oxygen vacancies to form conductive filament plays a crucial role. The typical example is shown in Figure 8, in which a Magnéli phase of conical TiO_2 filament is formed after the electroforming process. The formation of the different phase from TiO_2 is related to the electrically-induced modification of the local oxygen content along filamentary structures and the corresponding modulation of the electronic properties associated with the occupation of the 3*d*-state at the neighboring Ti atoms[138]. Furthermore, different resistive switching mechanisms of TiO_2 based ReRAM devices have also been reported, including ECM in Ag/TiO_2/Mo-doped In_2O_3 structure[139], VCM in Pt/TiO_2/Pt in which oxygen vacancies migration formed conductive filaments[137, 140], charge trapping and detrapping in which oxygen vacancies of TiO_2 function as trap centers[71, 73, 75, 80, 141]. The diversity of the resistive switching mechanisms in TiO_2 based materials is ascribed to the rich chemical nature of TiO_2 containing different phases composed of Ti_nO_{2n-1} (n=3, 4, 5…) and relative easy oxygen vacancy migration in the TiO_2 matrix[142]. Recently, it was found in the planar Pt/TiO_2/Pt structure via in-situ TEM observation, the dissociation of Pt atoms deriving from the interaction between Pt and oxygen-deficient TiO_2 would lead to the formation of Pt filament bridging the anode and cathode, causing the electroforming process. Even though the migration of oxygen vacancies is also playing a role in this system, the experiment demonstrates that the anode electrode such as Pt is not as inert as normally assumed[140]. Furthermore, the oxygen affinity of the metal electrode and the interaction between the metal electrode and TiO_2 are found to be important in the resistive switching performance as well[143]. Cation of TiO_2 (Ti ions) are also found to be involved in resistive switching performance in some

systems[64]. These different switching mechanisms from experimental observation as well as resistive switching behavior make the nature of the switching mechanism of TiO_2 based ReRAM devices still unknown.

2.2.2. 1D TiO_2 nanomaterial based memristive devices

2.2.2.1 1D nanomaterial based memristive devices

In comparison with thin films, the introduction of nanowires (nanorods) in memristive devices offers structural advantages that are expected to improve the performance of memristive devices. Nanowire-based devices can be fabricated using a bottom-up approach, rendering a promising and reliable candidates for going beyond the scaling limitations of the top-down approach by standard photolithography process[144]. Furthermore, during resistive switching operation, nanowires will facilitate the formation of straight conduction paths that enhance carrier transport[21]. This is in contrast to the branched conducting filaments that normally occur in structures based on thin films[145]. As a result, high-quality memristor performance together with good stability and reproducibility can be realized[21]. In addition, the confined structure of nanowires enable the precise engineering of the conductive paths (channels) as well as the metal/semiconductor barriers via the application of biases, leading to the potential in multilevel memory performance, which offers much promise for high-density data storage in non-volatile memory devices[146-149]. For example, K Nagashima et al. demonstrated by using a single Co_3O_4 nanowire, a multistate bipolar resistive switching performance with endurance up to 10^8 cycles can be achieved, as shown in Figure 19.[146] Furthermore, the large specific surface area and the surface defects of the of nanowires would make a difference in terms of the electron transport from thin film based devices[150].

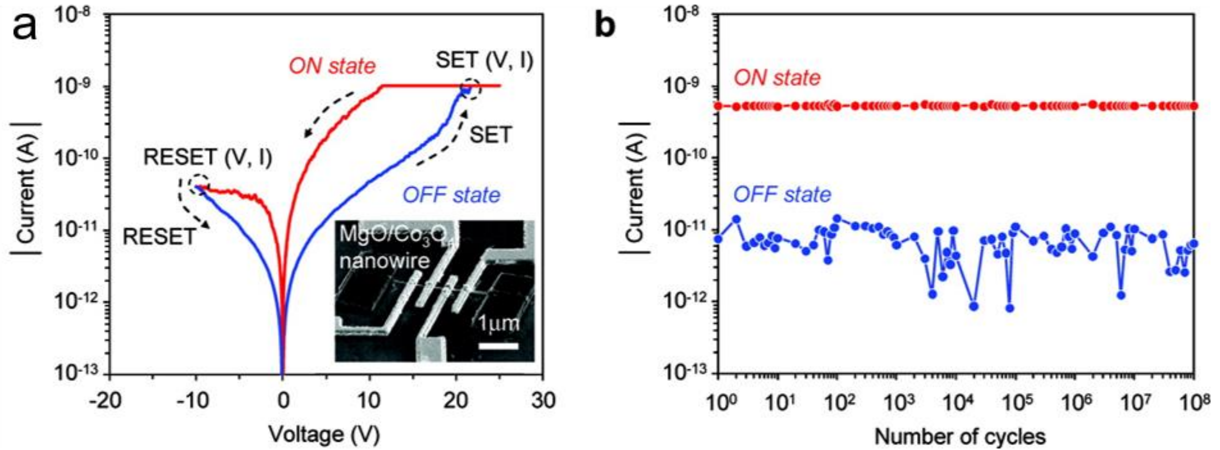

Figure 19. (a) Typical I-V sweeping results of individual MgO/Co_3O_4 nanowire device, inset, SEM image of the nanowire device. (b) Switching endurance performance up to 10^8 cycles. Adapted with permission[146]. Copyright 2010, American Chemical Society.

Many different nanowire-based ReRAM devices have been reported, including single nanowire based ReRAM devices such as TiO_2[148, 149, 151, 152], ZnO[153, 154], ZnO/TiO_2 nanowire[155], NiO[156], CuO_x[157, 158], VO_2[159], WO_3[160, 161], Ag_2S[162, 163], Co_3O_4[146], carbon nanotubes[164] and nanowire-array based ReRAM devices such as: TiO_2[165-168], alpha Fe_2O_3[169], ZnO[21, 76, 170, 171], $BiMnO_3$[172], NiO/Pt [147], Cu_2O[173], Ag_2S[174], ZnO/TiO_2 composites[175]. It should be noted that the switching mechanism of nanowire-based ReRAM devices might be different from conventionally thin film-based devices due to the morphology difference. For example, for the case of ZnO nanowire with active electrodes, it is experimentally demonstrated and theoretically studied that the Cu adatoms from the active electrode would form a conductive channel on the surface of nanowires and thus a percolation path for the electron transport, leading to the transition from HRS to LRS[176, 177]. Similar experimental observation was obtained for Zn_2SnO_4 nanowire based ReRAM devices with Cu electrode from energy disperse X-ray spectroscopy (EDX) elemental mapping in STEM, as demonstrated in Figure 20[178]. However, this surface-dominated switching is not feasible for gold-in-Ga_2O_3 core-shell nanowire based ReRAM devices, which shows invariable SET and RESET voltages regardless of the length of nanowires, which is attributed to the electron transport through the conducting paths formed at the Ga_2O_3 shell layer and Au metal core, as demonstrated in Figure 21[179].

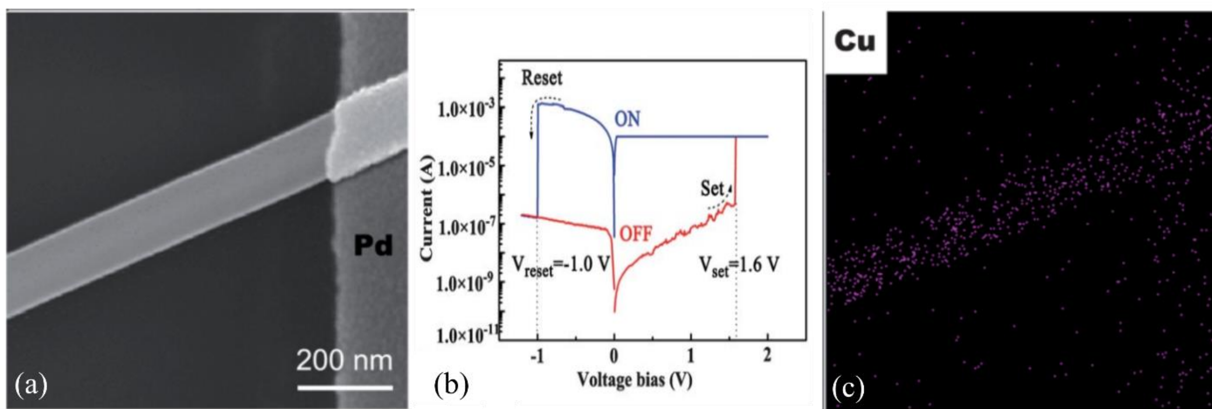

Figure 20. (a) SEM image of $Cu/Zn_2SnO_4/Pd$ device, (b) *I-V* characteristic bipolar resistive switching behavior, and (c) EDX Cu elemental mapping results for the device in the ON (LRS) state of (a) which demonstrated uniform Cu distribution on the nanowire. Adapted with permission[178]. Copyright 2012, Royal Society of Chemistry.

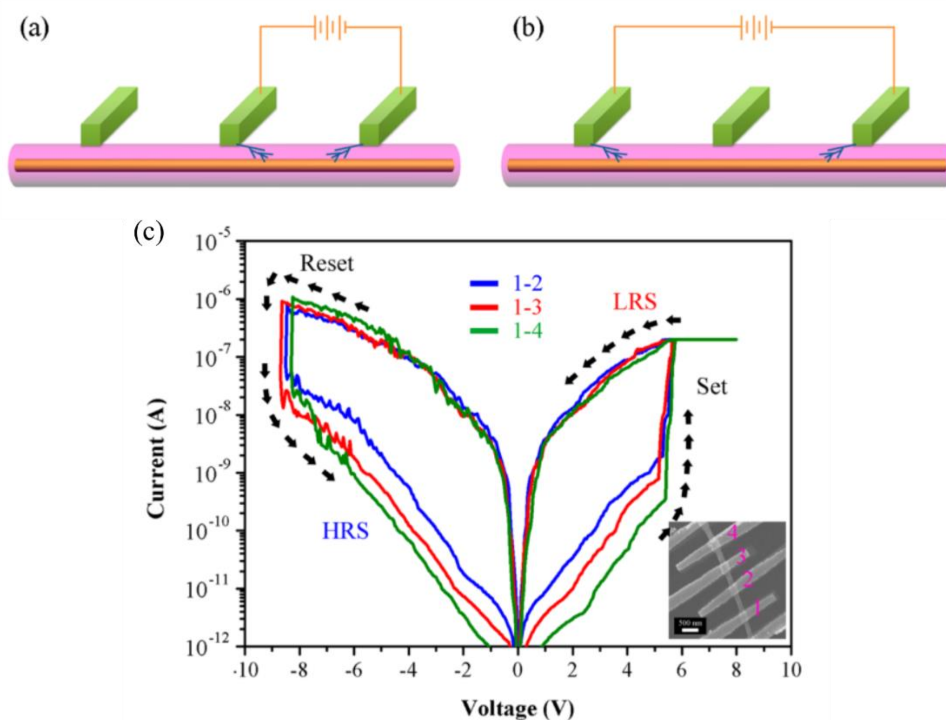

Figure 21. Schematic illustration of conducting paths and the transport mechanism that explain the properties of invariant set and reset voltages against different distances between electrodes. (a) Demonstration that oxygen vacancy filament connects to the gold core in the center of nanowire because the distance between two electrodes is much larger than the thickness of the Ga_2O_3 shell thickness. (b) Indication that the oxygen vacancy channel can link to the gold core due to the smaller diameter compared to the distance. (c) *I-V* characteristic of a single gold-in Ga_2O_3 core-shell nanowire with different distances between electrode and the inset is the SET chip image. Theses set and reset voltages are almost the same with different distances. Adapted with permission[179]. Copyright 2012, American Chemical Society.

2.2.2.2 1D TiO_2 nanomaterials based memristive devices

Various types of TiO_2 nanomaterials have demonstrated resistive switching behavior. The most commonly studied is the TiO_2 thin film based memristive devices and different switching mechanism have been studied[2, 68, 180-186]. Furthermore, solution-processed TiO_2 layer from sol-gel method also displayed reproducible resistive switching performance[187, 188]. Recently, Schmidt *et al.* studied the resistive switching performance of single TiO_2 nanoparticle using a conductive Pt tip, and it was found the crystalline shell of the individual nanoparticle is crucial for the resistive switching performance[189]. But realization of individual nanoparticle-based memristive devices is currently not feasible due to the complexity and cost of the fabrication process. Comparatively speaking, little research on 1D TiO_2 nanomaterials based memristive devices for different applications has been reported.

O'Kelly *et al.* first demonstrated the realization of a single TiO_2 nanowire based memristive device. It was shown that a single nanowire based memristor device is capable of displaying multilevel memory performance[149]. Furthermore, ternary synaptic plasticity performance of single nanowire based devices was also realized by Hong *et al.*, indicating great potential for the single TiO_2 nanowire as the building block for neuromorphic computing[151]. However, the demonstration of the memristive performance and synaptic plasticity both required a long electroforming process at high voltage even up to 200 V, which is not suitable for real applications. Furthermore, Lin *et al.* showed that the femtosecond laser irradiation on the single TiO_2 nanowire based device would result in improved controllable multilevel memory performance, as demonstrated in Figure 22[148]. The femtosecond laser irradiation would engineer the oxygen vacancy distribution locally at the TiO_2/Au interface via plasmonic-enhanced optical absorption, which leads to the stable multilevel memory performance without the conventionally required electroforming process. But the current fabrication process which includes time-consuming e-beam lithography and the variability from different samples are the concerns for single-nanowire based memristive devices.

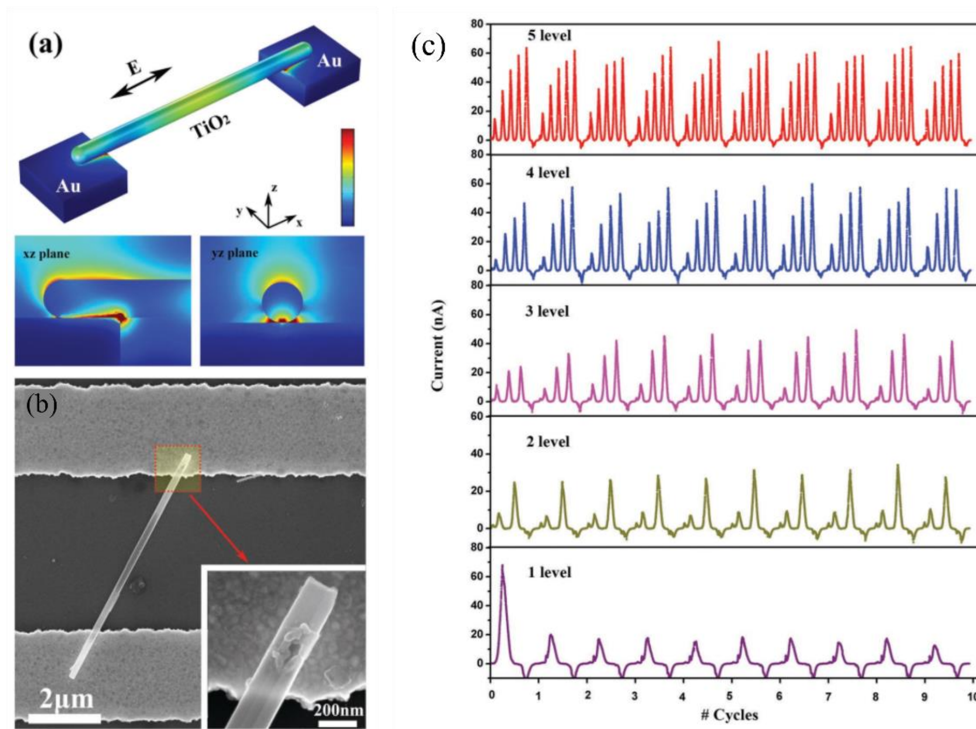

Figure 22. Simulation of electric field distribution around the femtosecond laser irradiated TiO_2 nanowire-Au electrode bridging structure at a polarized laser wavelength of 800 nm. The color scale indicates the magnitude of the generated electric field. (b) SEM images of bridged TiO_2-Au structure after fs laser irradiation. Inset shows magnified joints and the presence of spot welding. (c) Memory level profiles for femtosecond laser irradiated TiO_2-Au memory units. Repeatable memory behavior with selectable levels is displayed. Adapted with permission[148]. Copyright 2016, Wiley-VCH.

2.3. Hydrothermal synthesized TiO_2 nanowires and memristive devices

The hydrothermal method to obtain well-aligned nanowire arrays is easier compared with costly ways to get a TiO_2 thin film (by sputtering or atomic layer deposition process) as well as the individual nanowires. This widely used method to obtain nanowires and the corresponding memristive devices provide the possibility to control the electrical performance via the morphology and the properties of the nanowires, such as the electrolyte of the solution, the growth period of the hydrothermal process, etc. Moreover, the wide suitability of hydrothermal-growth of different metal oxide nanowire arrays on various substrates provided great potential of engineering the performance of obtained memristive devices[21, 172, 190]. These nanowire array based memristive devices also displayed unique characteristics such as light-controlled resistive switching behavior[169] and hydrophobic performance[21, 171] In the case of TiO_2, the growth of TiO_2 nanowire (nanorod) arrays on different substrates via hydrothermal process, including fluorine-doped tin

oxide (FTO) substrate[191], Ti foil[192], Si substrate[193], graphene sheets[194], etc. has been reported, as demonstrated in Figure 23. The key for the successful growth of nanorod arrays is the nucleation sites supplied by the substrate such as FTO and Ti or other pre-applied nucleation sites by depositing a seed layer on the substrate such as graphene and Si substrates. TiO_2 nanowire arrays have been applied in sensing[23-25], dye-sensitized solar cells[26, 27], supercapacitor[28] and field emission[29]. Recently, TiO_2 nanowire arrays, grown on bare FTO substrates by a hydrothermal process, have been reported showing resistive switching behavior[166-168]. The FTO substrate provides nucleation sites for the growth of the nanowire arrays and functions as the bottom electrode at the same time for the device. The *I-V* characteristic curve displayed reproducible resistive switching performance. However, the result showed that the realization of resistive switching behavior required a forming process[168] or displayed high-amplitude current response[166-168], which is not promising for the low-power consumption requirement for the future non-volatile memory devices. Whether these nanowire arrays-based devices could demonstrate multilevel memory were not studied either. Further optimization of the nanowire arrays should be performed for the application of resistive switching memory devices.

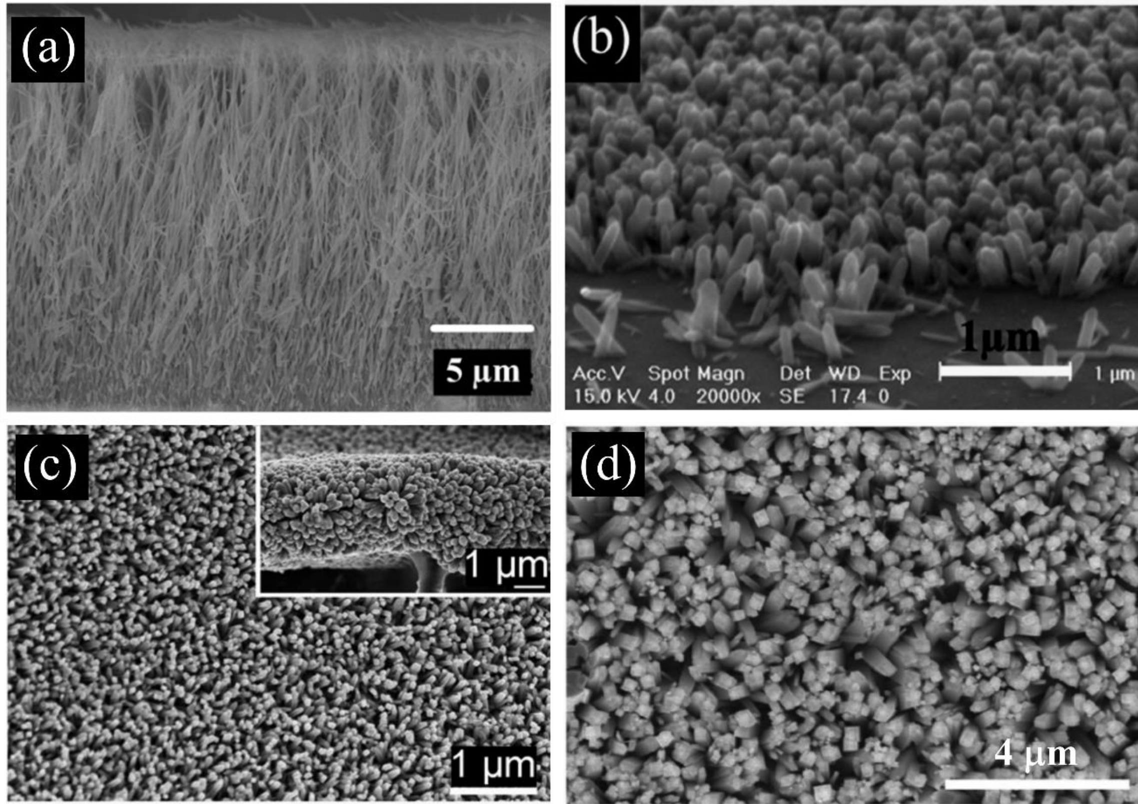

Figure 23. Hydrothermal grown TiO_2 nanowire (nanorod) arrays on different substrates, (a) Ti foil, adapted with permission[192]. Copyright 2008, American Institute of Physics. (b) Si substrate, adapted with permission[193]. Copyright 2010, AIP Publishing LLC. (c) graphene nanosheets (inset, cross-sectional view of the as-grown TiO_2-graphene-TiO_2 heterostructures), adapted with permission[194]. Copyright 2011, Wiley-VCH. (d) FTO glass substrate. Adapted with permission[191]. Copyright 2009, American Chemical Society.

2.4. Summary

Memristive devices have been receiving increasing attention in the past decade due to their great promise for next-generation non-volatile memory devices. Even though many types of materials demonstrated resistive switching performance, there is still a lack of materials (or combination of materials) to satisfy all the requirements for the application in future non-volatile memory devices. Furthermore, it was demonstrated that 1D nanomaterial based memristive devices would be advantageous compared with thin films. But an easy way to fabricate nanowire based memristive devices is still lacking to satisfy the requirements such as excellent low-current response, good uniformity and reliability, distinguishable resistance states and potential to display multilevel memory performance for the next-generation memory devices. TiO_2 based memristive devices are promising for memristive devices and it is possible to engineer the resistive switching

performance via different phases, morphology and stoichiometry of TiO_2. The goal of this research is to fabricate 1D TiO_2 nanowire based memristive devices via hydrothermal method and study their electrical performance and corresponding mechanism. Furthermore, different ways to engineer the electrical performance is studied to provide a better understanding of the nature of the resistive switching behavior.

Chapter 3. Resistive Switching Memory of TiO_2 Nanowire Networks Grown on Ti Foil by a Single Hydrothermal Method[195]

3.1. Overview

The resistive switching characteristics of TiO_2 nanowire networks directly grown on Ti foil by a single-step hydrothermal technique are discussed in this chapter. The Ti foil serves as the supply of Ti atoms for growth of the TiO_2 nanowires, making the preparation straightforward. It also acts as a bottom electrode for the device. A top Al electrode was fabricated by e-beam evaporation process. The Al/TiO_2 nanowire networks/Ti device fabricated in this way displayed a highly repeatable and electroforming-free (intrinsic) bipolar resistive behavior with retention for more than 10^4 s and an OFF/ON ratio of approximately 70. The switching mechanism of this Al/TiO_2 nanowire networks/Ti device is suggested to arise from the migration of oxygen vacancies under applied electric field. This provided a facile way to obtain metal oxide nanowire-based ReRAM device in the future.

3.2. Introduction

ReRAM devices utilizing an electric-field-induced resistance switching phenomena has attracted great attention for next-generation non-volatile memory due to its advantages of simple sandwich structure of metal/insulator/metal, high storage density and fast operation speed[68, 153]. Among different metal oxide materials that demonstrate potential for ReRAM, including NiO[196, 197], TiO_2[33, 68, 70], ZnO[153, 171, 198], VO_2[199], Ta_2O_5[52, 200], CuO[157], WO_3[201], etc. TiO_2 nanomaterial-based memory has been widely studied due to its ease of fabrication [68, 132] and its ability to demonstrate both unipolar[133, 134] and bipolar[73, 135, 136] resistive switching behavior. Compared to TiO_2 thin films used for ReRAM[70, 135, 136, 202, 203], few studies based on 1D TiO_2 nanomaterials for ReRAM have been reported. It was recently shown that a single TiO_2 nanowire-based resistive switching device demonstrated multi-level memory behavior[148, 149]. But the fabrication process of Au electrodes bridging a single nanowire required costly and time-consuming electron-beam lithography. Therefore, a facile way to fabricate TiO_2 nanowire-based ReRAM is required. Furthermore, TiO_2 nanorod[168, 204] and nanotube[165] arrays grown on FTO glass substrate by hydrothermal synthesis were also employed in resistive switching memory devices, however transparent conductive glass was required as a substrate. It was recently reported that TiO_2 nanowire networks could be grown

directly on a Ti foil via a hydrothermal method[24, 192, 205, 206] or oxidation process[207, 208] and the applications of these nanowires in dye-sensitized solar cells[205, 206] and field emission[207] were investigated. But the suitability of these TiO_2 nanowires for ReRAM devices and the corresponding switching mechanism have not been reported yet.

In this chapter, TiO_2 nanowire networks were directly grown on Ti foil by a hydrothermal method and their resistive switching behavior was investigated. Since the Ti foil serves both as the source of Ti during the synthesis of the TiO_2 nanowire, as well as a bottom electrode for the device, preparation of the device is straightforward, cost-effective and highly reproducible. Notably, the electrical contact between the nanowires and the bottom metal substrate is ensured. According to the current-voltage (*I-V*) measurements of the fabricated Al/TiO_2 nanowire networks/Ti device, a switching mechanism based on the migration of oxygen vacancies is proposed. The reliability of the fabricated device was examined by studying its retention and endurance performance.

3.3. Materials and Methods

The synthesis process of TiO_2 nanowire networks on Ti foil is demonstrated in Figure 24.[192, 205]. Briefly, a piece of Ti foil (99.9%) with a dimension of 1.5 cm×3.0 cm×0.127 mm (Sigma Aldrich) was ultrasonically cleaned in acetone, isopropanol and Milli-Q water for 10 minutes in sequence and then placed against the wall of a 125 mL Teflon-lined stainless steel autoclave filled with 40 mL of 1 M NaOH aqueous solution. Then, the sealed autoclave was put into an oven at a temperature of 220 ^{o}C for 20 h. Next the Ti foil covered with nanowires was taken out of the autoclave and immersed in 50 mL of 0.6 M HCl solution for one hour to exchange Na^+ with H^+. Finally the foil was annealed inside a furnace at 500 ^{o}C for 3 h in air to transform the $H_2Ti_2O_5{\cdot}H_2O$ nanowires to anatase nanowires. The color of the foil turned white after the calcination process.

During device fabrication, the top electrode was prepared by depositing an Al layer with a thickness of 150 nm through a shadow mask having circular holes (1 mm in diameter) using e-beam evaporation process (Intelvac e-beam evaporation system). The pressure was $< 4\times10^{-6}$ Torr and the deposition rate was 1Å/s. Electrical measurements were performed with a Keithley 2602A source-meter at ambient conditions. The bias voltage was applied to the top Al electrode and the Ti foil was grounded during electrical measurement.

For characterization of the TiO_2 nanowires, a field-emission scanning electron microscope (FESEM, LEO-1550) was used to check the surface morphology. Transmission electron

microscopy (TEM) (JEOL 2010F) was used to examine the structure and crystalline defects of TiO_2 nanowires. X-ray diffraction analysis (XRD, PANalytical X'pert PRO MRD) and Raman analysis (Reinshaw micro-Raman spectrometer) were used to identify the crystal structure and phase. Furthermore, X-ray photoelectron spectroscopy (XPS) measurement (Thermo VG Scientific ESCLab 250) was carried out to examine the surface chemical states of the nanowires.

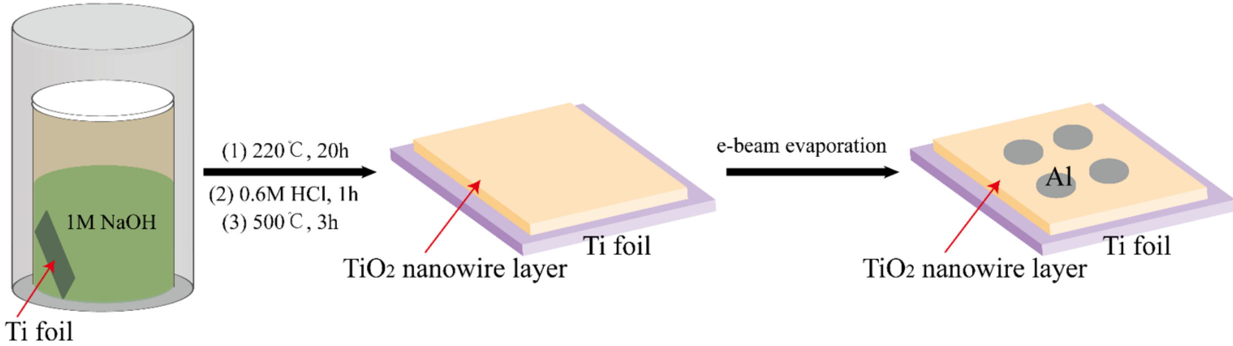

Figure 24. Schematic diagram of the fabrication process for TiO_2 nanowire network based device on Ti foil.

3.4. Results and Discussion

3.4.1. Characterization of TiO_2 nanowire networks

The SEM image illustrated in Figure 25(a) demonstrated a network of TiO_2 nanowires with lengths of several micrometers from the top view. The statistical summary of the whole SEM areas showed that the nanowires have an average diameter of 26±4 nm. The uniformity of the diameter of the nanowires indicated that the growth occurred predominantly through epitaxial addition of growth units to the tips[205]. During the hydrothermal process, the TiO_2 nanowires grow perpendicularly to the substrate first and then the tips of nanowires appear to bend and stick together to form a network of nanowires[205]. Therefore, the top Al electrode, as deposited, makes heterogeneous contact with the nanowires and the *I-V* characteristics then reflect the average contact with a large number of individual nanowires. TEM image of the TiO_2 nanowires (Figure 25(b)) showed the (101) plane of anatase in addition to many crystalline defects. These defects could have a significant effect on the resistive switching behavior of the fabricated devices as discussed later in this chapter.

A room temperature Raman spectrum of TiO_2 nanowires in Figure 25(c) showed peaks at 141, 194, 395, 512 and 634 cm^{-1}. These peaks are characteristic of the anatase phase. The peaks at 141, 194 and 634 cm^{-1} are assigned to the E_g modes while the other two peaks at 512 and 395 cm^{-1} are

assigned to the B_{1g} modes in TiO_2[209]. The XRD characterization results in Figure 25(d) further confirmed the phase of the TiO_2 nanowires, as the peaks of (101), (112) and (200) planes of anatase in agreement with the standard spectrum (JCPDS No. 21-1272). It should be noted that one of the anatase peaks at 38.57^o overlapped with the peaks of the Ti foil (JCPDS No. 44-1294).

Moreover, the surface chemical states of the TiO_2 nanowires were analyzed by XPS. Figure 25(e) showed peaks at binding energies of 459.4 and 465.1 eV, which can be assigned to Ti $2p_{3/2}$ and $2p_{1/2}$, respectively. These are typical XPS spectra of Ti^{4+} in TiO_2. The signal from Ti^{3+} was too small to be detected. Furthermore, two Gaussian peaks were observed in the fit to the O 1s spectrum (Figure 25(f)). The binding energy at 529.66 eV is assigned to the O^{2-} bond in TiO_2 while the binding energy at 531.33 eV can be attributed to oxygen vacancies in TiO_2[165]. XPS scans show that the synthesized TiO_2 nanowires contain locally distributed oxygen vacancies, in agreement with the HRTEM result in Figure 25(b).

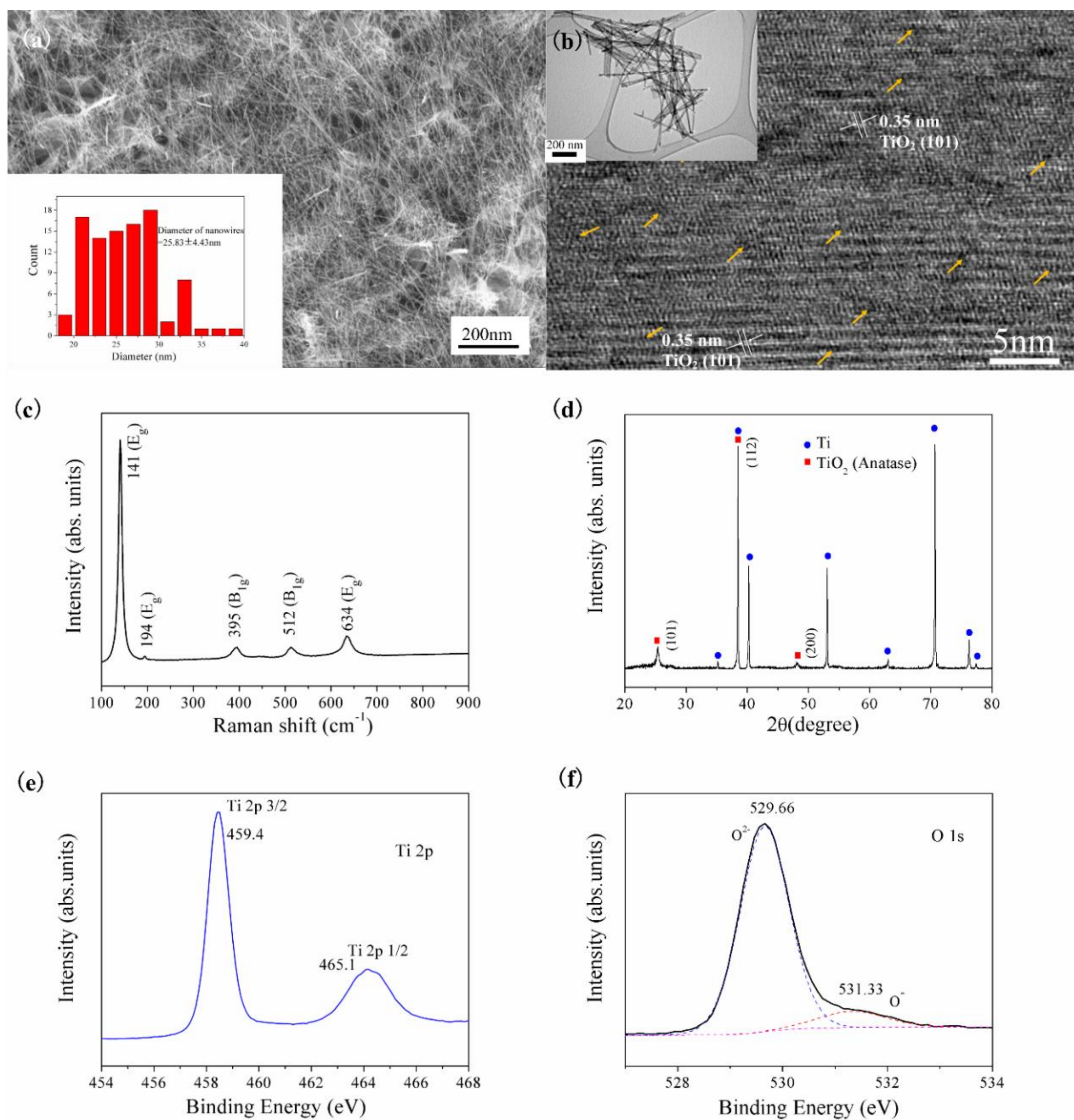

Figure 25. Characterization of TiO_2 nanowires, (a) Top view SEM image (inset, statistical summary of diameters of ~100 nanowires), (b) HRTEM image, yellow arrows indicate the crystalline defects (inset, TEM image of TiO_2 nanowires), (c) Raman spectrum, (d) XRD results, (e) Ti 2p XPS spectrum and (f) O 1s XPS spectrum

3.4.2. Electrical performance evaluation

3.4.2.1. Resistive switching characteristics

The resistive switching behavior was examined by applying the voltage as follows: 0 V→−10 V→0 V→10 V→0 V with a sweeping rate of 0.1 V/s. The *I-V* characteristic curve illustrated in Figure 26 demonstrated a typical bipolar switching behavior. The Al/TiO_2 nanowire networks/Ti device was initially in the high resistance state (HRS). During the application of the negative sweep

from 0 to −10 V, the negative current increased gradually and the device switched to low resistance state (LRS, ON state) (SET process). The device maintained the LRS during the forward voltage sweep but switched back to the HRS during the voltage sweep back from 10 V to 0 V (RESET process). Notably, the resistive switching behavior is obtained without an initial electroforming process, which was normally required for devices consisting of TiO_2 thin films[61, 70, 210]. This is expected to be due to the high concentration of defects (oxygen vacancies) in the TiO_2 nanowires after the synthesis process, as seen in the HRTEM image in Figure 24(b) and the O 1s XPS spectrum in Figure 24(f). Intrinsic resistive switching behavior has also been observed with metal oxide materials containing a large defect concentration without the electroforming process[157, 211, 212]. However, some devices require forming treatments, such as hydrogen annealing[170] and Ar^+ irradiation[213] to generate an oxygen vacancy layer to enable or enhance the resistive switching characteristics. This forming-free characteristic is attractive for ReRAM since it would simplify the memory operation and enable higher density memory devices[20].

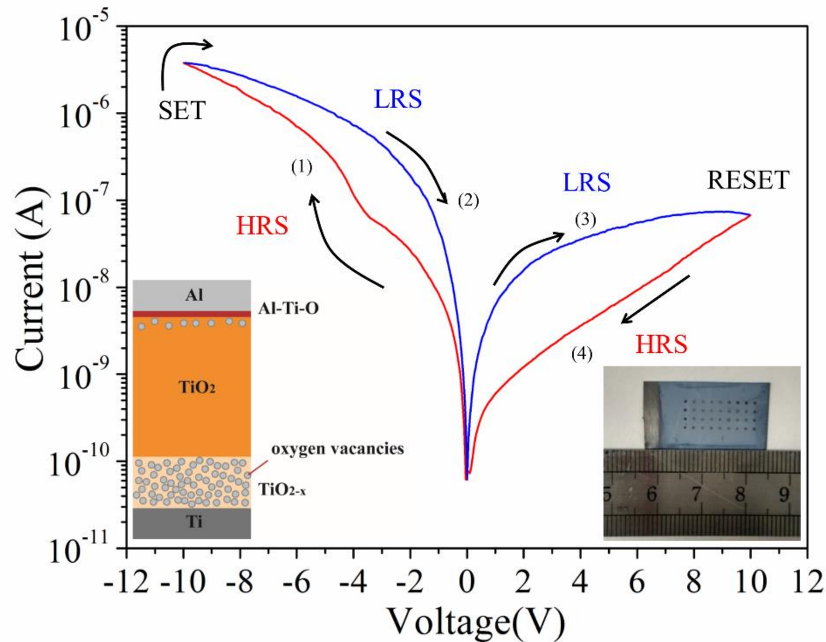

Figure 26. *I-V* characteristic curve of the Al/TiO_2 nanowire networks/Ti device (left inset, schematic diagram of interfaces in the device in the pristine state. Right inset, optical photo of an actual fabricated device on Ti foil)

It should be noted that this resistive switching behavior is quite different from Ref.[134], which showed that Ti/TiO_2 film/Al structures displayed linear *I-V* characteristic curves due to the Ohmic-Ohmic contact combination. The difference is expected to be ascribed to the reactions at the

Ti/TiO_2 and Al/TiO_2 interfaces during the synthesis of the TiO_2 nanowire networks and the deposition of Al layer. Generally, the Ti layer is regarded as a chemically reactive contact that will reduce the TiO_2 and create a locally high concentration of oxygen vacancies near the Ti/TiO_2 interface[135, 143, 214]. The formation reaction of oxygen vacancies is expressed in the Kröger-Vink notation[18] as

$$O_O^{\cdot\cdot} \rightarrow V_O^{\cdot\cdot} + 2e^- + \frac{1}{2}O_2 \qquad Eq.(1)$$

where, $O_O^{\cdot\cdot}$ is the oxygen on the TiO_2 lattice and $V_O^{\cdot\cdot}$ is a positively charged oxygen vacancy. The generation of oxygen vacancies near the interface between Ti and TiO_2 nanowires is enhanced during the calcination process due to an increase in the diffusion of Ti atoms into the TiO_2 layer at high temperature. Therefore, a non-stoichiometric TiO_{2-x} (x>0) layer with a high concentration of oxygen vacancies would be formed between the Ti foil and TiO_2 nanowires. Oxygen vacancies in TiO_2 act as n-type dopants with shallow donor states below the conduction band and would transform the insulating metal oxide into an electrically conductive semiconductor[33, 70]. In addition, oxygen vacancies in TiO_2 exhibit higher mobility than metal interstitials at room temperature, so that the number of oxygen vacancies in TiO_2 are expected to dominate resistive switching behavior [132]. The distribution of oxygen vacancies in the TiO_2 nanowire layer is expected to be uniform above the Ti/TiO_2 interface[170]. On the other hand, during the deposition of the Al layer, the high oxygen affinity of Al results in Al reacting with TiO_2, forming an interfacial insulating Al-Ti-O layer[68, 71-73]. Consequently oxygen vacancies are expected to be generated underneath the interfacial layer according to Eq.(1), although a much smaller concentration of vacancies is expected compared to the Ti/TiO_2 interface[70]. These interfaces in the pristine state are illustrated schematically in the inset of Figure 27. The different concentrations of oxygen vacancies distributed at the Al/TiO_2 interface and Ti/TiO_2 interface result in asymmetric barriers for charge transport, which plays an important role in the switching behavior of the device.

Furthermore, Figure 27 showed *I-V* characteristic curves under different sweeping voltages displayed similar bipolar resistive switching behavior in spite of difference in the achieved SET and RESET currents. These results highlight the repeatability of the Al/TiO_2 nanowire networks/Ti device. Asymmetrical or self-rectifying resistive switching can be seen in both Figures. 26 and 27. The origin of this self-rectifying property can be attributed to effect of the Al-Ti-O layer on the migration of oxygen vacancies as discussed in the next section.

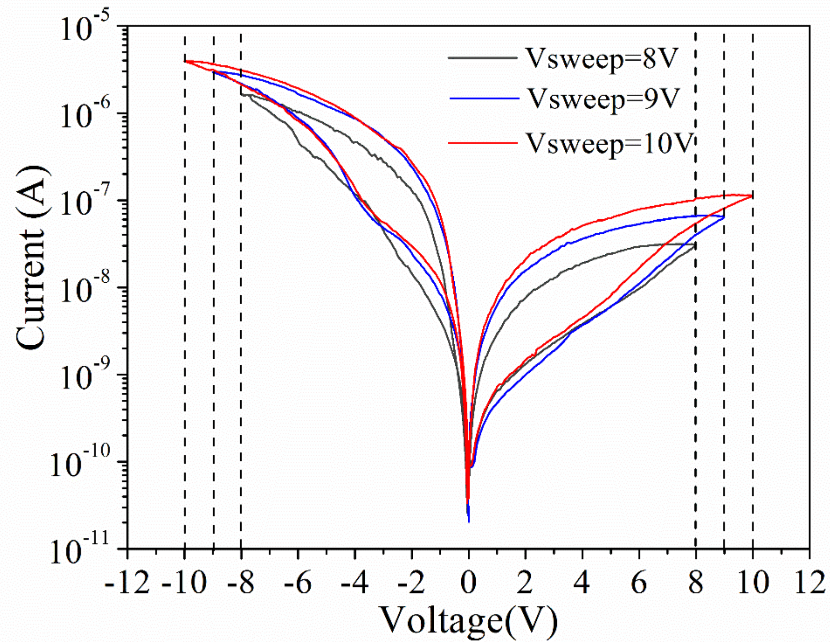

Figure 27. *I-V* characteristic curve of the Al/TiO_2 nanowire networks/Ti device under different voltages

3.4.2.2. Switching Mechanism Analysis

Based on the discussed *I-V* characteristic results, the resistive switching mechanism of the Al/TiO_2 nanowire networks/Ti device is proposed. As explained, the concentration of oxygen vacancies at the Al/TiO_2 interface and Ti/TiO_2 interface is different. These oxygen vacancies are mobile under external electrical field[215]. When the Al top electrode is under a negative bias, the oxygen vacancies in the pristine state (Figure 28(b)) migrate towards the top electrode, forming pathways with high electrical conductivity. It is expected that the geometry of the confined TiO_2 nanowire provides a large surface area and a direct pathway for the migration of oxygen vacancies for stable switching behavior[157]. Simultaneously, electrons would be injected from the Al electrode and drift to the bottom Ti electrode. Once one or more conductive pathways are formed from the top electrode to bottom electrode, the device is switched ON, as illustrated in Figure 28(a). Moreover, some oxygen vacancies may accumulate at the Al-Ti-O layer, which functions as an insulating layer to inhibit out-diffusion of oxygen[71]. This insulating layer may play an important role in the switching behavior since the formation and dissociation of this layer is expected to be closely related to the migration of oxygen vacancies under electric field [68, 72]. Under negative bias, the migration of oxygen vacancies to the Al electrode may result in the partial dissolution of this

insulating layer, whereas this layer would be widened when the Al top layer is under a positive bias.

In the RESET process, the oxygen vacancies in the TiO_2 matrix are repelled towards the bottom electrode, leading to the recovery of a higher concentration of oxygen vacancies near the Ti bottom layer, and widening of the Al-Ti-O layer as oxygen vacancies drift away from this layer[70]. The presence of a potential barrier in the Al/Al-Ti-O interfacial layer would suppress electron tunneling through the interface and inhibit the formation of conducting channels. Conversely, as oxygen vacancies migrate to the top Al electrode under an applied negative bias, the interfacial layer begins to thin, increasing the probability of electron tunneling and enhancing the formation of conductive channels. As a result, the final current flowing at +10 V is much less than that at −10 V. This is characteristic of asymmetrical or self-rectifying resistive switching behavior, as seen in Figures 26 and 27. To verify the source of the self-rectifying performance, an identical device was measured without the top electrode, that is, the probe tip (which is made of tungsten) is directly in contact with the top surface of the TiO_2 nanowire layer. The bipolar resistive switching performance existed for the device as well, but no self-rectifying feature was observed.

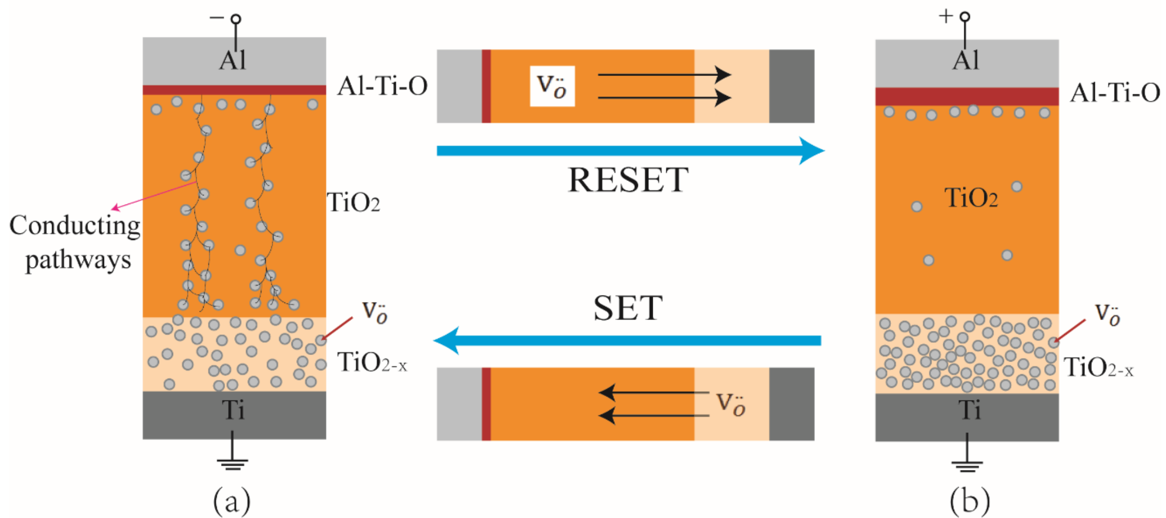

Figure 28. Schematic illustration of (a) SET and (b) RESET process of the Al/TiO_2 nanowire networks/Ti device

Further insight into the role of the Al-Ti-O interfacial layer on the resistive switching performance can be obtained by investigating the effect of the thickness of the TiO_2 nanowire network. This thickness can be varied by changing the hydrothermal growth time. The effect of different growth times (different thickness) on the *I-V* characteristics is illustrated in Figure 29. These data can be compared with those in Figure 26 which was obtained for a hydrothermal growth

time of 20 h. A self-rectifying resistive switching response is also observed for growth time of 4, 12 and 16 h in addition to 20 h, and the rectification ratio diminishes as the growth time is increased. As discussed, the interfacial Al-Ti-O layer plays an important role in determining the asymmetrical response. The relative effect of this component increases with decreasing thickness of the TiO_2 nanowire layer so that an increase in growth time to 24 h results in bipolar resistive switching with no obvious self-rectifying feature. The data in Figure 29(a) suggests that self-rectifying resistive switching of our Al/TiO_2 nanowire networks/Ti could, after further optimization, be used to mitigate sneak-current issues in the crossbar-based integration system for ReRAM devices[198].

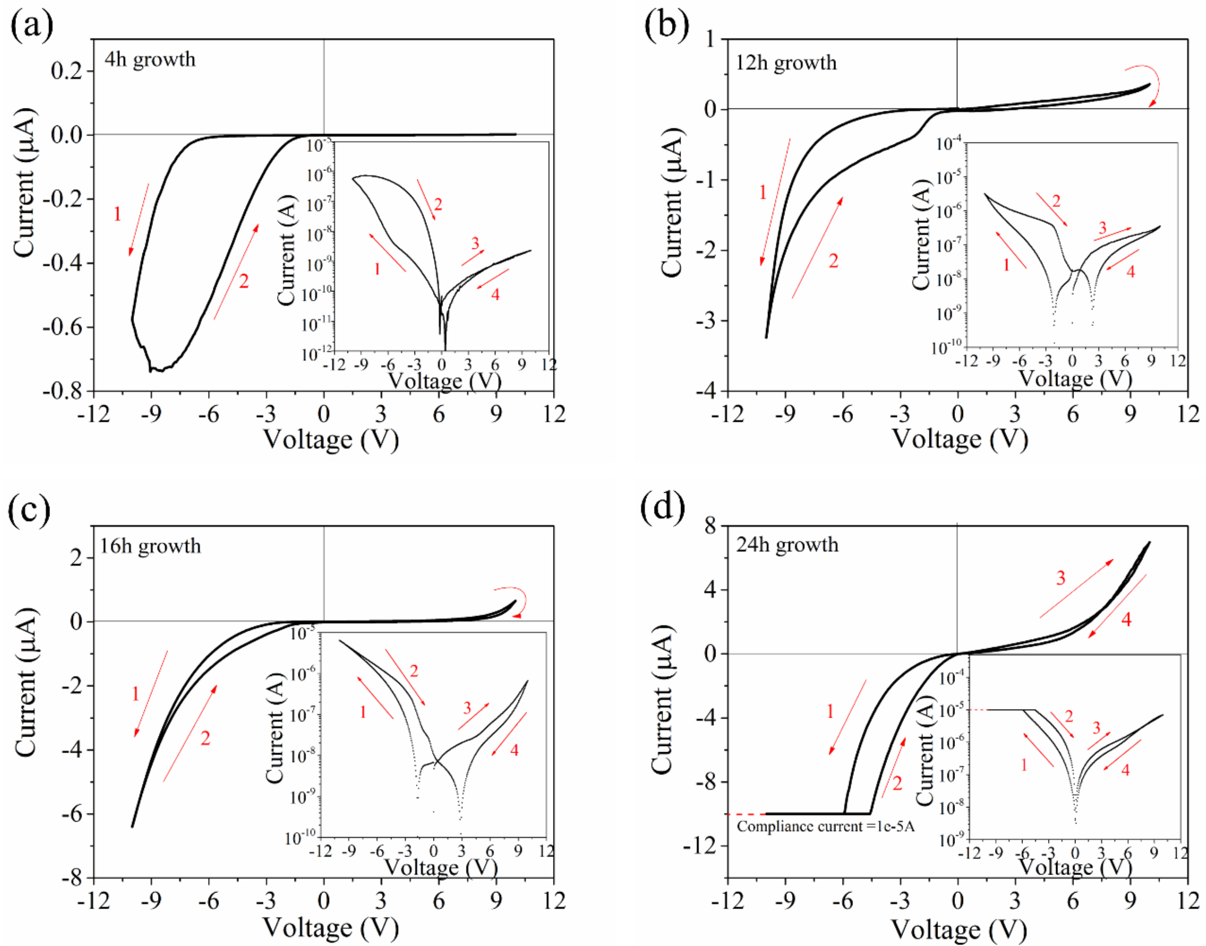

Figure 29. *I-V* characteristic curves of the Al/TiO_2 nanowire networks/Ti device with different thicknesses of the nanowire layers via the control of the hydrothermal growth time, (a) 4 h growth time, (b) 12 h growth time, (c) 16 h growth time and (d) 24 h growth time

In order to understand the conduction mechanism of the fabricated Al/TiO_2 nanowire networks/Ti device, the *I-V* curves in Figure 26 were fitted on a double-logarithmic scale, as shown in Figure 30. The overall curve is in good agreement with the trap-associated SCLC theory[71, 73,

[157]. For the positive sweeping (Figure 30(a)), the LRS follows an Ohmic conduction with a slope of ~1, consistent with the presence of conductive pathways formed by the migration of oxygen vacancies in the device after the SET process[170]. The *I-V* characteristics in the HRS consist of three regions: the Ohmic region (I~V) with a slope of ~1 at low bias, the Child's square law region ($I \sim V^2$) with a slope of 2.44 at higher bias and a region with rapidly changing current near the RESET point (slope: 4.23). The higher slope (>2) compared with the Child's law in which the current is proportional to the square of the voltage might be due to the expected variation in thickness of the insulating Al-Ti-O layer. This large slope can also be found in similar ReRAM devices in which Al acts as an electrode[71, 73, 216].

The *I-V* characteristic curve for the negative voltage in Figure 30(b) also demonstrated SCLC-like behavior but the fitted slope values in different regions are generally larger than those under positive voltage sweeping. This could be due to the concentration gradient of oxygen vacancies that exists in the pristine state (high concentration of vacancies at the bottom Ti/TiO_2 interface and low concentration underneath the Al-Ti-O layer), which would lead to diffusion of these oxygen vacancies. The diffusion combined with the drift of the oxygen vacancies under an applied negative bias could lead to accelerated migration of vacancies, resulting in higher slopes when transitioning from the HRS to LRS, as compared to the transition from LRS to HRS under positive sweeping. Furthermore, dissociation of the insulating Al-Ti-O layer due to migration of oxygen vacancies under negative bias also decreases the overall resistance of the device, which would contribute to higher values of the slopes. This SCLC-like behavior for both positive and negative sweeping voltages can also be found with increasing sweeping cycles of the device.

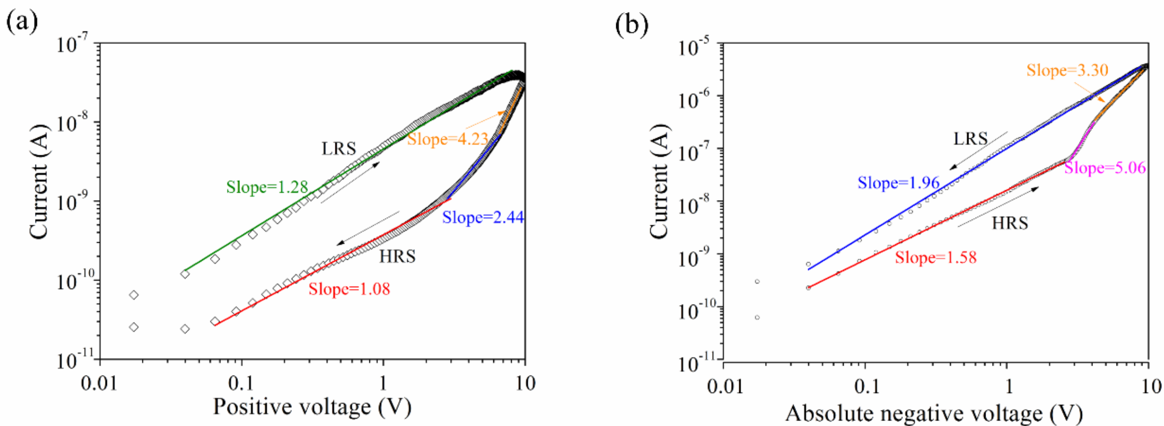

Figure 30. *I-V* characteristic curves under positive (a) and negative (b) sweeping voltages on a double-logarithmic scale

The above analysis indicates that Al/TiO_2 nanowire networks/Ti device as fabricated exhibit a similar *I-V* response and switching mechanism as that seen in devices using a uniform TiO_2 layer coated with an Al electrode. Such devices are fabricated by time-consuming and costly reactive sputtering[73] or plasma-enhanced atomic layer deposition[68, 71, 72, 80, 216] processes. Therefore, our results indicate that the TiO_2 nanowire networks grown on Ti foil by a single-step hydrothermal process have potential in the application of ReRAM devices.

3.4.2.3. Endurance and Retention Study

To determine the electrical stability of the fabricated Al/TiO_2 nanowire networks/Ti device, an endurance study was performed by applying a cycling sweeping process. The results illustrated in Figure 31(a) showed that the resistance for the OFF state remained stable beyond 60 cycles, while the resistance for the ON state underwent a fluctuation. Nevertheless, the calculated OFF/ON resistance ratio is around 70, large enough to serve as a feasible memory element in ReRAM. Study of endurance under pulsed operation is planned for future work, together with characterization of the device in relation to stability. Furthermore, a data retention test was performed by examining the resistance change with a reading voltage of 1 V for a long period of time after switching the device to ON and OFF states at −10 V and 10 V, respectively. The retention results for the ON and OFF states in Figure 31(b) demonstrated no remarkable degradation up to 10^4 s with a high resistance ratio, confirming the non-volatile nature of the device. The endurance and retention results emphasized good stability of the fabricated Al/TiO_2 nanowire networks/Ti device for future use as ReRAM.

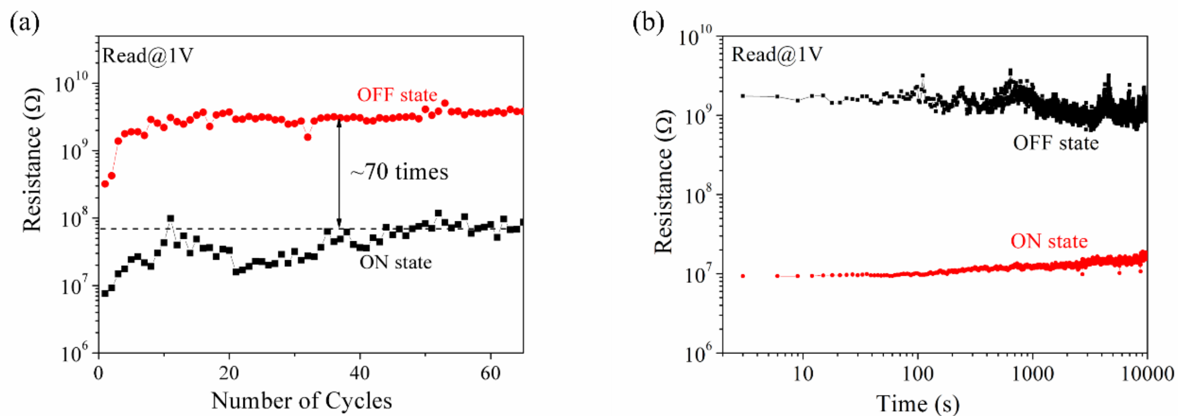

Figure 31. (a) Endurance and (b) retention performance of the Al/TiO_2 nanowire networks/Ti device

3.5. Conclusions

In summary, forming-free bipolar resistive switching behavior was successfully demonstrated in TiO_2 nanowire networks directly grown on Ti foil by a one-step hydrothermal process. The prepared Al/TiO_2 nanowire networks/Ti device exhibited reproducible and stable electrical performance with a high OFF/ON ratio that persisted for up to 10^4 s. The interaction of Ti foil with the TiO_2 nanowires during the synthesis process results in the generation of large density of oxygen vacancies at the Ti/TiO_2 interface, which is likely responsible for the forming-free resistive switching behavior without the requirement of electroforming process. The low amplitude of both SET and RESET currents together with distinguishable ratios are promising for the low-power ReRAM devices. The switching mechanism of the device is proposed to be the migration of oxygen vacancies under electric field. These results provide an easy way to prepare nanowire-based ReRAM devices with good electrical performance.

However, the resistive switching characteristic for the TiO_2 nanowire networks on Ti foil shows some variation of cell-to-cell behavior. Though all the fabricated Al-TiO_2 nanowire network-Ti foil devices shows similar bipolar resistive switching behavior, the resistance ratio among these devices have a wide distribution from 20 to 100. One possible cause might be non-uniform layer distribution after the Al deposition since the random TiO_2 nanowire networks can possess certain dimensions of holes. This can intrinsically leads to the difference in the electrical performance of the fabricated device.

Chapter 4. Reliable and Low-Power Multilevel Resistive Switching in TiO_2 Nanorod Arrays Structured with a TiO_x Seed Layer[217]

4.1. Overview

The electrical performance of TiO_2 nanorod array (NRA) based resistive switching memory devices is examined in this chapter. The formation of a seed layer on the FTO glass substrate after treatment in $TiCl_4$ solution, before the growth of TiO_2 NRAs on the FTO substrate via a hydrothermal process, is shown to significantly improve the resistive switching performance of the resulting TiO_2 NRA-based device. As fabricated, the Al/TiO_2 NRA/TiO_x layer/FTO device displayed electroforming-free bipolar resistive switching behavior while maintaining a stable ON/OFF ratio for more than 500 direct sweeping cycles over a retention period of 3×10^4 s. Meanwhile, the programming current as low as ~10^{-8} A and 10^{-10} A for low resistance state and high resistance state respectively makes the fabricated devices suitable for low-power memristor applications. The TiO_x precursor seed layer not only promotes the uniform and preferred growth of TiO_2 nanorods on the FTO substrate, but also functions as an additional source layer of trap centers due to its oxygen deficient composition. Our data suggests that the primary conduction mechanism in these devices arises from trap-mediated SCLC. Multilevel memory performance in this new device is achieved by varying the SET voltage. The origin of this effect is also discussed.

4.2. Introduction

1D nanomaterials, especially those involving semiconducting and metal oxide nanowires (nanorods), have recently gained much interest for different nanoelectronic and optoelectronic applications due to their unique physical and chemical behaviors inherently different from the parent bulk as well as thin film materials. Through careful design and controlled synthesis, nanowires will provide the building blocks for new systems of unique photonic and electronic devices[218, 219]. Furthermore, the incorporation of nanowires into complex functional units via layer-by-layer assembly[220] and nanojoining[221] will enable the creation of smaller devices exhibiting novel functionality.

A new type of nanodevice, resistive switching random access memory (ReRAM) is now becoming of interest for next-generation non-volatile memory devices due to its simple structure, promising switching speed as well as excellent scalability[16]. Such devices represent a practical

application of the fourth circuit element: the memristor[33]. In comparison with thin films, the introduction of nanowires (nanorods) in ReRAM devices offers structural advantages that are expected to improve the performance of memristive devices. For example, during resistive switching operation, nanowires will facilitate the formation of straight conduction paths that enhance carrier transport[21]. This is in contrast to the branched conducting filaments that normally occur in structures based on thin films[145]. As a result, high-quality memristor performance together with good stability and reproducibility can be realized[21]. In addition, the confined structure of nanowires enable the precise engineering of the conductive paths (channels) as well as the metal/semiconductor barriers via the application of biases, leading to multilevel memory performance[146-149], which offers much promise for high-density data storage in non-volatile memory devices.

Many different kinds of 1D semiconductor nanomaterials were proposed for ReRAM devices, including TiO_2,[148, 149, 168] Si/a-Si core-shell nanowires,[222] ZnO,[68, 162, 170, 171] CuO_x[157, 158], Co_3O_4,[146] WO_3,[161] NiO[196, 197], Ag_2S[162] and NiO/Pt nanowire arrays[147]. Much interest has been devoted to TiO_2 which has been widely studied as a typical metal oxide material exhibiting resistive switching due to its intrinsic variety of possible crystal phases and the associated richness of switching dynamics[132]. However, compared with the widely studied TiO_2 thin film for ReRAM devices, there has been little research on 1D TiO_2 nanomaterials[148, 149, 168]. It was reported that a single TiO_2 nanowire-based heterojunction can exhibit multilevel memory performance, but the realization of resistive switching required a prolonged (20 min) high voltage forming process, which is not desirable for device operation[149]. In another study, a similar Au-TiO_2 nanowire-Au heterostructure was processed with femtosecond laser irradiation to engineer the distribution of oxygen vacancies, and this resulted in improved controllable multilevel memory performance[148]. However, nanowire-based ReRAM devices from single nanowires are not economic due to the cost and complexity of the e-beam lithographic process required to fabricate the electrodes bridging the individual nanowires. Therefore, it is important to find simple cost-effective ways to obtain nanowire based ReRAM devices which combine excellent low-current response, good uniformity and reliability, distinguishable resistance states and potential to display multilevel memory performance as required for the next-generation non-volatile memory devices.

The hydrothermal method to obtain well-aligned nanorod arrays (NRAs) is easier compared with costly ways to get a TiO_2 thin film (by sputtering or atomic layer deposition) as well as the

individual nanowires. This commonly used method to obtain nanowires provided the possibility to control the electrical performance of the corresponding ReRAM devices via the morphology and the properties of the nanowires, such as the electrolyte of the solution, the growth period of the hydrothermal process, etc. Moreover, the wide suitability of hydrothermal-growth of metal oxide nanowire arrays on different substrates provided great potential of engineering the performance of obtained ReRAM devices from the interface perspective[21, 172, 190]. Recently, TiO_2 NRAs, grown on bare FTO substrates by a hydrothermal process, have been reported showing resistive switching behavior[168]. The FTO substrate provides nucleation sites for the growth of the NRAs and functions as the bottom electrode for the device. However, once again, the result showed that the realization of resistive switching behavior required a forming process and displayed high-amplitude current response[168]. The possibility that TiO_2 NRAs-based ReRAM devices can be used for multilevel memory devices and mechanisms related to this property in such devices have yet to be reported.

In this chapter, an electroforming-free low-power multilevel bipolar resistive switching behavior in TiO_2 NRAs on FTO glass substrates was proposed. The key to obtaining these properties is $TiCl_4$ treatment of the FTO substrate to create an oxygen deficient TiO_x seed layer on the substrate before the hydrothermal process. This seed layer ensures the preferential growth of a uniform, vertically oriented TiO_2 NRAs structure on the substrate. The improved NRA morphology results in a significant improvement in stability, controllability of the resistive switching performance, as well as enabling bias-engineering of multilevel memory. Furthermore, the resistive switching characteristics of this new device is compared with that of a unit formulated without the TiO_x seed layer and the difference in switching mechanisms in such structures are also suggested.

4.3. Experimental Section

4.3.1. TiO_2 NRA synthesis and device fabrication

The synthesis process of TiO_2 NRAs on a FTO glass substrate incorporating a seed layer is illustrated in Figure 32[223-225]. In the first step, the FTO substrate (40 mm×20 mm×2 mm, 12~15 Ω/□) after thoroughly cleaning in acetone, isopropanol and MilliQ water for 15 minutes was immersed for 30 min in a 0.15 M $TiCl_4$ solution at 70 ^{o}C and then underwent heat treatment at 550 ^{o}C for an additional 30 min. This generated a seed layer on the surface of the FTO substrate. The

seeded-FTO substrate was then placed against the wall of the Teflon-sealed autoclave containing a solution of 30 mL H_2O, 30 mL concentrated hydrogen chloride aqueous solution and 1.0 mL titanium butoxide. This was held at a temperature of 150 °C for 20 h. The resulting TiO_2 NRAs were rinsed with water and dried with nitrogen gas, and was further annealed in air at 550 °C for 3 h, after which it was ready for materials characterization and device fabrication. For comparison, the same procedure was used to produce the TiO_2 NRAs on a bare FTO substrate without the initial treatment in $TiCl_4$ solution. For device fabrication, an upper Al layer with a thickness of 50~100 nm was deposited on the top surface of the TiO_2 NRAs by e-beam evaporation process with a shadow mask. The diameter of the top electrode was 1 mm.

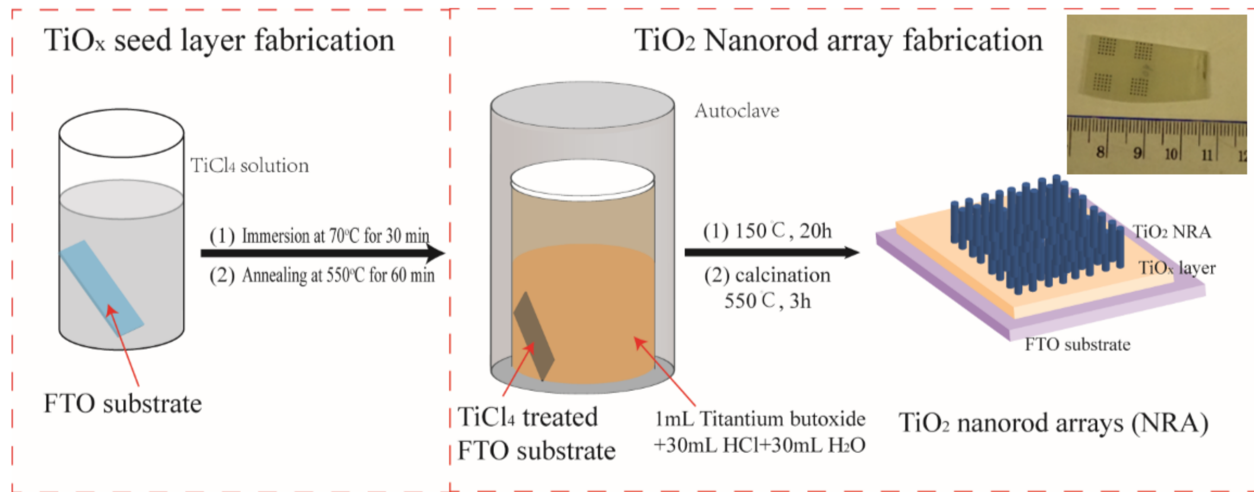

Figure 32. Schematic diagram of the fabrication process of TiO_2 NRA with seed layer, top right: optical photo for a fabricated TiO_2 NRA based device with Al top electrode.

4.3.2. Characterization

The morphology of the TiO_2 NRAs was examined by scanning electron microscopy (SEM, LEO-1550). Transmission electron microscopy (TEM) and high resolution transmission electron microscopy (HRTEM, JEOL 2000) operation was carried out at an acceleration voltage of 200 kV. X-ray diffraction analysis (XRD, PANalytical X'pert PRO MRD) in grazing incidence (GIXRD) mode was used for the phase and crystal structure analysis of the TiO_2 materials. Surface chemical states in the seed layer and TiO_2 NRAs were examined by X-ray photoelectron spectroscopy (XPS, Thermo-VG Scientific ESCALab 250). Electrical characterization of the prepared devices was performed with a Keithley 2602A source-meter. The bias voltage was applied to the top Al electrode and the FTO layer was grounded under ambient conditions.

4.4. Results and Discussion

4.4.1. Materials Characterization

4.4.1.1. SEM and TEM

Figures 33(a) and (b) show SEM images of the top of TiO_2 NRAs on a seeded FTO substrate. A well-defined and compact NRA with tetragonal crystallographic planes is observed. This is in contrast to the TiO_2 NRAs grown on bare FTO substrates, which have poor vertical orientation and intersecting nanorods (Figure 34). In photovoltaic applications, such as dye-sensitized solar cells, a seed layer would normally be introduced to prevent occasional electrical shorting due to direct contact between the redox electrolyte and FTO layer[223, 224]. In this present study, we adopt this method to improve the performance of TiO_2 NRA-based ReRAM devices. By immersing the FTO substrate into a $TiCl_4$ solution, a seed layer with a thickness of ~20 nm is typically deposited on the surface[223]. The seed layer is expected to promote the nucleation of nanorods on the FTO substrate, leading to well-defined dense NRAs with a preferred growth direction normal to the substrate[224, 226]. Preferential growth normal to the surface, and the formation of well separated nanorods, should restrict electron transport to individual nanorods minimizing cross-talk between adjacent nanorods. The Al top electrode deposited by e-beam evaporation fabricated on top of the NRAs would cover the top tip of the nanorod considering the thickness of 100 nm compared to the height of the NRAs. Due to the high compact nature of the NRAs with the seed layer, it would be difficult for these Al deposit to fall through the gap of the NRAs and cause the short-circuit failure of the fabricated devices.

The average height of the nanorods in the TiO_2 NRA is ~ 3 μm as calculated from a tilted cross-sectional view of the NRAs (inset in Figure 33(b)). Figure 33(c) shows a TEM image of an individual nanorod. The length of this nanorod has been truncated because of the preparation technique. The HRTEM and inset selected-area electron diffraction (SAED) pattern of the TiO_2 NRAs displayed in Figure 33(d) confirmed that the individual nanorod was single crystals. The HRTEM image shows a (110) inter-planar distance of 0.32 nm, suggesting that the preferred growth of the rutile TiO_2 nanorods occurs along the [001] crystal orientation, which is in agreement with NRAs synthesized elsewhere[26].

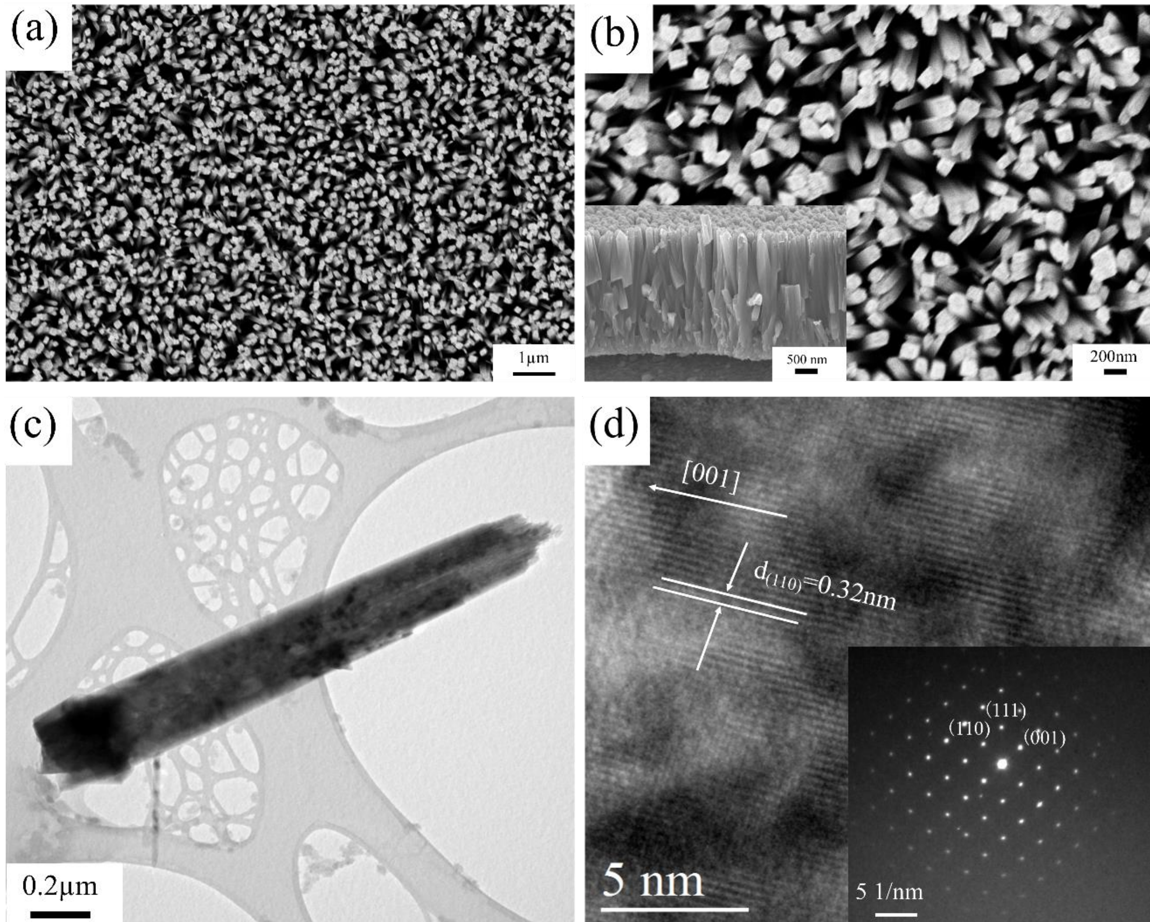

Figure 33. Morphology of TiO_2 NRAs prepared with a seed layer (a) low magnification top-view SEM image, (b) high magnification top-view SEM image (inset: 70° tilted cross-sectional view), (c) TEM image of a single TiO_2 nanorod, (d) HRTEM image of a TiO_2 nanorod (inset: SAED pattern of the same nanorod).

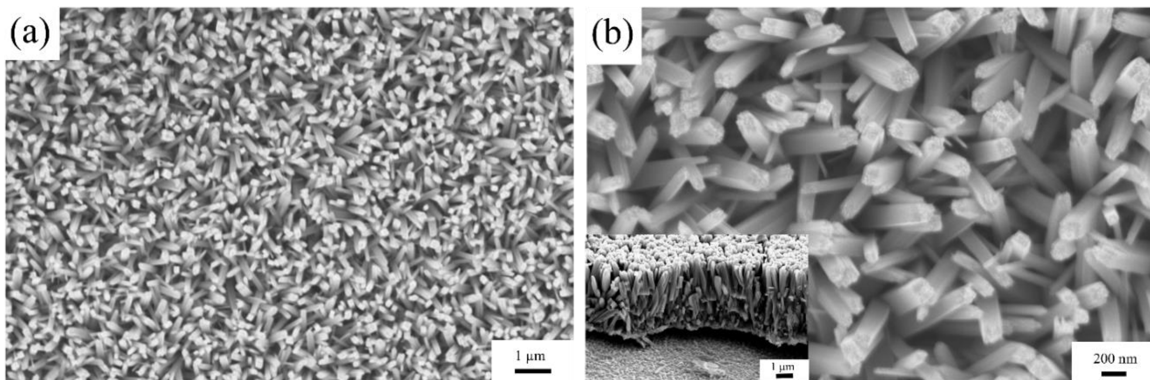

Figure 34. SEM images of TiO_2 NRA prepared without a seed layer, (a) Low magnification, (b) High magnification (inset, 70° cross-sectional view). Even though there seems a thin continuous layer at the base of the nanorod arrays, this thin layer did not engineer the orientation compared with the pre-applied seed layer on the surface of FTO substrate.

4.4.1.2. GIXRD

Figure 35 shows typical GIXRD characterization of the seed layer and the TiO_2 NRAs with and without the seed layer, respectively. It is evident that the seed layer after the annealing process is in the anatase phase (JCPDS file No. 21-1245), while the TiO_2 NRA appears as a pure tetragonal rutile phase (JCPDS file No. 21-1276) which is consistent with the HRTEM and SAED results in Figure 33(d). This is in agreement with the observation of rutile TiO_2 NRA on FTO substrates typically used for solar cells[223, 224]. Unlike the bare FTO substrate, the TiO_2 seed layer facilitates the epitaxial nucleation and growth of TiO_2 nanorods considering the decreased surface roughness of the seeded-FTO films after the treatment in $TiCl_4$ solution[224]. This leads to the enhancement of density and vertical growth of the nanorod array normal to the substrate. Furthermore, the crystallographic phase of obtained TiO_2 nanorods is not dependent on the phase of the seed layer, as researchers have demonstrated that both rutile[227] and anatase seed layers[194, 228, 229] lead to the growth of rutile nanorod arrays. The enhanced ratio of the intensities of the (002) to (101) XRD peaks in the TiO_2 NRA with a seed layer compared to the ratio of the NRA without a seed layer is suggestive of enhanced growth along the [001] direction perpendicular to the substrate[230, 231]. This preferred growth direction is also in agreement with the TEM results.

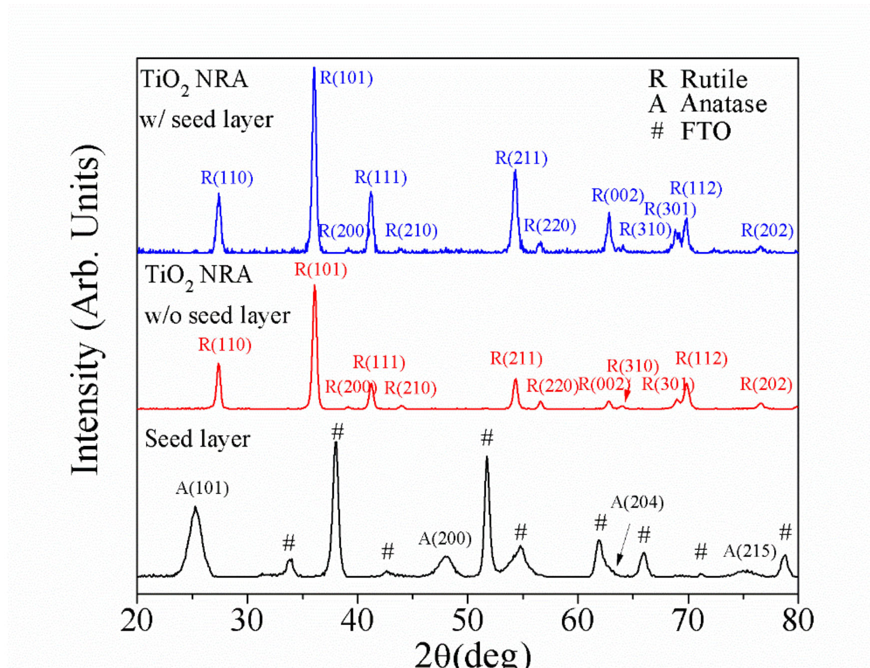

Figure 35. GIXRD characterization of the seed layer, TiO_2 NRAs prepared with and without a seed layer

4.4.1.3. XPS

Additional information regarding the surface states of the TiO_2 NRAs grown on the seed layer was obtained by XPS. The survey spectrum (Figure 36(a)) confirms the existence of C, Ti and O elements where the C atoms can be ascribed to a small concentration of carbon-based contaminants. High-resolution XPS spectra and their Gaussian deconvolution peak fittings of Ti 2p and O 1s are given in Figure 36(b) and Figure 36(c), respectively. The Ti 2p peaks at 464.18 eV and 458.50 eV can be attributed to Ti $2p_{2/1}$ and $2p_{3/2}$, respectively. The peak separation is calculated to be ~5.7 eV, which suggests the existence of Ti^{4+} oxidation states in the TiO_2 NRA[232]. A very weak peak centered at 457.28 eV can be attributed to Ti^{3+} states, which might originate from the reduction of Ti^{4+} by free electrons donated by oxygen vacancies[233]. The O 1s spectrum are fitted by two Gaussian peaks (Figure 36c). The peak at the lower binding energy is attributed to the Ti-O bonds while the peak at the higher binding energy is related with oxygen vacancies in the TiO_2 materials. This suggests that TiO_2 nanorods as-synthesized contain a low concentration of oxygen vacancies. These defects are expected to play an important role in the ReRAM devices fabricated from synthetic TiO_2 nanorod structures.

An analysis of surface states in the seed layer and in the TiO_2 NRA without the seed layer (Figures 37 and 38), can be used to find the proportion of individual oxygen chemical states in each component. The resulting percentages are summarized in Table 1. We find that the oxygen vacancy concentration in the TiO_2 NRA incorporating a seed layer is much smaller than that observed in the seed layer itself and the TiO_2 NRA formed without the seed layer. This indicates that TiO_2 NRAs grown on the seed layer are less electrically conductive. The reason for the difference in oxygen vacancies for NRAs grown with and without seed layer is under further investigation. One possible explanation is the post-annealing process for reducing the concentration of oxygen vacancies in both NRAs. The NRAs prepared with the seed layer have a more compact morphology and smaller diameter (correspondingly higher surface areas), leading to a further reduction in oxygen vacancies concentration under the same annealing condition. This difference of concentration influences the initial resistance state of as fabricated ReRAM devices (see Section 4.4.2). As the fraction of oxygen vacancies in the seed layer exceeds 30%, this layer is highly oxygen deficient. In our discussion, the seed layer will be denoted as TiO_x where $x<2$. It should be noted that an additional small shoulder on the O 1s state was occasionally observed in some TiO_2 NRA samples. This peak can be attributed to the presence of surface hydroxyl groups

(-OH) (Figure 38). The effect of residual surface -OH on the resistive switching behavior is expected to be negligible since the dominating mechanism for TiO_2 based ReRAM devices is known to arise from oxygen vacancies[234].

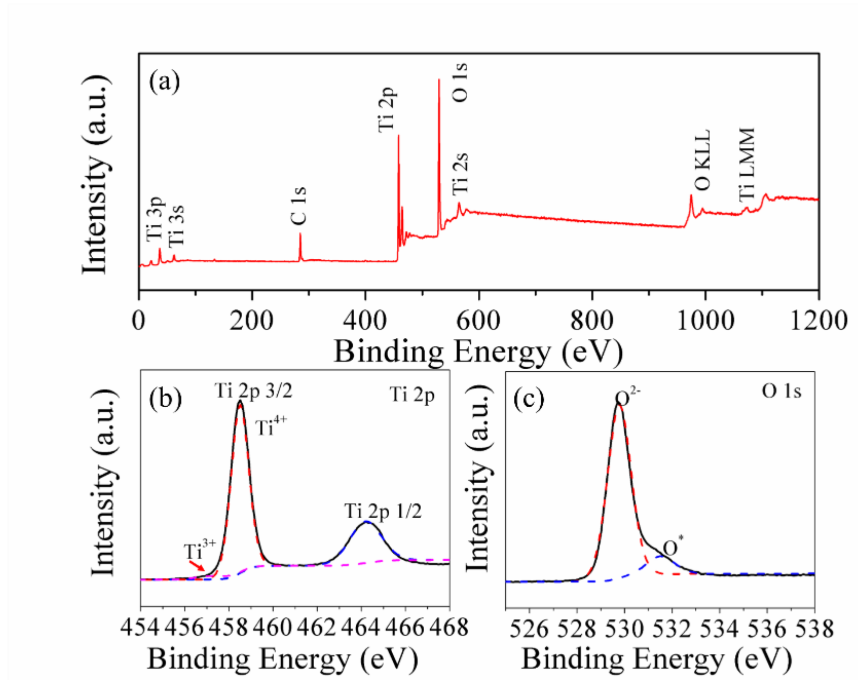

Figure 36. XPS spectra of TiO_2 NRA prepared with a seed layer: (a) survey, (b) Ti 2p and (c) O 1s

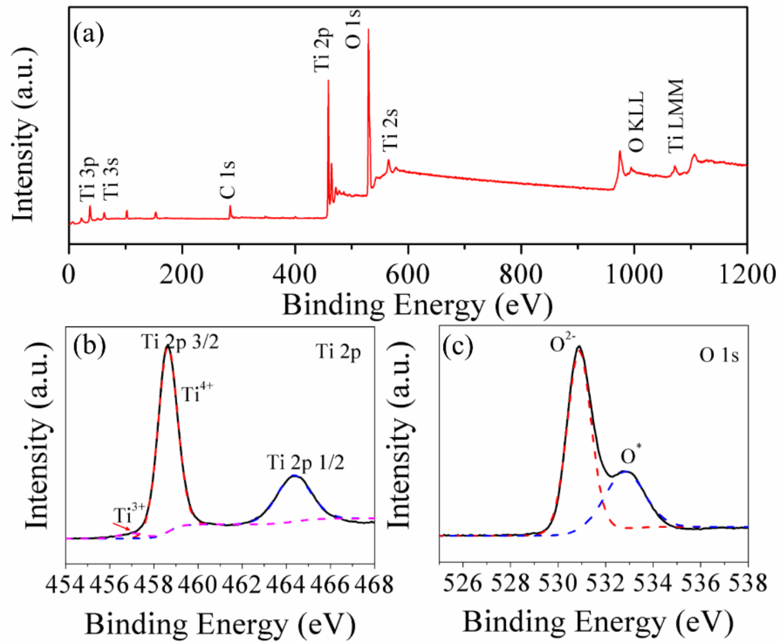

Figure 37. XPS spectra of TiO_x seed layer: (a) survey, (b) Ti 2p and (c) O 1s

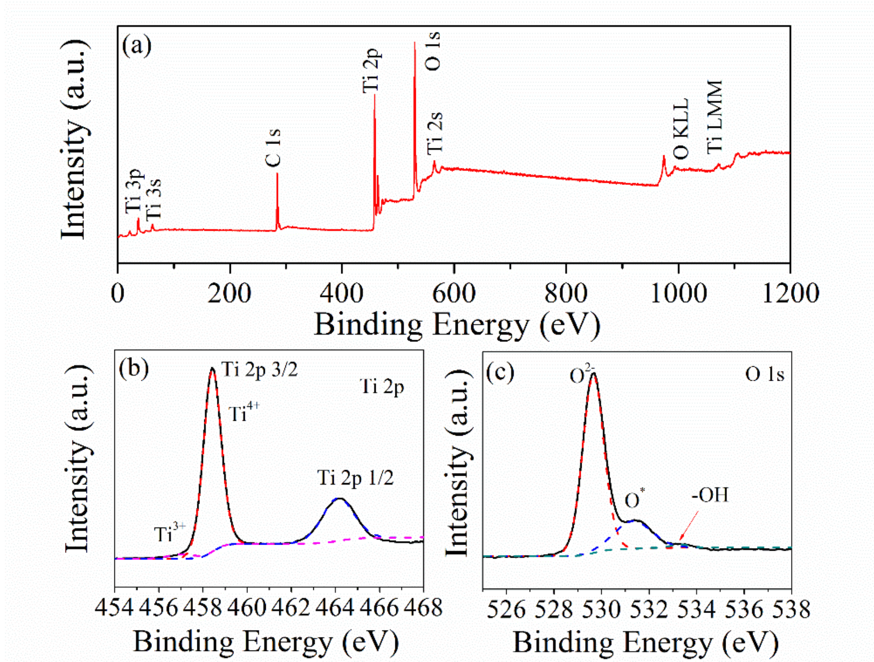

Figure 38. XPS spectra of TiO_2 NRA prepared without a seed layer: (a) survey, (b) Ti 2p and (c) O 1s

Table 1. Fractional percentage of oxygen (O 1s) states in samples (%)

Samples	O^{2-}(TiO_2)	O^*(TiO_{2-x}, oxygen vacancies)	Others (OH, etc.)
Seed layer	66.45	33.55	---
TiO_2 NRA without a seed layer	77.80	21.03	1.17
TiO_2 NRA with a seed layer	89.02	10.98	---

4.4.2. Electrical Characterization

4.4.2.1. Resistive switching behavior

Figure 39 is a record of the resistive switching behavior over 100 successive cycles in TiO_2 NRA based ReRAM devices as prepared with and without a seed layer. Both devices display prototypical bipolar resistive switching characteristic. As shown in Figure 39(a), when the voltage sweeps from 0 to +4 V in the Al/TiO_2 NRA/TiO_x layer/FTO device, the device switches from the high resistance state (HRS) to the low resistance state (LRS) and a non-volatile ‘ON’ state was obtained (SET process). The LRS remained after negative voltage was applied until the negative voltage is high enough to switch the device from LRS to HRS and an ‘OFF’ state was achieved (RESET process). The resistive switching performance of the Al/TiO_2 NRA/FTO device is similar, but the polarity of the ON/OFF transition is reversed (Figure 39(b)). It is important to note that the

resistive switching behavior in both devices was obtained without the usual electroforming process[168]. These results are also consistent with the behavior of single ~6μm-long TiO_2 nanowire-based multilevel memory devices previously studied in our group, which demonstrated intrinsic (forming-free) resistive switching characteristics attributed to the existed oxygen vacancies in the individual nanowire[148]. This forming-free property, related to the introduction of oxygen vacancies in the switching layer, is desirable for ReRAM in the electronic industry as it simplifies operation and enables high density memory devices[20].

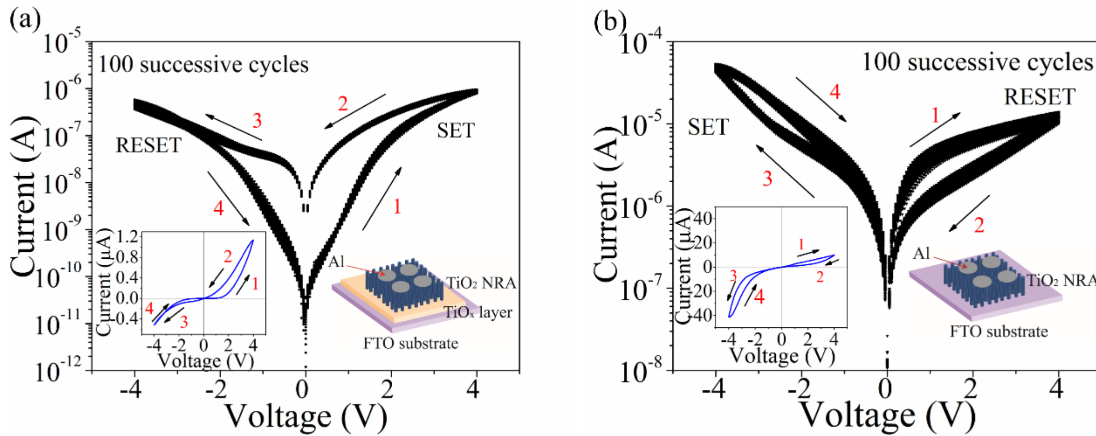

Figure 39. *I-V* curves of (a) Al/TiO_2 NRA/TiO_x layer/FTO device and (b) Al/TiO_2 NRA/FTO device for 100 successive cycles (for each figure, left inset: *I-V* curve for a typical cycle and right inset: schematic design of the device)

To be noted, although Al was used as the top electrode, the *I-V* performance of the present Al/TiO_2 NRA/TiO_x layer/FTO device was not the same as that of other TiO_2 thin film devices using Al as the top electrode[68, 72, 235]. In thin film devices, the interaction between Al and TiO_2 to form an insulating Al-Ti-O layer which functions as a source of oxygen ions improves the resistive switching behavior. In our fabricated Al/TiO_2 NRA/TiO_x layer/FTO device, the Al layer is expected to enhance performance compared to devices using the Pt[168] electrodes because of its oxygen affinity and ability to form an interfacial Al-Ti-O layer. However, the switching mechanism in the current devices is dominated by the TiO_2 NRAs since the thickness of the Al-Ti-O layer is likely 3~5 nm[68], which is much less than the height of the TiO_2 NRAs (~3 μm). As a result, the resistance of an Al-Ti-O layer will be much smaller than the total resistance of the TiO_2 NRA layer. This hypothesis is confirmed by the polarity at which the device transitions from the HRS to LRS. This polarity is opposite to the negative polarity required for thin film TiO_2 devices with an Al top electrode in which the interfacial Al-Ti-O layer is expected to be crucial in

determining the resistive switching behavior[75, 80, 195]. In addition, the smooth change of the *I-V* curves of both devices indicates that the switching mechanism in our devices is likely dominated by uniformly distributed valence states or space charge at the interface rather than the formation and rupture of filament in response to electric field[80, 236].

Other differences are also apparent in the properties of devices prepared with and without the TiO_x seed layer. For example, the current amplitude in the Al/TiO_2 NRA/TiO_x layer/FTO device is approximately one order of magnitude less than that of the device prepared without a seed layer, indicating that the Al/TiO_2 NRA/TiO_x layer/FTO device is more insulating. This suggests that the higher concentration of oxygen vacancies observed in the TiO_2 NRAs in the absence of a seed layer makes the device more electrically conductive. Due to the large difference between the thickness of the seed layer (~20 nm) and the height of the nanorods, the resistance of the seed layer is small compared to that of the NRAs and the electrical performance can then be dominantly ascribed to the TiO_2 NRAs. Variations in the concentration of oxygen vacancies in the nanorods in the two types of device may also be responsible for differences between the initial states in resistive switching operations, in which the fabricated Al/TiO_2 NRA/TiO_x layer/FTO device starts from the HRS under sweeping operations, while the initial condition for Al/TiO_2 NRA/FTO devices is the LRS. This behavior is indicated by the arrows in Figure 39.

I-V curves under cyclic voltage sweeping show that the bipolar resistive switching response in Al/TiO_2 NRA/TiO_x layer/FTO devices is more stable and repeatable while maintaining a relatively high ON/OFF ratio (>20). Stable electrical performance can be associated with the compact, fine surface morphology of the TiO_2 NRAs grown on the seed layer. TiO_2 nanorods constrain current flow along their longitudinal axis due to their small cross section. This leads to the formation of direct conduction paths for electrons and the minimization of interactions between channels in adjacent nanorods. Such structures also facilitate the deposition of compact Al electrodes. To illustrate this point, the resistive switching behavior of Al/TiO_2 NRA/FTO devices is characterized by high fluctuation and a small ON/OFF ratio, as demonstrated in Figure 40. Both of these properties are not desirable for industrial applications of ReRAM devices in the electronic industry[20]. It is important to note that the higher cell uniformity in these Al/TiO_2 NRA/TiO_x layer/FTO devices with distinguishable resistance states ensure that they are promising as a candidate for non-volatile ReRAM devices, as demonstrated in Figure 41. From the above analysis,

it can be concluded that the introduction of a TiO_x seed layer can significantly improve the resistive switching performance of the TiO_2 NRA based ReRAM devices.

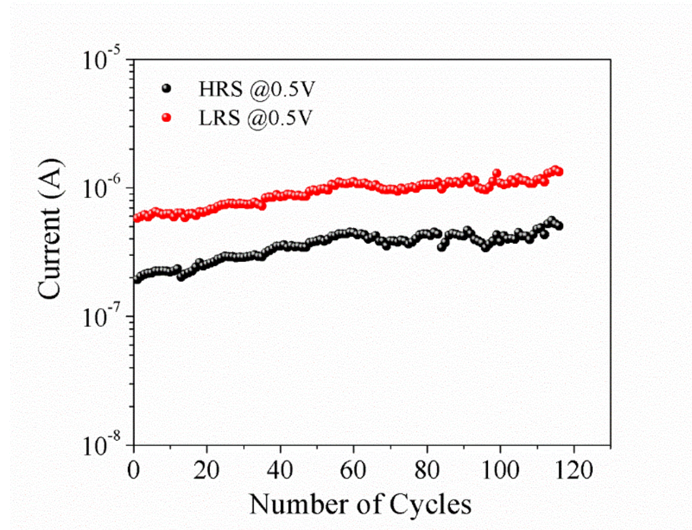

Figure 40. Endurance study of Al/TiO_2 NRA/FTO device under voltage sweeping

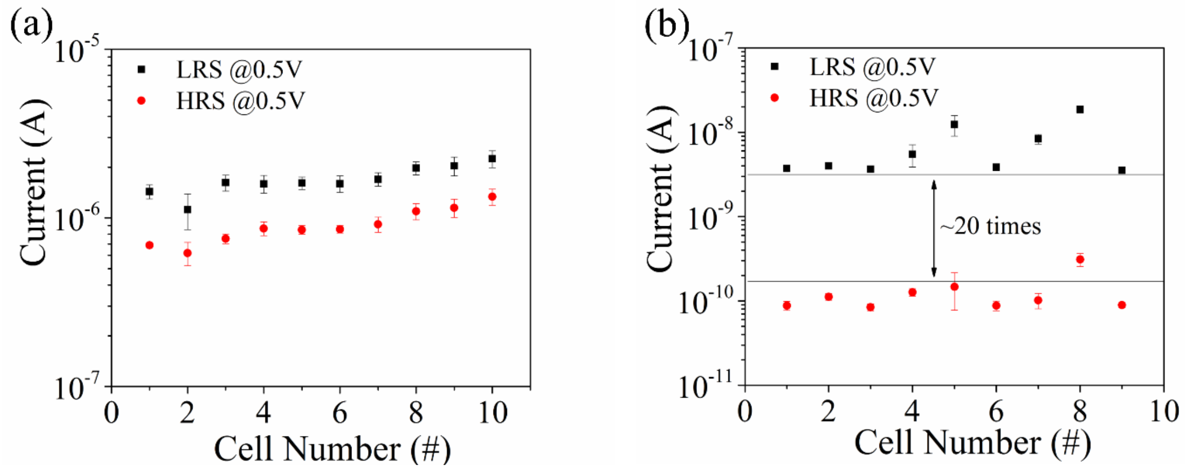

Figure 41. Cell uniformity performance check by examining the current response at specific read voltage for different cells (a) Al/TiO_2 NRA/FTO devices and (b) Al/TiO_2 NRA/TiO_x layer/FTO device. (The standard deviations are from the summary of 10 repeated *I-V* sweeping cycles). For the Al/TiO_2 NRA/FTO devices, the ON/OFF ratio is relatively small, which is difficult to distinguish between two different resistance states in the application of ReRAM devices. Furthermore, the big variation in current response among different cells (for example, the LRS current response for cell No.2 is in the same range of the HRS current response for cell Nos. 8-10) also make the Al/TiO_2 NRA/FTO devices not suitable for the ReRAM devices in the electronic industry. Comparatively speaking, the Al/TiO_2 NRA/TiO_x layer/FTO devices displayed a better cell uniformity of the electrical performance in terms of the relatively stable and low HRS current and larger ON/OFF ratios. Even though there is a variation in the LRS current response among different cells, all the ON/OFF ratios are big enough for distinguishing from two different states.

4.4.2.2. Endurance and retention Study

The endurance performance of the fabricated Al/TiO_2 NRA/TiO_x layer/FTO device is given in Figure 42(a) by direct-current cyclic sweeping operations. It was found that this new device maintains a high stable ON/OFF ratio (>20) over at least 500 cycles. This ratio is sufficient to distinguish different states in potential ReRAM devices. The cumulative probability curve of both LRS and HRS resistances illustrated that the distribution of LRS and HRS resistances is in the range of 1.3×10^8 Ω and ~5.3×10^9 Ω, respectively, with very good cycle-to-cycle uniformity as demonstrated by the cumulative probability curve in Figure 43. The coefficient of variations for LRS and HRS resistances (defined as the standard deviation of the measured resistance divided by the mean values) for more than 500 cycles are 0.04 and 0.15, respectively, suggesting promising stable resistive switching performance. It is also apparent that the low current amplitude (<10^{-8} and 10^{-10}A for LRS and HRS read at 0.5 V, respectively) during resistive switching is very promising with respect to low operating power and heat generation requirements for emerging applications of memristor devices such as logic and neuromorphic devices[22, 237]. Furthermore, data retention of the Al/TiO_2 NRA/TiO_x layer/FTO device was studied by probing the current changes in the OFF and ON state for a long period of time. As seen in Figure 42(b), a well-defined ON/OFF ratio, showing only limited fluctuations, was obtained in the device for more than 3×10^4 s. Robust endurance, low operating power, together with long retention time is indicative of the high reliability and non-volatile nature of these fabricated Al/TiO_2 NRA/TiO_x layer/FTO devices.

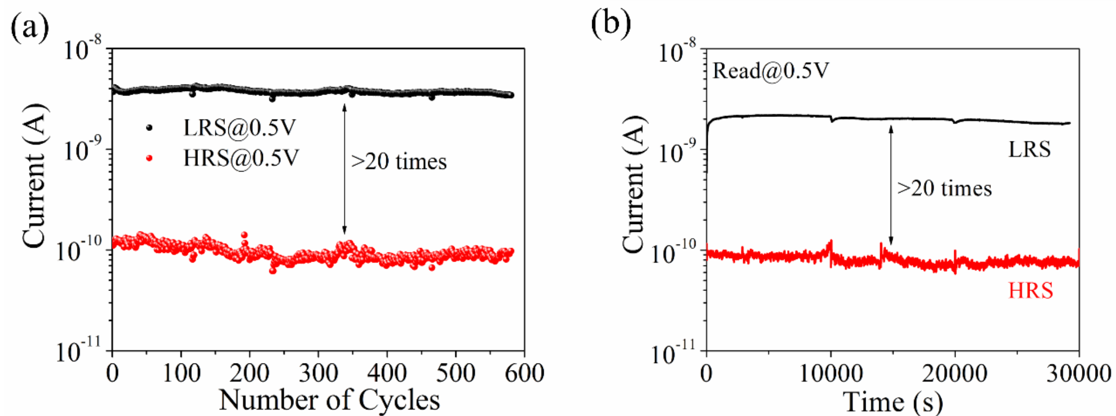

Figure 42. (a) Endurance and (b) retention performance of Al/TiO_2 NRA/TiO_x layer/FTO device

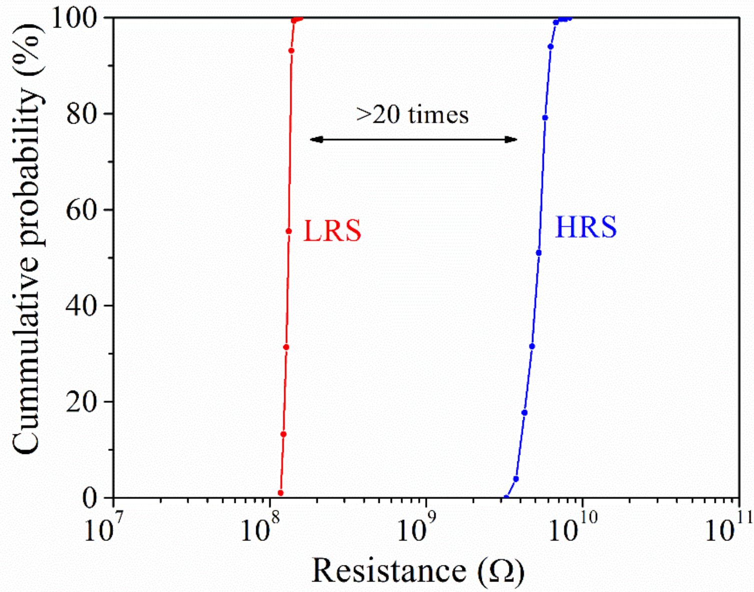

Figure 43. Cumulative probability curve for LRS and HRS resistances of Al/TiO_2 NRA/TiO_x layer/FTO device for ~550 cycles

4.4.2.3. Switching mechanism study

The conduction mechanism in the Al/TiO_2 NRA/TiO_x layer/FTO device can be obtained from an analysis of the *I-V* characteristic curves shown on a log-log scale in Figure 44. Under positive bias, the Schottky barrier at the FTO/TiO_x interface limits the electron transport and the device is initially in the HRS, given the difference between the work function of the FTO substrate (4.7 eV) and the ideal Fermi level of TiO_2 (4.2 eV)[238]. The *I-V* characteristic for the HRS consists of three different regions, the Ohmic region ($I \propto V$) which is dominated by thermally generated free carriers, the Child's law region ($I \propto V^2$), where traps are being filled by electrons, and the trap-filled-limit region including a threshold voltage (V_{TFL}) and steep current rise. The V_{TFL} in our device is ~1 V, which corresponds to the voltage at which all traps are filled by electrons, after which the electrons flow through the conduction band, switching the device from HRS to LRS. This behavior can be easily understood from the trap-controlled SCLC mechanism, in which the oxygen vacancies serve as electron traps that would form/rupture electron transport channels[135]. Oxygen vacancies are present in the individual nanorods as well as in the TiO_x seed layer due to its high oxygen deficiency. As the voltage sweeps from +4 V to 0 V, the *I-V* curve first has a slope of ~1.62 as the traps remain filled. A slope of 1.62 instead of 2, as expected for a space charge limited current, can be attributed to trapping in the interfacial layer formed in the vicinity of the Al electrode during the metal deposition process[71]. Migration of oxygen vacancies in the nanorods as well as in the

TiO_x seed layer would also play a role in the deviation of slopes[42, 73]. When the voltage approaches zero, the slope decreases to ~1, as the injection of carriers is reduced and Ohmic conduction dominates.

During the RESET process (Figure 44(b)), the Al electrode is negatively biased, and electrons start to be injected from this layer towards bottom FTO electrode. The slope of the *I-V* curve is ~1.0 when the bias voltage is less than −0.4 V. As the voltage becomes more negative, the slope initially decreases before increasing to >2.0. This suggests that the traps associated with oxygen vacancies remain filled. As the voltage sweeps from −4 V to 0 V, the slope of the curve first decreases from ~3 to ~2 as the voltage approaches −0.4 V. The slope then becomes ~1 at lower negative voltage down to 0 V, indicating that the current arises from free carriers. This behavior suggests that electrons are released from all of the traps at ~ −0.4 V and the device re-transitions from the LRS to HRS.

As to the switching mechanism of the TiO_2 NRA device without the seed layer, due to the higher concentration of oxygen vacancies in the NRAs, the device shows a higher conductivity compared to the TiO_2 NRA device with the seed layer. Furthermore, the I-V performance did not fit with the SCLC conduction mechanism, suggesting a different switching mechanism. We propose that the high concentration of oxygen vacancies on the surface of NRA render these smaller distance among these defects, therefore leading to a higher probability of electron hopping pathways. Upon the application of positive electric field on the Al electrode, electrons hop from various defects from the FTO electrode to the Al electrode. Meanwhile, some of the oxygen vacancies on the surface will trap the electrons, reducing the hopping probability. Therefore, when we sweep from 4 V to 0 V, the device will shows smaller conductivity, leading to the transition from LRS to HRS (as indicated in the arrows in Figure 39(b)). Vice versa, a negative electric field promote the electrons to hop from Al electrode, and at the same time, detrapping some of the oxygen vacancies. This process can lead to the transition from HRS to LRS.

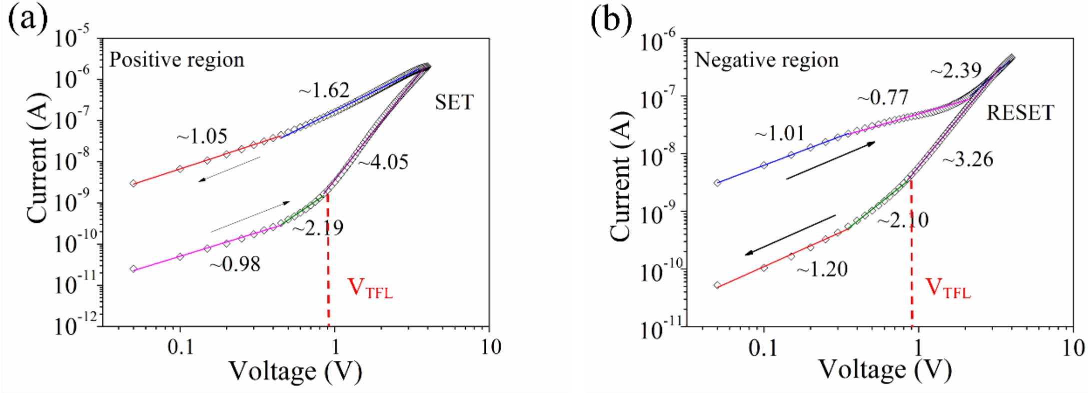

Figure 44. Log-log *I-V* response for the Al/TiO_2 NRA/TiO_x layer/FTO device, (a) Positive region and (b) Negative region

Further understanding of the conduction mechanism in fabricated Al/TiO_2 NRA/TiO_x layer/FTO devices can be obtained by the *I-V* response at different temperatures (Figure 45(a) and 45(b)). The resulting temperature-dependent ON/OFF ratio is shown in Figure 45(c). It can be seen that the LRS resistance decreases as the temperature decreases. In addition, the LRS resistance at a 0.5 V read voltage increases linearly with temperature, as shown in Figure 45(d). This indicates an Ohmic behavior under LRS as evidenced by a slope of ~1 under low read voltages in Figure 45(a). In contrast, the current response in the HRS at different temperatures is more complicated (Figure 45(b)). The HRS current is controlled with the SCLC mechanism over a range of temperature,[74] as illustrated in Figure 45(b). To identify the physical mechanism, the Child's Law current response at different temperatures is plotted as ln(*I*) vs. *1000/T* in Figure 45(e). Based on the SCLC theory, the current in the Child's Law region can be expressed as:

$$I = \frac{9}{8} A\varepsilon\mu\theta \frac{V_a^2}{d^3} \qquad Eq.(2)$$

$$\theta = \frac{N_c}{N_t} \exp[\frac{-(E_c - E_{trap})}{KT}] \qquad Eq.(3)$$

This solution is based on the assumption that the electrons traps (oxygen vacancies in our case) are restricted to a single discrete energy level (E_{trap}). In the equations, A is the effective area for the conduction channels, μ is the mobility, ε and d are the permittivity and thickness of the oxide layer, respectively. Furthermore, V_a is the applied voltage, E_c is the energy at the conduction band minima, N_c the effective density of states in the conduction band at temperature T, N_t the total trap density and K is the Boltzmann's constant.

From *Eq.(2)* and *Eq.(3)*, the current response *ln(I)* in this region is a linear function of *1000/T*, with a slope $-(E_c-E_{trap})/1000k$. Arrhenius plots of measured data at different read voltages are

given in Figure 45(e). The activation energy calculated from these data at different read voltages is, $\Delta E = E_c - E_{trap}$ = 0.18~0.20 eV (Figure 45(f)). Thus energy levels associated with these traps are more shallow than trap levels arising from oxygen vacancies in bulk TiO_2, which are theoretically calculated to lie 0.8~1.0 eV below the conduction band[74, 239, 240]. This difference in trap levels might be attributed to the proximity of the surface in the high surface-to-volume ratio of nanorods and the role of the surface in reducing the energy for vacancy formation. Furthermore, the diffusion of defects from inside the nanorod to the surface will also increase the surface defect density[241]. Similar reports about the ZnO nanowire arrays showed much higher photocurrent response compared with the thin film under the same thickness condition, mainly due to the increasing of self-induced surface defects[242]. The overall effect is that the trap states of the oxygen vacancies are expected to be shallower below the conduction band, compared to those in TiO_2 thin films. Research about the relationship between the surface defects of nanorods and the corresponding resistive switching performance is ongoing.

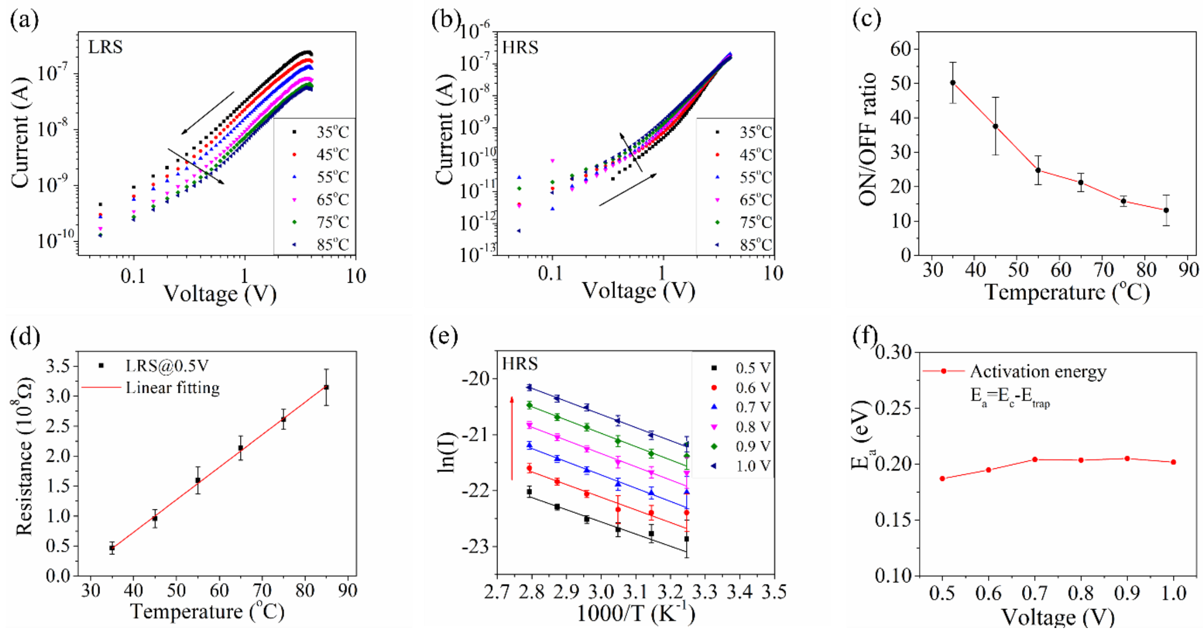

Figure 45. Log-log *I*-*V* curves of (a) LRS and (b) HRS at different temperatures, (c) ON/OFF ratio vs. temperature, (d) Linear fit for LRS resistance, (e) ln(*I*) vs. 1000/*T* and corresponding fits at specific read voltages and (f) activation energy $\Delta E = E_c - E_{trap}$ calculated from the slopes in (e) plotted as a function of *V*. The standard deviations for (c), (d) and (e) are from the statistical average of 15 repeatable cycles. All measurements were carried out under ambient atmospheric conditions.

A tentative model of the switching mechanism for an Al/TiO_2 NRA/TiO_x layer/FTO device is schematically illustrated in Figure 46. In its pristine state, the device possesses a limited

concentration of oxygen vacancies at the FTO/TiO_x interface as well as in the NRAs (Figure 46(b)). These oxygen vacancies yield a series of electron traps as shown below the TiO_2 conduction band. The traps are gradually filled with electrons when a forward bias is applied to the Al electrode. Figure 46(c) corresponds to the forward region below the V_{TFL}. After all of these traps are filled the current abruptly increases as the device transitions from HRS to LRS (Figure 46(d))[211]. Significant detrapping of these oxygen vacancies occurs when a high negative voltage is applied on the top Al electrode, which would switch the device back from LRS to HRS.

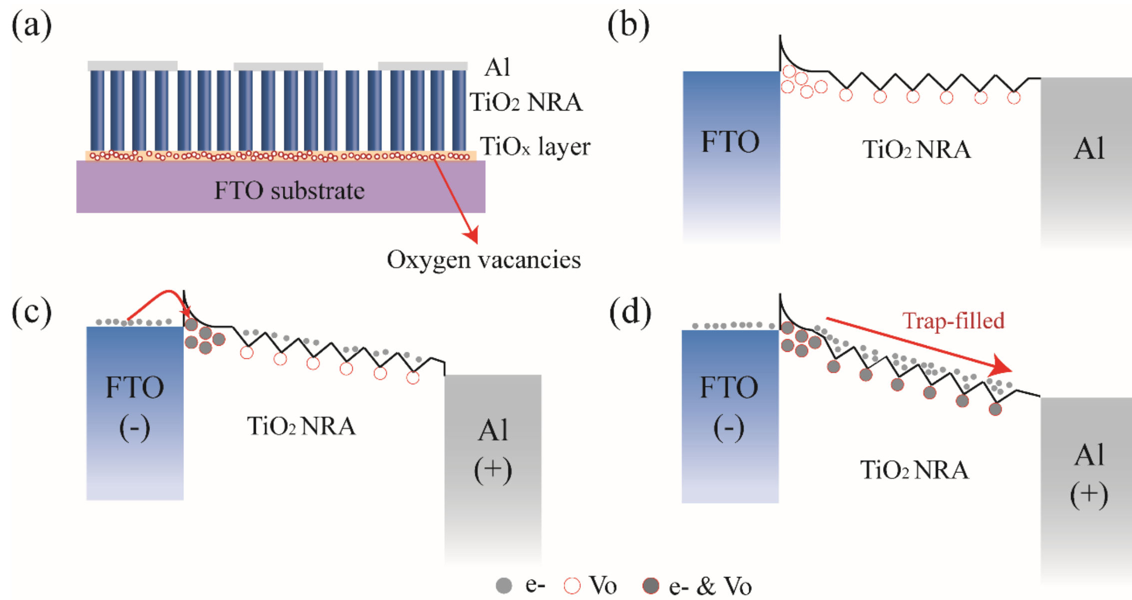

Figure 46. Schematic representation of the switching mechanism in fabricated Al/TiO_2 NRA/TiO_x layer/FTO device, (a) cross-sectional design, (b) pristine state, (c) positive bias, $0 \rightarrow V_{TFL}$, traps are partially filled, (d) positive bias, $V_{TFL} \rightarrow 4$ V$\rightarrow 0$ V, traps are fully filled, the device has transitioned from HRS to LRS

4.4.2.4. Multilevel memory behavior

The potential for obtaining multilevel memory in the TiO_2 NRA based device was studied by applying different SET voltages while keeping the RESET voltage at −4 V. Figure 47 shows well-defined differences in LRS current under cyclic sweeping operations, such that a 4-level memory may be feasible while maintaining a nearly constant HRS current (Read @0.5 V). The 4-level memory performance was measured to be stable for 80 cycles, and the measurements indicate that this behavior can be extended to more cycles given the very small variation in current in each level (Figure 47(b)). It was also found that a 6-level memory can be achievable using SET voltages of 5 and 6 V, even though the current response for higher voltage is not as distinguishable as for lower SET voltages, as demonstrated in Figure 48. Furthermore, the current response of LRS for

each level is still below 10^{-7} A under different SET voltages, suggesting significant potentials for low-power ReRAM devices. Overall, this indicates that the TiO_2 NRAs grown on a seed layer are very promising in multilevel memory devices. The multilevel memory performance for Al/TiO_2 NRA/FTO device is not achievable due to its poor reliability.

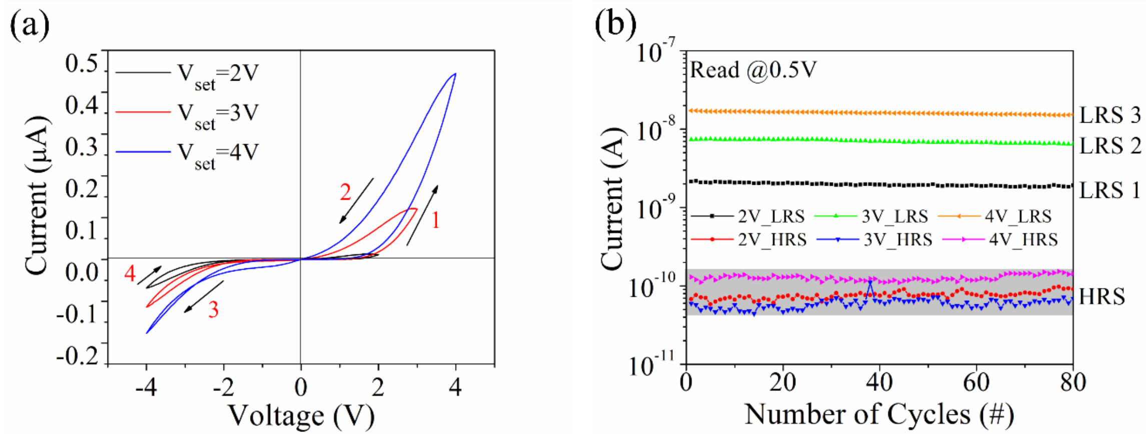

Figure 47. (a) *I-V* curve for Al/TiO_2 NRA/TiO_x layer/FTO device under different SET voltages and (b) demonstration of 4-level memory performance under cyclic voltage sweeping

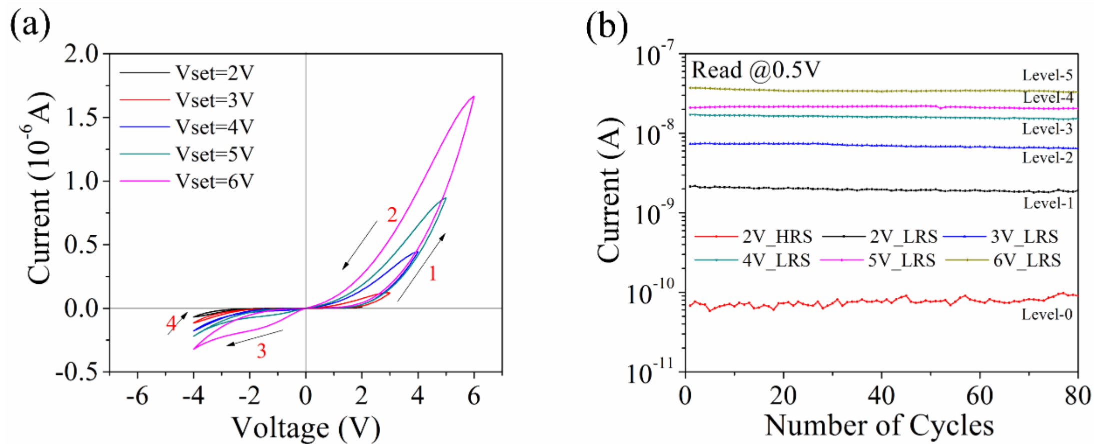

Figure 48. (a) *I-V* curves of Al/TiO_2 NRA/TiO_x layer/FTO device at different SET voltages and (b) demonstration of 6-level memory response in cyclic voltage sweeping

Though some metal oxide nanomaterials exhibit multilevel memory performance, the origin of multilevel memory is still controversial. It has been suggested that multilevel memory can be obtained by engineering of the size of conductive filaments (more generally, conduction paths) as determined by the accumulation of ions or defects controlled by the compliance current[57, 243], maximum voltages[56] and a series of applied voltages[148]. Different ionic charge traps or intermediate energy states below the valence band within the oxide layer have also been suggested.[244] Modification of the effective barrier height and narrowing of the depletion layer have

also been proposed to engineer a range of ON/OFF ratios[234] or different levels of current amplification[149]. In the current work, the origin of the multilevel memory performance in the fabricated devices has been studied by examining the *I-V* characteristics at different SET voltages on a log-log scale (Figure 49). This shows that the switching mechanism in the devices under all five SET voltages arises from SCLC[245]. Changes in the slope of the current for $V > V_{TFL}$ with SET voltage are also described via SCLC theory, as shown in Figure 50[38]. It can then be concluded that the accumulation of oxygen vacancies and size engineering of conductive paths or filaments can be excluded as the origin of a multilevel memory in the present device. For $V > V_{TFL}$, all available traps would have been filled and the injection carriers are mainly contributed by the increase in free electrons. Since higher applied voltages (V_a) would result in a larger number of free electrons, higher LRS current at the same low read voltages could be expected considering that the slopes for the LRS current response are approximately the same under different SET voltages. This could be the reason for the multilevel memory performance in our devices. Further studies on the dependence of *I-V* characteristic on pad size, and the effect of the height of the TiO_2 nanorod array on the multilevel memory response are being undertaken to clarify the switching mechanism in these Al/TiO_2 NRA/TiO_x layer/FTO devices.

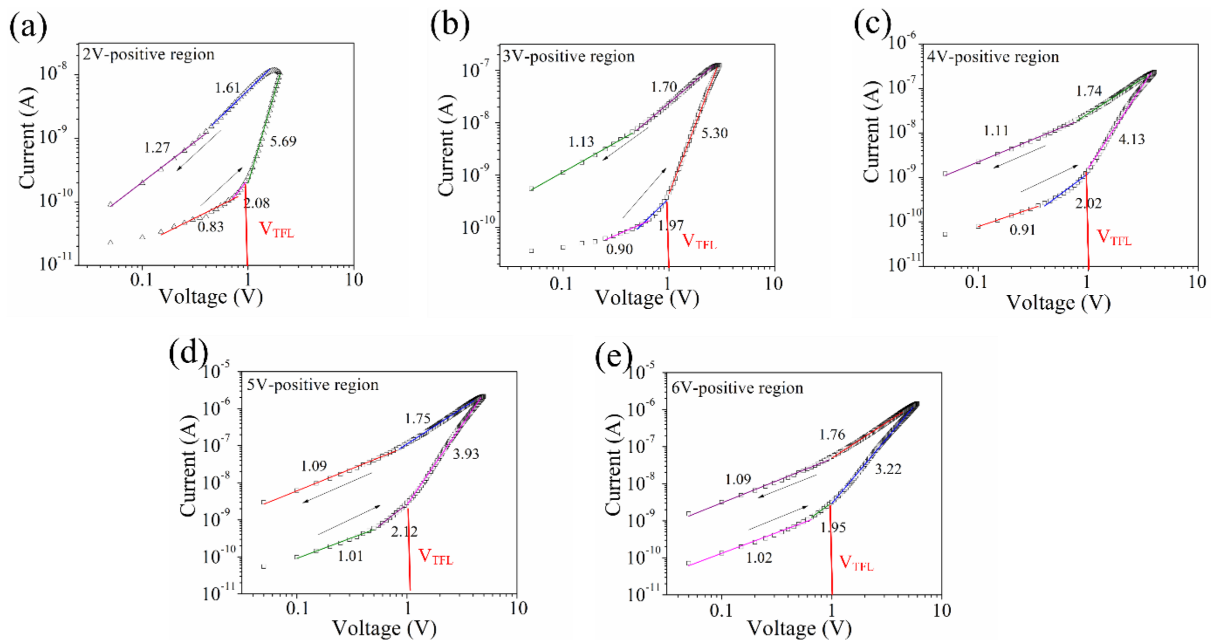

Figure 49. Log-log *I-V* curves for Al/TiO_2 NRA/TiO_x layer/FTO device at different SET voltages (a) V_{set}=2 V, (b)V_{set}=3 V, (c) V_{set}=4 V, (d)V_{set}=5 V, (e) V_{set}=6 V

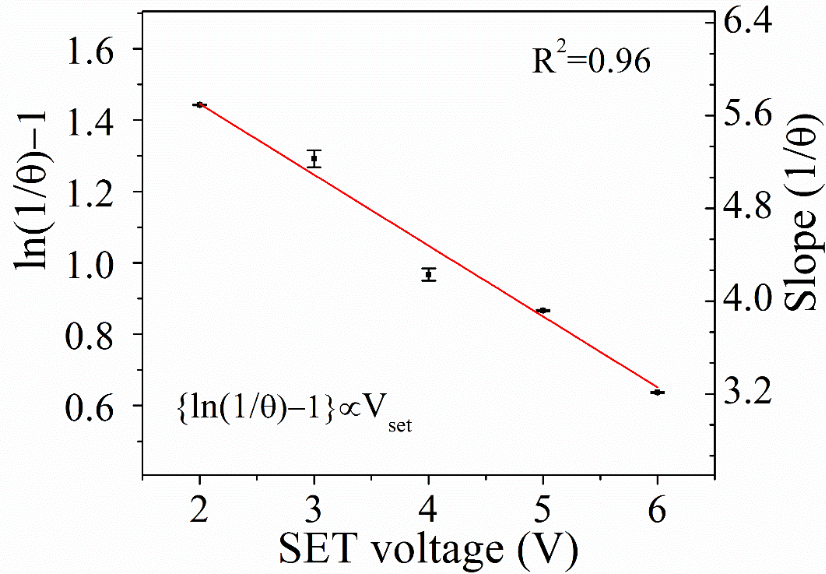

Figure 50. Slope of *I-V* curve of Al/TiO_2 NRA/TiO_x layer/FTO devices in the region with $V>V_{TFL}$ for different SET voltages (average of 10 cycles at each SET voltage). The *I-V* curve in this region is found to have a slope of $1/\theta$ based on SCLC theory where θ is $\theta=1/(1+N_t/N_c(exp(-q(V_a-V_{TFL})/KT))$. Then $ln(1/\theta)-1$ is inversely proportional to the applied SET voltage. For our device, the V_{TFL} is small and nearly constant (~1 V) for different SET voltages (V_a), so different SET voltages all result in sharply increasing current with the slope decreasing at higher SET voltage. These properties confirm that current flow in fabricated Al/TiO_2 NRA/TiO_x layer/FTO devices is controlled by a SCLC mechanism.

4.5. Conclusions

In this chapter, it was demonstrated the improved resistive switching performance in the devices based on TiO_2 NRAs on a FTO substrate by the introduction of a seed layer. The TiO_x seed layer on the surface of the FTO substrate enhances the vertical growth of TiO_2 NRAs normal to the substrate, leading to compact and fine nanorod morphology. Meanwhile, the concentration of oxygen vacancies of obtained NRAs is lower compared with NRAs prepared without the seed layer. The obtained Al/TiO_2 NRA/TiO_x layer/FTO devices exhibit a stable forming-free bipolar resistive switching behavior and maintain a higher ON/OFF ratio with lower switching currents under voltage sweeping over 500 cycles. The retention period is found to exceed 3×10^4 s. Switching in as-fabricated devices is controlled by a trap-mediated SCLC mechanism in which the existed oxygen vacancies in nanorods as well as in the seed layer function as trap centers. Furthermore, a multi-level memory feature of the device, each dominated by SCLC current flow,

is obtained in response to variations in the SET voltage. Such forming-free non-volatile multilevel resistive switching properties, low power operation, combined with robust endurance and retention, make Al/TiO_2 NRA/TiO_x layer/FTO devices promising candidates for future non-volatile ReRAM devices.

Chapter 5. Oxygen Vacancy Migration/Diffusion Induced Synaptic Plasticity in a Single Titanate Nanobelt[246]

5.1. Overview

Neuromorphic computational systems that emulate biological synapses in the human brain are fundamental in the development of artificial intelligence protocols beyond the standard von Neumann architecture. Such systems require new types of building blocks such as memristor that access a quasi-continuous and wide range of conductive states, which is still an obstacle for the realization of high-efficiency and large-capacity learning in neuromorphic simulation. Here, we introduce hydrogen and sodium titanate nanobelts, the intermediate products of hydrothermally-synthesis of TiO_2 nanobelts, to emulate the synaptic behavior. Devices incorporating a single titanate nanobelt demonstrate robust and reliable synaptic functions, including excitatory postsynaptic current, paired pulse facilitation, short term plasticity, potentiation and depression as well as learning-forgetting behavior. In particular, the gradual modulation of conductive states in the single nanobelt device can be achieved by a large number of identical pulses. The mechanism for synaptic functionality of the titanate nanobelt device is attributed to the competition between an electric field driven migration of oxygen vacancies and a thermally induced spontaneous diffusion. These results provide insight into the potential use of titanate nanobelts in synaptic applications requiring continuously addressable states coupled with high processing efficiency.

5.2. Introduction

The ability of human brain to perform high-level parallel information processing while consuming ultralow power, demonstrates that the brain has a superior architecture compared to that of less efficient conventional von Neumann systems where memory and processing units are physically separated.[96, 247] The synapse is a basic element of the human brain and provides the functional interneuron link through which information is transmitted in the neural networks.[100] Synapses are considered the most important functional units involving learning and memory response in the human brain.[122, 248] Most notably, the synaptic transmission that relates the signal delivered from a presynaptic neuron to the resulting signal produced in a postsynaptic neuron is plastic and results in the potentiation and depression of short-term or long-term synaptic strength, enabling synaptic computation[249, 250] or learning/memory[109, 251] in the brain. A significant recent

development is that memristive or resistive switching memory devices based on a variety of new materials such as Ag_2S, perovskite, organic PEDOT:PSS, Ag ion doped dielectric films[11, 13, 106, 115, 252, 253] and field effect transistor (FET) devices[254-256] have been used as building blocks with similar physical (e.g., plastic) response to mimic biological synaptic functions. Two-terminal memristive devices, which have been used in imaging and facial recognition in neuromorphic computing,[123-125] have several advantages compared to the FET configuration. These include reduced complexity of the device structure and fabrication process, as well as lower energy consumption.[10] In practice, conductance in a biological synapse is modulated by the exchange of Ca^{2+} or Na^{+} ions between the membrane and the synaptic junction in response to an action potential, whereas conductance in a memristive device is controlled by the migration of metallic ions[11, 13] or oxygen ions/vacancies[257] on application of a sweeping voltage or pulse. The use of memristor in neuromorphic computing applications requires a non-abrupt switching mechanism, i.e., the continuous modulation of conduction, analogous memory functionality and repeatable response.[112] This can be achieved by considering the internal dynamic of ion migration in memristor device, the so-called second-order memristor[109, 258], and several intriguing synaptic functions such as synaptic metaplasticity[111] and triplet spike-timing dependent plasticity (STDP)[259] have been achieved based on the second-order memristive system. The availability of memristive devices with excellent performance such as multi-conductive states and timing dependent plasticity, as required for the simulation of important synaptic responses such as learning, potentiation and depression, is therefore key to the development of neuromorphic systems.[260]

Nanowires or nanobelts are promising as building blocks for bottom-up fabrication in nanoelectronics. In particular, the study of artificial synaptic behavior based on individual 1D TiO_2 nanowires/nanobelts devices suggest that oxygen vacancies in the TiO_2, and the migration of these vacancies under an applied electric field, are responsible for resistive switching and the accompanying synaptic response[151, 261]. One of the most widely-used way to synthesize TiO_2 nanowires is the hydrothermal process[262]. In a typical hydrothermal synthesis of TiO_2 nanobelts from precursor nanoparticles such as commercial P25 nanoparticles, the first step involves the conversion of nanoparticles to sodium titanate nanobelts ($Na_2Ti_3O_7$). These are then converted to hydrogen titanate ($H_2Ti_3O_7$) in an ionic exchange process before finally becoming TiO_2 nanobelts during the annealing process.[263] $Na_2Ti_3O_7$ and $H_2Ti_3O_7$ nanobelts each have a layered crystalline structure consisting of octahedral [TiO_6] units as in TiO_2 nanobelts[262, 264] and exhibit similar

characteristics to TiO_2 nanobelts in applications such as gas sensing,[262] energy storage,[265, 266] photocatalysis[233, 267] and field emission.[268, 269] This suggests that the presence and migration of oxygen vacancies, is an important factor in all of these three materials[267, 270, 271]. However, the study of these intermediate products have largely been ignored for different applications compared to the well-studied TiO_2 nanobelts. It would be more cost-effective and green if these intermediate nanobelts can be used in memristive synaptic devices since several more steps are needed to obtain TiO_2 nanobelts from these intermediate materials in hydrothermal process. Therefore, a study of synaptic response in $Na_2Ti_3O_7$ and $H_2Ti_3O_7$ nanobelts is then of interest as this expands the research to titanate in addition to materials based on titanium metal oxide materials. It also enables a comparison of conduction mechanisms in all three materials in relation to their intrinsic properties.

In this research, we examined the synaptic response of $Na_2Ti_3O_7$ and $H_2Ti_3O_7$ nanobelts, the intermediate products of hydrothermally-synthesized TiO_2 nanobelts. Several synaptic functions, analogous to those seen in biological systems, are achieved in individual $H_2Ti_3O_7$ nanobelt devices. These functions include an excitatory postsynaptic current (EPSC), paired pulse facilitation (PPF), short-term plasticity, potentiation and depression as well as learning-forgetting response. The mechanism involved in the synaptic response can be associated with a competition between the migration of oxygen vacancies driven by the electric field and subsequent spontaneous diffusion due to the resulting gradient in vacancy concentration. Individual $Na_2Ti_3O_7$ nanobelt devices also exhibit similar characteristics but carry smaller currents under similar excitation conditions.

5.3. Experimental Section

5.3.1. Synthesis of sodium and hydrogen titanate nanobelts

Sodium and hydrogen titanate nanobelts were synthesized from the hydrothermal process of TiO_2 nanobelts as reported previously[148, 263]. Typically, P25 (2 gram) Aeroxide TM (Sigma Aldrich, Canada) was dissolved in NaOH alkaline solution (60 mL, 10 M) and then poured into a Teflon-lined stainless steel autoclave (125 mL, Parr Instruments). The autoclave was kept in a furnace at a temperature of 190 ^oC for 72 h. After cooling down the autoclave naturally, the suspended nanobelts were taken out and washed with ultrapure water. Sodium titanate ($Na_2Ti_3O_7$) nanobelts were obtained after this process. Hydrogen titanate ($H_2Ti_3O_7$) nanobelts could be obtained through an ionic exchange process for 12 h by transferring the $Na_2Ti_3O_7$ nanobelts into a beaker containing

HCl solution (400 mL, 0.1 mol). The $Na_2Ti_3O_7$ and $H_2Ti_3O_7$ nanobelts were dried separately in a furnace at 80 ^oC for 8 h to obtain powders. Finally, nanobelt (0.5 mg) from powders was dispersed in acetone (20 mL) for device fabrication.

5.3.2. Device fabrication and characterization

The 4 μm gap Au electrodes were pre-fabricated on a SiO_2 wafer by standard photolithography and a lift-off process. The diluted nanobelt solution was drop-cast on the Au electrodes and dried in air. Devices with bridged nanobelts were examined with an Olympus BX51 optical microscope prior to electrical characterization. The electrical performance of single-nanobelt devices was evaluated using an Agilent B2985A Electrometer/High Resistance Meter and a home-made probe station. One end of the two electrodes was grounded and all the voltages were applied from the other end throughout the entire measurement.

5.3.3. Material characterization

Scanning electron microscope (SEM) (ZEISS LEO 1550) and transmission electron microscopy (TEM) (JEOL 2010F) were used to examine the microstructure of the nanobelts and configuration of the devices. Stoichiometry of the nanobelts was identified from X-ray diffraction (XRD, PANalytical X'pert PRO MRD). The bonding states of elemental sodium, titanium and oxygen in the nanobelts were examined by X-ray photoelectron spectroscopy (Thermo-VG Scientific ESCALab 250).

5.4. Results and Discussion

5.4.1. Material Characterization

Figure 51 demonstrates the material characterization results of as-synthesized $H_2Ti_3O_7$ nanobelts. The nanobelts have a characteristic rectangular cross section, as indicated by the inset magnified SEM images in Figure 51(a). The width of the nanobelt, as imaged in SEM and TEM scans, is typically 50-200 nm (Figures 51(a) and 51(b)). A scanning TEM (STEM) image of a representative nanobelt and its corresponding line-scan obtained from electron energy loss spectroscopy indicate that the nanobelt has a width-to-height ratio of 4.2:1, consistent with a quasi-rectangular cross-section. (Figure 52). This geometry ensures good electrical contact with the Au electrode. The high resolution TEM (HRTEM) image (Figure 51(c)) of the nanobelt demonstrate a large concentration of void defects (indicated with arrows) with the measured interplanar spacing

being ~0.20 nm, corresponding to the (204) plane of the $H_2Ti_3O_7$ crystal. Theses defects could be the existence of oxygen vacancies in the nanobelts, which is further confirmed by the Gaussian devolution peak of the O 1s spectrum centered at 532.5 eV (Figure 51(d) and 51(e)). The overall stoichiometry of nanobelts is $H_2Ti_3O_7$ as determined from the characteristic peaks by XRD measurement (Figure 51(f)).

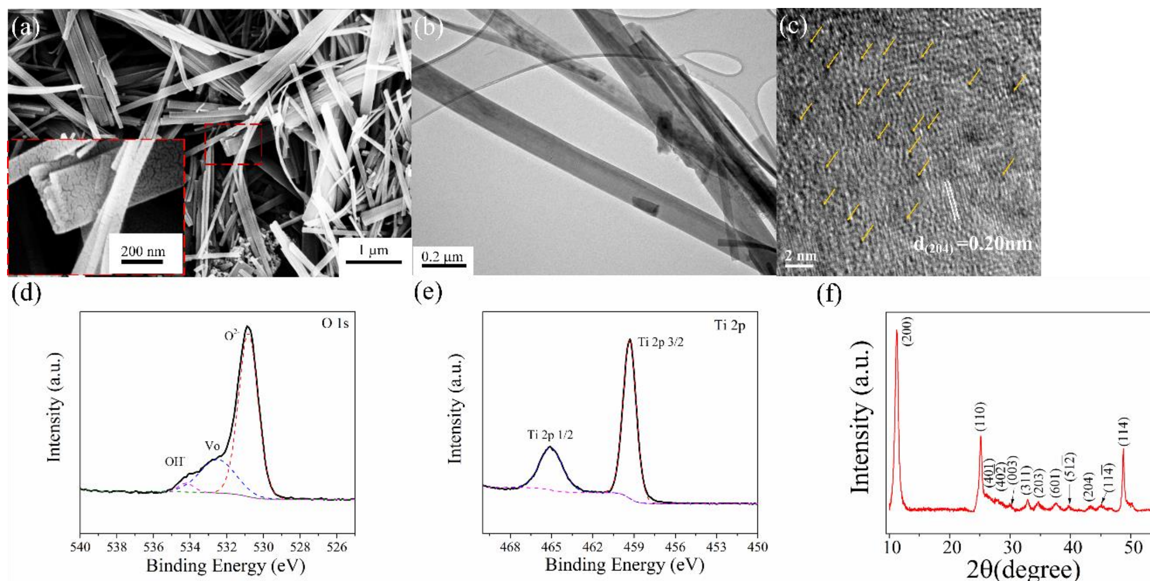

Figure 51. Material characterization of $H_2Ti_3O_7$ nanobelts, (a) SEM image, inset shows a magnified view of the selected region. These images reveal that the nanobelts have a rectangular cross-section with a width of 50-200 nm and a length of several µm. (b) TEM image, (c) HRTEM image (arrows point out defects in the crystalline structure), (d) O1s XPS spectra. The peak at 532.5 eV is attributed to oxygen vacancies (concentration ~26.33%), while the small shoulder at 534.2 eV is attributed to the OH^- group in the $H_2Ti_3O_7$ nanobelts (concentration ~ 2.95%). The strongest peak arises from oxygen in the lattice. (e) Ti 2p XPS spectra, (f) XRD characterization of $H_2Ti_3O_7$ nanobelts and their characteristic peaks indexed from the JCPDS database (No. 47-0561). Some characteristic peaks of $H_2Ti_3O_7$ are indicated with arrows.

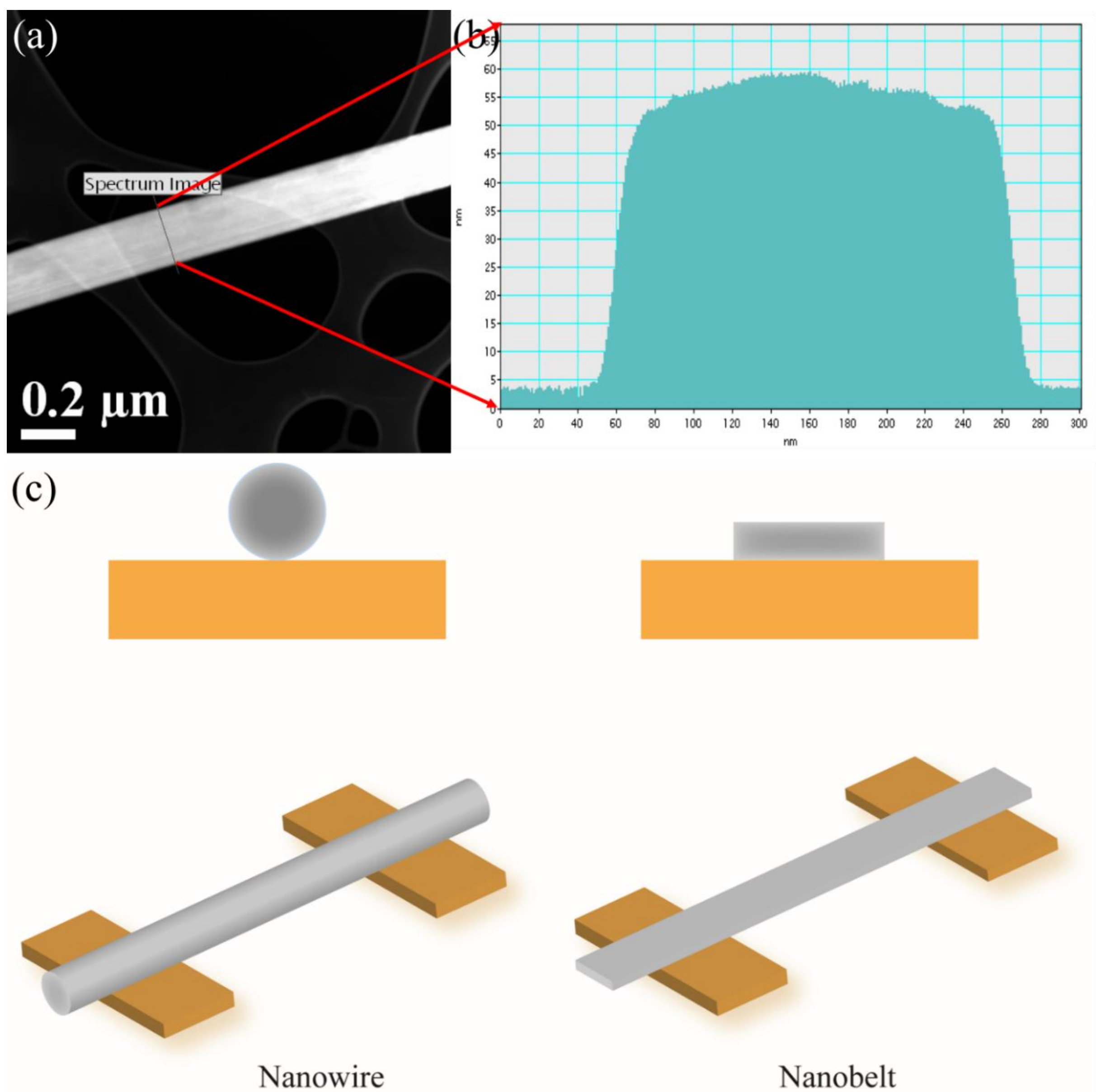

Figure 52. Comparison of contact geometry for nanowire vs. nanobelt. (a) Scanning TEM (STEM) image of a representative nanobelt and (b) its corresponding line-scan obtained from electron energy loss spectroscopy. This indicates that the nanobelt has a width of ~230 nm and a height of ~55 nm, with a width-to-height ratio of 4.2:1. These dimensions are consistent with a quasi-rectangular cross-section. (c) Schematic diagram showing the contact morphology at the Au electrodes for nanowire vs. nanobelt structures.

5.4.2. Synaptic performance

5.4.2.1. Excitatory postsynaptic current

A schematic representation of the chemical pathways during transmission in a biological synapse is shown in Figure 53(a). The transmission of information between neurons involves the release of a neurotransmitter from the presynaptic terminal, followed by diffusion across the cleft and binding to postsynaptic receptors.[255] Neurotransmitters are contained in synaptic vesicles that cluster near the cell membrane in the axon terminal of the presynaptic neuron. Once an action potential propagates along the presynaptic axon and reaches the axon terminal, voltage-gated calcium (Ca^{2+}) channels are activated and allow the flow of Ca^{2+} ions into the presynaptic terminal. This triggers fusion of the synaptic vesicle to the plasma membrane, resulting in the release of neurotransmitters in the synaptic cleft. These neurotransmitters dock with receptors on the postsynaptic neuron, triggering further molecular reactions that ultimately change the membrane potential of the postsynaptic neuron, generating a postsynaptic current.[122]

Figure 53(b) is a schematic representation of an artificial synapse as it occurs in a single nanobelt device, and the inset SEM image demonstrates the device consisting of two Au electrodes separated by a 4 μm gap bridged with a single $H_2Ti_3O_7$ nanobelt. Under external stimulus, spikes or action potentials in the presynaptic neuron (left electrode) are transmitted through the synapse (nanobelt) to the postsynaptic neuron (right electrode). This generates an excitatory postsynaptic current (EPSC). To simulate this excitatory response in our device, a series of 50 ms presynaptic pulses with amplitudes of 8, 10, 12, 15, 18 and 20 V were applied to one of the Au electrodes. These pulses were well separated in time (~4 s). The EPSC response of the device under this excitation regime is as shown in Figure 53(c). It can be seen that the peak value of the EPSC increases from 0.53 nA to 4.45 nA as the amplitude of the presynaptic pulses increases from 8 V to 20 V. This type of EPSC response is similar to that observed in biological excitatory synapses.[122] The energy introduced into the device for a single pulse is $E_{con} = I_{avg} \times t \times V$, where I_{avg} is the average EPSC, t is the pulse duration and V is the pulse amplitude. Calculated values of E_{con} are shown in Figure 53(d). The smallest energy consumption is estimated to be 212 pJ for the 8 V pulse. This power consumption could be further lowered by reducing the pulse duration to < 50 ms.

After the spike, the current in single nanobelt device assume its baseline value. When the interval between pulses is much longer than the pulse duration (e.g. 4~5 second interval vs. 50 ms

duration), the EPSC induced by a given pulse does not affect the EPSC produced by the next spike.[11, 122] Under these excitation conditions, the device exhibits a highly reproducible and controllable multilevel current response (Figure 53(e)). The multilevel performance was tested up to 2000 cycles as shown in Figure 53(f). These data demonstrate a discrete, well separated current response, indicating that the multilevel conductive states of the single $H_2Ti_3O_7$ nanobelt device are highly robust.

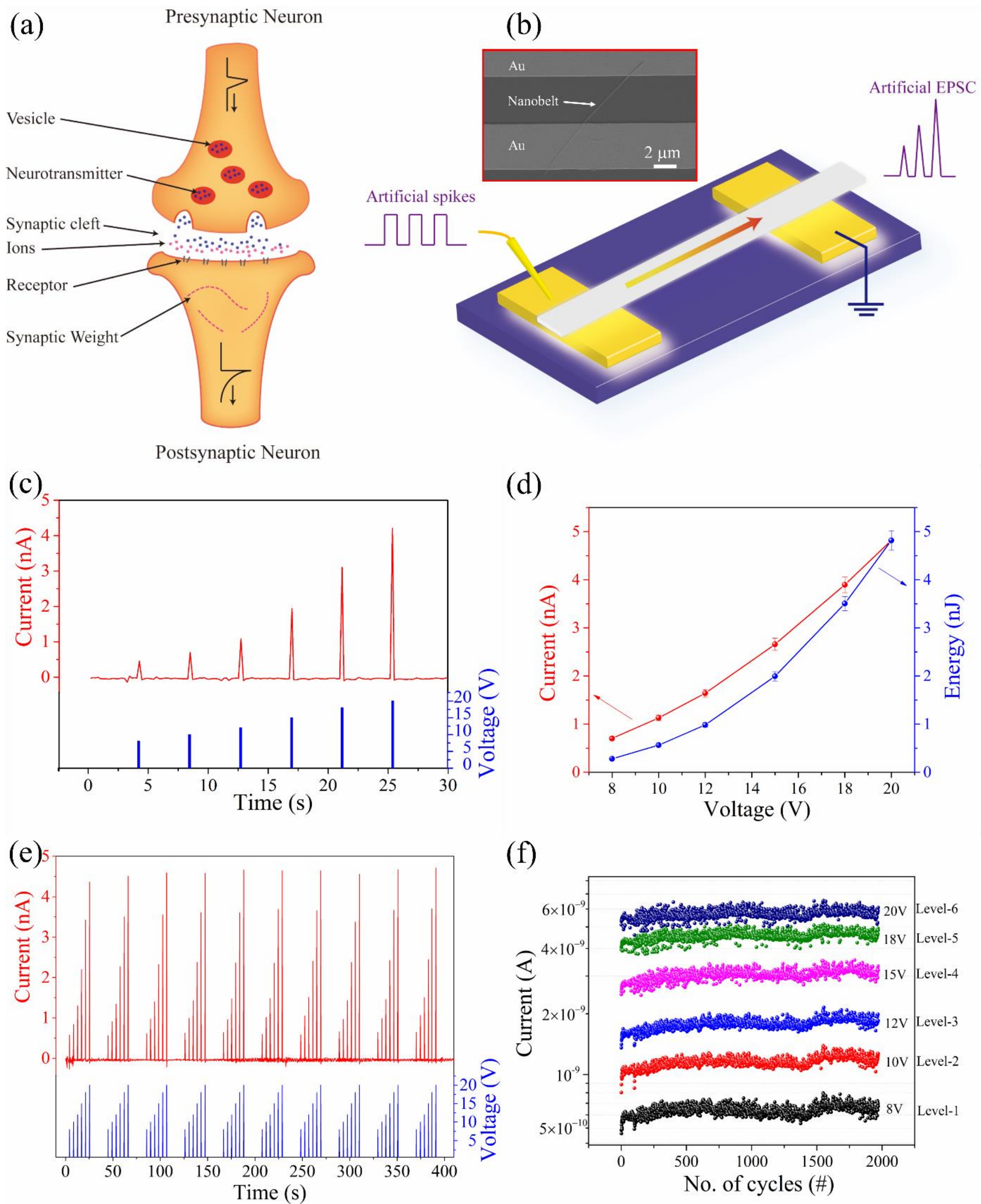

Figure 53. EPSC response, (a) schematic of a synapse, (b) schematic of the nanobelt device for the synaptic response study and SEM image of nanobelt device, (c) EPSC performance for a series of 50 ms pulses with amplitudes 8, 10, 12, 15, 18 and 20 V, respectively, (d) summary of EPSCs and the corresponding calculated energy consumption, where the average currents and corresponding standard deviation are calculated from the current

responses over 2000 cycles as shown in (f), (e) EPSC during 10 cycles of EPSC excited as in (c), the interval period among adjacent cycles is 20 s. (f) EPSC evolution over 2000 cycles with pulse amplitudes as in (c).

5.4.2.2. Short term plasticity

Synaptic plasticity, defined as the change in the synaptic strength in response to external stimuli over time, is considered to be the foundation for learning and memory in the human brain.[100] In general, when two identical spikes arrive in rapid succession, the EPSC for the second spike is enhanced if the time interval between the spikes is short enough that carriers cannot relax to their initial equilibrium state between spikes, as illustrated schematically in Figure 53(b). This then leads to short-term synaptic enhancement or potentiation.[272] This response was successfully simulated in the present nanobelt device by applying two and ten consecutive identical +8 V pulses with inter-pulse intervals ranging from 100 to 3000 ms. Figure 54(a) shows a typical example of short-term potentiation obtained at an inter-pulse interval of 500 ms. The amount of synaptic gained weight for two and ten equal pre-synaptic pulses was calculated as a function of the interval period as a way of mimicking neural paired-pulse facilitation (PPF) and post-tetanic potentiation (PTP) responses in a biological system. PPF measures the conductance increase that occurs on application of two consecutive presynaptic pulses, while PTP quantifies the increase in response for a given number of spikes. The plasticity of the device can be described according to the PPF and PTP index models[257, 272]

$$PPF = (I_2 - I_1)/ I_1 \times 100\% \quad (1)$$

$$PTP = (I_{10} - I_1)/ I_1 \times 100\% \quad (2)$$

In Equation (1) and (2), I_1, I_2 and I_{10} correspond to the current of the first, second and tenth pulse, respectively. From Figures 54(b) and 54(c), the amplitudes of the EPSC in the second (PPF) and tenth (PTP) pulses are 53% and 436% higher, respectively, compared to the EPSC from the first pulse at an inter-pulse interval of 100 ms. The high PTP index suggests the possibility that the nanobelt device may act as a dynamic high-pass filter.[254] The enhancement ratio is found to decrease with increasing inter-pulse time interval. This effect is also known as spike rate-dependent plasticity (SRDP), whereby higher spike frequency leads to a larger increase in gained synaptic weight. Fitting of the PPF and PTP curves shows that the device plasticity decays exponentially vs. inter-pulse time interval.[272] In biological systems, a certain time interval is needed for the residual Ca^{2+} concentration to relax to their equilibrium level after an action potential is terminated. When another identical stimulus follows shortly after the initial stimulus,

a net increase in the synaptic response will occur, as in PPF. When many stimuli are applied and the inter-pulse interval is short, the synaptic transmission is progressively enhanced, as in PTP.

Figures 54(d)-(f) show the enhancement in the current response during the application of 100 consecutive pulses. The duration, interval period and peak voltage per pulse are all seen to affect the overall current amplitude.[14, 50] This potentiation behavior in the nanobelt device mimics the synaptic release of neurotransmitters in vesicles in response to a series of action potentials in which the frequency, duration as well as amplitude of action potentials can stimulate a larger number of neurotransmitters, and thus a higher current response.[255] As can be seen in Figures 54(d)-(f), the accumulation of the current response does not scale linearly with an increase in the number of pulses. This suggests that more conductive states could be achieved using shorter pulse duration and lower pulse amplitude, as this would inhibit saturation, i.e., slowing the increase in synaptic weight. By extending the number of identical low amplitude (10 V) pulses up to 1000 and using a variety of pulse durations, the current response can be gradually increased as shown in Figure 55. A two order of magnitude change in current accumulation was achieved through >1000 steps. It is apparent that the current continues to increase throughout the steps, but that the rate of increase is reduced as the number of pulses increases. More than 2000 modulation states can be achieved by applying a series of identical 50 and 100 ms, 10 V pulses, respectively (Figure 56). A gradual increase in current response is particularly important if the device is to mimic the analog nature of the synaptic weight change,[103] effective neural regulation and adaptive learning in neuromorphic computation.[121] With more resistance states, better learning efficiency and a greater capacity for an effective neuromorphic computing response is possible.[121, 260] This indicates that $H_2Ti_3O_7$ nanobelts may be an attractive candidate for achieving high-efficiency learning in neuromorphic computing.

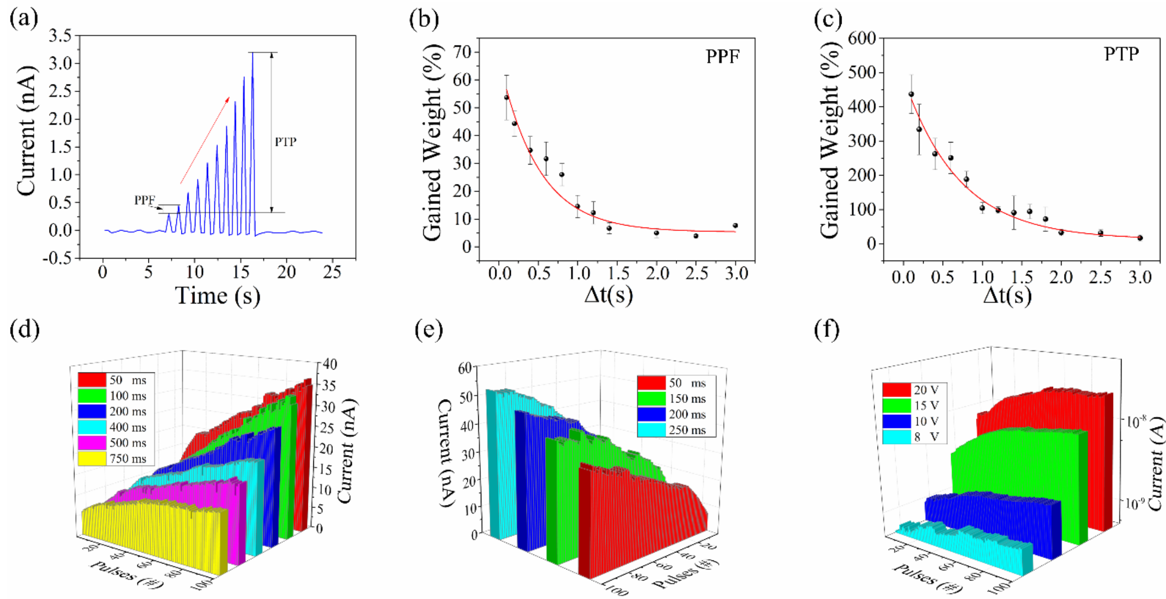

Figure 54. Short-term plasticity response. (a) Current enhancement for 10 consecutive, identical 8 V pulses. PPF and PTP are defined as shown, (b-c) Relationship between gained weight (%) for PPF and PTP vs. the time interval between two consecutive pulses. The fitted exponential curves $y=A_1\times\exp(-x/t_1)+y_0$ are shown. For the PPF, $A_1=0.625$, $t_1=0.499$ s, $y_0=0.053$ while for PTP, $A_1=4.722$, $t_1=0.707$ s, $y_0=0.124$, (d-f) Accumulating current response on excitation with 100 identical consecutive pulses plotted vs. (d) time interval between pulses (50 ms duration, 20 V pulse), (e) pulse duration (50 ms interval, 20 V pulse), and (f) pulse amplitude (pulse duration and interval are 50 ms).

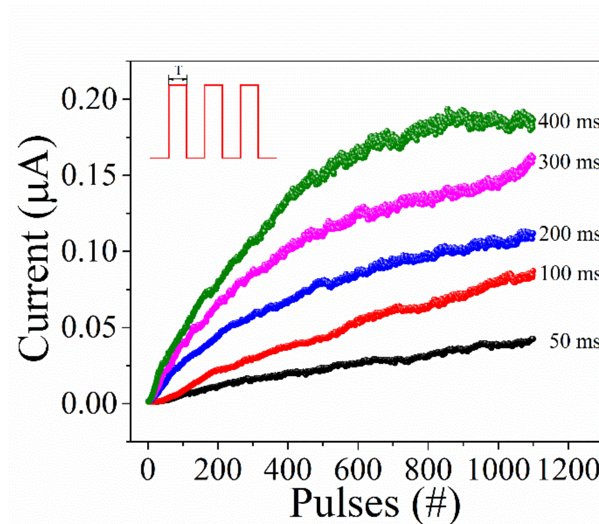

Figure 55. Current accumulation vs. number of identical consecutive 10 V pulses. The pulse duration, T, is as shown.

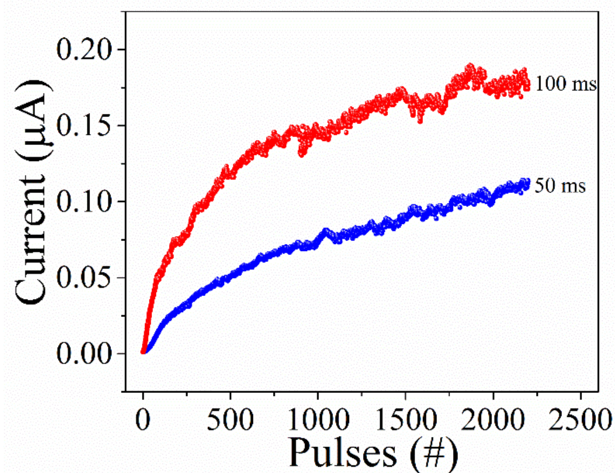

Figure 56. Evolution of the potentiation response on application of up to 2200 identical pulses. The pulse duration for each pulse is as indicated. Pulse amplitude is 10 V.

5.4.2.3. Potentiation and depression

In a system designed to implement artificial synapses, modulation of conductance can be used to emulate the effect of potentiation and depression on synaptic weight. This simulates the strengthening and weakening of pre- and post-synaptic neurons. To replicate this response, 100 consecutive +20 V, 100 ms, pulses followed by 100 consecutive −10 V, 100 ms, pulses were applied to the system. The resulting current response was read at 2 V and showed a reproducible potentiation and depression response as summarized in Figure 57(a) and (b). The pulse peak current in this test is given in Figure 58. The read-out current increases firstly in response to the positive input pulses, demonstrating potentiation. Subsequent negative pulses cause the current to decrease, resulting in depression of the response. The robustness of the potentiation and depression response was confirmed by a test involving 50 potentiation and 50 depression states for 5,000 cycles (a total of 50,000 pulses) as shown in Figure 57 and Figure 59. To test whether a larger number of potentiation and depression states are possible, the conductance was measured during application of >2000, +10 V/−6 V 100 ms pulse cycles (Figure 57d). In the region of potentiation, the conductance of the device increases and eventually becomes saturated. In the depression region, the conductance rapidly decreases during the first 300 pulses, and then remains essentially constant on the additional negative pulses. The latter effect might be due to the limited migration of oxygen vacancies on application of low electric-field −6 V pulse after the device has been returned to its initial state. The current response vs. time in this experiment is shown in Figure 60. This suggests

that a single nanobelt device can be used to combine a large number of potentiation and depression states in a simple structure. Moreover, the potentiation and depression response can also be generated in the $H_2Ti_3O_7$ nanobelt device by sweeping voltages (Figure 60). On the application of consecutive positive and negative sweeping voltages, the current amplitude first continuously increases (Figure 61(a)) and then decreases (Figure 61(b)). The cyclic current response vs. time and the corresponding conductance at the peak voltage are shown in Figures 61(c) and 61(d). It is also demonstrated in Figure 57 that depression is faster than potentiation in the $H_2Ti_3O_7$ nanobelt device. With higher amplitude negative pulses (e.g., −15 V and −20 V rather than −10 V), fewer negative pulses are sufficient to drive the current back to its original value (Figure 62). After the current returns to the baseline level, additional negative pulses contribute to the generation of higher current when the device is excited with opposite polarity pulses.[260, 273]

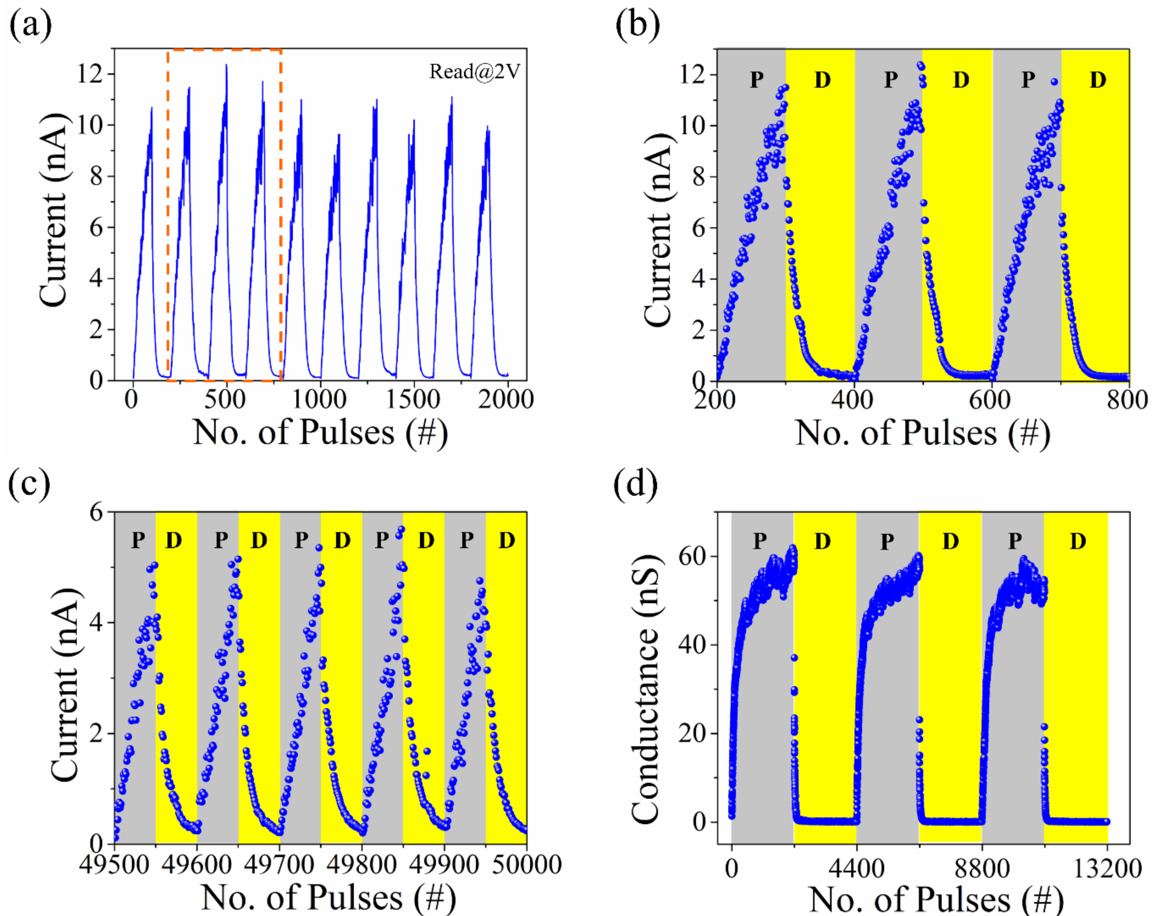

Figure 57. Potentiation and depression response. (a) 100, +20 V 100 ms pulses followed by 100, −10 V 100 ms pulses. The test was repeated for 10 cycles. Current was measured by a 2 V, 100 ms read pulse immediately after each potentiation and depression pulse. (b) Expanded view of the highlighted segment in (a). (c) Test over 50, 000 pulses with 50 potentiation and 50 depression pulses as before. The response in the last 5 cycles is shown. (d) Test

carried out to illustrate the large number of potentiation and depression states. Each cycle involved 2200, +10 V, 100 ms pulses followed by 2200, −6 V, 100 ms pulses. P and D indicate potentiation and depression, respectively.

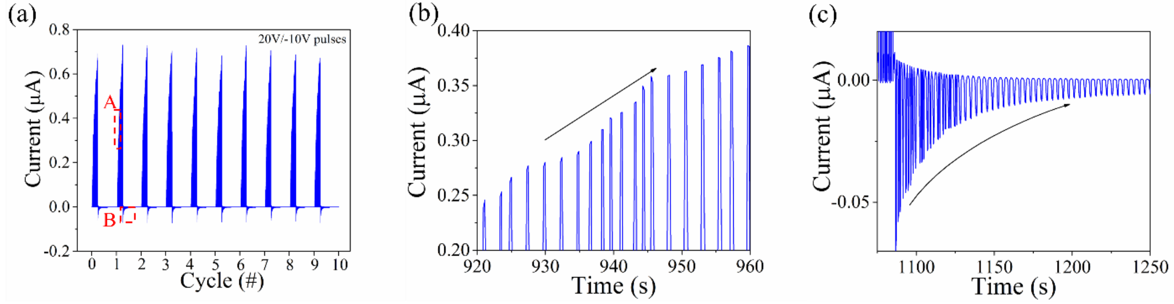

Figure 58. Potentiation and depression response. (a) 10 cycles of potentiation and depression response for 100 consecutive, 100 ms, +20 V pulses followed by 100 consecutive, 100 ms, −10 V pulses. A 2 V read voltage was applied after each pulse to obtain the current, (b) Expanded view of the area (A) in (a) demonstrating current potentiation. (c) Expanded view of the area (B) in (a) demonstrating current depression.

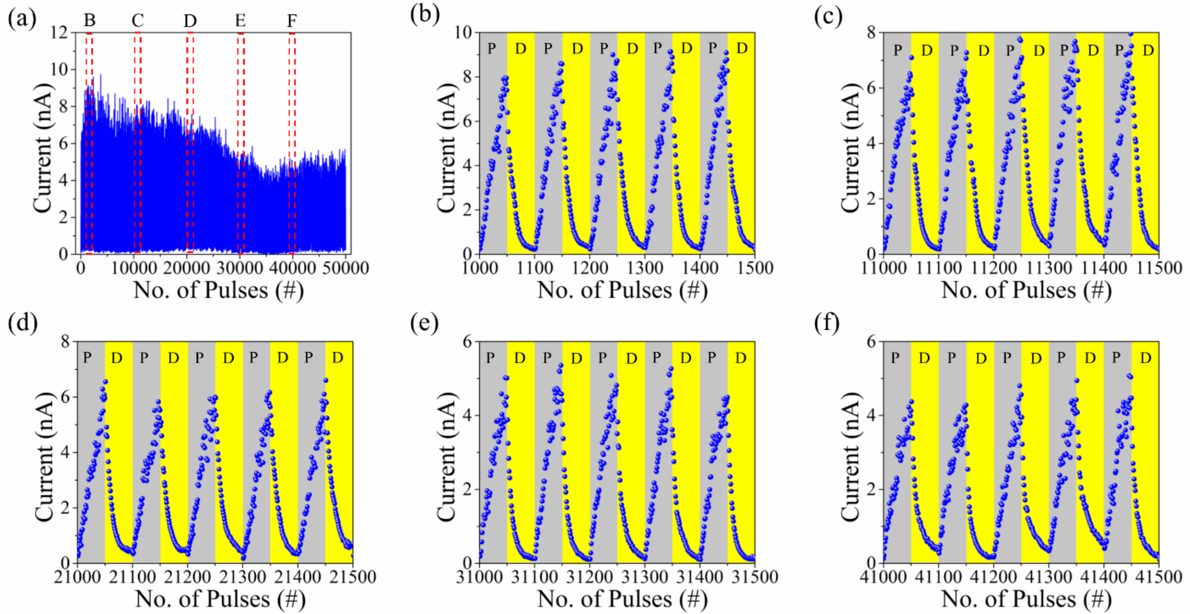

Figure 59. Potentiation/depression characteristics and current response for up to 50,000 pulses illustrating the robustness of the system and (b-f) demonstrated expanded view in selected region (B-F) in (a). P and D in (b-f) indicate potentiation and depression, respectively.

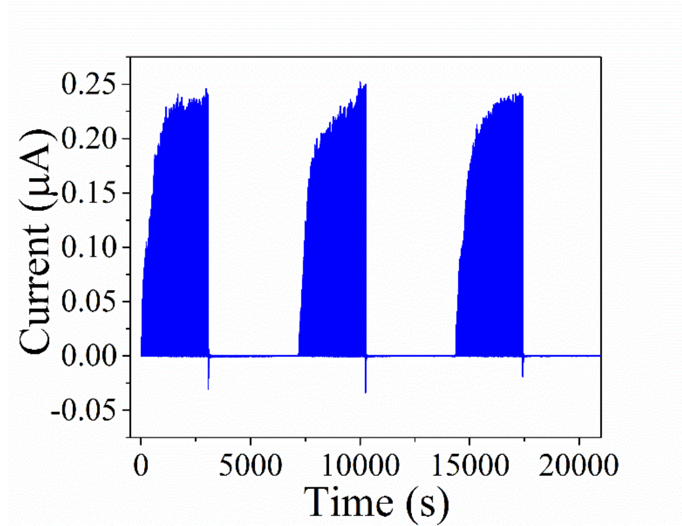

Figure 60. Current response for 2200 positive (+10 V) and negative (−6 V) pulses with identical durations of 100 ms, respectively.

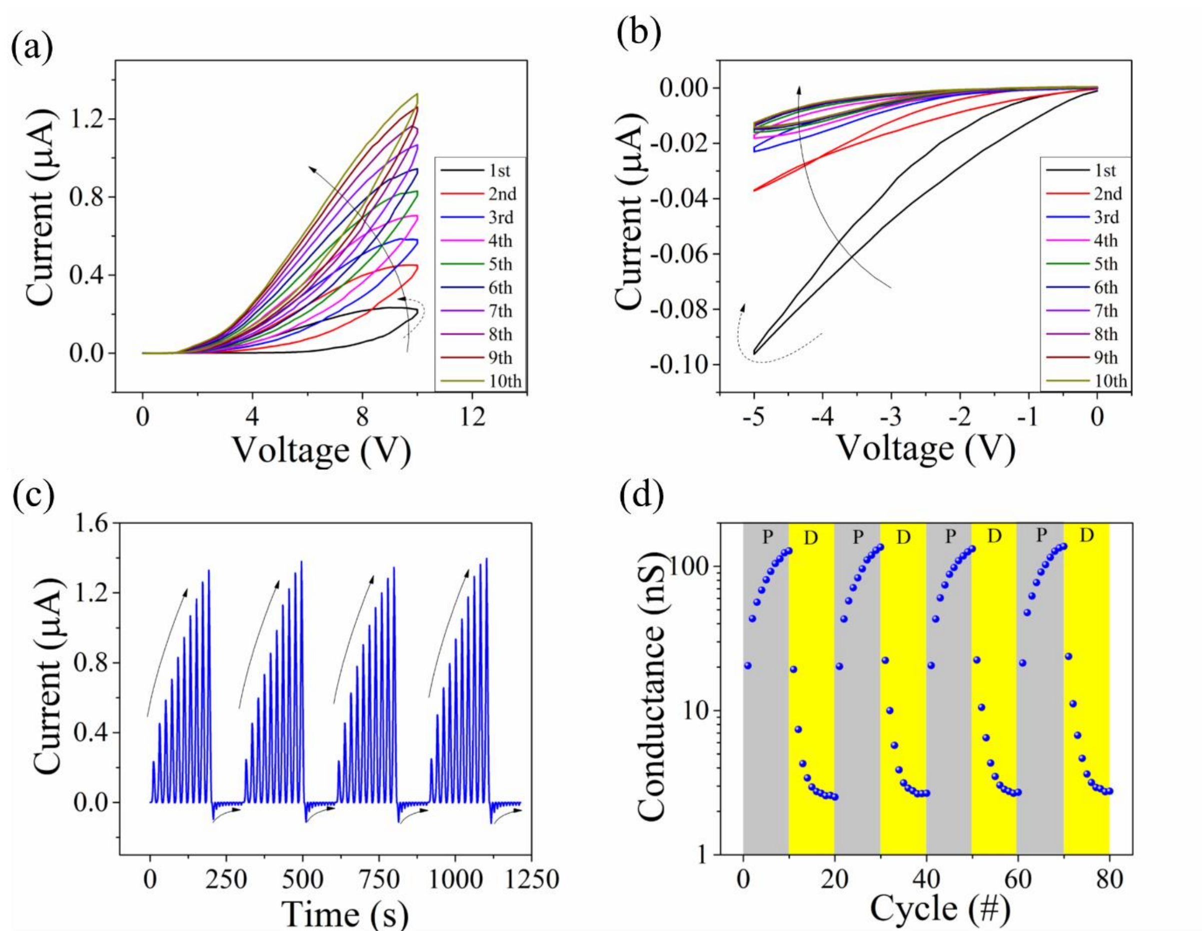

Figure 61. Nonlinear transmission characteristic of single positive and negative sweeping behavior. (a) *I-V* characteristics of the single nanobelt device at positive sweeping voltages (0 to 10 V then back to 0 V). (b) *I-V*

characteristics of the single nanobelt device at negative sweeping voltages (0 to −5 V then back to 0 V). (c) The curve of current response from (a) and (b) versus time. 4 cycles of potentiation and depression by sweeping voltage is demonstrated. (d) The conductance variation of the device with the sweeping cycles in (c). Reproducible potentiation (P) and depression (D) can be observed.

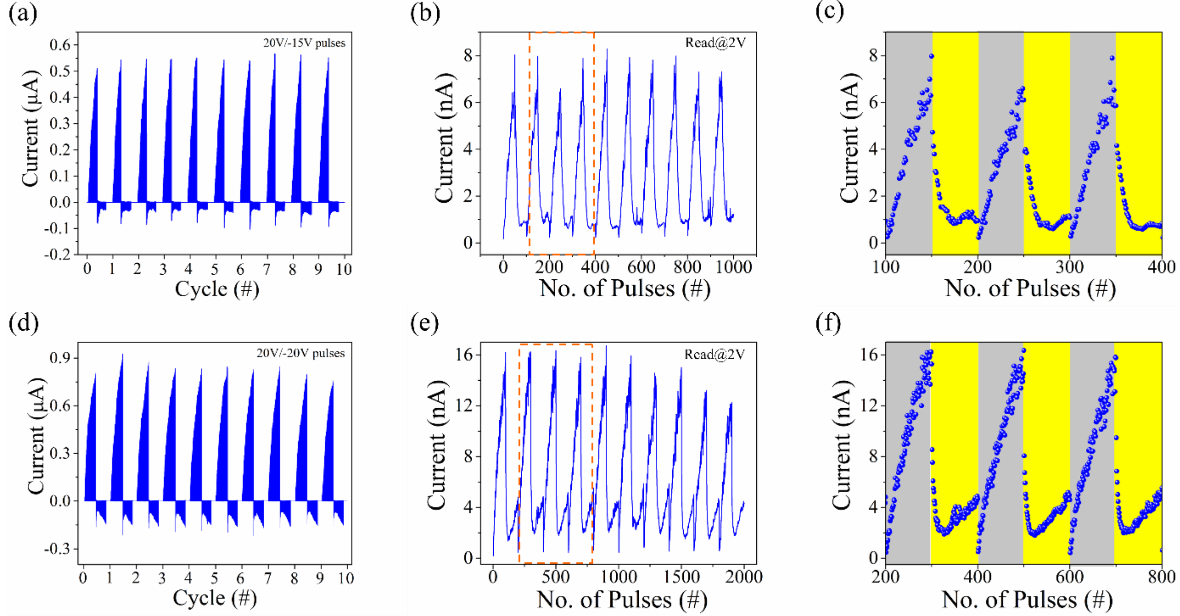

Figure 62. Potentiation and quasi-depression response for different negative pulse amplitudes (a-c) 100 consecutive 20 V, 100 ms pulses followed by 100 consecutive −15 V, 100 ms pulses. (d-e) 100 consecutive 20 V 100 ms pulses followed by 100 consecutive −20 V, 100 ms pulses. All the pulses have a duty cycle of 50%. The current responses in (b) (c) (e) and (f) are extracted after each pulse at a 2 V read voltage.

5.4.2.4. Learning and forgetting response

We have also investigated the current accumulation and decay properties in these single $H_2Ti_3O_7$ nanobelt devices to replicate the learning/forgetting response of human memory. Potentiation after application of a number of identical 500 ms pulses simulates the learning process, while forgetting can be simulated by following the subsequent decay of the current response. As before, the readout voltage was +2 V. The resulting potentiation and decay curve is shown in Figure 63(a). When the exciting pulses are removed, the declining current is well described by an exponential decay, that is $I=I_0+Ae^{-t/\tau}$, where I_0 is the steady state current, t is time, A is a pre-factor, and τ is a time constant, which indicates the forgetting rate (Figure 63(b)). The spontaneous decay of current in the present device is analogous to the loss of memory or forgetting curve in a human brain.[108, 274] We further studied the relaxation process of the device subject to a different number of applied pulses. It is shown in Figure 63(c) that, by increasing the number of pulses to 400, the remaining normalized synaptic weight at 100 s increases from <3% for 5 pulses to around 42%.

Significantly, it is found that the time increases by a factor of 10 for the synaptic weight to decrease to 5% when the number of pulse is 400 (~ 625 s) compared to that observed when the pulse number is 5 (~ 59 s). Meanwhile, the time constant increases with the increasing of number of pulses as demonstrated in Figure 63(d). This suggests the potential for a transition from short-term potentiation (STP) to long-term potentiation (LTP) in the single nanobelt device by repeated stimulation.[11] This enhancement in stability induced by the repeated application of input pulses resembles the increase in synaptic strength through frequent stimulation by action potentials found in biological neural systems.[11, 275]

Several important synaptic responses such as EPSC, SRDP and potentiation and depression response have also been measured in a single $Na_2Ti_3O_7$ device (Figures 64-67). In each case, the response is similar to that in the $H_2Ti_3O_7$ nanobelt devices except that the current amplitudes are different indicating the larger resistivity of the $Na_2Ti_3O_7$ nanobelt. These results show that $H_2Ti_3O_7$ and $Na_2Ti_3O_7$ nanobelts, appearing as intermediate products in the formulation of TiO_2 nanobelts by hydrothermal synthesis, are suitable for synaptic functionality emulation.

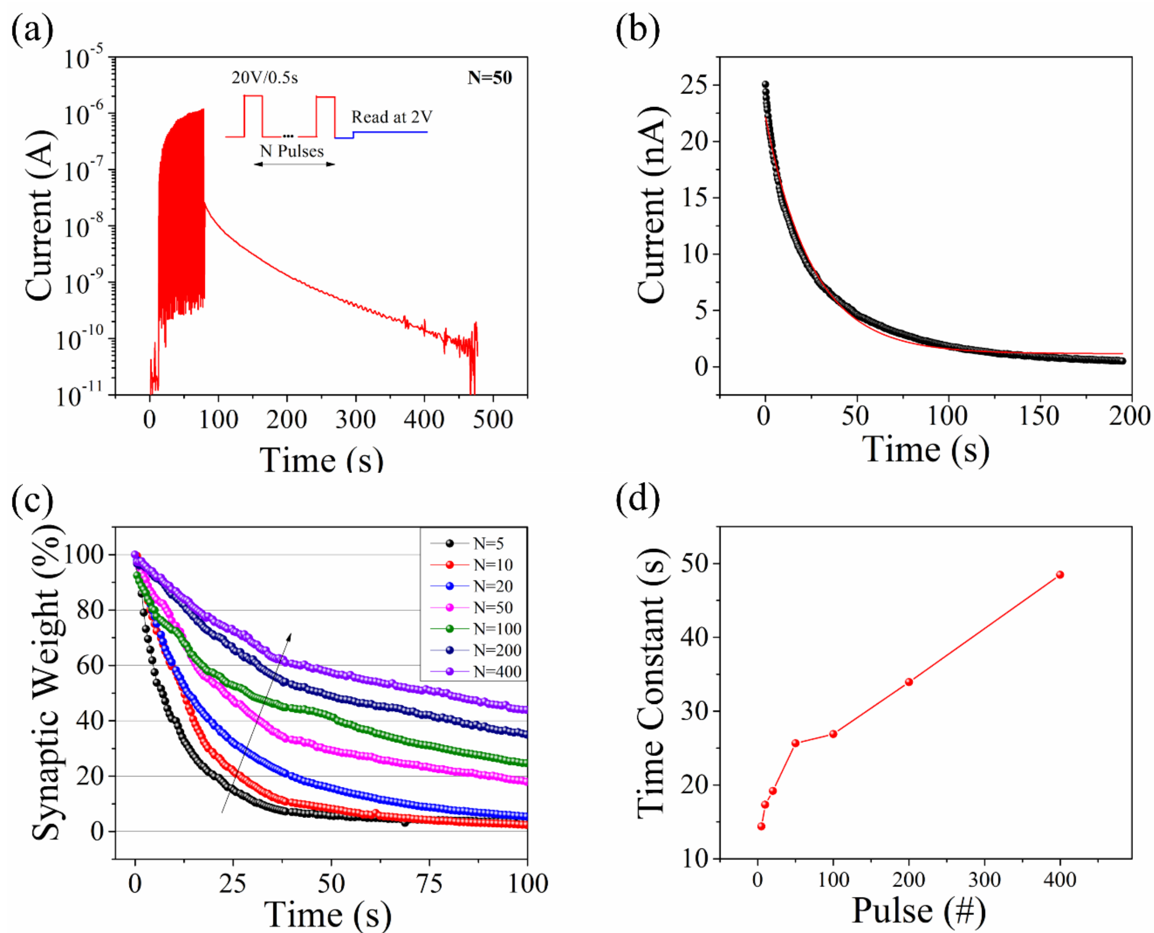

Figure 63. Learning and forgetting response and STP-to-LTP transition induced by repeated stimulation. (a) Learning and forgetting curve with 50, 500 ms, 20 V pulses. Current during relaxation was read at 2 V. (b) Current decay curve and its fit to the equation of $I=I_0+Ae^{-t/\tau}$, where I_0=1.16 nA, A=20.9 nA and τ is 25.64 s. (c) Current decay behavior with the number of pulses up to 400 and (d) time constant summary up to 400 pulses.

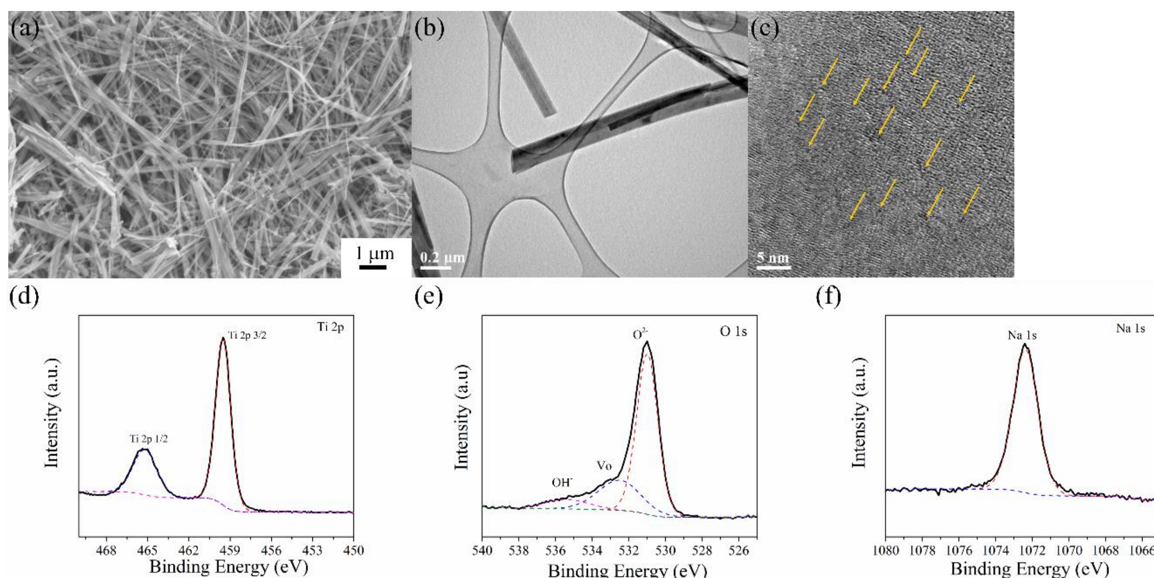

Figure 64. Material characterization of $Na_2Ti_3O_7$ nanobelts. (a) SEM image, (b) TEM image, (c) HRTEM image (arrows point out defects in the crystalline structure), (d) Ti 2p XPS spectrum (e) O1s XPS spectrum. The peak at 532.52 eV is attributed to oxygen vacancies (concentration ~ 25.00%), while the small shoulder at 535.3 eV is attributed to the OH- group in the $Na_2Ti_3O_7$ nanobelts (concentration ~ 8.12%). The strongest peak arises from oxygen in the lattice (concentration ~ 66.89%). (f) Na 1s XPS spectrum.

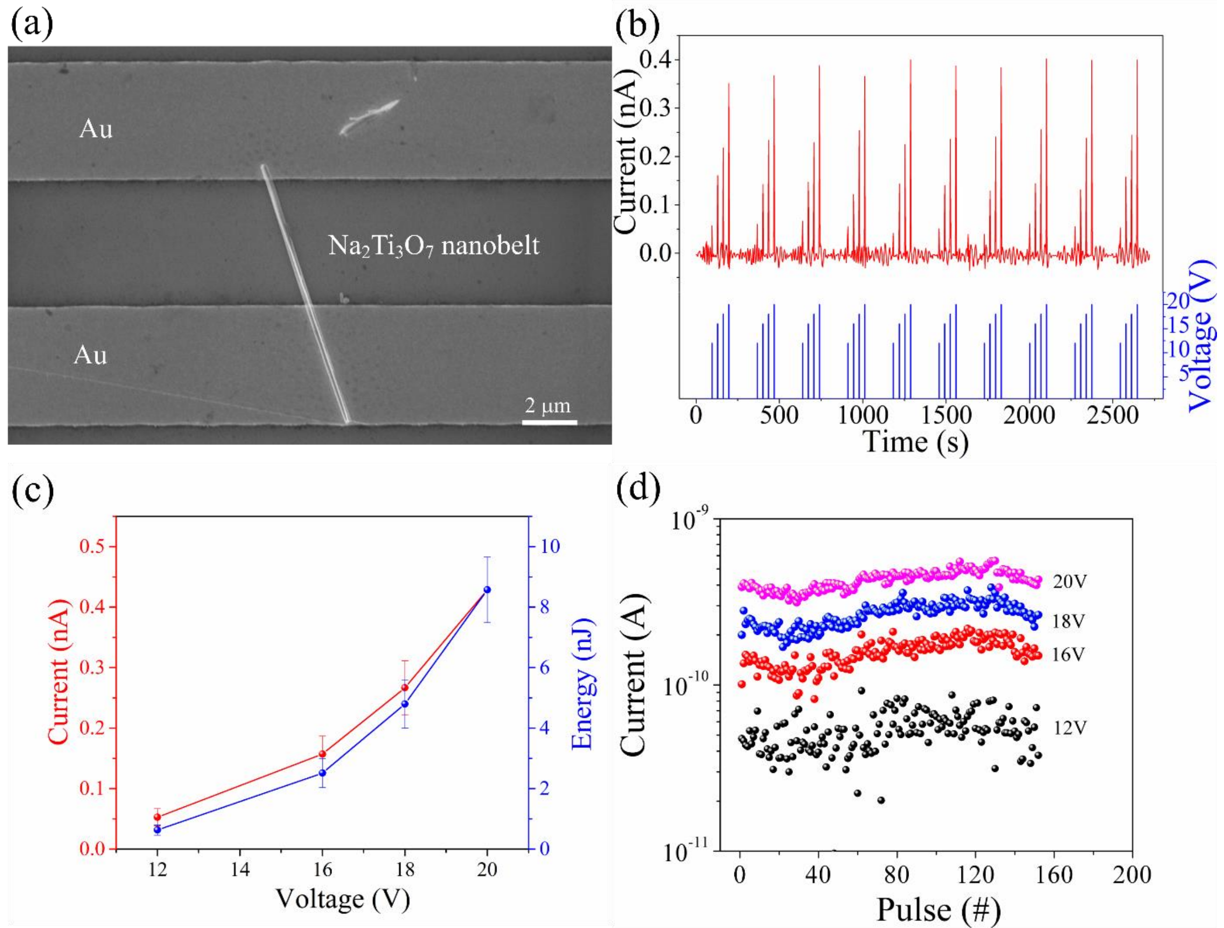

Figure 65. EPSC performance in a single $Na_2Ti_3O_7$ nanobelt device. (a) SEM image of the device. (b) EPSC response with a series of 12, 16, 18 and 20 V pulses 100 ms long pulses. (c) The current response for different pulse amplitudes and calculated energy consumption. The calculated energy consumption is 630 pJ at a voltage of 12 V. (d) Summary of EPSC over more than 150 cycles with different pulse amplitudes. Variation in the current response for the 12 V pulse can be attributed to a low signal-to-noise ratio in the low current measurement.

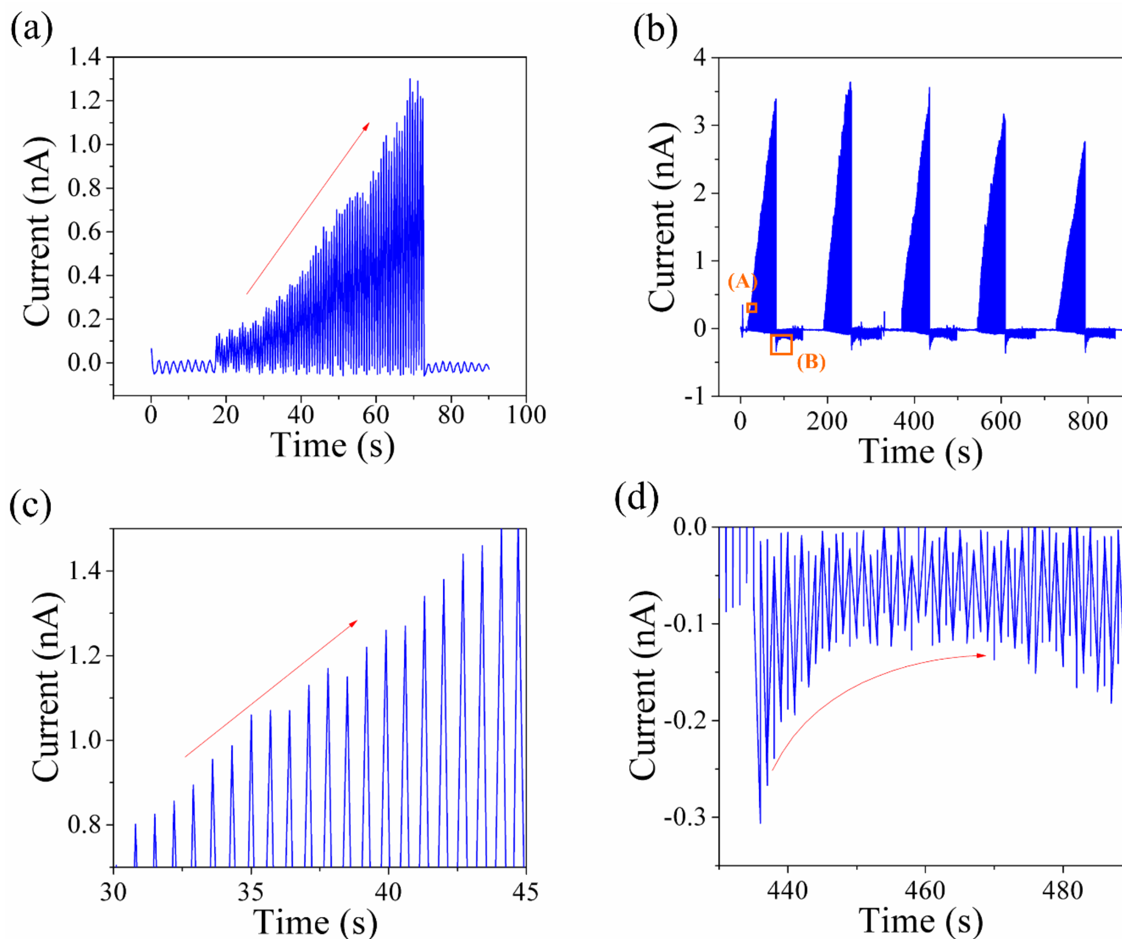

Figure 66. Current accumulation and potentiation/depression response in a single $Na_2Ti_3O_7$ nanobelt device. (a) Current obtained under excitation with consecutive, identical, +20 V, 300 ms pulses. The total number of pulses is 75. (b) Potentiation and depression response over 5 cycles. Each cycle consists of 100 identical +20 V, 300 ms, pulses followed by 100 identical −10 V, 300 ms, pulses. (c) Detailed view for the selected region (A) for the current potentiation in (b). (d) Detailed view for the selected region (B) for the current depression in (b).

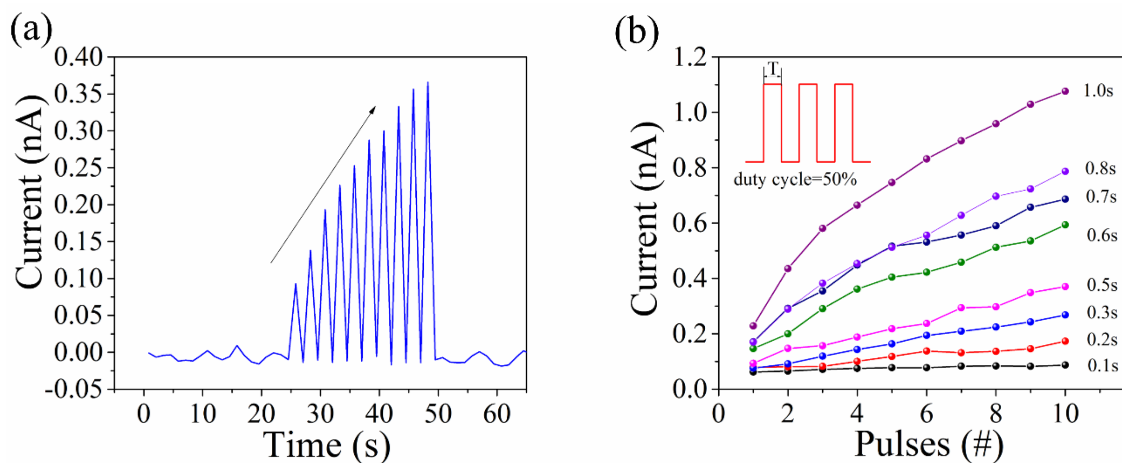

Figure 67. Spike rate-dependent synaptic plasticity of single $Na_2Ti_3O_7$ nanobelt devices under excitation with positive/negative pulses. (a) Evolution of current accumulation during 10 consecutive, +20 V, 400 ms, pulses, (b) current response vs. number of pulses with different positive pulse durations.

5.4.3. Kinetic mechanism

Similar to the analysis in single TiO_2 nanowire device[148, 261], it is suggested that the oxygen vacancies in the titanate nanobelts could be very important in abovementioned synaptic performance. To examine the role of oxygen vacancies on the synaptic response of single $H_2Ti_3O_7$ nanobelt devices, the temperature dependent time decay of the current (read at 2 V) after excitation with 50 identical, +20 V, 500 ms pulses (same as Figure 63(a)) is shown in Figure 68. Figure 68(a) indicates that the current decays more rapidly at higher temperature. This is consistent with the thermally activated diffusion of oxygen vacancies subject to an activation energy, E.[60, 63] The process is described by Equation 3 where the time constant τ, is temperature dependent, k is the Boltzmann constant, T is the absolute temperature and A_0 is the pre-exponential rate constant,[12]

$$A_0 + ln\frac{1}{\tau(T)} = \frac{E}{kT} \quad (3)$$

A plot of $ln(1/\tau(T))$ as a function of $1000/T$ is shown in Figure 68(b) and yields $E = 0.33$ eV. This suggests a direct relation between the oxygen vacancy diffusion and forgetting/relaxation response behavior in Figure 63. Furthermore, the contact properties of the Au/nanobelt junction have been determined by examining its current response under a direct voltage sweep from −15 V to 15 V. It was found that the *I-V* curve is nearly symmetrical implying that the device can be described by the model of back-to-back Schottky barriers in series with a resistor.[276, 277] (Figure 69). Under these conditions, oxygen vacancies would migrate towards one end of the Au/nanobelt interface under the applied electric field. This will lower the Schottky barrier at this interface, resulting in a rectifying-like *I-V* curve.[105] To confirm this assumption, we measured the *I-V* curves directly after sweeping from 0 to 10 V and found a positive rectification response. Similarly, a reverse rectification characteristic is produced immediately after application of a 0 to −10 V sweep voltage (Figure 70).

We have also investigated the temperature dependent current decay process in single TiO_2 and $Na_2Ti_3O_7$ nanobelt devices and have calculated the activation energies for diffusion using Equation (3). The resulting activation energies for TiO_2 and $Na_2Ti_3O_7$ nanobelt devices are 0.42 eV and 0.41 eV, respectively (Figure 71). Similar values of the activation energy in all three types of nanobelt device suggest a common diffusion mechanism. The primary diffusion mechanism in all three

types of nanobelt device can then be attributed to oxygen vacancies although the diffusion of H^+ and Na^+ ions might play a limited role on $H_2Ti_3O_7$ and $Na_2Ti_3O_7$ nanobelts.

The low activation energies for diffusion in these three types of nanobelt device compared to those found for many other oxides can be attributed to the geometrical effect of the nanowire/nanobelt structure. A recent theoretical report shows that a higher concentration of oxygen vacancies exists near and on the surface of ZnO nanowires. This facilitates the diffusion of oxygen vacancies in the nanowire structure compared to that occurring in bulk ZnO because of the lower activation energy associated with surface defects.[278] This conclusion is supported by a recent study of oxygen diffusion in sputtered TiO_2 films which shows that the activation energy for diffusion in the thin film is of 1.05 eV.[279] Theoretical studies of migration of oxygen vacancies along different plane directions in bulk TiO_2 also imply activation energies of 0.69-1.75 eV.[280] These values are consistent with the relatively low activation energies derived from our study of diffusion in single nanobelt devices.

The electrical characteristics of these nanobelt devices are then described by back-to-back Schottky barriers whose properties are determined by the migration and diffusion of oxygen vacancies. In the absence of a bias, symmetrical Schottky barriers are formed at each junction between the nanobelt and an Au electrode (Figure 72(a)). When an electric field is applied by biasing the device, oxygen vacancies distributed within the nanobelt migrate and accumulate at one of the Au/nanobelt interfaces resulting in a reduction of the effective Schottky barrier.[70, 143, 149, 151] This facilitates the injection of electrons from the Au electrode into the semiconductor nanobelt, enhancing current flow in the forward direction.[281] The resistance of the device therefore decreases when oxygen vacancies accumulate at this end. Meanwhile, the corresponding increase in the density of defects at this end of the nanobelt gives rise to a concentration gradient. This gradient drives a diffusive flow of vacancies in an opposite direction to the electric field (Figure 72(b)). As diffusion is thermally activated and has an activation energy, *E*, relaxation of the current following excitation in the forward direction is temperature dependent. The dynamic competition between these two mechanisms leads to different synaptic functions. As the number of pulses increases, these effects begin to cancel each other so that the current does not continue to grow at the same rate. The equilibrium established between migration and diffusion also results in current saturation as the number of pulses is increased. If the bias is reversed immediately after a positive voltage pulse, the electric field accelerates the flow of vacancies arising from diffusion and speeds

up the overall depression response. This is also the reason for faster depression behavior than potentiation in the single nanobelt device. After a small number of negative voltage pulses, the device returns to its initial state and the Schottky barrier is re-established. Because of the identical nature of the Schottky barriers at each Au/nanobelt interface, the application of additional voltage pulses in the negative direction results in a similar response as that seen in the positive direction.

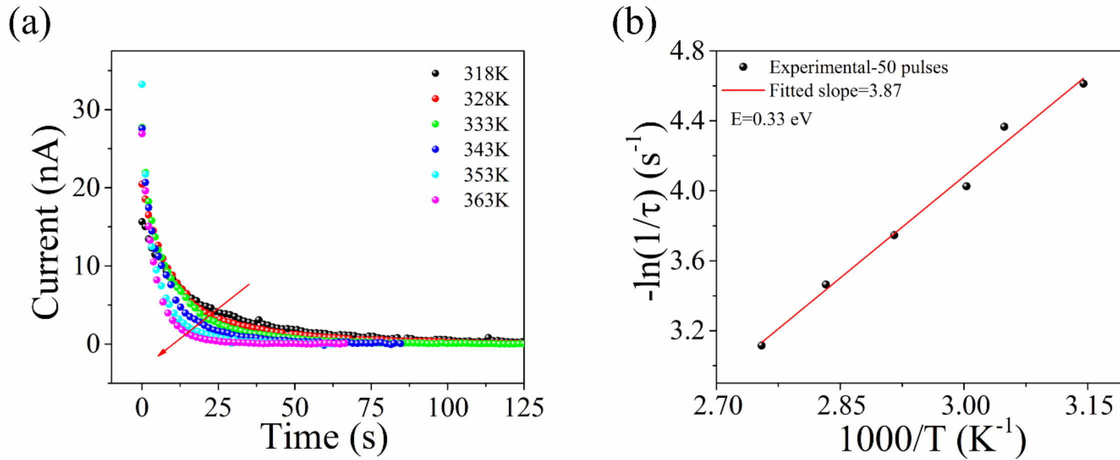

Figure 68. Synaptic mechanism study. (a) Temperature dependence of the current decay following excitation with 50 consecutive +20 V, 500 ms, pulses. The current was read at 2 V, (b) Plot of ln(1/τ) vs. 1000/T showing exponential dependence. The linear fit from Equation 3 is shown and implies that the diffusion activation energy is E=0.33 eV.

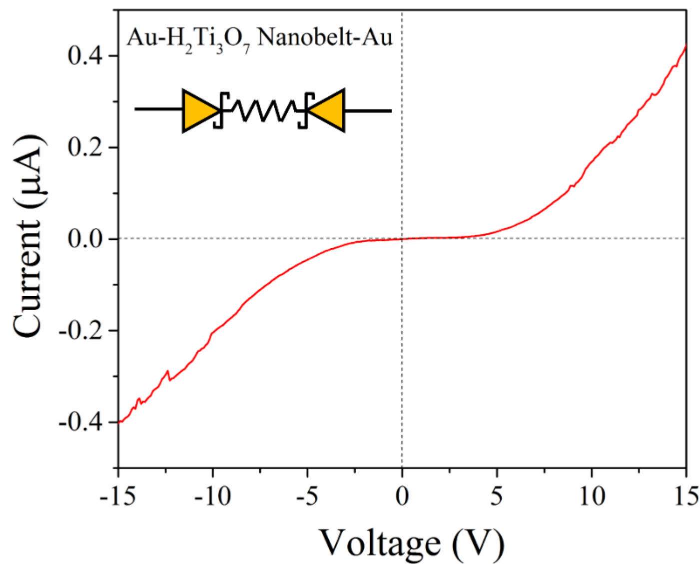

Figure 69. *I-V* curve for the electrical contact at the interfaces between Au electrodes and the $H_2Ti_3O_7$ nanobelt.

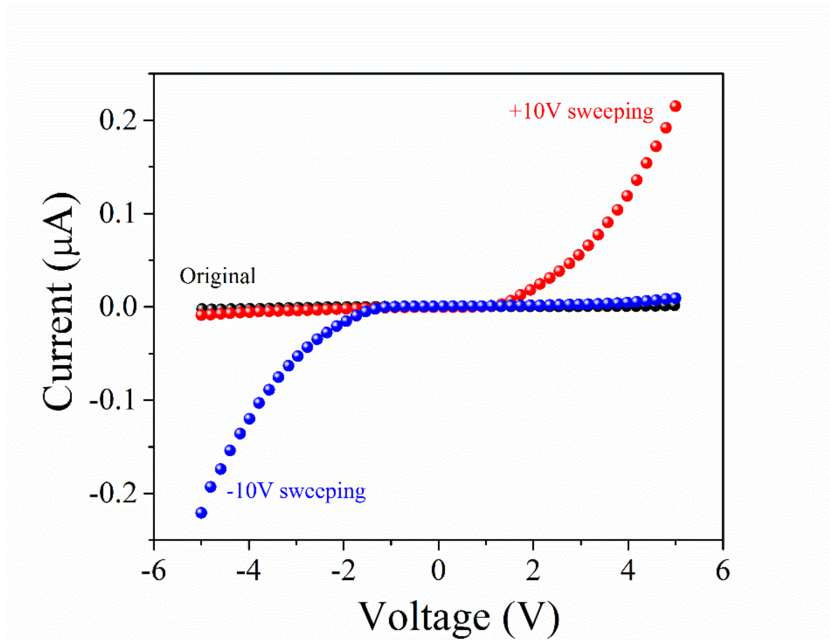

Figure 70. *I-V* curves for the volatile rectification behavior of single $H_2Ti_3O_7$ nanobelt device. The original *I-V* curve is obtained by sweeping from −5 to +5 V. The positive rectification curve is obtained by sweeping from −5 V to +5 V immediately after the positive sweeping from 0 to 10 V. Similarly, the negative rectification curve is obtained by sweeping from −5 V to +5 V immediately after the negative sweeping from 0 to −10 V. The sweeping speed is 50 mV s^{-1}.

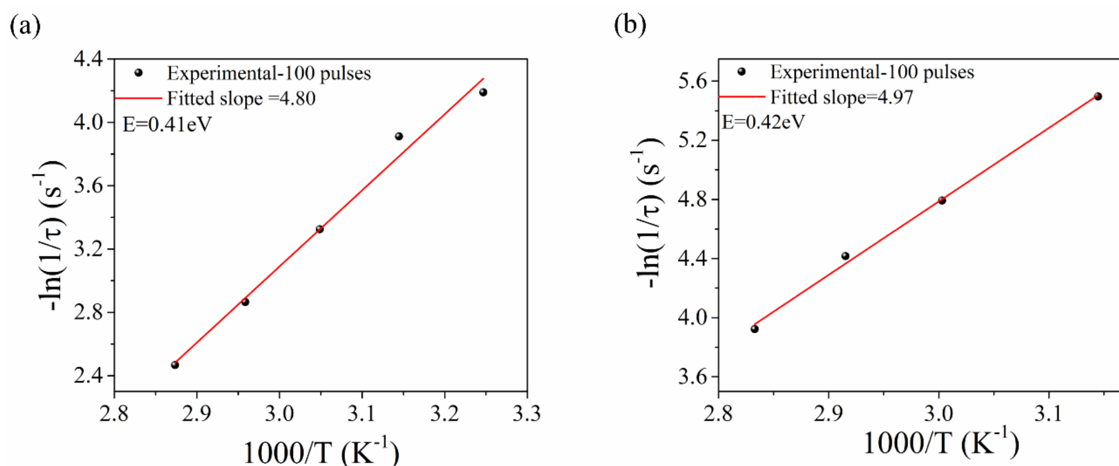

Figure 71. Plot of ln(1/τ) vs. 1000/T and linear fit from Equation 3 in main text for (a) single $Na_2Ti_3O_7$ and (b) single TiO_2 nanobelt devices from temperature dependence of current decay behavior following excitation with 100 consecutive +20 V, 500 ms, pulses. The calculated diffusion activation energy are E=0.41 eV and E=0.42 eV, respectively.

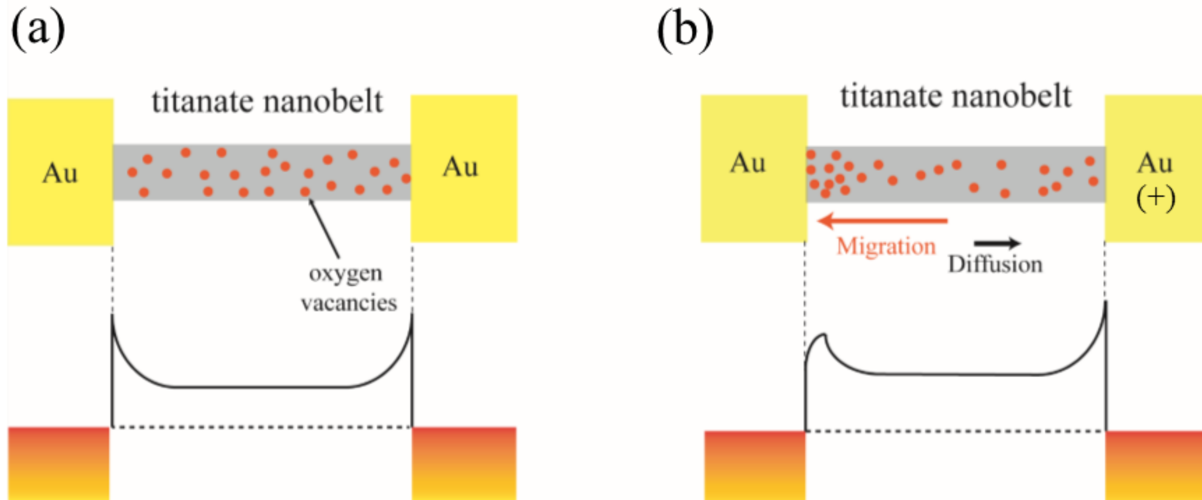

Figure 72. Schematic of the synaptic response mechanism. (a) In the initial state oxygen vacancies are distributed randomly throughout the nanobelt, and a Schottky barrier is formed at each Au/nanobelt interface. (b) With applied positive electric field, the accumulation of oxygen vacancies at the left interface of the Au/nanobelt leads to a reduction in the strength of the Schottky barrier, increasing the conductivity of the device. Back diffusion of these defects in response to the concentration gradient would recover the Schottky barrier, leading to a decrease in the current response.

5.5. Conclusions

The synaptic properties of memristor devices based on single $H_2Ti_3O_7$ and $Na_2Ti_3O_7$ nanobelts have been investigated. Excellent synaptic functionalities including the EPSC, short-term plasticity, potentiation and depression as well as learning-forgetting responses, have been successfully demonstrated in a single nanobelt device. The gradual modulation in conductance with a large number of identical pulses is also realized. The synaptic response are shown to derive from the modulation of a Schottky barrier at the electrode/nanobelt interface due to migration of oxygen vacancies driven by an applied electric field, and moderated by thermal diffusion in response to a gradient in defect concentration. Such intriguing properties of synaptic devices based on individual $H_2Ti_3O_7$ and $Na_2Ti_3O_7$ nanobelts, similar to the TiO_2 nanobelts, not only show that these materials have a promising future in neuromorphic computing applications, but also suggest an alternative direction for material selection for synaptic functionality emulation study.

Chapter 6. Threshold Switching in Single TiO_2 Nanobelt Device Emulating an Artificial Nociceptor

6.1. Overview

Electronic devices that can simulate the dynamics of neurotransmission in the human body are of great interest for the development of artificial intelligence in modern information technology. In this chapter, an artificial nociceptor realized by a single TiO_2 nanobelt device with a unique capacitive-coupled threshold switching behavior is demonstrated. Via thermal admittance spectroscopy and temperature dependent sweeping study, the properties of the nanobelt devices are determined by Schottky emission at low bias and by defect assisted quantum tunneling at high bias subject to a threshold voltage. The low activation energy associated with dynamic electron trapping gives rise to a voltage-dependent volatile threshold switching behavior. This threshold switching behavior allows the emulation of several characteristic features of a nociceptor, a critical type of sensory neuron in the human body, including "threshold", "relaxation", "no adaptation", "allodynia" and "hyperalgesia" behaviors, essential for the realization of electronic sensory receptors that detect noxious stimuli and signal rapid warning to the central nervous system. One-dimensional metal oxide nanobelt devices of this type yield multifunctional nociceptor performance that is fundamental for applications in artificial intelligence systems, representing a key step in the realization of neural integrated devices via a bottom-up approach.

6.2. Introduction

The development of artificial neural networks that can emulate their biological counterparts is very promising and highly desired, especially in the era of Big Data.[96, 282] Compared to conventional digital computers designed according to the von Neumann configuration, in which the arithmetic/logic units and memory units are separated, the brain outperforms digital computers due to its dramatically different configuration, in which arithmetic calculation and memory operate simultaneously without the burden of data transmission. Hardware implementation of neuromorphic systems has attracted much interest due to the great potential inherent in machine learning at low power consumption. Conventional systems based on complementary metal-oxide semiconductor (CMOS) devices have been used for the emulation of synaptic behaviors,[283, 284] but these transistor devices bear little phenomenological similarity to the biological synapse[105] and the

realization of neuromorphic computing systems by traditional transistor devices requires the construction of large-scale parallel logic and switching cells. This is accompanied by high power consumption, complex structural configurations and intrinsic difficulty in scaling down to meet the needs of future nanoelectronic devices. Solid state devices that can accurately emulate the functions and plasticity of biological synapses will be the most important basic building blocks in brain-inspired computation systems.[103]

The memristor as a two-terminal device, bears a striking resemblance to the biological synapse. Indeed, the resistance of a memristor is adjusted by the flow of charge through it, making the device ideal for mimicking the dynamics of biological synapses. Memristor is also more advantageous compared to transistors due to their simple structure, high switching speed and easy integration into the networks required in the development of complex emergent behaviors. The functionality offered by a single memristor device can be used to replace up to 10 transistors on a chip,[30] making it ideal for data storage, neuromorphic applications and large-scale integration. Ion drift memristors have been widely studied as examples of systems that enable emulation of biological synapses. They exhibit a wide range of useful properties, including provision of a high number of resistance states, together with the ultrafast switching speeds that are important for neuromorphic computing applications such as pattern and face classification,[123-125] and sparse coding.[126] However, the nonvolatile nature of these devices make them biologically unrealistic, which severely limit the realization of various synaptic functions.[13, 285] It has also been demonstrated theoretically that a second-order memristor which takes into consideration both the conductance of the memristor device and its internal dynamics such as heat dissipation or mobility decay, is required to emulate the timing-controlled Ca^{2+} dynamics including frequency-dependent plasticity and timing-based plasiticy.[109]

Recently, artificial synaptic devices based on volatile threshold switching, such as diffusive memristive devices,[13, 286-288] oxygen vacancy based devices,[289] a graphene/MoS_2 heterojunctions[290] as well as bio-membrane based devices[285] are gaining increasing attention due to their resemblance of Ca^{2+} dynamics in biological synapses. In biological synapses, synaptic plasticity are regulated by Ca^{2+} dynamics and information gathered by various sensory organs in the human body are transduced into electrical impulses, which are then processed by an elaborate and intricate network of neurons through the release of neurotransmitters within the human brain. The rise and subsequent spontaneous decay of Ca^{2+} concentration at the axon terminal caused by

electrical neuronal stimuli (action potentials) regulates the release of these neurotransmitters into the synaptic cleft. During the release of the neurotransmitters, the Ca^{2+} gated channel will not open until the action potential is higher than a threshold value. When the integrated or total sum of the synaptic potential exceeds its threshold, the postsynaptic neuron will fire an action potential, i.e. the neuron responds or conveys information to its connecting neurons and the process continues. After transmission, the subsequent spontaneous decay of ion concentration at the axon terminal returns the presynaptic neuron to its previous state.[101, 102, 291] This process is at the root of information processing and memory in the brain. Thus, simulating the role of Ca^{2+} dynamics is key to the realization of bio-realistic artificial synapses. In volatile threshold switching devices, the abrupt change of current response that occurs upon exceeding a threshold voltage is also quite similar to the actual neurotransmission process. Spontaneous decay of the current response after applying the threshold voltage without the need for a reset circuit is similar to the decay of ion concentration after the release of neurotransmitter in a neuron.[292] Relaxation to the original rest state after switching to the low resistance state provides an internal timing mechanism and allows the device to naturally emulate the rate- and timing-dependent synaptic effects in a bio-realistic fashion. Due to these advantages, the threshold switching behavior is highly suited to the emulation of brain activity in detecting the threshold level in a decision-making process.[291] An example for the emulation would be the initiation of an escape from potential threats that involve an artificial nociceptor, which is a type of neuron that requires a certain threshold action potential for triggering an active response to pain stimulation.[293-295]

Threshold switching devices for neuromorphic computing applications are normally based on the formation and dissolution of conductive filaments, including Ag filaments or nano-clusters[104, 296-301] and oxygen vacancies.[302-304] It is found that by tuning the compliance current, a transition from threshold switching to nonvolatile memory performance can be achieved due to the inherent thermal stability of the conductive filaments.[286, 290, 296, 298, 305-307] However, the abrupt nature of traditional threshold switching performance makes it unsuitable for potentiation and depression emulation of synaptic computation. This occurs because the relatively abrupt SET process for the filament formation in these threshold switching devices makes it difficult to implement gradual weight changes, as required in neuromorphic applications, where non-abrupt analog-like switching transitions and a wide dynamic range of conductance states are preferred.[117]

In this work, we report that a fundamentally different threshold switching behavior can be achieved in a single TiO_2 nanobelt device. A symmetrical voltage-dependent threshold switching behavior is obtained, controlled by a transition from Schottky emission at low bias to trap assisted quantum tunneling at higher bias. We also find that the presence of defects on the nanobelt is associated with a low activation energy for electron transport, together with dynamic charge trapping/detrapping, leading to a volatile threshold switching behavior instead of the nonvolatile performance observed in corresponding thin film devices. Significantly, the threshold switching performance of this new device facilitates the emulation of a nociceptor, including aspects of "threshold dynamics", "relaxation", "no adaptation", and "allodynia and hyperalgesia" behavior. Using thermal admittance spectroscopy and temperature-dependent sweeping, the charge transport mechanism of the nanobelt device has been systematically studied. These results demonstrate that an individual nanobelt device can be utilized as a reliable building block for the realization of artificial sensory systems based on nanostructures grown with a bottom-to-top approach. This represents an essential milestone on the way to realizing nanowire based artificial neural networks.

6.3. Experimental Section

6.3.1. Synthesis of TiO_2 nanobelts

TiO_2 nanobelts were synthesized via a hydrothermal process from TiO_2 nanoparticles[246]. Typically, 0.75 g commercial TiO_2 nanoparticles, P25 (Sigma Aldrich, Canada) was dissolved in 10M sodium hydroxide alkaline solution (60 mL) and then was poured into a Teflon-lined stainless-steel autoclave (capacity: 125 mL, Parr Instruments). The autoclave was kept in a furnace at a temperature of 250 ^{o}C for 24h. The suspended nanobelts were taken out from the autoclave after being cooled down naturally and were washed with ultrapure water. The obtained nanobelts were immersed in 0.1 M HCl solution for 12 h for ionic exchange. Afterwards, the solution was filtered and the obtained residues were then dried in a furnace at 80 ^{o}C for 8 h to obtain the nanobelt powders. Finally, the obtained powder was annealed at 700°C for 2h to obtain the anatase TiO_2 nanobelts. For the device fabrication, the TiO_2 nanobelts were harvested by sonication 0.5 mg in pure acetone solution before the device fabrication.

6.3.2. Device fabrication and characterization

Pt electrodes are fabricated on a SiO_2/Si substrate with standard photolithography and lift-off process. To fabricate the TiO_2 nanobelt device, electrodes are firstly rinsed with acetone,

isopropanol and ultrapure water, respectively and dried with flowing nitrogen gas. The devices are treated in an oxygen plasma machine (Tergeo Series, PIE Scientific) at a power of 75 W for 40 s to lead to a hydrophilic nature of the surface of the electrode. Diluted solution of TiO_2 nanobelts are then drop-cast on Pt electrodes and dried in air. Samples with bridged TiO_2 nanobelt on the electrodes are located using optical microscopy before electrical characterization.

6.3.3. Material characterization

The morphology and device of TiO_2 nanobelts were characterized by scanning electron microscopy (SEM, LEO 1530). Oxygen chemical states of TiO_2 nanobelts were examined by X-ray photoelectron spectroscopy (XPS, Thermo-VG Scientific ESCALab 250). Transmission electron microscopy (TEM) and high-resolution transmission electron microscopy (HRTEM, FEI Titan 80-300 LB) are used to characterize the nanobelts at the voltage of 300 kV. Electrical performance of the single nanowire devices was evaluated using K4200A semiconductor parameter analyzer equipped with a probe station (MPI TS150). Thermal admittance spectroscopy characterization were performed at a pressure below 2×10^{-6} mbar in the dark using a commercially available deep level transient spectroscopy (DLTS) system from Semetrol. The sample was held constant for 10 min to ensure the thermal equilibrium at different temperatures before the measurements.

6.4. Results and Discussion

6.4.1. I-V sweeping performance and mechanism study

6.4.1.1 I-V sweeping performance

Uniform TiO_2 nanobelts were obtained via a hydrothermal process followed by thermal annealing at 700 ^{o}C for 2 h (Materials and Methods).[148, 246] Typically, these nanobelts have a width of 50-200 nm, thickness of 15-50 nm and length in the range of 5-20 μm, as shown in the scanning electron microscopy (SEM) image (Figure 73(a)). High resolution transmission electron microscopy (HRTEM) characterization of one TiO_2 nanobelt confirms the single crystalline nature with a wide distribution of void defects as highlighted in Figure 73(b). The oxygen 1s X-ray photoelectron spectroscopy (XPS) spectrum of the nanobelts shows the existence of defect oxygen peaks centered at 531.28 eV and 533.18 eV, corresponding to oxygen vacancies (20.25%) and hydroxide groups (7.98%), respectively (Figure 73(c)). Pt electrodes were fabricated via a standard

photolithography process on a Si/SiO_2 wafer. The distance between adjacent electrodes is 1 μm (Figure 73(d) and 73(e)). Afterwards, the diluted TiO_2 nanobelt solution was deposited on the electrodes. Individual nanobelts were located for further electrical characterization (Figure 73(f)).

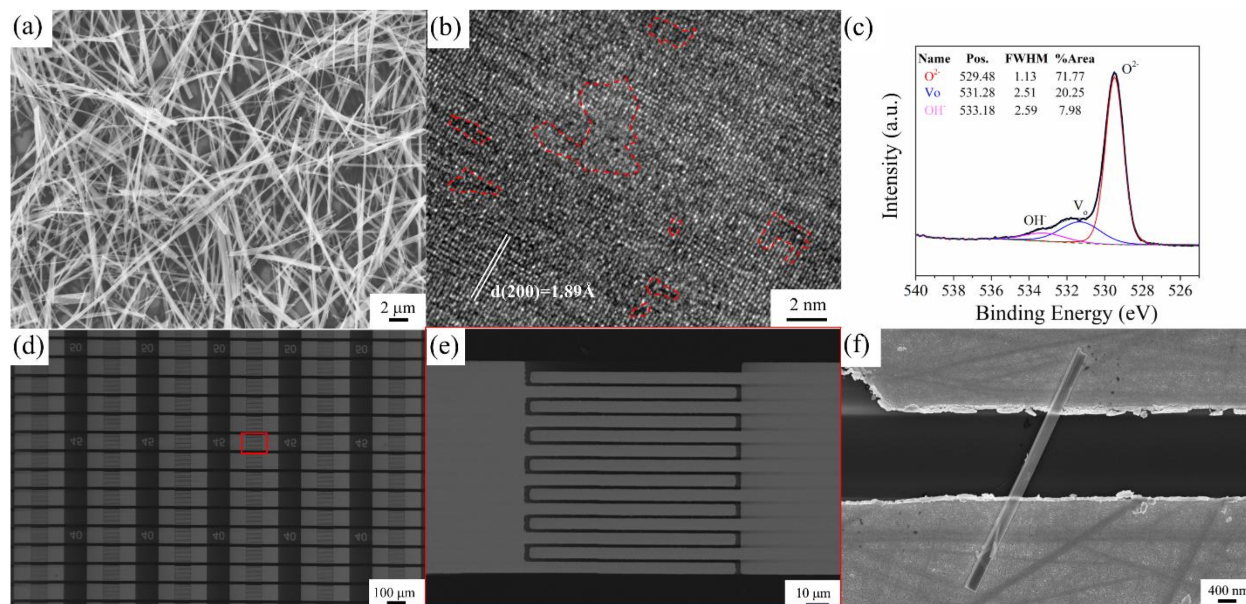

Figure 73. Material characterization of TiO_2 nanobelts and the architecture of a TiO_2 nanobelt device (a) SEM image, (b) HRTEM image with void defects highlighted in red, (c) O 1s XPS spectrum, (d) Low-magnification SEM image of Pt-Pt electrodes fabricated on the SiO_2 wafer, (e) High magnification SEM image for a typical pair of interdigitated Pt-Pt electrodes, (f) SEM image of a typical TiO_2 nanobelt device on paired electrodes.

Figures 74(a) and 74(b) show the I-V sweeping performance of the single TiO_2 nanobelt device on Pt-Pt electrodes at a constant sweep rate of 0.1V/s on linear and semi-logarithmic scales, respectively. A symmetrical hysteresis curve is observed in Figure 74(a), implying resistive switching behavior. As shown in Figure 74(b), when the voltage is less than 3V, the device is initially in a highly insulating state with currents in the sub-pA range. At a higher voltage, the current response abruptly increases with the increase of electric field, changing from an insulating state (high resistance state, HRS) to a voltage dependent conductive state (low resistance state, LRS). When sweeping back from 20V to 0V, the current spontaneously relaxes to its baseline value as indicated by the arrows and numbers in both Figures 74(a) and 74(b). This is a typical feature of volatile switching behavior. The devices also demonstrate symmetrical behavior for the range of negative voltage sweeping, implying threshold switching behavior for both polarities. This is significantly different from the nonvolatile memory behavior observed in the widely-studied Pt-TiO_2 thin film-Pt sandwich devices, which can maintain their resistance state.[33, 70, 141] In contrast to most other reported threshold switching behaviors based on the filament formation

and rupture of Ag ions[296-300] or oxygen vacancies,[302-304] the present TiO_2 nanobelt devices demonstrate a threshold switching performance without the need for a compliance current, as normally required for filament-based threshold switching devices in both/either SET or RESET processes to avoid permanent breakdown. This helps to avoid some limitations imposed on the scaling down of these devices as integration of other electronic components such as a transistor are normally required to restrict the working current in this type of configuration.[308] The continuous current change, which can facilitate the adjustable weight changes desired in neuromorphic computing, implies that the mechanism is different from abrupt filament formation and rupture observed in other reported threshold switching devices. The symmetrical threshold switching behavior in the single TiO_2 nanobelt device could also be used as a selector for solving the sneak path problem in crossbar architectures.[104]

The single nanobelt device shows reproducible performance with a resistance ratio up to 1.3×10^4 for a sweeping range of 20 V (Figure 74(c)). This LRS/HRS ratio is dependent on the sweeping voltage, as shown in Figure 74(d), which could provide potential for the precise resistance state to be tuned by the applied electric field. A statistical summary of 26 devices with identical geometry fabricated on a single chip was obtained and the results showed a logarithmic normal distribution of the resistance ratio (Figure 74(e)). The device-to-device variation could be attributed to the difference between contact areas of individual nanobelts on the electrodes. It is also found that the as-fabricated TiO_2 nanobelt devices are characterized by a highly repeatable and symmetrical switching behavior when excited with bipolar pulses over 10,000 cycles. This shows that these devices are highly robust (Figure 74(f)).

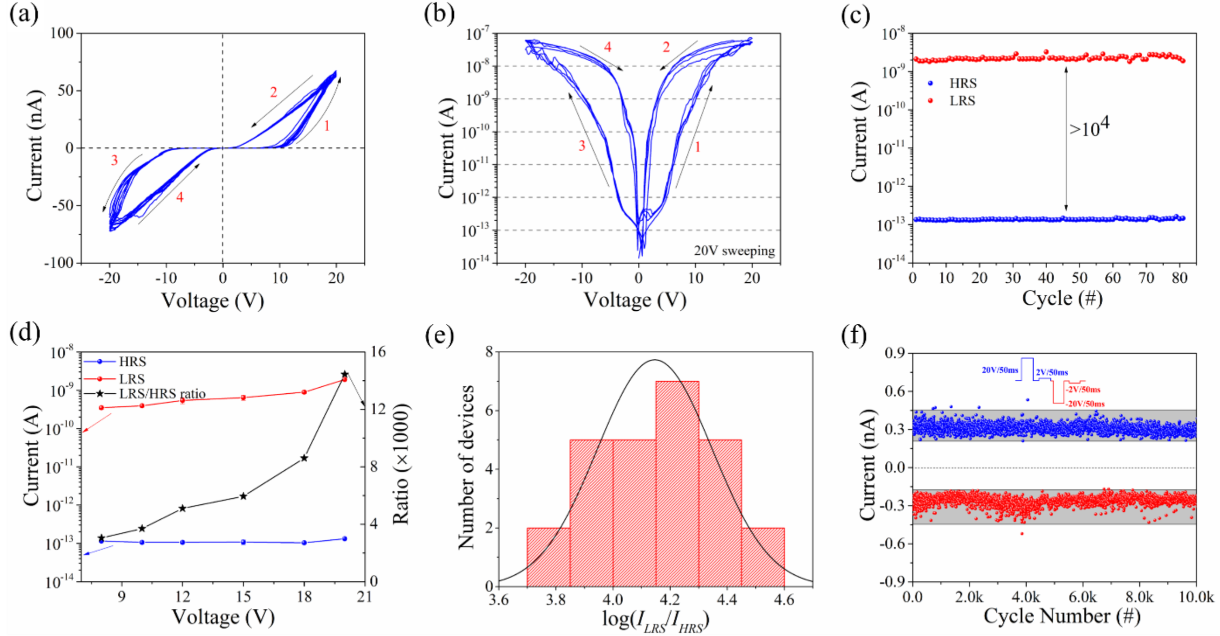

Figure 74. Threshold switching sweeping performance for single TiO_2 nanobelt devices. (a) Sweeping performance at 20 V at a constant sweeping rate of 0.1 V/s plotted on a linear scale, (b) corresponding I-V curve plotted on a semi-logarithmic scale. (c) LRS/HRS ratio for the device at the reading voltage of 3 V over 80 sweeping cycles in (b). (d) Sweeping voltage dependent performance and summary of LRS/HRS ratio at the reading voltage of 3V. (e) Statistical summary for the LRS/HRS ratio among 26 devices having identical geometries. (f) Endurance performance for 10,000 cycles at room temperature. The inset shows one cycle of the applied pulses, where the 2 V, 50 ms and -2 V, 50 ms pulses are used as read pulses. The device did not fail during the measurement, showing a high degree of robustness.

To further explore this threshold switching behavior, the sweeping performance under different voltages for a constant sweep rate of 0.1 V/s has been evaluated as shown in Figure 75. The full range of sweeping behavior can be found in Figures 76 and 77. It can be seen that, at a small sweeping bias such as 2 V, the single nanobelt device responds with the charging and discharging cyclic voltammetry curves of a capacitor-resistor circuit(Figures 75(a) and 75(d)).[309] This characteristic likely arises due to the Schottky barrier created between the electrode and the nanobelt. When the bias exceeds 3 V, the device exhibits a symmetric resistive switching performance at high bias while the contribution of the capacitive response remained at low bias (Figures 75(b) and 75(e), Figures 76(c) and 77(c)). This implies that the single TiO_2 nanobelt device changes from a capacitive behavior to a capacitive-coupled memristor behavior when the sweeping bias exceeds 3 V. The capacitive-coupled memristive effect has been previously reported in the case of nonvolatile memory devices,[309] but, to the best of our knowledge, this is the first time that this characteristic has been reported in volatile threshold switching devices. Further

increasing the sweeping bias up to 10 V (Figures 75(c) and 75(f)) and 20 V (Figures 76(i) and 77(i)) will lead to an increased current for the resistive switching behavior, but the devices still have a small capacitive contribution at low bias. This is why the I-V curve of the TiO_2 nanobelt device is not pinched to zero, in great contrast to the zero-crossing behavior typically observed in memristive devices. In our devices, since no redox reactions have occurred, the capacitive effect remains during switching. This property is unique and is quite different from the characteristics of other threshold switching devices, in which the filament formation and rupture leads to memristive behavior with a zero-crossing feature and abrupt change between resistance states.

The high aspect ratio of the nanobelt implies that the performance of the single nanobelt device can be susceptible to the presence of surface trapping sites.[310] This would result in an I-V behavior that could be independent of the electrodes. To test this possibility, we fabricated single TiO_2 nanobelt devices on different electrodes. As shown in Figure 78, the devices constructed with Au-Au and Ti-Ti electrodes both demonstrated similar volatile threshold switching characteristics, differing only in current amplitude compared to the device using Pt-Pt electrodes. With Ti electrodes, the theoretical difference between the Ti work function (4.33 eV) and the TiO_2 Fermi level (4.2 eV) is small enough to lead to an Ohmic contact. Nevertheless, the sweeping performance is similar to that observed for the Pt and Au electrodes, indicating that at least, partial Fermi level pinning[311-316] may be occurring due to the surface-dominating nature of the TiO_2 nanobelts. A similar transition from a capacitive behavior to a capacitive-coupled memristive behavior is observed for the device with Au-Au electrodes (Figure 79).

It should be noted that the defects in the TiO_2 nanobelts are critical for obtaining a resistive switching response.[221] We tested this by further annealing the as-deposited TiO_2 nanobelts for 2h at 700 ^oC. Nanobelts subject to this treatment are almost perfectly single-crystalline as evident from HRTEM (Figures 80(a) and 80(b)). However, such devices exist in a highly insulating capacitive state up to a sweeping voltage of 40 V (Figure 80(c)). This suggests that the defects in the TiO_2 nanobelts are critical to produce resistive switching behavior.

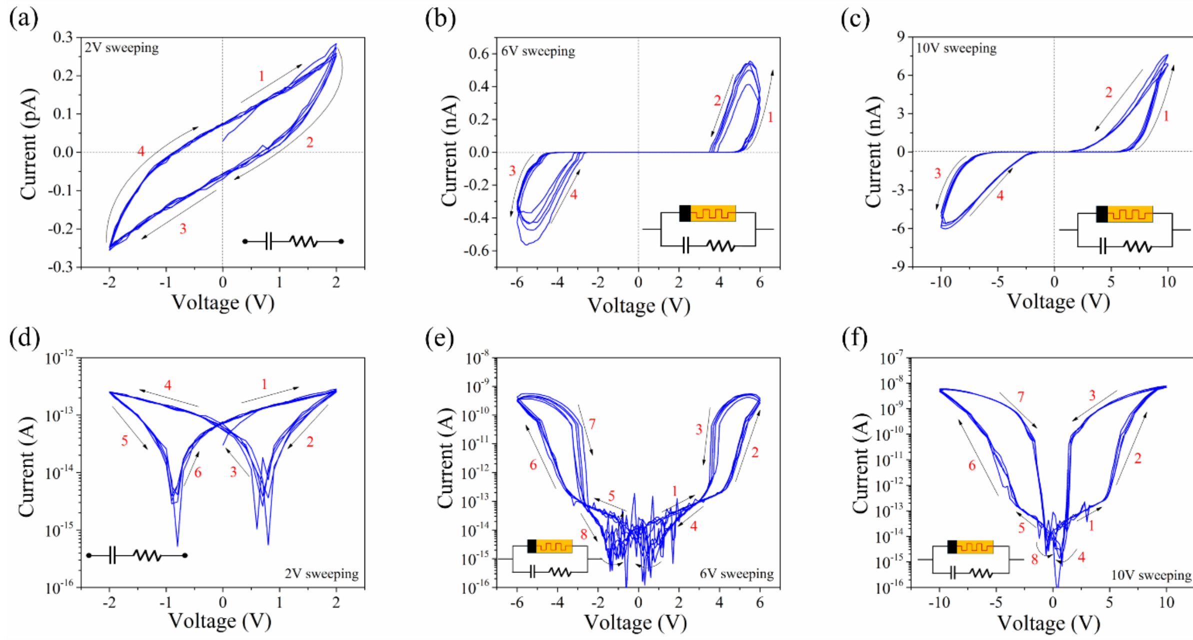

Figure 75. I-V sweeping performance for the single TiO_2 nanobelt device at different sweeping voltages. At low sweeping range such as 2 V ((a) and (d)), the device demonstrated a typical charging and discharging cyclic voltammetry curves of a capacitor with a series resistor. However, at higher bias such as 6 V ((b) and (e)) and 10V ((c) and (f)), the volatile threshold switching performance is observed with the capacitive contribution from low bias. Inset of each figure shows the equivalent circuit of the devices at different sweeping voltages.

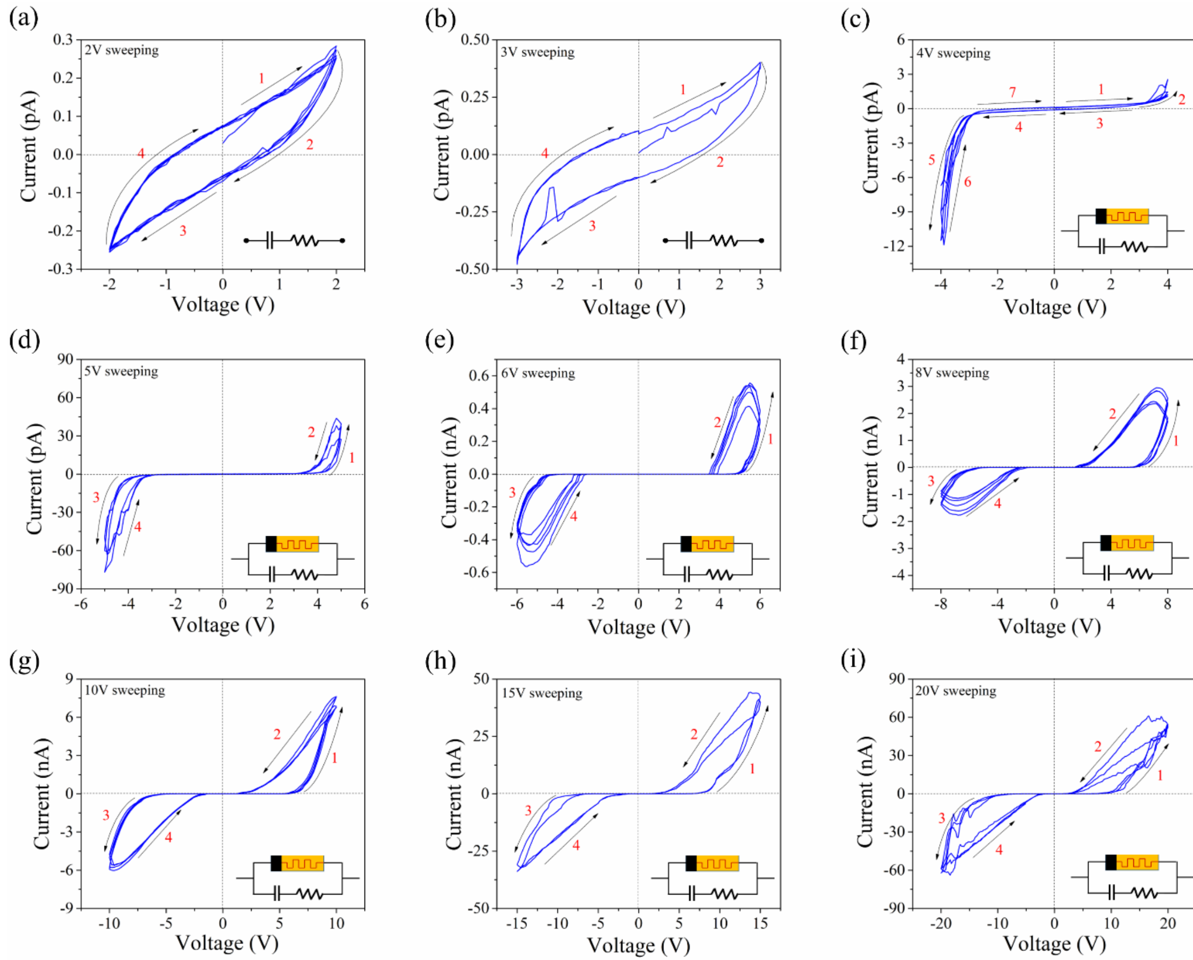

Figure 76. Sweeping behavior for Pt-TiO_2 nanobelt-Pt device under sweeping voltages at (a) 2 V, (b) 3 V, (c) 4 V, (d) 5 V, (e) 6 V. (f) 8 V, (g) 10 V, (h) 15 V and (i) 20 V in a linear scale.

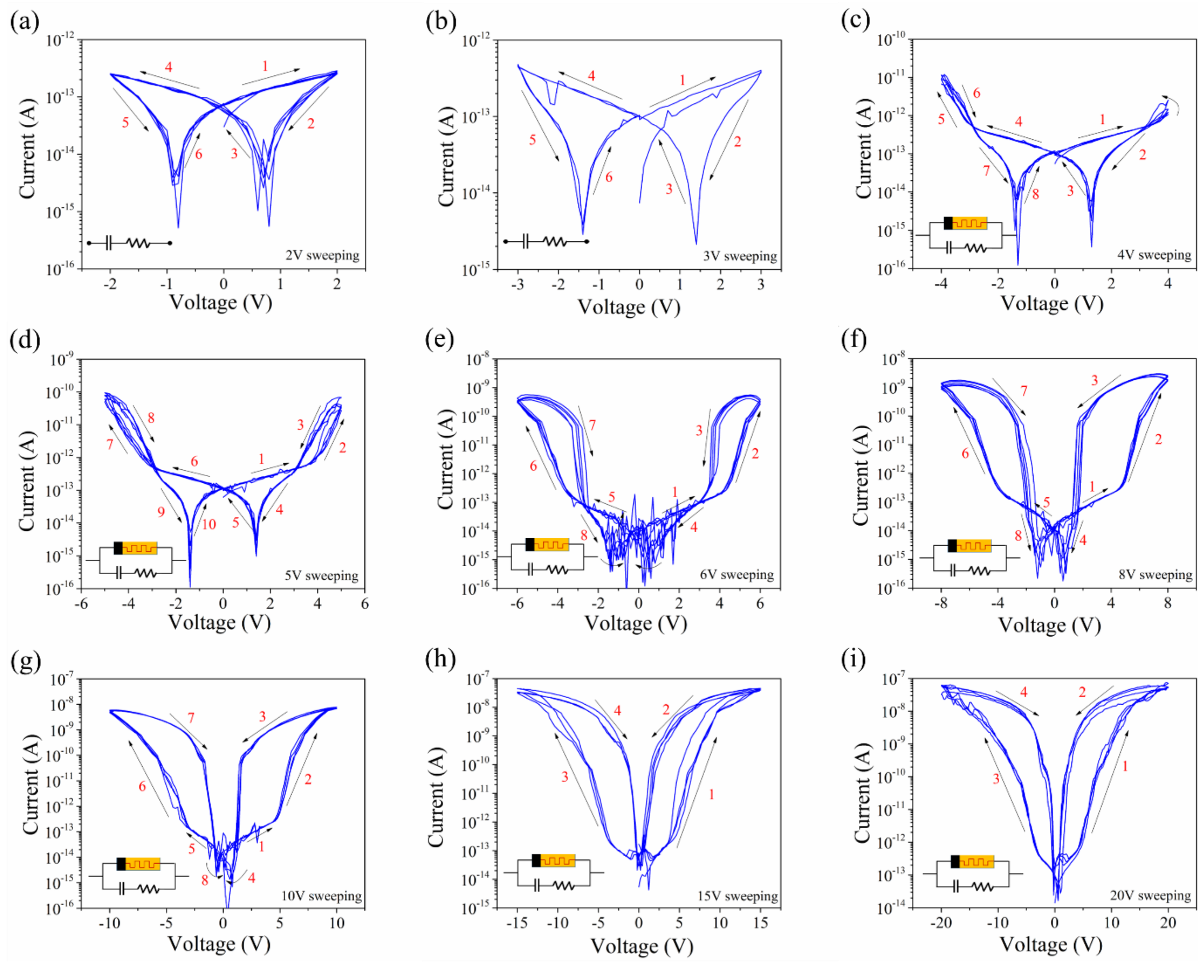

Figure 77. Sweeping behavior for Pt-TiO_2 nanobelt-Pt device under sweeping voltages at (a) 2 V, (b) 3 V, (c) 4 V, (d) 5 V, (e) 6 V. (f) 8 V, (g) 10 V, (h) 15 V and (i) 20 V in a semi-logarithmic scale.

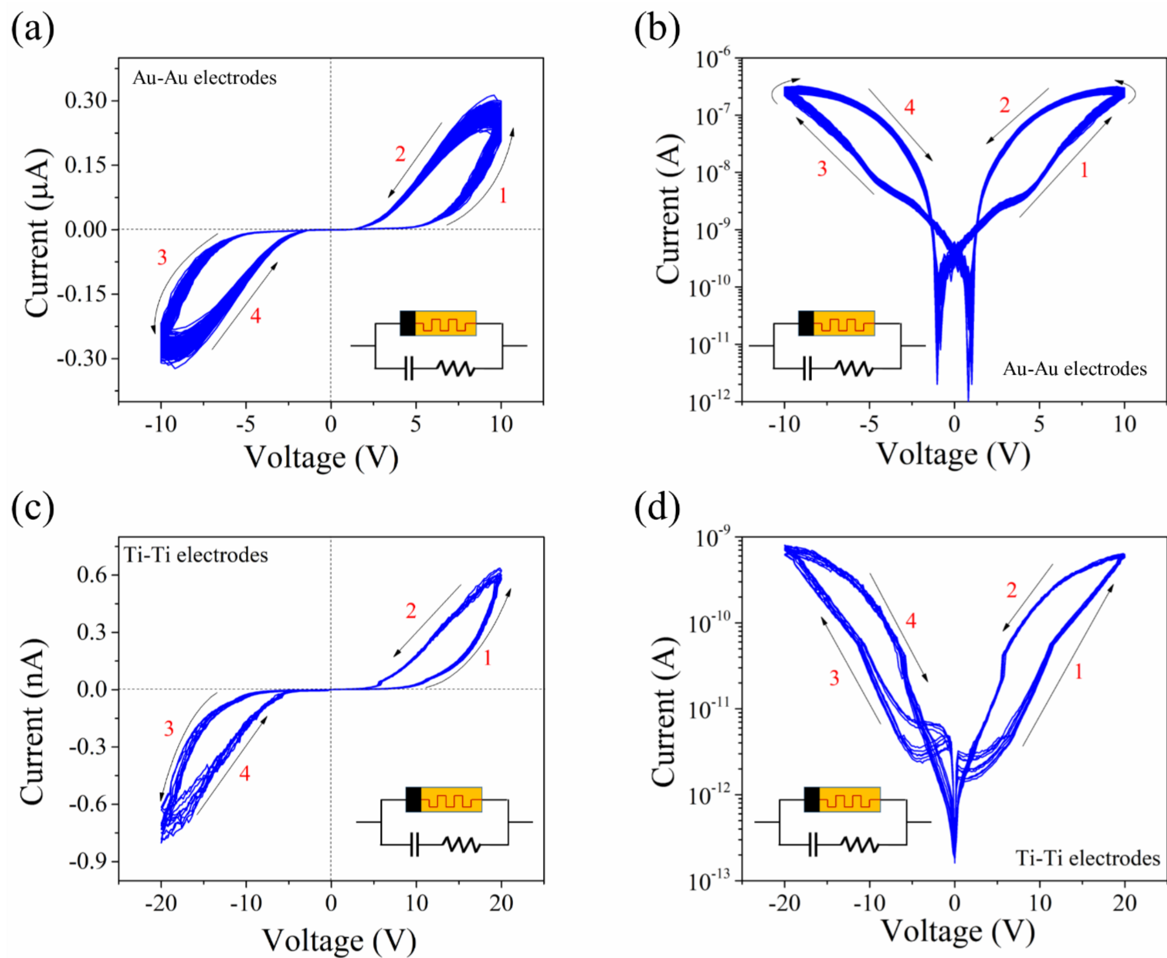

Figure 78. I-V sweeping performance for TiO_2 nanobelt on paired Au-Au electrode, (a) line scale and (b) semi-logarithm sale, and on paired Ti-Ti electrodes, (c) line scale and (d) semi-logarithm sale. The sweeping rate is 0.1 V/s for both measurement.

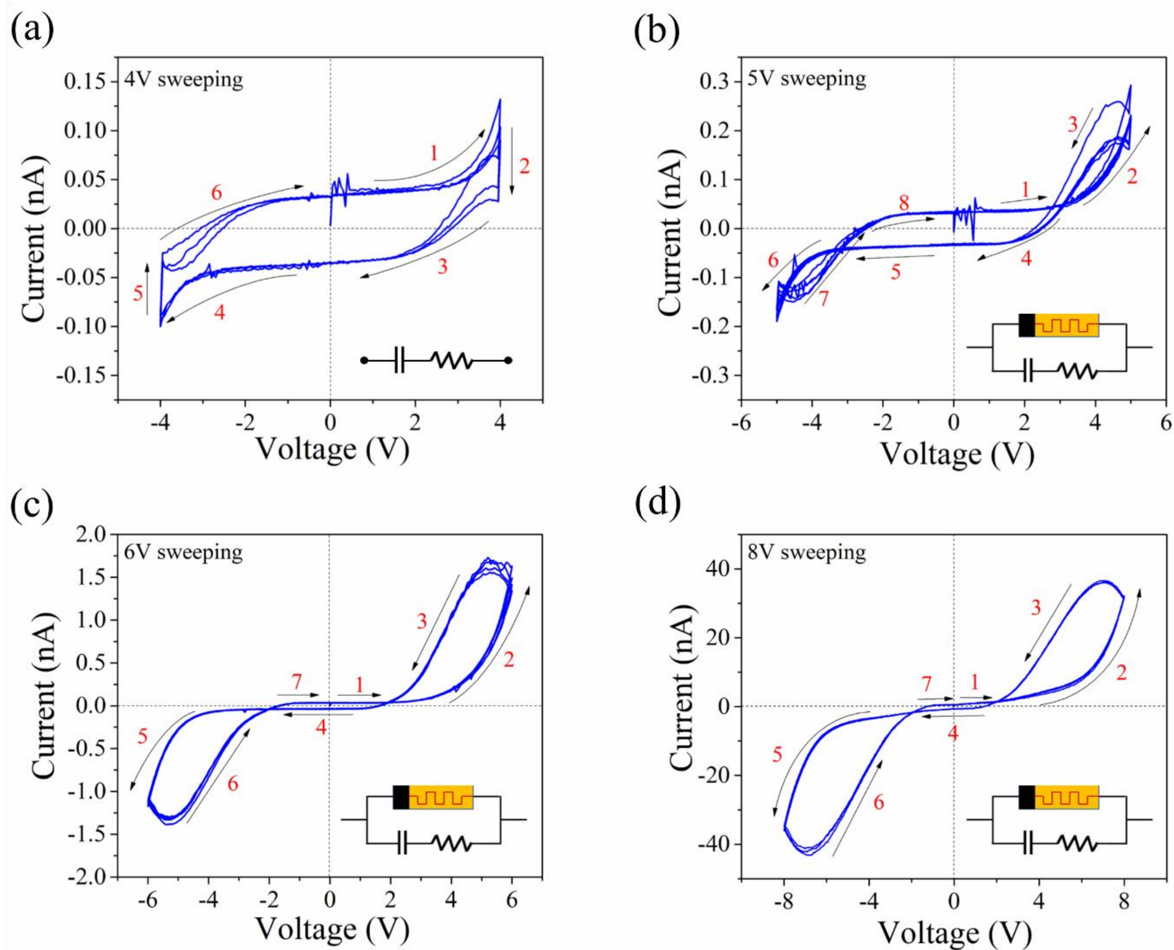

Figure 79. Transition from a capacitor behavior to a memristor with a capacitive contribution for single TiO_2 nanobelt device on paired Au-Au electrodes.

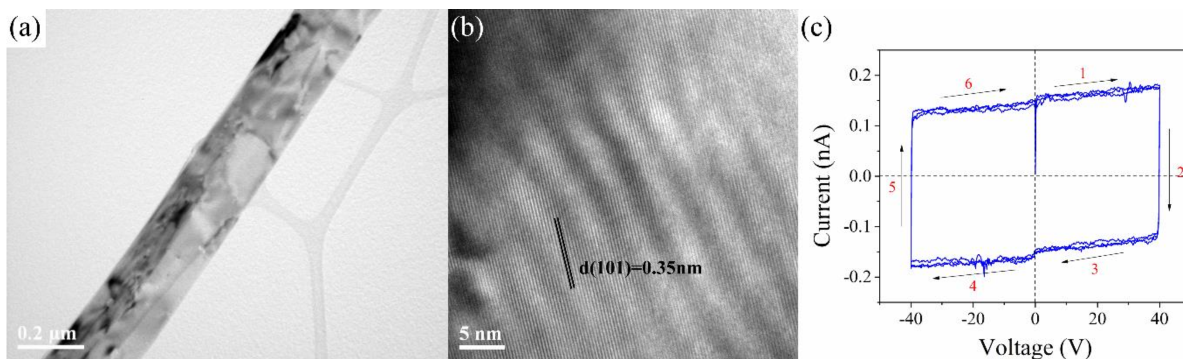

Figure 80. I-V sweeping performance for TiO_2 nanobelt on paired Pt-Pt electrodes with different concentration of defect by further annealing the obtained TiO_2 nanobelts at 700 °C for 2 h. (a) TEM and (b) HRTEM characterization of nanobelts, (c) I-V sweeping performance, a highly insulating capacitive performance is obtained for the TiO_2 nanobelt device with very few defects

6.4.1.2 Charge transport mechanism

To study the charge transport behavior of these TiO_2 nanobelt devices, the I-V sweeping performance is examined at different temperatures, as shown in Figure 81. With increasing temperatures, the current response increases significantly, implying a temperature-related charge transport mechanism in the single TiO_2 nanobelt devices (Figure 81(a)). Due to the symmetrical behavior of the current response, only the current under forward voltages is fitted with possible charge transport equations at different stages that are divided by threshold voltage, V_{th}. In Stage I, the linear slope dependence of $ln(J/T^2)$ with $1/T$ implies the introduction of a Schottky barrier. The typical Schottky emission equation is expressed as[317]

$$J = A^{*}T^{2}exp\left[\frac{-q(\emptyset_{B}-\sqrt{qE/4\pi\varepsilon_{r}\varepsilon_{0}})}{kT}\right] \quad (1)$$

where, J is the current density, A^* is the effective Richardson constant in the dielectric material, q is electron charge, k is Boltzmann's constant, T is the absolute temperature, E is the electric field, $\emptyset_B$ is the barrier height, ε_r is the optical dielectric constant, and ε_0 is the permittivity of the dielectric material in vacuum. From this equation, a Schottky plot of $ln(J/T^2)$ versus $1/T$ at different voltages and $ln(J/T^2)$ versus $E^{1/2}$ at different temperatures should be linear, as confirmed in Figures 81(b) and 82(a). In Stage I, an effective Schottky barrier must be formed at the interface between the Pt electrodes and the TiO_2 nanobelt layer. An effective Schottky barrier height of $\emptyset_{B-I} =$ 0.80±0.04 eV is obtained from the intercept of the $ln(J/T^2)$-$E^{1/2}$ curve. This barrier is smaller than the theoretical barrier (1.2 eV) obtained from the difference between the Pt work function (5.2 eV) and the TiO_2 electron affinity (4.0 eV)[318]. The lower effective Schottky barrier obtained from the fit could be due to the existence of electron traps at surface defects that promote the injected electron transfer from the electrode. This phenomenon has been widely explored in one-dimensional semiconductor nanomaterial-based devices.[277, 310, 319, 320]

Furthermore, due to the highly defective nature of the TiO_2 nanobelts, oxygen vacancies or hydroxide groups on the surface function as localized charge-carrier centers providing paths for injected electrons to hop from one localized site to another when an external electric field is applied. At low electric field in Stage I, the temperature dependence of the resistance of the TiO_2 nanobelt device can be described using a Mott-variable range hopping (VRH) conduction mechanism according to the equation[276]

$$R = R_{0}exp((\frac{T_{0}}{T})^{\frac{1}{4}}) \quad (2)$$

where T_0 and R_0 are constants determined by the material. From this equation, the device resistance, $ln(R)$, is proportional to $1/T^{1/4}$, as evident in Figure 81(c). This suggests that the injected electrons from the electrode can hop to a range of different localized states at the Pt/TiO_2 interface, where a high concentration of defects is present.

At Stage II, the current response is best fitted with the trap assisted tunneling (TAT) equation[321]

$$J = Aexp(\frac{-8\pi\sqrt{2qm^*}}{3hE}\emptyset_T^{3/2}) \tag{3}$$

Where, A is a constant, ϕ_T is the trap energy level with respect to the conduction band edge of the oxide, m^* is the electron effective mass in the dielectric material, and h is Planck's constant. We use $m^*=1.0m_0$ (where m_0 is the mass of an electron) as an estimate of the trap energy level in our device.[322, 323] From equation 3, we obtain a linear relationship between $ln(J)$ and $1/E$ with a slope dependent on the effective trap energy level, ϕ_T, as given in Figure 81(d). The derived trap energy state is $\emptyset_{T-II}$ = 35.3±2.7 meV for stage II. Trap assisted tunneling typically occurs when the electrons tunnel through a thin highly defective dielectric layer promoted by defects. In the present system, the surface defects at the Pt/TiO_2 interface are likely to function as trap centers that promote injected electron tunneling from the electrode to the conduction band of the TiO_2 nanobelt.

The properties of the trapping states in the TiO_2 nanobelt device has also been examined using thermal admittance spectroscopy.[324] The technique consists of calculating the derivative of the junction capacitance with respect to the angular frequency of the small voltage perturbation (50 mV) applied to the devices by varying the temperature. Defect states within the bandgap contribute to the junction capacitance depending on their energy and spatial location. For the present device, in the transition from low to high frequency, a step capacitance accompanied by a loss peak is observed near the frequency $\nu_{\max}$ (Figures 83(a) and 83(b)). Analysis of these data yields an activation energy ΔE of 38±2 meV and an attempt-to-escape frequency of 2.6 x 10^4 s^{-1} at 300 K. The activation energy ΔE is defined as the difference between the defect state energy E_T and the conduction band energy ΔE as $\Delta E = E_C - E_T$ or the difference between the defect state energy E_T and valence band energy E_V as $\Delta E = E_T - E_V$ for hole traps, respectively. In the present devices, only the electron traps are considered due to the N-type semiconductor nature for TiO_2. The inferred trap depth is much shallower than that of oxygen vacancies in defect states below the conduction band in TiO_2 (Figure 83(c)).[325, 326] But it is in the same range as that obtained from the TAT fit for Stage II, suggesting that surface defects are critical in determining the charge transport

behavior of the TiO_2 nanobelt devices. The density of states (DOS) can also be obtained as shown in Figure 83(d), and shows a Gaussian peak centered at the fitted activation energy at different temperatures. The full width at half maximum of the DOS is estimated to be 29 meV.

The TAT equation also applies in the high voltage range in Stage III in the low resistance state. Here, the data gives a much smaller slope for the fitted equation (Figure 81(e)). The trap energy level derived from this fit is $\emptyset_{T-III}$ = 14.7±0.5 meV for Stage III. This suggests that the hysteresis behavior is probably due to the difference in the effective trap energy. When sweeping from 0 to 10 V, TAT occurs and some of the traps are occupied by charge trapping, leading to the reduction of number of TAT paths. On sweeping back from 10 V to 0 V, traps in deeper levels might already be filled and some shallower traps could be involved in the charge transport mechanism, leading to a shallower derived trap energy. Thus it is suggested that from Stage II to Stage III, this nonequilibrium trapping dynamics by the surface states of the TiO_2 nanobelts lead to the difference in the current response from the same trap assisted tunneling mechanism, leading to observed hysteresis in current,[310] i.e., resistive switching behavior. This assumption is also supported by the sweeping voltage dependent hysteresis behavior shown in Figures 74(d) and Figures 75-77. The application of a larger electric field allows further trapping of electrons by available trap states, correspondingly increasing the hysteresis effect and therefore resulting in a higher LRS/HRS ratio. This nonequilibrium dynamic trapping behavior is further supported by sweeping-rate I-V performance of the device, as shown in Figure 84, where a higher sweeping rate leads to a decrease of the hysteresis effect due to the limited timescale for charge trapping.

In Stage IV, the I-V response can be fit with the Schottky emission equation, as shown in Figure 81(f) and Figure 82(b). At this stage, the effective Schottky barrier is estimated to be $\emptyset_{B-IV}$ = 0.67±0.03 eV. The small variation in the value of the derived Schottky barrier in the Stages IV and Stage I is likely caused by charge trapping as well as changes in the available trap density in response to the electric field.

Overall, it is proposed that the switching mechanism of the single TiO_2 nanobelt device can be described by dynamic nonequilibrium charge trapping process that modulate the Schottky barrier profile as well as the quantum trap assisted tunneling process. The existence of defects in TiO_2 nanobelts causes tailoring of the DOS compared to that of pure TiO_2 (Figure 81(g)).[327] Many of these available trap sites at the Pt/TiO_2 interface are likely empty initially, which makes the pristine device remain in HRS due to the Schottky barrier at zero bias (Figure 81(h)). In this regime, charge

transport is dominated by Schottky emission at low forward electric field in Stage I (Figure 81(i)) and hopping of electrons to various localized trap sites occurs. When a sufficiently high positive voltage is applied to the electrode causing the trap level to be pulled down to below the Fermi energy level, the trap sites start to be filled by electron injection from the Pt electrode. The available trap states at the Pt/TiO_2 interface leads to a defect promoted (or trap-assisted) tunneling response in Stage II (Figure 81(j)). Meanwhile, the dynamic electron trapping causes the modulation of trap-assisted tunneling process, leading to the hysteresis response in Stage III (Figure 81(k)). The accumulated electron trapping under applied electric field could possibly causes the effective Schottky barrier to be lowered in Stage IV, in which the spontaneous charge detrapping occurred, making the device return to the initial state (Figure 81(l)).

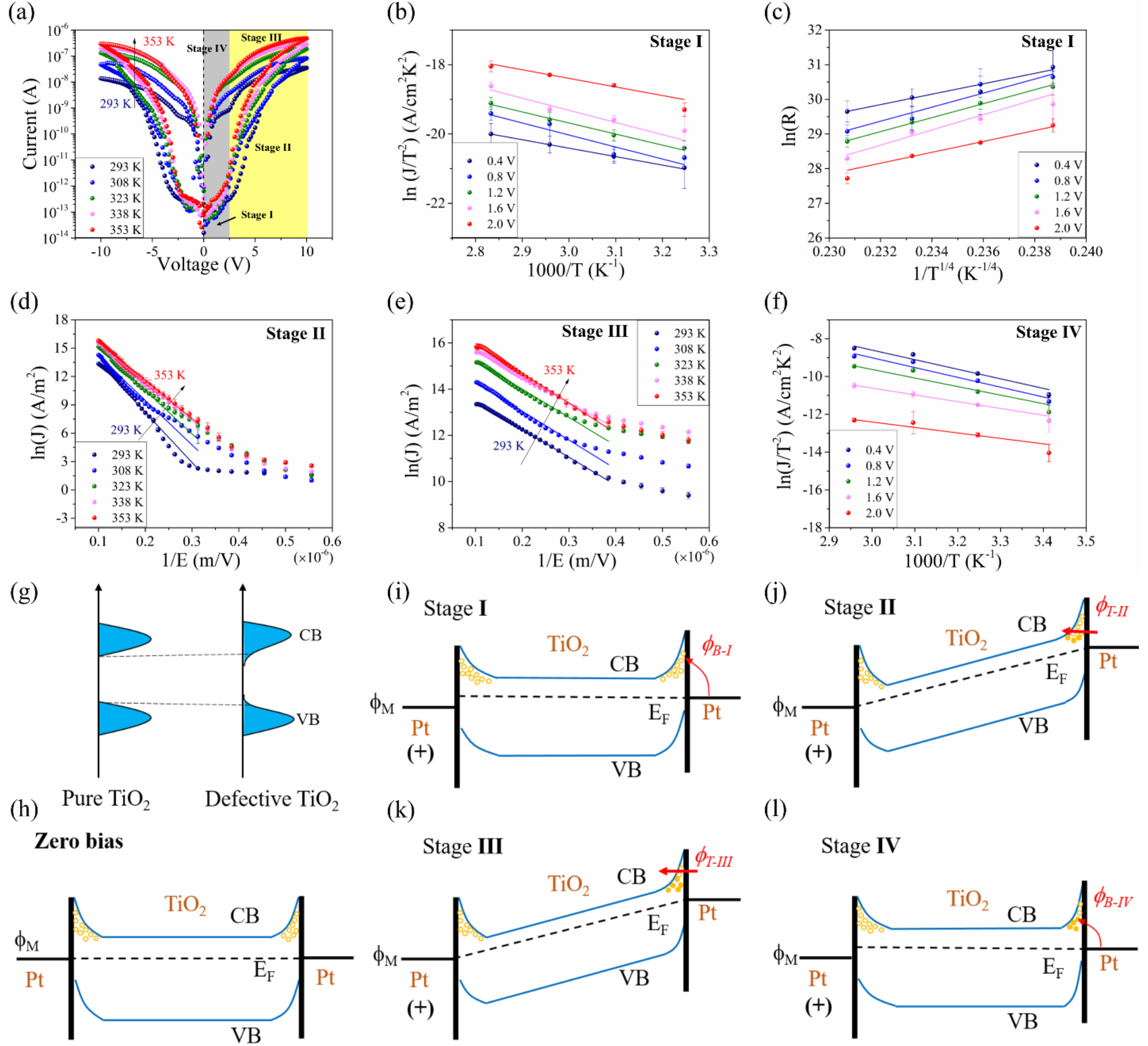

Figure 81. Charge transport mechanism for a single TiO_2 nanobelt device. (a) Temperature dependent sweeping performance at temperatures from 293 K to 353 K. A constant sweeping rate of 0.1 V/s is used for all the measurements. Four stages associated with application of a bias are highlighted for fitting with different equations. (b) $ln(J/T^2)$ as a function of inverse temperature ($1/T$) for voltages in Stage I. (c) $ln(R)$ as a function of temperature ($T^{-1/4}$) at different low voltages in Stage I. (d) $ln(J)$ as a function of inverse electric field $(1/E)$ at different temperatures for voltages in Stage II. (e) $ln(J)$ as a function of inverse electric field $(1/E)$ at different temperatures for different voltages in Stage III. (f) $ln(J/T^2)$ as a function of inverse temperature ($1/T$) in Stage IV at different temperature. Five sweeping cycles were obtained at each temperature and average values and standard deviations were calculated correspondingly. (g) Schematic diagram of DOS distribution of pure TiO_2 vs TiO_2 containing defects. (h) Schematic band diagram for the TiO_2 nanobelt device at zero bias. (i-l) Schematic band diagram for the TiO_2 nanobelt device in Stage I, II, III and IV, respectively.

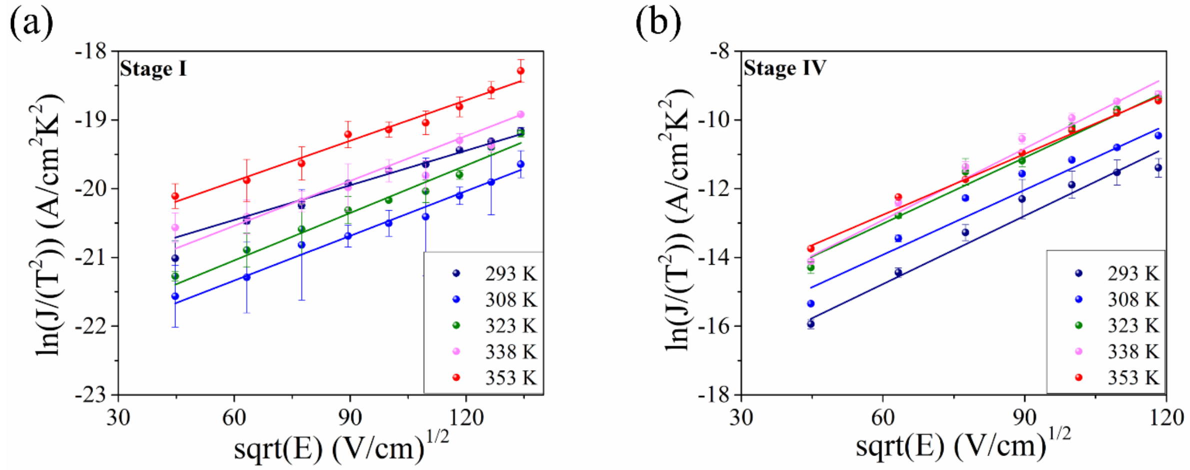

Figure 82. Charge transport mechanism study for a single TiO_2 nanobelt device. (a) $ln(J/T^2)$ as a function of square root of the electric field ($E^{1/2}$) at various temperatures in Stage I. (b) $ln(J/T^2)$ as a function of square root of the electric field ($E^{1/2}$) at various temperatures in Stage IV. All the measurement is the same as described in Figure 81.

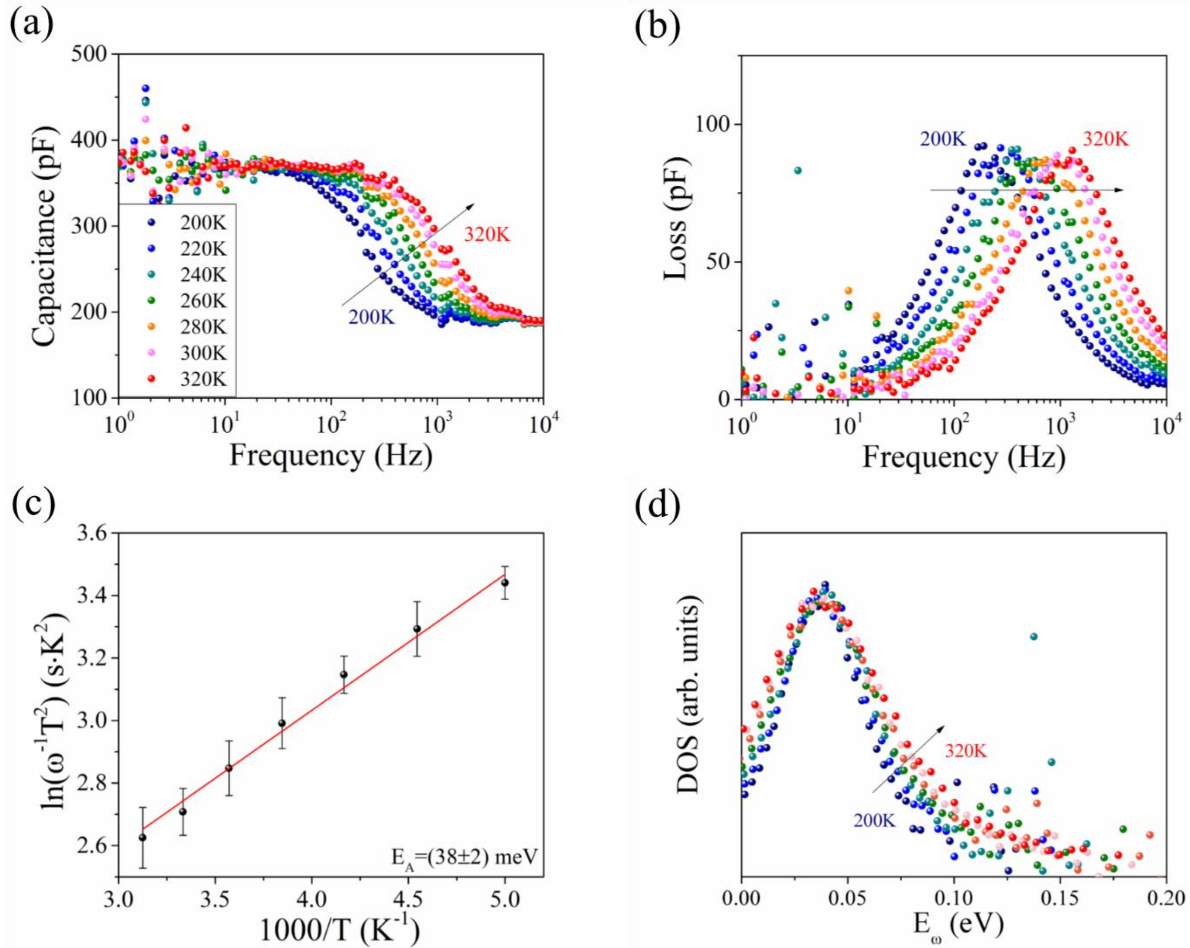

Figure 83. Thermal admittance spectroscopy characterization for TiO_2 nanobelt devices. (a) Capacitance and (b) loss spectra measured in the dark at 0 V with an AC perturbation of 50 mV. (c) Arrhenius plot of the observed

thermal emission rates as a function of temperature. The linear fit shown in red reveals the activation energy and the attempt-to-escape frequency. (d) Density of trap states (DOS) at different temperatures as a function of the demarcation energy E_{ω}.

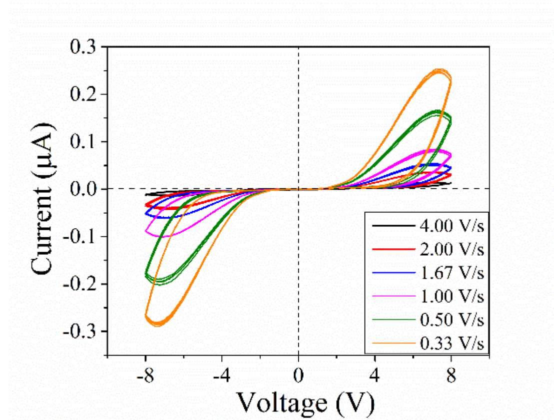

Figure 84. Sweeping rate dependent I-V performance for single TiO_2 nanobelt device on paired Au-Au electrodes.

6.4.2. Artificial nociceptor performance

6.4.2.1. Threshold dynamics

Previously, we demonstrated that the devices based on a single titanate nanobelt could be used for emulation of key features of an artificial synapse, including excitatory postsynaptic current (EPSC), paired pulse facilitation, short-term plasticity, potentiation and depression, etc.[246] As a continuation of this work, we show that such threshold switching performance in a single TiO_2 nanobelt device can be used for the emulation of artificial nociceptor devices.[293-295, 328] A nociceptor is a critical and special sensory neuron receptor whose role is to detect a variety of noxious stimuli generated by different types of stimuli such as mechanical, thermal, electrical, optical, etc. The response of the nociceptor is to rapidly transmit pain signals to the central nervous system to initiate a motor response in the human body to avoid potential damage to the organism. It not only possesses the threshold switching and relaxation dynamics that occur for neurotransmission in normal neurons when exposed to noxious stimuli, but also demonstrates its characteristic features such as "No adaptation", "Allodynia" and "Hyperalgesia" upon repeated stimuli and excessive intensive stimuli, respectively. Figure 85(a) is a schematic diagram of the neuron transmission process in a nociceptor. Various types of noxious stimuli that are detected at the periphery terminal can activate the receptor complexes via a receptor potential to initiate an action potential that will be transmitted along the length of axons to the dorsal horn of the spinal cord.[329, 330] When a defined depolarization threshold for the presynaptic membrane is reached,

voltage-gated sodium channels are activated, and an action potential is generated. Afterwards, potassium channels are opened to repolarize the presynaptic membrane, leading to the closing of the sodium channel gate. This will allow the sodium channel to return to a closed resting. An action potential travels along the axon to the presynaptic terminals, triggering the release of neurotransmitters to the postsynaptic terminal in the spinal cord through the voltage-gated calcium channels.

Similarly, in the threshold switching devices, the devices will not be switched to the conductive state if the input voltage is below a certain value (Figure 85(b)). In our TiO_2 nanobelt device, the threshold voltage determines the electric field that leads to the trapping of injected electrons. For voltages less than this value, only passive resistance occurs. Upon removal of the voltage, a relaxation process returns the TiO_2 nanobelt device to its initial state due to the spontaneously detrapping process, similar to the process when action potential returns to the resting state in the nociceptor. In the neuron transmission in a nociceptor, the triggering of the action potential is highly dependent on the intensity, duration and the number of stimuli. To simulate this property, we used different numbers of electrical pulses having various amplitudes and pulse width (Figure 85(c) and Figure 85(d)). We set the threshold current as 1×10^{-10} A, below which the stimuli is not considered as effective for the artificial nociceptor. With a single electrical pulse of 50 ms width, the device was found not to be switched on until the pulse amplitude reached 6V. Further increase of the amplitude to 10 V resulted in a larger output current (Figure 85(c)). This is consistent with the increase of response intensity corresponding to a higher concentration of Na^+ and Ca^{2+} residue leading to a larger action potential in the nociceptor. With a fixed pulse amplitude (in this case 5 V), we observed that a sufficiently long pulse width (400 ms) was necessary to reach the threshold value for the device and a further increase in pulse length led to a larger output current (Figure 86). As to the effect of pulse number, different numbers of 50 ms pulses with amplitudes of 4 V, 4.5 V and 5 V were applied. It was shown that a much higher number of pulses (20 pulses) is needed for the 4 V pulse to reach the threshold current value compared to the 5 V pulse (4 pulses) (Figure 85(d)).

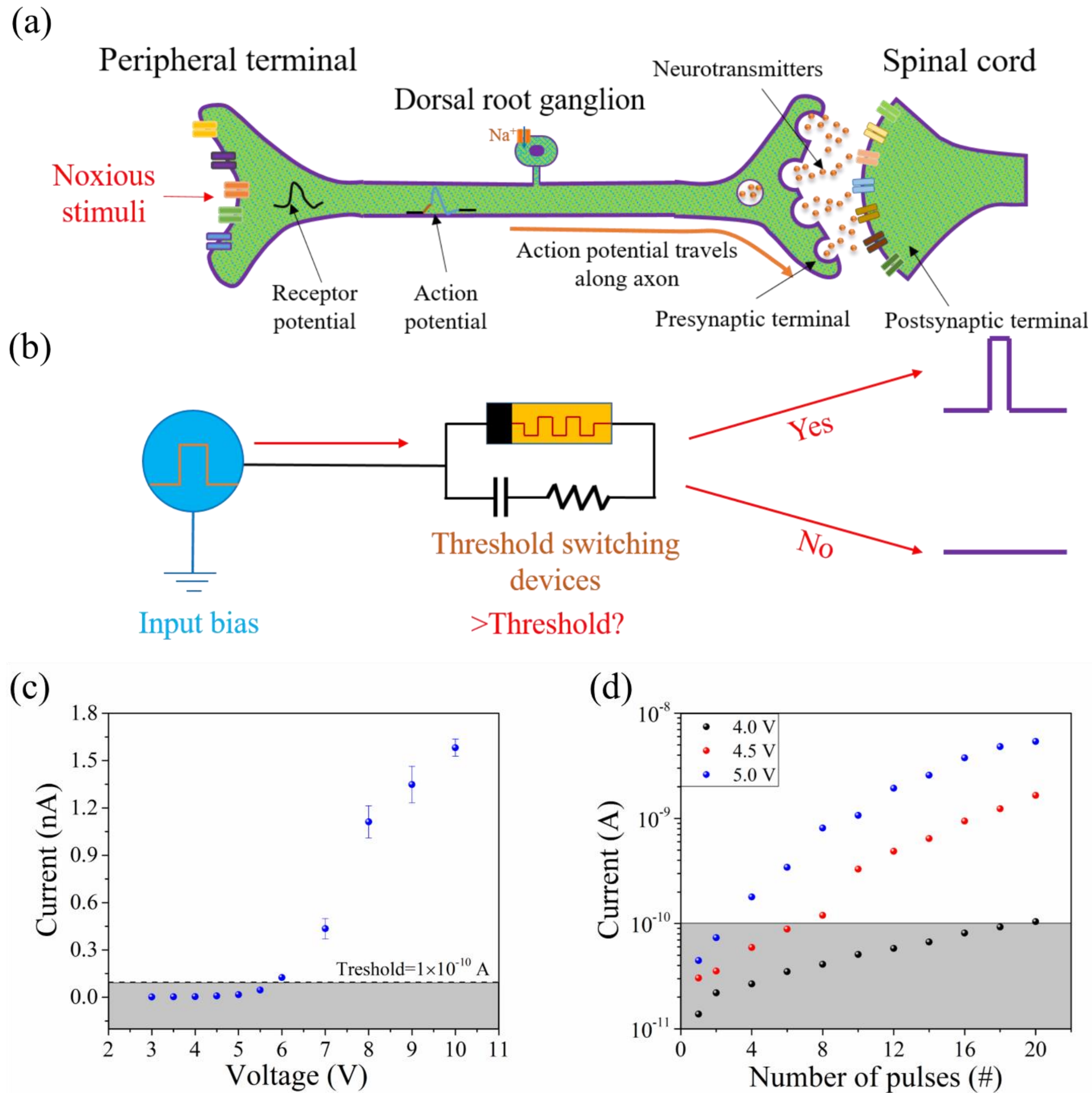

Figure 85. Threshold dynamics of the single TiO_2 nanobelt devices emulating a nociceptor. (a) Schematic of neuron transmission for a nociceptor. (b) Schematic diagram for threshold switching in the device. The threshold value will determine the output current response, below which, no or insignificant current response is detected. (c) Response of the single TiO_2 nanobelt device to single pulses with different amplitudes from 3 V to 10 V. (d) Response of the single TiO_2 nanobelt device to number of pulses at various pulse amplitude.

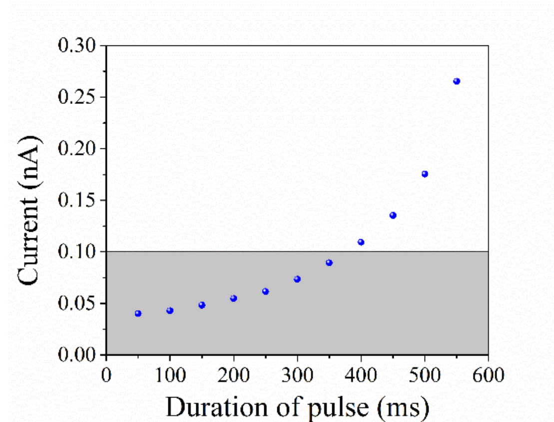

Figure 86. Response of the single TiO_2 nanobelt device to a single 5 V pulse with different durations.

6.4.2.2. Nociceptor features

Other different characteristics of a nociceptor have been evaluated for the TiO_2 nanobelt devices, as shown in Figure 87. As revealed in the charge transport mechanism study, defect centers in the TiO_2 nanobelt function as electron traps. Therefore, with the applied bias, it is expected that the increase in the conductivity of the nanobelt device upon application of pulses will gradually slows down (as more traps are filled) until it reaches saturation, indicating a dynamic equilibrium is achieved under repeated stimuli. To test this hypothesis, a number of pulses amplitudes of 10 V, 15 V and 20 V were applied to the devices and the resulting current response is shown in Figure 87(a). The generated current increases gradually after each pulse, suggesting that electrons injected by the applied pulses are gradually filling the available trap states and in turn facilitating smoother conduction for subsequent pulses. It was also observed that the current increases until saturation, indicating that the present devices can be used for the emulation of the "no adaptation" feature of nociceptors, in which the neuron will not adapt to further repeated noxious stimuli as the sensitivity of the nociceptor gradually reduces upon exposure to external stimuli for a prolonged time.[293] Pulses with higher amplitude yield a higher saturation current. Saturation may occur due to an equilibrium between the trap-filling rate determined by the electrical field and the spontaneously occurring trap-emptying rate. In this case, more trap states will be filled at equilibrium when the pulse amplitude is higher (larger electric field), such that conduction will be facilitated and the saturation current is higher.

After the stimuli are removed, the nociceptor starts the relaxation process and finally recovers its initial uninjured state. This relaxation behavior is examined in the single TiO_2 nanobelt device by applying a single pulse and recording the transient current at a reading voltage. As can be seen

in Figure 87(b), a single 50 ms 10 V pulse leads to an EPSC. The transient current recorded at a 2 V reading voltage shows relaxation to the original high-resistance state after a defined period. This response is similar to the relaxation behavior in nociceptors whereby the neuron relaxes back to the initial state upon the removal of the noxious stimuli. During this time, detrapping of electrons from defects in the TiO_2 nanobelts could recover the initial high resistance state with a Schottky barrier at the Pt/TiO_2 interface. A fit to the temperature-dependent current relaxation curves yields an activation energy of 0.27 eV.[246] This can be associated with the activation energy for the release of electrons from trap centers (Figure 87(c)).

A nociceptor will show an enhanced response at a reduced threshold after injury, known as "Allodynia" and "Hyperalgesia". This is illustrated schematically in Figure 87(d).[293-295] To demonstrate these allodynia and hyperalgesia properties, a pulse with relatively high amplitude (15 V or 20 V) is used to generate an injured condition. The measured current response at an injured condition and uninjured conditions as a function of applied voltage is shown in Figure 87(e). Before the application of the 20 V 50 ms pulse on the TiO_2 nanobelt device, the "uninjured" nociceptor device initially has low current responses. This changes significantly in the "injured" nociceptor device. The injured nociceptor devices have a higher output current response, while the threshold voltage shifts to lower values. This demonstrates that a smaller threshold voltage is required to switch on a more seriously injured device, successfully emulating the "allodynia" and "hyperalgesia" properties of a nociceptor. To reveal the variation of this response with time, a sequence of input pulses was applied at different interval times after the application of the injury pulse (Figure 87(f)). We can see that as the time interval increased, the current response to the input pulse decreases and is expected to relaxed to the initial state when the device is not damaged, revealing the relaxation and recovery property over time for the nociceptor, as previously outlined in Figures 87(b) and 87(c). Similarly, the TiO_2 nanobelt device demonstrated "allodynia" and "hyperalgesia" behavior under different time interval. This can be attributed to the fact that the original, high-amplitude pulse partly filling up the traps resulting in an increase in the conductivity of the device. Before it relaxes to the initial state due to the charge detrapping processes, further application of pulses would result in an enhanced current response as well as the threshold value being reached at lower pulse amplitude. Furthermore, detrapping of electrons after the application of the pulses is a spontaneous process resulting in a gradual relaxation over time, suggesting that "injured" nociceptor devices can eventually recover from the injured state. It is evident from the

above analysis that all five features of a nociceptor, notably "threshold", "relaxation", "no adaptation", "allodynia" and "hyperalgesia" can be realized in a single TiO_2 nanobelt device.

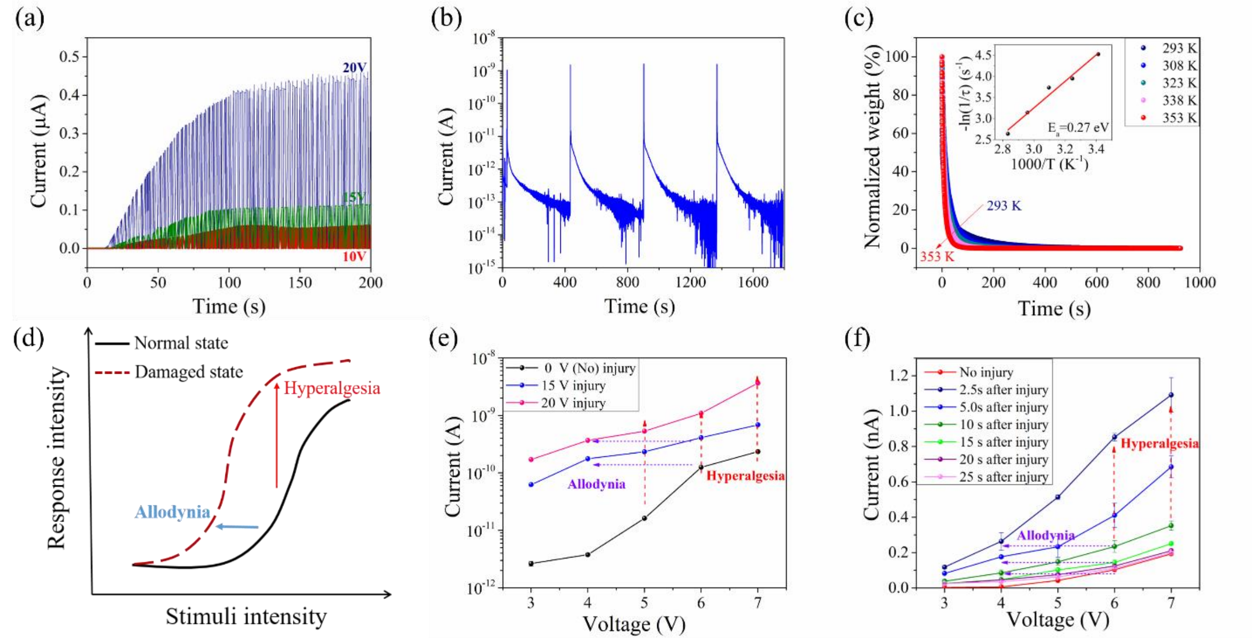

Figure 87. Nociceptive behavior. (a) No adaptation response, different voltage amplitudes for the devices to reach the saturation state. (b) Relaxation response, 50 ms 10 V EPSC transient current over 4 cycles, current is read at 2 V, (c) Temperature dependent current transient behavior read at 2 V after the 50 ms 10 V was applied, inset, activation energy from analysis of transient current at different temperatures. (d) Schematic diagram of the allodynia and hyperalgesia features with increasing stimuli intensity in normal (uninjured) and damaged (injured) conditions. (e) Current response for a train of pulses from 3 V to 7 V (50 ms) after the stimulation of high amplitude pulses (15 V and 20 V pulse, 50 ms), showing allodynia and hyperalgesia characteristics. (f) Current response to a train of pulses from 3 V to 7 V (50 ms) after the stimulation of high amplitude pulse (15 V 50 ms pulse) with different time interval, showing allodynia and hyperalgesia characteristics.

6.5. Conclusions

We have presented a unique threshold switching behavior based on a single TiO_2 nanobelt device. Current flows in the TiO_2 nanobelt device in response to a Schottky limited process at low bias to defect assisted quantum tunneling process at high bias, together with dynamic charge trapping/detrapping with shallow trap energy levels at different stages. As a result, a volatile voltage-dependent threshold switching performance is obtained and is used to mimic all key features of a nociceptor including "threshold", "relaxation", "no adaptation", "allodynia" and "hyperalgesia". These results demonstrate that a single one-dimensional metal oxide nanomaterial can be used as a building block for the realization of artificial receptor devices in place of complex

circuits, paving the way for the realization of nanowire or nanobelt based artificial neural networks via a bottom-up approach.

Chapter 7. Conclusions and Outlook

The research focused on 1D TiO_2 nanomaterial based memristive devices for the applications of non-volatile memory and artificial synapse and the corresponding switching mechanism. Three types of one dimensional TiO_2 nanomaterials, i.e., TiO_2 nanowire networks on Ti foil, TiO_2 nanorod arrays on FTO substrate and single TiO_2 nanobelt and its precursor nanobelts are studied. These studies provide a thorough study on one dimensional nanomaterial based memristor devices and its application in neuromorphic applications, paving the way for the integration of one-dimensional material for the future application via a bottom-up approach. The detailed conclusions for the research are as follows:

(1) For the study of TiO_2 nanowires on the Ti foil, a forming-free bipolar resistive switching behavior was successfully demonstrated in TiO_2 nanowire networks directly grown on Ti foil by a one-step hydrothermal process. The prepared Al/TiO_2 nanowire networks/Ti device exhibited reproducible and stable electrical performance with a high OFF/ON ratio that persisted for up to 10^4 s. The interaction of Ti foil with the TiO_2 nanowires during the synthesis process results in the generation of large density of oxygen vacancies at the Ti/TiO_2 interface, which is likely responsible for the forming-free resistive switching behavior. The low amplitude of both SET and RESET currents together with distinguishable ratios are promising for the low-power ReRAM devices. The switching mechanism of the device is proposed to be the migration of oxygen vacancies under electric field.

(2) For the study of TiO_2 nanorod arrays on the FTO substrate, an improved resistive switching performance is obtained in the devices based on TiO_2 NRAs on a FTO substrate by the introduction of a seed layer. The TiO_x seed layer on the surface of the FTO substrate enhances the vertical growth of TiO_2 NRAs normal to the substrate, leading to compact and fine nanorod morphology. Meanwhile, the concentration of oxygen vacancies of obtained NRAs is lower compared with NRAs prepared without the seed layer. The obtained Al/TiO_2 NRA/TiO_x layer/FTO devices exhibit a stable forming-free bipolar resistive switching behavior and maintain a higher ON/OFF ratio with lower switching currents under voltage sweeping over 500 cycles. The retention period is found to exceed 3×10^4 s. Switching in as-fabricated devices is controlled by a trap-mediated SCLC mechanism in which the existed oxygen vacancies in nanorods as well as in the seed layer

function as trap centers. Furthermore, a multi-level memory feature of the device, each dominated by SCLC current flow, is obtained in response to variations in the SET voltage. Such forming-free non-volatile multilevel resistive switching properties, low power operation, combined with robust endurance and retention, make Al/TiO_2 NRA/TiO_x layer/FTO devices promising candidates for future non-volatile ReRAM devices.

(3) For the study of single TiO_2 nanobelt and its precursor nanobelt during the hydrothermal process, synaptic properties of memristor devices based on single TiO_2, $H_2Ti_3O_7$ and $Na_2Ti_3O_7$ nanobelts have been investigated. Excellent synaptic functionalities including the EPSC, short-term plasticity, potentiation and depression as well as learning-forgetting responses, have been successfully demonstrated in a single nanobelt device. The gradual modulation in conductance with a large number of identical pulses is also realized. Such intriguing properties of synaptic devices based on individual $H_2Ti_3O_7$ and $Na_2Ti_3O_7$ nanobelts, similar to the TiO_2 nanobelts, not only show that these materials have a promising future in neuromorphic computing applications, but also suggest an alternative direction for material selection for synaptic functionality emulation study.

(4) To further study the charge transport mechanism of the single TiO_2 nanobelt based devices, we studied and proposed a model of a unique capacitive coupled threshold switching performance. Furthermore, the threshold switching behavior of the single TiO_2 nanobelt devices allow the emulation of several key features of artificial nociceptor devices, including “threshold”, “relaxation”, “no adaptation”, “allodynia” and “hyperalgesia” behaviors, promising for the artificial receptor systems in the artificial intelligence. In summary, one-dimensional metal oxide nanobelt devices of this type yield multifunctional nociceptor performance that is fundamental for applications in artificial intelligence systems, representing a key step in the realization of neural integrated devices via a bottom-up approach.

As to the future work, there are some experiments on one dimensional nanomaterial-based devices that can be done to improve the understanding of the resistive switching mechanism and further improve the resistive switching performance such as higher ON/OFF ratio, better endurance performance, and improved artificial synaptic behaviors. The detailed research for the future is listed as follows:

(1) It has demonstrated in all of these three types of one dimensional TiO_2 materials, the surface defects on the materials, i.e., oxygen vacancies play an important role in the charge transport behavior as well as the resistive switching mechanism. Further experiments can be done to tune the concentration of oxygen vacancies in the TiO_2 nanowires by further annealing at different temperatures and study how the change of concentration of oxygen vacancies will affect the resistive switching performance and corresponding resistive switching mechanism. Furthermore, how to characterize the surface defects in the one-dimensional TiO_2 nanomaterials and relate these defects to its electrical performance is still a challenge to overcome.
(2) For the case of memristor devices based on TiO_2 nanowire networks on Ti foil and TiO_2 nanorod arrays on FTO substrate, only Al was used for the top electrode. A list of other promising electrodes, such as Pt, Ti, Cr could be considered to give a better understanding of the charge transport behavior of the devices and potentially, improved performance.
(3) For the case of single TiO_2 nanobelt device, we studied the resistive switching performance based on same type of electrodes on both ends. Further study can be performed to change the type of electrode on one end and study the performance on dissimilar electrodes. Furthermore, whether we can achieve non-volatile memory performance with single TiO_2 nanobelt device is still an important concern. The performance on dissimilar electrodes such as Pt and Ag electrode combination could be tested.
(4) Furthermore, in the research program, we only studied the two-terminal resistive switching behavior based on TiO_2 nanowires. Further study, more specifically, on single TiO_2 nanobelt devices, can be done to fabricate the multi-terminal devices, which can be used for the emulation of heterosynaptic behavior. For example, a back gated TiO_2 nanobelt based transistor can be fabricated on the degenerated Si wafer and a third terminal can be used for the performance modulation of artificial synapse.
(5) In the research program, we only studied the performance of individual devices. However, for the study of neuromorphic computing, it is more important to integrate individual devices together for the practical application of memristive devices. This can be achieved by assembling the single TiO_2 nanobelts as well as metal nanowires into stacked nano-crossbar structure as demonstrated in Figure 88 with typical nanowire alignment methods such as fluidic flowing, electrophoretic alignment, etc. Electrodes can be fabricated

similarly on the end of the nanobelt. The resistive switching behavior would be expected to occur at the metal/semiconductor interface upon the application of electric field. This can be used for the study of neuromorphic computing application with one-dimensional nanomaterials.

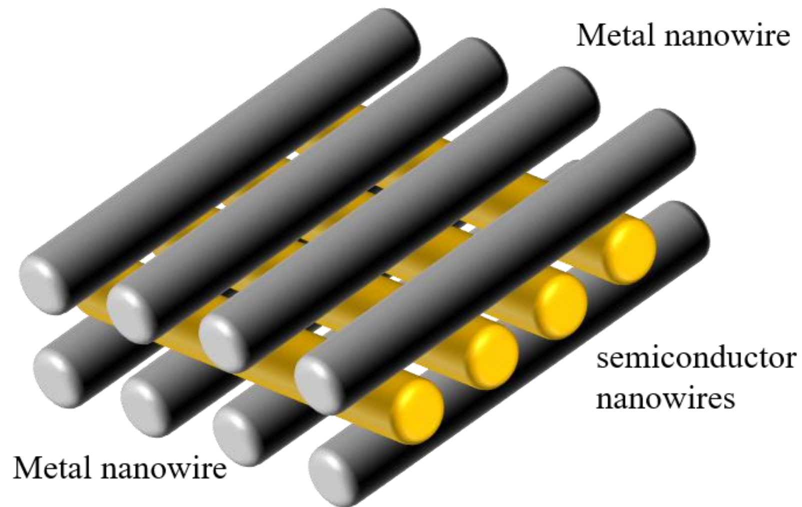

Figure 88. Proposed nanowire crossbar structure for the integration of nanowire devices for the practical application in neuromorphic computing

Letters of Copyright permission

Figure 2

This Agreement between University Avenue West 200 ("You") and Springer Nature ("Springer Nature") consists of your license details and the terms and conditions provided by Springer Nature and Copyright Clearance Center.

License Number	4593130350070
License date	May 20, 2019
Licensed Content Publisher	Springer Nature
Licensed Content Publication	Nature Materials
Licensed Content Title	A fast, high-endurance and scalable non-volatile memory device made from asymmetric Ta_2O_{5-x}/TaO_{2-x} bilayer structures
Licensed Content Author	Myoung-Jae Lee, Chang Bum Lee, Dongsoo Lee, Seung Ryul Lee, Man Chang et al.
Licensed Content Date	Jul 10, 2011
Licensed Content Volume	10
Licensed Content Issue	8
Type of Use	Thesis/Dissertation
Requestor type	academic/university or research institute
Format	print and electronic
Portion	figures/tables/illustrations
Number of figures/tables/illustrations	1
High-res required	no
Will you be translating?	no
Circulation/distribution	<501
Author of this Springer Nature content	no
Title	One-dimensional titanium dioxide nanomaterial based memristive device and its neuromorphic computing applications
Institution name	University of Waterloo
Expected presentation date	Jul 2019
Portions	Figure 1(b) on Page 2
Requestor Location	University Avenue West 200 University Avenue West 200 Waterloo, ON N2L 3G1 Canada Attn: University Avenue West 200
Total	0.00 CAD

Figure 3

This Agreement between University Avenue West 200 ("You") and Springer Nature ("Springer Nature") consists of your license details and the terms and conditions provided by Springer Nature and Copyright Clearance Center.

License Number	4593130565255
License date	May 20, 2019
Licensed Content Publisher	Springer Nature
Licensed Content Publication	Nature Materials
Licensed Content Title	Nanoionics-based resistive switching memories
Licensed Content Author	Rainer Waser, Masakazu Aono
Licensed Content Date	Nov 1, 2007
Licensed Content Volume	6
Licensed Content Issue	11
Type of Use	Thesis/Dissertation
Requestor type	academic/university or research institute
Format	print and electronic
Portion	figures/tables/illustrations
Number of figures/tables/illustrations	1
High-res required	no
Will you be translating?	no
Circulation/distribution	<501
Author of this Springer Nature content	no
Title	One-dimensional titanium dioxide nanomaterial based memristive device and its neuromorphic computing applications
Institution name	University of Waterloo
Expected presentation date	Jul 2019
Portions	Figure 1 on Page 2
Requestor Location	University Avenue West 200 University Avenue West 200 Waterloo, ON N2L 3G1 Canada Attn: University Avenue West 200
Total	0.00 CAD

Figure 4

This Agreement between University Avenue West 200 ("You") and John Wiley and Sons ("John Wiley and Sons") consists of your license details and the terms and conditions provided by John Wiley and Sons and Copyright Clearance Center.

License Number	4593131096280
License date	May 20, 2019
Licensed Content Publisher	John Wiley and Sons
Licensed Content Publication	Advanced Functional Materials
Licensed Content Title	Physics of the Switching Kinetics in Resistive Memories
Licensed Content Author	Stephan Menzel, Ulrich Böttger, Martin Wimmer, et al
Licensed Content Date	Jun 18, 2015
Licensed Content Volume	25
Licensed Content Issue	40
Licensed Content Pages	20
Type of use	Dissertation/Thesis
Requestor type	University/Academic
Format	Print and electronic
Portion	Figure/table
Number of figures/tables	2
Original Wiley figure/table number(s)	Figure 1
Will you be translating?	
Title of your thesis / dissertation	One-dimensional titanium dioxide nanomaterial based memristive device and its neuromorphic computing applications
Expected completion date	Jul 2019
Expected size (number of pages)	1
Requestor Location	University Avenue West 200 University Avenue West 200 Waterloo, ON N2L 3G1 Canada Attn: University Avenue West 200
Publisher Tax ID	EU826007151
Total	0.00 CAD

Figure 5

This Agreement between University Avenue West 200 ("You") and John Wiley and Sons ("John Wiley and Sons") consists of your license details and the terms and conditions provided by John Wiley and Sons and Copyright Clearance Center.

License Number	4593140107757
License date	May 20, 2019
Licensed Content Publisher	John Wiley and Sons
Licensed Content Publication	Advanced Materials
Licensed Content Title	In Situ Observation of Voltage-Induced Multilevel Resistive Switching in Solid Electrolyte Memory
Licensed Content Author	Sang-Jun Choi, Gyeong-Su Park, Ki-Hong Kim, et al
Licensed Content Date	Jun 14, 2011
Licensed Content Volume	23
Licensed Content Issue	29
Licensed Content Pages	6
Type of use	Dissertation/Thesis
Requestor type	University/Academic
Format	Print and electronic
Portion	Figure/table
Number of figures/tables	1
Original Wiley figure/table number(s)	Figure 1
Will you be translating?	No
Title of your thesis / dissertation	One-dimensional titanium dioxide nanomaterial based memristive device and its neuromorphic computing applications
Expected completion date	Jul 2019
Expected size (number of pages)	1
Requestor Location	University Avenue West 200 University Avenue West 200 Waterloo, ON N2L 3G1 Canada Attn: University Avenue West 200
Publisher Tax ID	EU826007151
Total	0.00 CAD

Figure 6

This Agreement between University Avenue West 200 ("You") and Springer Nature ("Springer Nature") consists of your license details and the terms and conditions provided by Springer Nature and Copyright Clearance Center.

License Number	4593170417427
License date	May 20, 2019
Licensed Content Publisher	Springer Nature
Licensed Content Publication	Nature Communications
Licensed Content Title	Observation of conducting filament growth in nanoscale resistive memories
Licensed Content Author	Yuchao Yang, Peng Gao, Siddharth Gaba, Ting Chang, Xiaoqing Pan et al.
Licensed Content Date	Mar 13, 2012
Licensed Content Volume	3
Type of Use	Thesis/Dissertation
Requestor type	academic/university or research institute
Format	print and electronic
Portion	figures/tables/illustrations
Number of figures/tables/illustrations	1
High-res required	no
Will you be translating?	no
Circulation/distribution	<501
Author of this Springer Nature content	no
Title	One-dimensional titanium dioxide nanomaterial based memristive device and its neuromorphic computing applications
Institution name	University of Waterloo
Expected presentation date	Jul 2019
Portions	Figure 5
Requestor Location	University Avenue West 200 University Avenue West 200 Waterloo, ON N2L 3G1 Canada Attn: University Avenue West 200
Total	0.00 CAD

Figure 8

This Agreement between University Avenue West 200 ("You") and Springer Nature ("Springer Nature") consists of your license details and the terms and conditions provided by Springer Nature and Copyright Clearance Center.

License Number	4593170581290
License date	May 20, 2019
Licensed Content Publisher	Springer Nature
Licensed Content Publication	Nature Nanotechnology
Licensed Content Title	Atomic structure of conducting nanofilaments in TiO2 resistive switching memory
Licensed Content Author	Deok-Hwang Kwon, Kyung Min Kim, Jae Hyuck Jang, Jong Myeong Jeon, Min Hwan Lee et al.
Licensed Content Date	Jan 17, 2010
Licensed Content Volume	5
Licensed Content Issue	2
Type of Use	Thesis/Dissertation
Requestor type	academic/university or research institute
Format	print and electronic
Portion	figures/tables/illustrations
Number of figures/tables/illustrations	1
High-res required	no
Will you be translating?	no
Circulation/distribution	<501
Author of this Springer Nature content	no
Title	One-dimensional titanium dioxide nanomaterial based memristive device and its neuromorphic computing applications
Institution name	University of Waterloo
Expected presentation date	Jul 2019
Portions	Figure 5
Requestor Location	University Avenue West 200 University Avenue West 200 Waterloo, ON N2L 3G1 Canada Attn: University Avenue West 200
Total	0.00 CAD

Figure 9

This Agreement between University Avenue West 200 ("You") and Springer Nature ("Springer Nature") consists of your license details and the terms and conditions provided by Springer Nature and Copyright Clearance Center.

License Number	4593170716912
License date	May 20, 2019
Licensed Content Publisher	Springer Nature
Licensed Content Publication	Nature Communications
Licensed Content Title	In situ observation of filamentary conducting channels in an asymmetric Ta_2O_{5-x}/TaO_{2-x} bilayer structure
Licensed Content Author	Gyeong-Su Park, Young Bae Kim, Seong Yong Park, Xiang Shu Li, Sung Heo et al.
Licensed Content Date	Sep 6, 2013
Licensed Content Volume	4
Type of Use	Thesis/Dissertation
Requestor type	academic/university or research institute
Format	print and electronic
Portion	figures/tables/illustrations
Number of figures/tables/illustrations	1
High-res required	no
Will you be translating?	no
Circulation/distribution	<501
Author of this Springer Nature content	no
Title	One-dimensional titanium dioxide nanomaterial based memristive device and its neuromorphic computing applications
Institution name	University of Waterloo
Expected presentation date	Jul 2019
Portions	Figure 4
Requestor Location	University Avenue West 200 University Avenue West 200 Waterloo, ON N2L 3G1 Canada Attn: University Avenue West 200
Total	0.00 CAD

Figure 10

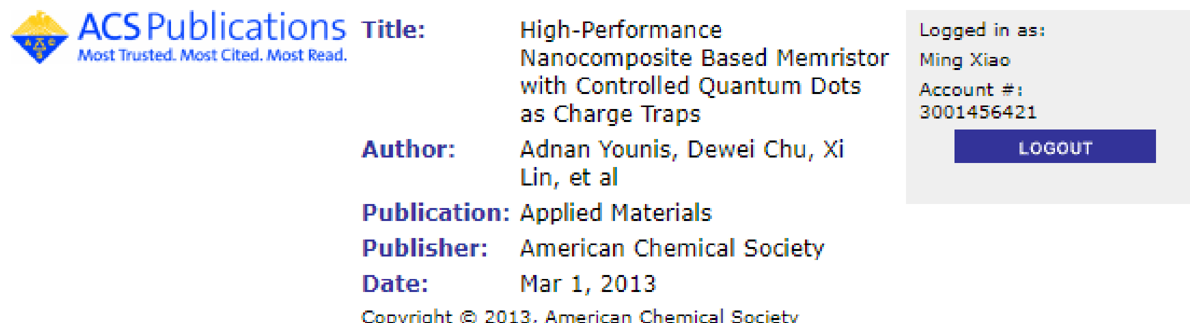
ACS Publications
Most Trusted. Most Cited. Most Read.

Title: High-Performance Nanocomposite Based Memristor with Controlled Quantum Dots as Charge Traps
Author: Adnan Younis, Dewei Chu, Xi Lin, et al
Publication: Applied Materials
Publisher: American Chemical Society
Date: Mar 1, 2013

Copyright © 2013, American Chemical Society

Logged in as:
Ming Xiao
Account #:
3001456421
LOGOUT

PERMISSION/LICENSE IS GRANTED FOR YOUR ORDER AT NO CHARGE

This type of permission/license, instead of the standard Terms & Conditions, is sent to you because no fee is being charged for your order. Please note the following:

- Permission is granted for your request in both print and electronic formats, and translations.
- If figures and/or tables were requested, they may be adapted or used in part.
- Please print this page for your records and send a copy of it to your publisher/graduate school.
- Appropriate credit for the requested material should be given as follows: "Reprinted (adapted) with permission from (COMPLETE REFERENCE CITATION). Copyright (YEAR) American Chemical Society." Insert appropriate information in place of the capitalized words.
- One-time permission is granted only for the use specified in your request. No additional uses are granted (such as derivative works or other editions). For any other uses, please submit a new request.

Figure 12

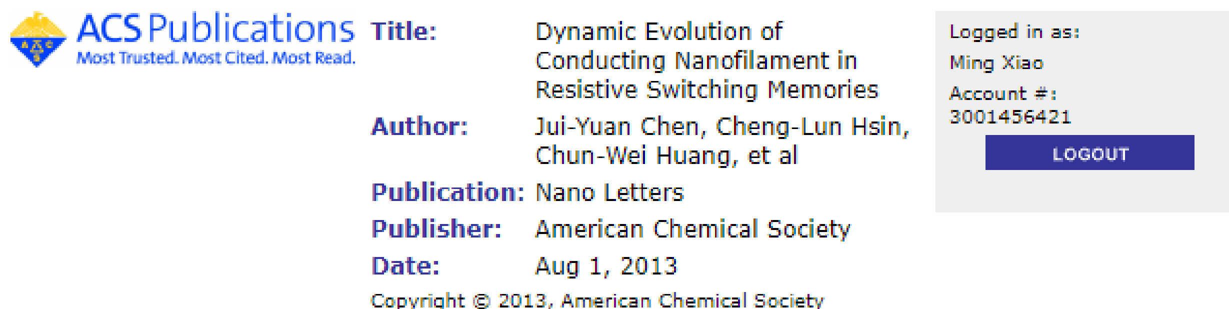

PERMISSION/LICENSE IS GRANTED FOR YOUR ORDER AT NO CHARGE

This type of permission/license, instead of the standard Terms & Conditions, is sent to you because no fee is being charged for your order. Please note the following:

- Permission is granted for your request in both print and electronic formats, and translations.
- If figures and/or tables were requested, they may be adapted or used in part.
- Please print this page for your records and send a copy of it to your publisher/graduate school.
- Appropriate credit for the requested material should be given as follows: "Reprinted (adapted) with permission from (COMPLETE REFERENCE CITATION). Copyright (YEAR) American Chemical Society." Insert appropriate information in place of the capitalized words.
- One-time permission is granted only for the use specified in your request. No additional uses are granted (such as derivative works or other editions). For any other uses, please submit a new request.

Figure 14

This Agreement between University Avenue West 200 ("You") and Springer Nature ("Springer Nature") consists of your license details and the terms and conditions provided by Springer Nature and Copyright Clearance Center.

License Number	4593171191567
License date	May 20, 2019
Licensed Content Publisher	Springer Nature
Licensed Content Publication	Nature
Licensed Content Title	‘Memristive’ switches enable ‘stateful’ logic operations via material implication
Licensed Content Author	Julien Borghetti, Gregory S. Snider, Philip J. Kuekes, J. Joshua Yang, Duncan R. Stewart et al.
Licensed Content Date	Apr 8, 2010
Licensed Content Volume	464
Licensed Content Issue	7290
Type of Use	Thesis/Dissertation
Requestor type	academic/university or research institute
Format	print and electronic
Portion	figures/tables/illustrations
Number of figures/tables/illustrations	1
High-res required	no
Will you be translating?	no
Circulation/distribution	<501
Author of this Springer Nature content	no
Title	One-dimensional titanium dioxide nanomaterial based memristive device and its neuromorphic computing applications
Institution name	University of Waterloo
Expected presentation date	Jul 2019
Portions	Figure 2
Requestor Location	University Avenue West 200 University Avenue West 200 Waterloo, ON N2L 3G1 Canada Attn: University Avenue West 200
Total	0.00 CAD

Figure 16

This Agreement between University Avenue West 200 ("You") and Springer Nature ("Springer Nature") consists of your license details and the terms and conditions provided by Springer Nature and Copyright Clearance Center.

License Number	4593171367983
License date	May 20, 2019
Licensed Content Publisher	Springer Nature
Licensed Content Publication	Nature Materials
Licensed Content Title	Short-term plasticity and long-term potentiation mimicked in single inorganic synapses
Licensed Content Author	Takeo Ohno, Tsuyoshi Hasegawa, Tohru Tsuruoka, Kazuya Terabe, James K. Gimzewski et al.
Licensed Content Date	Jun 26, 2011
Licensed Content Volume	10
Licensed Content Issue	8
Type of Use	Thesis/Dissertation
Requestor type	academic/university or research institute
Format	print and electronic
Portion	figures/tables/illustrations
Number of figures/tables/illustrations	1
High-res required	no
Will you be translating?	no
Circulation/distribution	<501
Author of this Springer Nature content	no
Title	One-dimensional titanium dioxide nanomaterial based memristive device and its neuromorphic computing applications
Institution name	University of Waterloo
Expected presentation date	Jul 2019
Portions	Figure 1
Requestor Location	University Avenue West 200 University Avenue West 200 Waterloo, ON N2L 3G1 Canada Attn: University Avenue West 200
Total	0.00 CAD

Figure 17 (a-c)

This Agreement between University Avenue West 200 ("You") and John Wiley and Sons ("John Wiley and Sons") consists of your license details and the terms and conditions provided by John Wiley and Sons and Copyright Clearance Center.

License Number	4593180013563
License date	May 20, 2019
Licensed Content Publisher	John Wiley and Sons
Licensed Content Publication	Advanced Materials
Licensed Content Title	Memristive Physically Evolving Networks Enabling the Emulation of Heterosynaptic Plasticity
Licensed Content Author	Yuchao Yang, Bing Chen, Wei D. Lu
Licensed Content Date	Oct 20, 2015
Licensed Content Volume	27
Licensed Content Issue	47
Licensed Content Pages	8
Type of use	Dissertation/Thesis
Requestor type	University/Academic
Format	Print and electronic
Portion	Figure/table
Number of figures/tables	1
Original Wiley figure/table number(s)	Figure 2
Will you be translating?	No
Title of your thesis / dissertation	One-dimensional titanium dioxide nanomaterial based memristive device and its neuromorphic computing applications
Expected completion date	Jul 2019
Expected size (number of pages)	1
Requestor Location	University Avenue West 200 University Avenue West 200 Waterloo, ON N2L 3G1 Canada Attn: University Avenue West 200
Publisher Tax ID	EU826007151
Total	0.00 CAD

Figure 17(d)

This Agreement between University Avenue West 200 ("You") and John Wiley and Sons ("John Wiley and Sons") consists of your license details and the terms and conditions provided by John Wiley and Sons and Copyright Clearance Center.

License Number	4593180146842
License date	May 20, 2019
Licensed Content Publisher	John Wiley and Sons
Licensed Content Publication	Advanced Electronic Materials
Licensed Content Title	Multifunctional Nanoionic Devices Enabling Simultaneous Heterosynaptic Plasticity and Efficient In-Memory Boolean Logic
Licensed Content Author	Yuchao Yang, Minghui Yin, Zhizhen Yu, et al
Licensed Content Date	May 11, 2017
Licensed Content Volume	3
Licensed Content Issue	7
Licensed Content Pages	8
Type of use	Dissertation/Thesis
Requestor type	University/Academic
Format	Print and electronic
Portion	Figure/table
Number of figures/tables	1
Original Wiley figure/table number(s)	Figure 1
Will you be translating?	No
Title of your thesis / dissertation	One-dimensional titanium dioxide nanomaterial based memristive device and its neuromorphic computing applications
Expected completion date	Jul 2019
Expected size (number of pages)	1
Requestor Location	University Avenue West 200 University Avenue West 200 Waterloo, ON N2L 3G1 Canada Attn: University Avenue West 200
Publisher Tax ID	EU826007151
Total	0.00 CAD

Figure 17(e-f)

This Agreement between University Avenue West 200 ("You") and Springer Nature ("Springer Nature") consists of your license details and the terms and conditions provided by Springer Nature and Copyright Clearance Center.

License Number	4595970224586
License date	May 25, 2019
Licensed Content Publisher	Springer Nature
Licensed Content Publication	Nature Materials
Licensed Content Title	Ionic modulation and ionic coupling effects in MoS2 devices for neuromorphic computing
Licensed Content Author	Xiaojian Zhu et al
Licensed Content Date	Dec 17, 2018
Type of Use	Thesis/Dissertation
Requestor type	academic/university or research institute
Format	print and electronic
Portion	figures/tables/illustrations
Number of figures/tables/illustrations	2
High-res required	no
Will you be translating?	no
Circulation/distribution	<501
Author of this Springer Nature content	no
Title	One-dimensional titanium dioxide nanomaterial based memristive device and its neuromorphic computing applications
Institution name	University of Waterloo
Expected presentation date	Jul 2019
Portions	Figures 4 and 5
Requestor Location	University Avenue West 200 University Avenue West 200 Waterloo, ON N2L 3G1 Canada Attn: University Avenue West 200
Total	0.00 CAD

Figure 17(g)

This Agreement between University Avenue West 200 ("You") and Springer Nature ("Springer Nature") consists of your license details and the terms and conditions provided by Springer Nature and Copyright Clearance Center.

License Number	4593180396036
License date	May 20, 2019
Licensed Content Publisher	Springer Nature
Licensed Content Publication	Nature
Licensed Content Title	Multi-terminal memtransistors from polycrystalline monolayer molybdenum disulfide
Licensed Content Author	Vinod K. Sangwan, Hong-Sub Lee, Hadallia Bergeron, Itamar Balla, Megan E. Beck et al.
Licensed Content Date	Feb 21, 2018
Licensed Content Volume	554
Licensed Content Issue	7693
Type of Use	Thesis/Dissertation
Requestor type	academic/university or research institute
Format	print and electronic
Portion	figures/tables/illustrations
Number of figures/tables/illustrations	1
High-res required	no
Will you be translating?	no
Circulation/distribution	<501
Author of this Springer Nature content	no
Title	One-dimensional titanium dioxide nanomaterial based memristive device and its neuromorphic computing applications
Institution name	University of Waterloo
Expected presentation date	Jul 2019
Portions	Figure 4
Requestor Location	University Avenue West 200 University Avenue West 200 Waterloo, ON N2L 3G1 Canada Attn: University Avenue West 200
Total	0.00 CAD

Figure 18

This Agreement between University Avenue West 200 ("You") and Springer Nature ("Springer Nature") consists of your license details and the terms and conditions provided by Springer Nature and Copyright Clearance Center.

License Number	4593180551632
License date	May 20, 2019
Licensed Content Publisher	Springer Nature
Licensed Content Publication	Nature Nanotechnology
Licensed Content Title	Sparse coding with memristor networks
Licensed Content Author	Patrick M. Sheridan, Fuxi Cai, Chao Du, Wen Ma, Zhengya Zhang et al.
Licensed Content Date	May 22, 2017
Licensed Content Volume	12
Licensed Content Issue	8
Type of Use	Thesis/Dissertation
Requestor type	academic/university or research institute
Format	print and electronic
Portion	figures/tables/illustrations
Number of figures/tables/illustrations	1
High-res required	no
Will you be translating?	no
Circulation/distribution	<501
Author of this Springer Nature content	no
Title	One-dimensional titanium dioxide nanomaterial based memristive device and its neuromorphic computing applications
Institution name	University of Waterloo
Expected presentation date	Jul 2019
Portions	Figure 4
Requestor Location	University Avenue West 200 University Avenue West 200 Waterloo, ON N2L 3G1 Canada Attn: University Avenue West 200
Total	0.00 CAD

Figure 19

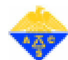

Title: Resistive Switching Multistate Nonvolatile Memory Effects in a Single Cobalt Oxide Nanowire

Author: Kazuki Nagashima, Takeshi Yanagida, Keisuke Oka, et al

Publication: Nano Letters

Publisher: American Chemical Society

Date: Apr 1, 2010

Copyright © 2010, American Chemical Society

Logged in as:
Ming Xiao
Account #:
3001456421
LOGOUT

PERMISSION/LICENSE IS GRANTED FOR YOUR ORDER AT NO CHARGE

This type of permission/license, instead of the standard Terms & Conditions, is sent to you because no fee is being charged for your order. Please note the following:

- Permission is granted for your request in both print and electronic formats, and translations.
- If figures and/or tables were requested, they may be adapted or used in part.
- Please print this page for your records and send a copy of it to your publisher/graduate school.
- Appropriate credit for the requested material should be given as follows: "Reprinted (adapted) with permission from (COMPLETE REFERENCE CITATION). Copyright (YEAR) American Chemical Society." Insert appropriate information in place of the capitalized words.
- One-time permission is granted only for the use specified in your request. No additional uses are granted (such as derivative works or other editions). For any other uses, please submit a new request.

Figure 20

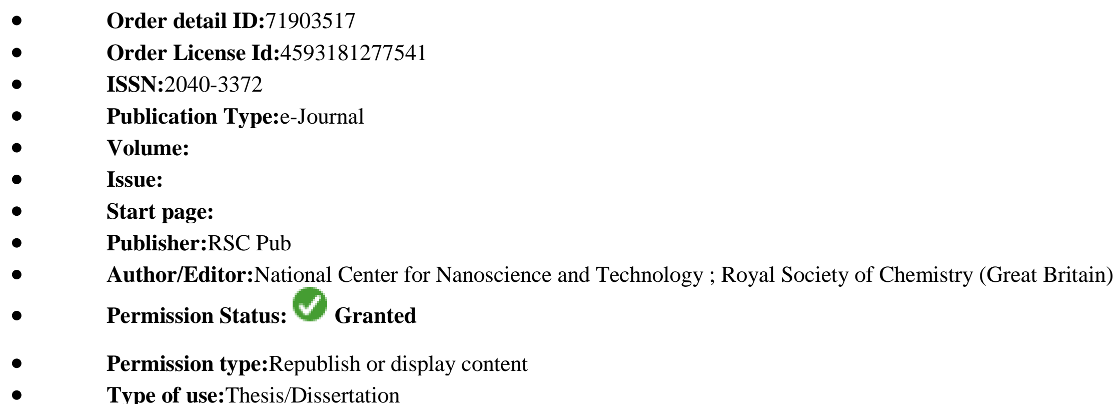

- **Order detail ID:**71903517
- **Order License Id:**4593181277541
- **ISSN:**2040-3372
- **Publication Type:**e-Journal
- **Volume:**
- **Issue:**
- **Start page:**
- **Publisher:**RSC Pub
- **Author/Editor:**National Center for Nanoscience and Technology ; Royal Society of Chemistry (Great Britain)
- **Permission Status:** **Granted**
- **Permission type:**Republish or display content
- **Type of use:**Thesis/Dissertation

○

Requestor type	Academic institution
Format	Print, Electronic
Portion	image/photo
Number of images/photos requested	1
The requesting person/organization	Ming Xiao
Title or numeric reference of the portion(s)	Figure 4
Title of the article or chapter the portion is from	High performance bipolar resistive switching memory devices based on Zn2SnO4 nanowires
Editor of portion(s)	N/A
Author of portion(s)	Dong, H. Zhang, X. Zhao, D. Niu, Z. Zeng, Q. Li, J. Cai, L. Wang, Y. Zhou, W. Gao, M. Xie, S.
Volume of serial or monograph	N/A
Page range of portion	Page 3
Publication date of portion	29 Feb 2012
Rights for	Main product
Duration of use	Current edition and up to 5 years
Creation of copies for the disabled	no
With minor editing privileges	no
For distribution to	Canada
In the following language(s)	Original language of publication
With incidental promotional use	no
Lifetime unit quantity of new product	Up to 499
Title	One-dimensional titanium dioxide nanomaterial based memristive device and its neuromorphic computing applications
Institution name	University of Waterloo
Expected presentation date	Jul 2019

Figure 21

Title: Bipolar Resistive Switching of Single Gold-in-Ga_2O_3 Nanowire

Author: Chia-Wei Hsu, Li-Jen Chou

Publication: Nano Letters

Publisher: American Chemical Society

Date: Aug 1, 2012

Copyright © 2012, American Chemical Society

Logged in as:
Ming Xiao
Account #:
3001456421
LOGOUT

PERMISSION/LICENSE IS GRANTED FOR YOUR ORDER AT NO CHARGE

This type of permission/license, instead of the standard Terms & Conditions, is sent to you because no fee is being charged for your order. Please note the following:

- Permission is granted for your request in both print and electronic formats, and translations.
- If figures and/or tables were requested, they may be adapted or used in part.
- Please print this page for your records and send a copy of it to your publisher/graduate school.
- Appropriate credit for the requested material should be given as follows: "Reprinted (adapted) with permission from (COMPLETE REFERENCE CITATION). Copyright (YEAR) American Chemical Society." Insert appropriate information in place of the capitalized words.
- One-time permission is granted only for the use specified in your request. No additional uses are granted (such as derivative works or other editions). For any other uses, please submit a new request.

Figure 22

This Agreement between University Avenue West 200 ("You") and John Wiley and Sons ("John Wiley and Sons") consists of your license details and the terms and conditions provided by John Wiley and Sons and Copyright Clearance Center.

License Number	4593190136689
License date	May 20, 2019
Licensed Content Publisher	John Wiley and Sons
Licensed Content Publication	Advanced Functional Materials
Licensed Content Title	Plasmonic-Radiation-Enhanced Metal Oxide Nanowire Heterojunctions for Controllable Multilevel Memory
Licensed Content Author	Luchan Lin, Lei Liu, Kevin Musselman, et al
Licensed Content Date	Jul 4, 2016
Licensed Content Volume	26
Licensed Content Issue	33
Licensed Content Pages	8
Type of use	Dissertation/Thesis
Requestor type	University/Academic
Format	Print and electronic
Portion	Figure/table
Number of figures/tables	1
Original Wiley figure/table number(s)	Figure 1 and Figure 4
Will you be translating?	No
Title of your thesis / dissertation	One-dimensional titanium dioxide nanomaterial based memristive device and its neuromorphic computing applications
Expected completion date	Jul 2019
Expected size (number of pages)	1
Requestor Location	University Avenue West 200 University Avenue West 200 Waterloo, ON N2L 3G1 Canada Attn: University Avenue West 200
Publisher Tax ID	EU826007151
Total	0.00 CAD

Figure 23(a)

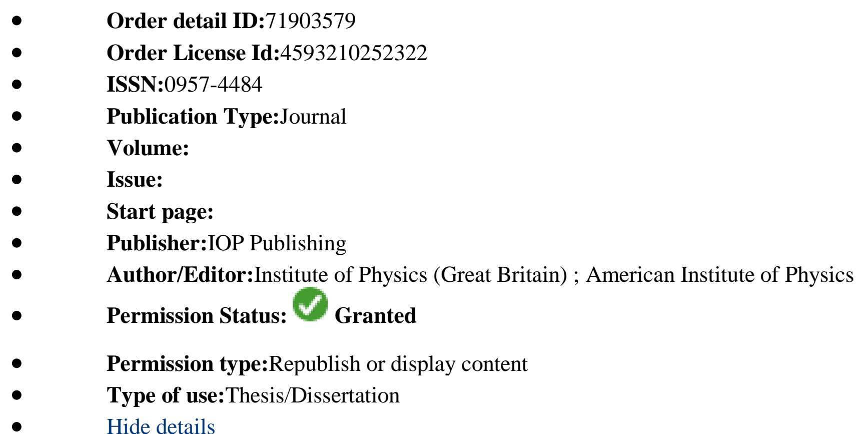

- **Order detail ID:**71903579
- **Order License Id:**4593210252322
- **ISSN:**0957-4484
- **Publication Type:**Journal
- **Volume:**
- **Issue:**
- **Start page:**
- **Publisher:**IOP Publishing
- **Author/Editor:**Institute of Physics (Great Britain) ; American Institute of Physics
- **Permission Status:** **Granted**
- **Permission type:**Republish or display content
- **Type of use:**Thesis/Dissertation
- Hide details

○

Requestor type	Academic institution
Format	Print, Electronic
Portion	image/photo
Number of images/photos requested	1
The requesting person/organization	Ming Xiao/University of Waterloo
Title or numeric reference of the portion(s)	Figure 2
Title of the article or chapter the portion is from	Oriented single crystalline titanium dioxide nanowires
Editor of portion(s)	N/A
Author of portion(s)	Liu B, Boercker J E, Aydil E S
Volume of serial or monograph	N/A
Page range of portion	Page 4
Publication date of portion	25 Nov 2008
Rights for	Main product
Duration of use	Current edition and up to 5 years
Creation of copies for the disabled	no
With minor editing privileges	no
For distribution to	Canada
In the following language(s)	Original language of publication
With incidental promotional use	no
Lifetime unit quantity of new product	Up to 499
Title	One-dimensional titanium dioxide nanomaterial based memristive device and its neuromorphic computing applications
Institution name	University of Waterloo
Expected presentation date	Jul 2019

Figure 23(b)

This Agreement between University Avenue West 200 ("You") and AIP Publishing ("AIP Publishing") consists of your license details and the terms and conditions provided by AIP Publishing and Copyright Clearance Center.

License Number	4593210340491
License date	May 20, 2019
Licensed Content Publisher	AIP Publishing
Licensed Content Publication	Applied Physics Letters
Licensed Content Title	Hydrothermal synthesis of ordered single-crystalline rutile TiO2 nanorod arrays on different substrates
Licensed Content Author	Hong-En Wang, Zhenhua Chen, Yu Hang Leung, et al
Licensed Content Date	Jun 28, 2010
Licensed Content Volume	96
Licensed Content Issue	26
Type of Use	Thesis/Dissertation
Requestor type	University or Educational Institution
Format	Print and electronic
Portion	Figure/Table
Number of figures/tables	1
Title of your thesis / dissertation	One-dimensional titanium dioxide nanomaterial based memristive device and its neuromorphic computing applications
Expected completion date	Jul 2019
Estimated size (number of pages)	1
Requestor Location	University Avenue West 200 University Avenue West 200 Waterloo, ON N2L 3G1 Canada Attn: University Avenue West 200
Total	0.00 CAD

Figure 23(c)

This Agreement between University Avenue West 200 ("You") and John Wiley and Sons ("John Wiley and Sons") consists of your license details and the terms and conditions provided by John Wiley and Sons and Copyright Clearance Center.

License Number	4593210599811
License date	May 20, 2019
Licensed Content Publisher	John Wiley and Sons
Licensed Content Publication	Chemistry - A European Journal
Licensed Content Title	A General Approach for the Growth of Metal Oxide Nanorod Arrays on Graphene Sheets and Their Applications
Licensed Content Author	Rujia Zou, Zhenyu Zhang, Li Yu, et al
Licensed Content Date	Oct 31, 2011
Licensed Content Volume	17
Licensed Content Issue	49
Licensed Content Pages	6
Type of use	Dissertation/Thesis
Requestor type	University/Academic
Format	Print and electronic
Portion	Figure/table
Number of figures/tables	1
Original Wiley figure/table number(s)	Figure 1
Will you be translating?	No
Title of your thesis / dissertation	One-dimensional titanium dioxide nanomaterial based memristive device and its neuromorphic computing applications
Expected completion date	Jul 2019
Expected size (number of pages)	1
Requestor Location	University Avenue West 200 University Avenue West 200 Waterloo, ON N2L 3G1 Canada Attn: University Avenue West 200
Publisher Tax ID	EU826007151
Total	0.00 CAD

Figure 23(d)

Title:	Growth of Oriented Single-Crystalline Rutile TiO2 Nanorods on Transparent Conducting Substrates for Dye-Sensitized Solar Cells
Author:	Bin Liu, Eray S. Aydil
Publication:	Journal of the American Chemical Society
Publisher:	American Chemical Society
Date:	Mar 1, 2009

Copyright © 2009, American Chemical Society

Logged in as:
Ming Xiao
Account #:
3001456421
LOGOUT

PERMISSION/LICENSE IS GRANTED FOR YOUR ORDER AT NO CHARGE

This type of permission/license, instead of the standard Terms & Conditions, is sent to you because no fee is being charged for your order. Please note the following:

- Permission is granted for your request in both print and electronic formats, and translations.
- If figures and/or tables were requested, they may be adapted or used in part.
- Please print this page for your records and send a copy of it to your publisher/graduate school.
- Appropriate credit for the requested material should be given as follows: "Reprinted (adapted) with permission from (COMPLETE REFERENCE CITATION). Copyright (YEAR) American Chemical Society." Insert appropriate information in place of the capitalized words.
- One-time permission is granted only for the use specified in your request. No additional uses are granted (such as derivative works or other editions). For any other uses, please submit a new request.

Reference

1. Chang, S. H.; Lee, S. B.; Jeon, D. Y.; Park, S. J.; Kim, G. T.; Yang, S. M.; Chae, S. C.; Yoo, H. K.; Kang, B. S.; Lee, M. J.; Noh, T. W., Oxide Double-Layer Nanocrossbar for Ultrahigh-Density Bipolar Resistive Memory. *Advanced Materials* **2011,** *23* (35), 4063-4067.
2. Lee, D.; Park, J.; Park, J.; Woo, J.; Cha, E.; Lee, S.; Moon, K.; Song, J.; Koo, Y.; Hwang, H., Structurally Engineered Stackable and Scalable 3D Titanium-Oxide Switching Devices for High-Density Nanoscale Memory. *Advanced Materials* **2015,** *27* (1), 59-64.
3. Hota, M. K.; Hedhili, M. N.; Wang, Q. X.; Melnikov, V. A.; Mohammed, O. F.; Alshareef, H. N., Nanoscale Cross-Point Resistive Switching Memory Comprising p-Type SnO Bilayers. *Advanced Electronic Materials* **2015,** *1* (3), 1400035.
4. B. Govoreanu; G. S. Kar; Y-Y. Chen; V. Paraschiv; S. Kubicek; A. Fantini; I.P. Radu; L. Goux; S. Clima; R. Degraeve; N. Jossart; O. Riehard; T. Vandeweyer; K. Seo; P. Hendrickx; G. Pourtois; H. Bender; L. Altimine; D. J. Wouters; J. A. Kittl; M. Jurczak, 10×10 nm^2 Crossbar Resistive RAM with Excellent Performance, Reliability and Low-Energy Operations, **2011**, *IEEE Electron Device Meeting*, IEDM, 729-732.
5. Siemon, A.; Breuer, T.; Aslam, N.; Ferch, S.; Kim, W.; van den Hurk, J.; Rana, V.; Hoffmann-Eifert, S.; Waser, R.; Menzel, S.; Linn, E., Realization of Boolean Logic Functionality Using Redox-Based Memristive Devices. *Advanced Functional Materials* **2015,** *25* (40), 6414-6423.
6. Huang, P.; Kang, J.; Zhao, Y.; Chen, S.; Han, R.; Zhou, Z.; Chen, Z.; Ma, W.; Li, M.; Liu, L.; Liu, X., Reconfigurable Nonvolatile Logic Operations in Resistance Switching Crossbar Array for Large-Scale Circuits. *Advanced Materials* **2016**, *28*, 9758-9764.
7. Borghetti, J.; Snider, G. S.; Kuekes, P. J.; Yang, J. J.; Stewart, D. R.; Williams, R. S., 'Memristive' Switches Enable 'Stateful' Logic Operations via Material implication. *Nature* **2010,** *464* (7290), 873-876.
8. Qiangfei Xia; Robinett, W.; Cumbie, M. W.; Banerjee, N.; Cardinali, T. J.; Yang, J. J.; Wu, W.; Li, X.; Tong, W. M.; Strukov, D. B.; Snider, G. S.; Medeiros-Ribeiro, G.; Williams, R. S., Memristor-CMOS Hybrid Integrated Circuits for Reconfigurable Logic. *Nano Letters* **2009**, *9*, 3640-3645.
9. Ting, C.; Yuchao, Y.; Wei, L., Building Neuromorphic Circuits with Memristive Devices. *IEEE Circuits and Systems Magazine* **2013,** *13* (2), 56-73.

10. Jo, S. H.; Chang, T.; Ebong, I.; Bhadviya, B. B.; Mazumder, P.; Lu, W., Nanoscale Memristor Device as Synapse in Neuromorphic Systems. *Nano Letters* **2011,** *10* (8), 1297-1301.

11. Ohno, T.; Hasegawa, T.; Tsuruoka, T.; Terabe, K.; Gimzewski, J. K.; Aono, M., Short-Term Plasticity and Long-Term Potentiation Mimicked in Single Inorganic Synapses. *Nature Materials* **2011**, *10*, 591-595.

12. Tian, H.; Guo, Q.; Xie, Y.; Zhao, H.; Li, C.; Cha, J. J.; Xia, F.; Wang, H., Anisotropic Black Phosphorus Synaptic Device for Neuromorphic Applications. *Advanced Materials* **2016,** *28* (25), 4991-4997.

13. Wang, Z.; Joshi, S.; Savel'ev, S. E.; Jiang, H.; Midya, R.; Lin, P.; Hu, M.; Ge, N.; Strachan, J. P.; Li, Z.; Wu, Q.; Barnell, M.; Li, G. L.; Xin, H. L.; Williams, R. S.; Xia, Q.; Yang, J. J., Memristors with Diffusive Dynamics as Synaptic Emulators for Neuromorphic Computing. *Nature Materials* **2016**, *16*, 101-110.

14. Pershin, Y. V.; Di Ventra, M., Memory Effects in Complex Materials and Nanoscale Systems. *Advances in Physics* **2011,** *60* (2), 145-227.

15. Waser, R., Redox-based Resistive Switching Memories. *Journal of Nanoscience & Nanotechnology* **2012,** *12* (10), 7628-7640.

16. Pan, F.; Gao, S.; Chen, C.; Song, C.; Zeng, F., Recent progress in Resistive Random Access Memories: Materials, Switching Mechanisms, and Performance. *Materials Science & Engineering R-Reports* **2014**, *83*, 1-59.

17. Yang, J. J.; Strukov, D. B.; Stewart, D. R., Memristive Devices for Computing. *Nature Nanotechnology* **2013,** *8* (1), 13-24.

18. Jeong, D. S.; Thomas, R.; Katiyar, R. S.; Scott, J. F.; Kohlstedt, H.; Petraru, A.; Hwang, C. S., Emerging Memories: Resistive Switching Mechanisms and Current Status. *Reports on Progress in Physics. Physical Society* **2012,** *75* (7), 076502.

19. Chen, A., A Review of Emerging Non-Volatile Memory (NVM) Technologies and Applications. *Solid-State Electronics* **2016**, *125*, 25-38.

20. Waser, R.; Dittmann, R.; Staikov, G.; Szot, K., Redox-Based Resistive Switching Memories - Nanoionic Mechanisms, Prospects, and Challenges. *Advanced Materials* **2009,** *21* (25-26), 2632-2663.

21. Park, J.; Lee, S.; Lee, J.; Yong, K., A Light Incident Angle Switchable ZnO Nanorod Memristor: Reversible Switching Behavior Between Two Non-Volatile Memory Devices. *Advanced Materials* **2013,** *25* (44), 6423-6429.

22. Kim, K. M.; Zhang, J.; Graves, C.; Yang, J. J.; Choi, B. J.; Hwang, C. S.; Li, Z.; Williams, R. S., Low-Power, Self-Rectifying, and Forming-Free Memristor with an Asymmetric Programing Voltage for a High-Density Crossbar Application. *Nano Letters* **2016**, *16*, 6724-6732.

23. Huang, Y.-C.; Tsai, F.-S.; Wang, S.-J., Preparation of TiO_2 Nanowire Arrays through Hydrothermal Growth Method and Their pH Sensing Characteristics. *Japanese Journal of Applied Physics* **2014,** *53* (6S), 06JG02.

24. Ren, S.; Liu, W., One-step Photochemical Deposition of PdAu Alloyed Nanoparticles on TiO_2 Nanowires for Ultra-Sensitive H_2 Detection. *Journal of Materials Chemistry-A* **2016,** *4* (6), 2236-2245.

25. Sun, N.; Li, X.; Wang, Z.; Zhang, R.; Wang, J.; Wang, K.; Pei, R., A Multiscale TiO_2 Nanorod Array for Ultrasensitive Capture of Circulating Tumor Cells. *ACS Applied Materials & Interfaces* **2016,** *8* (20), 12638-12643.

26. Wang, G.; Wang, H.; Ling, Y.; Tang, Y.; Yang, X.; Fitzmorris, R. C.; Wang, C.; Zhang, J. Z.; Li, Y., Hydrogen-Treated TiO_2 Nanowire Arrays for Photoelectrochemical Water Splitting. *Nano Letters* **2011,** *11* (7), 3026-3033.

27. Zhou, Z. J.; Fan, J. Q.; Wang, X.; Zhou, W. H.; Du, Z. L.; Wu, S. X., Effect of Highly Ordered Single-Crystalline TiO_2 Nanowire Length on the Photovoltaic Performance of Dye-Sensitized Solar Cells. *ACS Applied Materials & Interfaces* **2011,** *3* (11), 4349-4353.

28. Lu, X.; Wang, G.; Zhai, T.; Yu, M.; Gan, J.; Tong, Y.; Li, Y., Hydrogenated TiO_2 Nanotube Arrays for Supercapacitors. *Nano Letters* **2012,** *12* (3), 1690-1696.

29. Li, Y.; Fang, X.; Koshizaki, N.; Sasaki, T.; Li, L.; Gao, S.; Shimizu, Y.; Bando, Y.; Golberg, D., Periodic TiO_2 Nanorod Arrays with Hexagonal Nonclose-Packed Arrangements: Excellent Field Emitters by Parameter Optimization. *Advanced Functional Materials* **2009,** *19* (15), 2467-2473.

30. Chua, L. O., Memristor-The Missing Circuit Element. *IEEE Transactions on Circuit Theory* **1971,** *18* (5), 507-519.

31. Chua, L. O.; Kang, S. M., Memristive Devices and Systems. *Proceeding of IEEE* **1976,** *64* (2), 209-223.

32. Prodromakis, T.; Toumazou, C.; Chua, L., Two Centuries of Memristors. *Nature Materials* **2012,** *11* (6), 478-481.

33. Strukov, D. B.; Snider, G. S.; Stewart, D. R.; Williams, R. S., The Missing Memristor Found. *Nature* **2008,** *453* (7191), 80-83.

34. Chanthbouala, A.; Crassous, A.; Garcia, V.; Bouzehouane, K.; Fusil, S.; Moya, X.; Allibe, J.; Dlubak, B.; Grollier, J.; Xavier, S.; Deranlot, C.; Moshar, A.; Proksch, R.; Mathur, N. D.; Bibes, M.; Barthelemy, A., Solid-state Memories Based On Ferroelectric Tunnel Junctions. *Nature Nanotechnology* **2012,** *7* (2), 101-104.

35. Shen, J.; Cong, J.; Shang, D.; Chai, Y.; Shen, S.; Zhai, K.; Sun, Y., A Multilevel Nonvolatile Magnetoelectric Memory. *Scientific Reports* **2016,** *6*, 34473.

36. Wong, H. S. P.; Raoux, S.; Kim, S.; Liang, J.; Reifenberg, J. P.; Rajendran, B.; Asheghi, M.; Goodson, K. E., Phase Change Memory. *Proceeding of IEEE* **2010,** *98* (12), 2201-2227.

37. Menzel, S.; Böttger, U.; Wimmer, M.; Salinga, M., Physics of the Switching Kinetics in Resistive Memories. *Advanced Functional Materials* **2015,** *25* (40), 6306-6325.

38. Linn, E.; Rosezin, R.; Kuegeler, C.; Waser, R., Complementary Resistive Switches for Passive Nanocrossbar Memories. *Nature Materials* **2010,** *9* (5), 403-406.

39. Chua, L., Resistance Switching Memories are Memristors. *Applied Physics a-Materials Science & Processing* **2011,** *102* (4), 765-783.

40. Chua, L., If It's Pinched It's a Memristor. *Semiconductor Science and Technology* **2014,** *29* (10), 104001.

41. Tsuchiya, T.; Terabe, K.; Aono, M., In Situ and Non-Volatile Bandgap Tuning of Multilayer Graphene Oxide in an All-Solid-State Electric Double-Layer Transistor. *Advanced Materials* **2014,** *26* (7), 1087-1091.

42. Kim, S. K.; Kim, J. Y.; Choi, S.-Y.; Lee, J. Y.; Jeong, H. Y., Direct Observation of Conducting Nanofilaments in Graphene-Oxide-Resistive Switching Memory. *Advanced Functional Materials* **2015**, *25*, 6710-6715.

43. Kim, S. K.; Kim, J. Y.; Jang, B. C.; Cho, M. S.; Choi, S.-Y.; Lee, J. Y.; Jeong, H. Y., Conductive Graphitic Channel in Graphene Oxide-Based Memristive Devices. *Advanced Functional Materials* **2016,** *26* (41), 7406-7414.

44. Santini, C. A.; Sebastian, A.; Marchiori, C.; Jonnalagadda, V. P.; Dellmann, L.; Koelmans, W. W.; Rossell, M. D.; Rossel, C. P.; Eleftheriou, E., Oxygenated Amorphous Carbon for Resistive Memory Applications. *Nature Communications* **2015,** *6, 8600.*

45. Nau, S.; Wolf, C.; Popovic, K.; Blumel, A.; Santoni, F.; Gagliardi, A.; di Carlo, A.; Sax, S.; List-Kratochvil, E. J. W., Inkjet-Printed Resistive Switching Memory Based on Organic Dielectric Materials: From Single Elements to Array Technology. *Advanced Electronic Materials* **2015,** *1* (1-2), 1400003.

46. Wang, H.; Zhu, B.; Ma, X.; Hao, Y.; Chen, X., Physically Transient Resistive Switching Memory Based on Silk Protein. *Small* **2016**, *12*, 2715-2719.

47. Yoon, J. H.; Song, S. J.; Yoo, I. H.; Seok, J. Y.; Yoon, K. J.; Kwon, D. E.; Park, T. H.; Hwang, C. S., Highly Uniform, Electroforming-Free, and Self-Rectifying Resistive Memory in the Pt/Ta_2O_5/HfO_{2-x}/TiN Structure. *Advanced Functional Materials* **2014,** *24* (32), 5086-5095.

48. Yoon, J. H.; Kim, K. M.; Song, S. J.; Seok, J. Y.; Yoon, K. J.; Kwon, D. E.; Park, T. H.; Kwon, Y. J.; Shao, X.; Hwang, C. S., Pt/Ta_2O_5/HfO_{2-x}/Ti Resistive Switching Memory Competing with Multilevel NAND Flash. *Advanced Materials* **2015,** *27* (25), 3811-3816.

49. Park, M.; Park, S.; Yoo, K. H., Multilevel Nonvolatile Memristive and Memcapacitive Switching in Stacked Graphene Sheets. *ACS Applied Materials & Interfaces* **2016**, *8*, 14046-14052.

50. Niu, G.; Kim, H. D.; Roelofs, R.; Perez, E.; Schubert, M. A.; Zaumseil, P.; Costina, I.; Wenger, C., Material Insights of HfO_2-Based Integrated 1-Transistor-1-Resistor Resistive Random Access Memory Devices Processed by Batch Atomic Layer Deposition. *Scientific Reports* **2016,** *6*, 28155.

51. Waser, R.; Aono, M., Nanoionics-based Resistive Switching Memories. *Nature Materials* **2007,** *6* (11), 833-840.

52. Lee, M.-J.; Lee, C. B.; Lee, D.; Lee, S. R.; Chang, M.; Hur, J. H.; Kim, Y.-B.; Kim, C.-J.; Seo, D. H.; Seo, S.; Chung, U. I.; Yoo, I.-K.; Kim, K., A Fast, High-Endurance And Scalable Non-Volatile Memory Device Made From Asymmetric Ta_2O_{5-x}/TaO_{2-x} Bilayer Structures. *Nature Materials* **2011,** *10* (8), 625-630.

53. You, B. K.; Kim, J. M.; Joe, D. J.; Yang, K.; Shin, Y.; Jung, Y. S.; Lee, K. J., Reliable Memristive-Switching Memory Devices Enabled by Densely-Packed Silver Nanocone Arrays as Electric-Field Concentrators. *ACS Nano* **2016**, *10*, 9478-9488.

54. Yang, Y. C.; Pan, F.; Liu, Q.; Liu, M.; Zeng, F., Room-Temperature-Fabricated Nonvolatile Resistive Memory for Ultrafast and High-Density Memory Application. *Nano Letters* **2009,** *9* (4), 1636-1643.

55. Torrezan, A. C.; Strachan, J. P.; Medeiros-Ribeiro, G.; Williams, R. S., Sub-nanosecond Switching Of a Tantalum Oxide Memristor. *Nanotechnology* **2011,** *22* (48), 485203.

56. Kannan, V.; Senthilkumar, V.; Rhee, J. K., Multi-level Conduction in NiO Resistive Memory Device Prepared by Solution Route. *Journal of Physics D-Applied Physics* **2013,** *46* (9), 095301.

57. Wang, Y.; Liu, Q.; Long, S.; Wang, W.; Wang, Q.; Zhang, M.; Zhang, S.; Li, Y.; Zuo, Q.; Yang, J.; Liu, M., Investigation of Resistive Switching in Cu-Doped HfO_2 Thin film for Multilevel Non-Volatile Memory Applications. *Nanotechnology* **2010,** *21* (4), 045202.

58. Rao, K. D. M.; Sagade, A. A.; John, R.; Pradeep, T.; Kulkarni, G. U., Defining Switching Efficiency of Multilevel Resistive Memory with PdO as an Example. *Advanced Electronic Materials* **2016,** *2* (2),1500286.

59. Choi, S. J.; Park, G. S.; Kim, K. H.; Cho, S.; Yang, W. Y.; Li, X. S.; Moon, J. H.; Lee, K. J.; Kim, K., In Situ Observation of Voltage-Induced Multilevel Resistive Switching in Solid Electrolyte Memory. *Advanced Materials* **2011,** *23* (29), 3272-3277.

60. Yang, Y.; Gao, P.; Gaba, S.; Chang, T.; Pan, X.; Lu, W., Observation of Conducting Filament Growth in Nanoscale Resistive Memories. *Nature Communications* **2012**, *3*, 732.

61. Kwon, D. H.; Kim, K. M.; Jang, J. H.; Jeon, J. M.; Lee, M. H.; Kim, G. H.; Li, X. S.; Park, G. S.; Lee, B.; Han, S.; Kim, M.; Hwang, C. S., Atomic Structure of Conducting Nanofilaments in TiO_2 Resistive Switching Memory. *Nature Nanotechnology* **2010,** *5* (2), 148-153.

62. Yang, J. J.; Inoue, I. H.; Mikolajick, T.; Hwang, C. S., Metal Oxide Memories Based on Thermochemical and Valence Change Mechanisms. *MRS Bulletin* **2012,** *37* (2), 131-137.

63. Park, G.-S.; Kim, Y. B.; Park, S. Y.; Li, X. S.; Heo, S.; Lee, M.-J.; Chang, M.; Kwon, J. H.; Kim, M.; Chung, U. I.; Dittmann, R.; Waser, R.; Kim, K., In situ Observation of Filamentary Conducting Channels in an Asymmetric Ta_2O_{5-x}/TaO_{2-x} Bilayer Structure. *Nature Communications* **2013,** *4, 2382*.

64. Wedig, A.; Luebben, M.; Cho, D. Y.; Moors, M.; Skaja, K.; Rana, V.; Hasegawa, T.; Adepalli, K. K.; Yildiz, B.; Waser, R.; Valov, I., Nanoscale Cation Motion in TaO_x, HfO_x and TiO_x Memristive Systems. *Nature Nanotechnology* **2016,** *11* (1), 67-74.

65. Moors, M.; Adepalli, K. K.; Lu, Q.; Wedig, A.; Baeumer, C.; Skaja, K.; Arndt, B.; Tuller, H. L.; Dittmann, R.; Waser, R.; Yildiz, B.; Valov, I., Resistive Switching Mechanisms on TaO_x and $SrRuO_3$ Thin-Film Surfaces Probed by Scanning Tunneling Microscopy. *ACS Nano* **2016,** *10* (1), 1481-1492.

66. Luebben, M.; Karakolis, P.; Ioannou-Sougleridis, V.; Normand, P.; Dimitrakis, P.; Valov, I., Graphene-Modified Interface Controls Transition from VCM to ECM Switching Modes in Ta/TaO_x Based Memristive Devices. *Advanced Materials* **2015,** *27* (40), 6202-6207.

67. Oka, K.; Yanagida, T.; Nagashima, K.; Kanai, M.; Xu, B.; Park, B. H.; Katayama-Yoshida, H.; Kawai, T., Dual Defects of Cation and Anion in Memristive Nonvolatile Memory of Metal Oxides. *Journal of the American Chemical Society* **2012,** *134* (5), 2535-2538.

68. Jeong, H. Y.; Lee, J. Y.; Choi, S.-Y., Interface-Engineered Amorphous TiO_2-Based Resistive Memory Devices. *Advanced Functional Materials* **2010,** *20* (22), 3912-3917.

69. Tsuruoka, T.; Valov, I.; Tappertzhofen, S.; van den Hurk, J.; Hasegawa, T.; Waser, R.; Aono, M., Redox Reactions at Cu,Ag/Ta_2O_5 Interfaces and the Effects of Ta_2O_5 Film Density on the Forming Process in Atomic Switch Structures. *Advanced Functional Materials* **2015,** *25* (40), 6374-6381.

70. Yang, J. J.; Pickett, M. D.; Li, X.; Ohlberg, D. A.; Stewart, D. R.; Williams, R. S., Memristive Switching Mechanism For Metal/Oxide/Metal Nanodevices. *Nature Nanotechnology* **2008,** *3* (7), 429-433.

71. Young Jeong, H.; Kyu Kim, S.; Yong Lee, J.; Choi, S.-Y., Role of Interface Reaction on Resistive Switching of Metal/Amorphous TiO_2/Al RRAM Devices. *Journal of The Electrochemical Society* **2011,** *158* (10), H979-H982.

72. Jeong, H. Y.; Lee, J. Y.; Choi, S.-Y.; Kim, J. W., Microscopic Origin of Bipolar Resistive Switching of Nanoscale Titanium Oxide Thin Films. *Applied Physics Letters* **2009,** *95* (16), 162108.

73. Shao, X. L.; Zhou, L. W.; Yoon, K. J.; Jiang, H.; Zhao, J. S.; Zhang, K. L.; Yoo, S.; Hwang, C. S., Electronic Resistance Switching in the Al/TiO_x/Al Structure for Forming-Free and Area-Scalable Memory. *Nanoscale* **2015,** *7* (25), 11063-74.

74. Kim, K. M.; Choi, B. J.; Lee, M. H.; Kim, G. H.; Song, S. J.; Seok, J. Y.; Yoon, J. H.; Han, S.; Hwang, C. S., A Detailed Understanding of the Electronic Bipolar Resistance Switching Behavior in Pt/TiO_2/Pt Structure. *Nanotechnology* **2011,** *22* (25), 254010.

75. Kim, S.; Choi, Y.-K., A Comprehensive Study of the Resistive Switching Mechanism in Al/TiO_x/TiO_2/Al-Structured RRAM. *IEEE Transactions on Electron Devices* **2009,** *56* (12), 3049-3053.

76. Younis, A.; Chu, D.; Lin, X.; Yi, J.; Dang, F.; Li, S., High-Performance Nanocomposite Based Memristor with Controlled Quantum Dots as Charge Traps. *ACS Applied Materials & Interfaces* **2013,** *5* (6), 2249-2254.

77. Bozano, L. D.; Kean, B. W.; Beinhoff, M.; Carter, K. R.; Rice, P. M.; Scott, J. C., Organic Materials and Thin-film Structures for Cross-Point Memory Cells Based on Trapping in Metallic Nanoparticles. *Advanced Functional Materials* **2005**, 1933-1939.

78. Sun, Y.; Lu, J.; Ai, C.; Wen, D., Nonvolatile Memory Devices Based On Poly(Vinyl Alcohol) + Graphene Oxide Hybrid Composites. *Physical Chemistry Chemical Physics:PCCP* **2016,** *18* (16), 11341-11347.

79. Wei, T.; Chen, G.; Zhang, S.; Chen, Y.; Hu, Y.; Jiang, R.; Li, Y., Nonvolatile Organic Resistive Switching Memory Based on Poly(o-methoxyaniline) Film. *Microelectronic Engineering* **2016,** *162*, 85-88.

80. Kim, S.; Jeong, H. Y.; Choi, S.-Y.; Choi, Y.-K., Comprehensive Modeling of Resistive Switching in the Al/TiO_x/TiO_2/Al Heterostructure Based on Space-Charge-Limited Conduction. *Applied Physics Letters* **2010,** *97* (3), 033508.

81. Chen, Y.; Song, H.; Jiang, H.; Li, Z.; Zhang, Z.; Sun, X.; Li, D.; Miao, G., Reproducible Bipolar Resistive Switching in Entire Nitride AlN/n-GaN Metal-Insulator-Semiconductor Device and its Mechanism. *Applied Physics Letters* **2014,** *105* (19), 193502.

82. Kim, J.; Jung, K.; Kim, Y.; Jo, Y.; Cho, S.; Woo, H.; Lee, S.; Inamdar, A. I.; Hong, J.; Lee, J. K.; Kim, H.; Im, H., Switching Power Universality in Unipolar Resistive Switching Memories. *Scientific Reports* **2016,** *6*, 23930.

83. Chen, J.-Y.; Hsin, C.-L.; Huang, C.-W.; Chiu, C.-H.; Huang, Y.-T.; Lin, S.-J.; Wu, W.-W.; Chen, L.-J., Dynamic Evolution of Conducting Nanofilament in Resistive Switching Memories. *Nano Letters* **2013,** *13* (8), 3671-3677.

84. Chien, W.-C.; Lee, M.-H.; Lee, F.-M.; Lin, Y.-Y.; Lung, H.-L.; Hsieh, K.-Y.; Lu, C.-Y. In A Multi-Level 40nm WO_X Resistive Memory with Excellent Reliability, *2011 International Electron Devices Meeting*, Washington **2011**.

85. Nagareddy, V. K.; Barnes, M. D.; Zipoli, F.; Lai, K. T.; Alexeev, A. M.; Craciun, M. F.; Wright, C. D., Multilevel Ultrafast Flexible Nanoscale Nonvolatile Hybrid Graphene Oxide-Titanium Oxide Memories. *ACS Nano* **2017,** *11* (3), 3010-3021.

86. Lin, S.-M.; Tseng, J.-Y.; Su, T.-Y.; Shih, Y.-C.; Huang, J.-S.; Huang, C.-H.; Lin, S.-J.; Chueh, Y.-L., Tunable Multilevel Storage of Complementary Resistive Switching on Single-Step Formation of $ZnO/ZnWO_x$ Bilayer Structure via Interfacial Engineering. *ACS Applied Materials & Interfaces* **2014,** *6* (20), 17686-17693.

87. Chae, S. C.; Lee, J. S.; Choi, W. S.; Lee, S. B.; Chang, S. H.; Shin, H.; Kahng, B.; Noh, T. W., Multilevel Unipolar Resistance Switching in TiO_2 Thin Films. *Applied Physics Letters* **2009,** *95* (9), 093508.

88. Sun, Z.; Ambrosi, E.; Bricalli, A.; Ielmini, D., Logic Computing with Stateful Neural Networks of Resistive Switches. *Advanced Materials* **2018**, e1802554.

89. Xu, N.; Yoon, K. J.; Kim, K. M.; Fang, L.; Hwang, C. S., Fully Functional Logic-In-Memory Operations Based on a Reconfigurable Finite-State Machine Using a Single Memristor. *Advanced Electronic Materials* **2018**, 1800189.

90. Linn, E.; Rosezin, R.; Tappertzhofen, S.; Bottger, U.; Waser, R., Beyond von Neumann--Logic Operations In Passive Crossbar Arrays Alongside Memory Operations. *Nanotechnology* **2012,** *23* (30), 305205.

91. Kim, T.-W.; Choi, H.; Oh, S.-H.; Wang, G.; Kim, D.-Y.; Hwang, H.; Lee, T., One Transistor-one Resistor Devices for Polymer Non-Volatile Memory Applications. *Advanced Materials* **2009,** *21* (24), 2497-2500.

92. Choi, B. J.; Zhang, J.; Norris, K.; Gibson, G.; Kim, K. M.; Jackson, W.; Zhang, M.-X. M.; Li, Z.; Yang, J. J.; Williams, R. S., Trilayer Tunnel Selectors for Memristor Memory Cells. *Advanced Materials* **2016,** *28* (2), 356-362.

93. Cha, E.; Woo, J.; Lee, D., Nanoscale (~10 nm) 3D vertical ReRAM and NbO_2 threshold selector with TiN electrode. *IEEE* **2013**.

94. Yoon, K. J.; Kim, G. H.; Yoo, S.; Bae, W.; Yoon, J. H.; Park, T. H.; Kwon, D. E.; Kwon, Y. J.; Kim, H. J.; Kim, Y. M.; Hwang, C. S., Double-Layer-Stacked one Diode-One Resistive Switching Memory Crossbar Array with an Extremely High Rectification Ratio of 10^9. *Advanced Electronic Materials* **2017,** *3* (7), 1700152.

95. Wang, G.; Lauchner, A. C.; Lin, J.; Natelson, D.; Palem, K. V.; Tour, J. M., High-Performance and Low-Power Rewritable SiO_x 1 kbit One Diode-One Resistor Crossbar Memory Array. *Advanced Materials* **2013,** *25* (34), 4789-4793.
96. Abbott, L. F.; Regehr, W. G., Synaptic computation. *Nature* **2004,** *431* (7010), 796-803.
97. Rosenblatt, F., The Perceptron: a Probabilistic Model for Information Storage and Organization in the Brain. *Psychological Review* **1958,** *65* (6), 386.
98. Rosenblatt, F., Perceptron Simulation Experiments. *Proceedings of the IRE* **1960,** *48* (3), 301-309.
99. Rosenblatt, F. Principles of Neurodynamics. Perceptrons and the Theory of Brain Mechanisms; Cornell Aeronautical Lab in Buffalo NY: **1961**.
100. Ng, G. W., Brain-mind Machinery: Brain-Inspired Computing And Mind Opening. *World Scientific*: **2009**.
101. Gold, J. I.; Shadlen, M. N., The Neural Basis of Decision Making. *Annual Review Neuroscience* **2007,** *30*, 535-574.
102. Gulledge, A. T.; Kampa, B. M.; Stuart, G. J., Synaptic Integration in Dendritic Trees. *Journal of Neurobiology Banner* **2005,** *64* (1), 75-90.
103. Kuzum, D.; Jeyasingh, R. G.; Lee, B.; Wong, H. S., Nanoelectronic Programmable Synapses based on Phase Change Materials for Brain-Inspired Computing. *Nano Letters* **2012,** *12* (5), 2179-2186.
104. Milano, G.; Luebben, M.; Ma, Z.; Dunin-Borkowski, R.; Boarino, L.; Pirri, C. F.; Waser, R.; Ricciardi, C.; Valov, I., Self-limited Single Nanowire Systems Combining All-in-one Memristive And Neuromorphic Functionalities. *Nature Communications* **2018,** *9* (1), 5151.
105. Yang, R.; Terabe, K.; Liu, G.; Tsuruoka, T.; Hasegawa, T.; Gimzewski, J. K.; Aono, M., On-demand Nanodevice With Electrical and Neuromorphic Multifunction Realized by Local Ion Migration. *ACS Nano* **2012,** *6* (11), 9515-9121.
106. Hasegawa, T.; Ohno, T.; Terabe, K.; Tsuruoka, T.; Nakayama, T.; Gimzewski, J. K.; Aono, M., Learning Abilities Achieved by a Single Solid-State Atomic Switch. *Advanced Materials* **2010,** *22* (16), 1831-1834.
107. Chang, T.; Jo, S. H.; Lu, W., Short-term Memory to Long-Term Memory Transition in a Nanoscale Memristor. *ACS Nano* **2011,** *5* (9), 7669-7676.

108. Wang, Z. Q.; Xu, H. Y.; Li, X. H.; Yu, H.; Liu, Y. C.; Zhu, X. J., Synaptic Learning and Memory Functions Achieved using Oxygen Ion Migration/Diffusion in an Amorphous InGaZnO Memristor. *Advanced Functional Materials* **2012,** *22* (13), 2759-2765.

109. Kim, S.; Du, C.; Sheridan, P.; Ma, W.; Choi, S.; Lu, W. D., Experimental Demonstration of a Second-Order Memristor and its Ability to Biorealistically Implement Synaptic Plasticity. *Nano Letters* **2015,** *15* (3), 2203-2211.

110. Yin, J.; Zeng, F.; Wan, Q.; Li, F.; Sun, Y.; Hu, Y.; Liu, J.; Li, G.; Pan, F., Adaptive Crystallite Kinetics in Homogenous Bilayer Oxide Memristor for Emulating Diverse Synaptic Plasticity. *Advanced Functional Materials* **2018**, 1706927.

111. Tan, Z. H.; Yang, R.; Terabe, K.; Yin, X. B.; Zhang, X. D.; Guo, X., Synaptic Metaplasticity Realized in Oxide Memristive Devices. *Advanced Materials* **2016,** *28* (2), 377-384.

112. Wang, Z. Y.; Wang, L. Y.; Nagai, M.; Xie, L. H.; Yi, M. D.; Huang, W., Nanoionics-Enabled Memristive Devices: Strategies and Materials for Neuromorphic Applications. *Advanced Electronic Materials* **2017,** *3* (7), 1600510.

113. Kim, B.-Y.; Hwang, H.-G.; Woo, J.-U.; Lee, W.-H.; Lee, T.-H.; Kang, C.-Y.; Nahm, S., Nanogenerator-induced Synaptic Plasticity and Metaplasticity of Bio-Realistic Artificial Synapses. *NPG Asia Materials* **2017,** *9* (5), e381.

114. Tan, Z. H.; Yin, X. B.; Yang, R.; Mi, S. B.; Jia, C. L.; Guo, X., Pavlovian Conditioning Demonstrated with Neuromorphic Memristive Devices. *Scientific Reports* **2017,** *7* (1), 713.

115. Yang, Y.; Chen, B.; Lu, W. D., Memristive Physically Evolving Networks Enabling the Emulation of Heterosynaptic Plasticity. *Advanced Materials* **2015,** *27* (47), 7720-7727.

116. Yang, Y.; Yin, M.; Yu, Z.; Wang, Z.; Zhang, T.; Cai, Y.; Lu, W. D.; Huang, R., Multifunctional Nanoionic Devices Enabling Simultaneous Heterosynaptic Plasticity and Efficient In-Memory Boolean Logic. *Advanced Electronic Materials* **2017**, 1700032.

117. John, R. A.; Tiwari, N.; Yaoyi, C.; Ankit; Tiwari, N.; Kulkarni, M.; Nirmal, A.; Nguyen, A. C.; Basu, A.; Mathews, N., Ultralow Power Dual-Gated Subthreshold Oxide Neuristors: An Enabler for Higher Order Neuronal Temporal Correlations. *ACS Nano* **2018,** *12* (11), 11263-11273.

118. Sangwan, V. K.; Lee, H.-S.; Bergeron, H.; Balla, I.; Beck, M. E.; Chen, K.-S.; Hersam, M. C., Multi-terminal Memtransistors From Polycrystalline Monolayer Molybdenum Disulfide. *Nature* **2018,** *554* (7693), 500-504.

119. Zhu, J.; Yang, Y.; Jia, R.; Liang, Z.; Zhu, W.; Rehman, Z. U.; Bao, L.; Zhang, X.; Cai, Y.; Song, L.; Huang, R., Ion Gated Synaptic Transistors Based on 2D van der Waals Crystals with Tunable Diffusive Dynamics. *Advanced Materials* **2018**, e1800195.

120. Zhu, X.; Li, D.; Liang, X.; Lu, W. D., Ionic Modulation And Ionic Coupling Effects in MoS_2 Devices for Neuromorphic Computing. *Nature Materials* **2018,** *18* (2), 141-148.

121. Yu, S.; Gao, B.; Fang, Z.; Yu, H.; Kang, J.; Wong, H. S., A Low Energy Oxide-based Electronic Synaptic Device For Neuromorphic Visual Systems with Tolerance to Device Variation. *Advanced Materials* **2013,** *25* (12), 1774-1779.

122. Xu, W.; Min, S. Y.; Hwang, H.; Lee, T. W., Organic Core-sheath Nanowire Artificial Synapses with Femtojoule Energy Consumption. *Science Advance* **2016,** *2* (6), e1501326.

123. Alibart, F.; Zamanidoost, E.; Strukov, D. B., Pattern Classification by Memristive Crossbar Circuits Using Ex Situ and In Situ Training. *Nature Communications* **2013,** *4*, 2072.

124. Yao, P.; Wu, H.; Gao, B.; Eryilmaz, S. B.; Huang, X.; Zhang, W.; Zhang, Q.; Deng, N.; Shi, L.; Wong, H. P.; Qian, H., Face Classification Using Electronic Synapses. *Nature Communications* **2017,** *8*, 15199.

125. Prezioso, M.; Merrikh-Bayat, F.; Hoskins, B. D.; Adam, G. C.; Likharev, K. K.; Strukov, D. B., Training and Operation of an Integrated Neuromorphic Network Based on Metal-Oxide Memristors. *Nature* **2015,** *521* (7550), 61-64.

126. Sheridan, P. M.; Cai, F.; Du, C.; Ma, W.; Zhang, Z.; Lu, W. D., Sparse Coding with Memristor Networks. *Nature Nanotechnology* **2017,** *12* (8), 784-789.

127. Bayat, F. M.; Prezioso, M.; Chakrabarti, B.; Nili, H.; Kataeva, I.; Strukov, D., Implementation of Multilayer Perceptron Network with Highly Uniform Passive Memristive Crossbar Circuits. *Nature Communications* **2018,** *9* (1), 2331.

128. Prezioso, M.; Mahmoodi, M. R.; Bayat, F. M.; Nili, H.; Kim, H.; Vincent, A.; Strukov, D. B., Spike-timing-dependent Plasticity Learning of Coincidence Detection with Passively Integrated Memristive Circuits. *Nature Communications* **2018,** *9* (1), 5311.

129. Serb, A.; Bill, J.; Khiat, A.; Berdan, R.; Legenstein, R.; Prodromakis, T., Unsupervised Learning In Probabilistic Neural Networks with Multi-State Metal-Oxide Memristive Synapses. *Nature Communications* **2016,** *7*, 12611.

130. Shi, Y.; Nguyen, L.; Oh, S.; Liu, X.; Koushan, F.; Jameson, J. R.; Kuzum, D., Neuroinspired Unsupervised Learning and Pruning with Subquantum CBRAM Arrays. *Nature Communications* **2018,** *9* (1), 5312.

131. Li, C.; Belkin, D.; Li, Y.; Yan, P.; Hu, M.; Ge, N.; Jiang, H.; Montgomery, E.; Lin, P.; Wang, Z.; Song, W.; Strachan, J. P.; Barnell, M.; Wu, Q.; Williams, R. S.; Yang, J. J.; Xia, Q., Efficient and Self-Adaptive In-Situ Learning in Multilayer Memristor Neural Networks. *Nature Communications* **2018,** *9* (1), 2385.

132. Szot, K.; Rogala, M.; Speier, W.; Klusek, Z.; Besmehn, A.; Waser, R., TiO_2-a Prototypical Memristive Material. *Nanotechnology* **2011,** *22* (25), 254001.

133. Oh, S. C.; Jung, H. Y.; Lee, H., Effect of the Top Electrode Materials on the Resistive Switching Characteristics of TiO_2 Thin Film. *Journal of Applied Physics* **2011,** *109* (12), 124511.

134. Hernández-Rodríguez, E.; Márquez-Herrera, A.; Zaleta-Alejandre, E.; Meléndez-Lira, M.; Cruz, W. d. l.; Zapata-Torres, M., Effect of Electrode Type in the Resistive Switching Behaviour of TiO_2 Thin Films. *Journal of Physics D: Applied Physics* **2013,** *46* (4), 045103.

135. Hu, C.; McDaniel, M. D.; Posadas, A.; Demkov, A. A.; Ekerdt, J. G.; Yu, E. T., Highly Controllable and Stable Quantized Conductance and Resistive Switching Mechanism in Single-Crystal TiO_2 Rrsistive Memory on Silicon. *Nano Letters* **2014,** *14* (8), 4360-7.

136. Du, Y.; Pan, H.; ShijieWang; TomWu; Feng, Y. P.; Pan, J.; ShenWee, A. T., Symmetrical Negative Differential Resistance Behavior of a Resistive Switching Device. *ACS Nano* **2012,** *6* (3), 2517-2524.

137. Strachan, J. P.; Pickett, M. D.; Yang, J. J.; Aloni, S.; Kilcoyne, A. L. D.; Medeiros-Ribeiro, G.; Williams, R. S., Direct Identification of the Conducting Channels in a Functioning Memristive Device. *Advanced Materials* **2010,** *22* (32), 3573-3577.

138. Rogala, M.; Bihlmayer, G.; Speier, W.; Klusek, Z.; Rodenbuecher, C.; Szot, K., Resistive Switching of a Quasi-Homogeneous Distribution of Filaments Generated at Heat-Treated TiO_2 (110)-Surfaces. *Advanced Functional Materials* **2015,** *25* (40), 6382-6389.

139. Vishwanath, S. K.; Kim, J., Resistive Switching Characteristics of all-Solution-based Ag/TiO_2/Mo-Doped In_2O_3 Devices for Non-Volatile Memory Applications.. *Journal of Material Chemistry-C.* **2016,** *4*, 10967-10972.

140. Jang, M. H.; Agarwal, R.; Nukala, P.; Choi, D.; Johnson, A. T. C.; Chen, I. W.; Agarwal, R., Observing Oxygen Vacancy Driven Electroforming in Pt-TiO_2-Pt Device via Strong Metal Support Interaction. *Nano Letters* **2016,** *16* (4), 2139-2144.

141. Kim, K. M.; Kim, G. H.; Song, S. J.; Seok, J. Y.; Lee, M. H.; Yoon, J. H.; Hwang, C. S., Electrically Configurable Electroforming and Bipolar Resistive Switching in Pt/TiO_2/Pt Structures. *Nanotechnology* **2010,** *21* (30), 305203.

142. Kim, H. J.; Yoon, K. J.; Park, T. H.; Kim, H. J.; Kwon, Y. J.; Shao, X. L.; Kwon, D. E.; Kim, Y. M.; Hwang, C. S., Filament Shape Dependent Reset Behavior Governed by the Interplay between the Electric Field and Thermal Effects in the Pt/TiO_2/Cu Electrochemical Metallization Device. *Advanced Electronic Materials* **2017**, 1600404.

143. Yang, J. J.; Strachan, J. P.; Miao, F.; Zhang, M. X.; Pickett, M. D.; Yi, W.; Ohlberg, D. A. A.; Medeiros-Ribeiro, G.; Williams, R. S., Metal/TiO_2 Interfaces for Memristive Switches. *Applied Physics a-Materials Science & Processing* **2011,** *102* (4), 785-789.

144. Milano, G.; Porro, S.; Valov, I.; Ricciardi, C., Recent Developments and Perspectives for Memristive Devices Based on Metal Oxide Nanowires. *Advanced Electronic Materials* **2019**, 1800909.

145. Park, G.-S.; Li, X.-S.; Kim, D.-C.; Jung, R.-J.; Lee, M.-J.; Seo, S., Observation of Electric-Field Induced Ni Filament Channels in Polycrystalline NiO_x Film. *Applied Physics Letters* **2007,** *91* (22), 222103.

146. Nagashima, K.; Yanagida, T.; Oka, K.; Taniguchi, M.; Kawai, T.; Kim, J. S.; Park, B. H., Resistive Switching Multistate Nonvolatile Memory Effects in a Single Cobalt Oxide Nanowire. *Nano Letters* **2010,** *10* (4), 1359-1363.

147. Huang, Y.-C.; Chen, P.-Y.; Huang, K.-F.; Chuang, T.-C.; Lin, H.-H.; Chin, T.-S.; Liu, R.-S.; Lan, Y.-W.; Chen, C.-D.; Lai, C.-H., Using Binary Resistors to Achieve Multilevel Resistive Switching in Multilayer NiO/Pt Nanowire Arrays. *NPG Asia Materials* **2014,** *6* (2), e85.

148. Lin, L. C.; Liu, L.; Musselman, K.; Zou, G. S.; Duley, W. W.; Zhou, Y. N., Plasmonic-Radiation-Enhanced Metal Oxide Nanowire Heterojunctions for Controllable Multilevel Memory. *Advanced Functional Materials* **2016,** *26* (33), 5979-5986.

149. O'Kelly, C.; Fairfield, J. A.; Boland, J. J., A Single Nanoscale Junction with Programmable Multilevel Memory. *ACS Nano* **2014,** *8* (11), 11724-11729.

150. Oka, K.; Yanagida, T.; Nagashima, K.; Tanaka, H.; Seki, S.; Honsho, Y.; Ishimaru, M.; Hirata, A.; Kawai, T., Specific Surface Effect on Transport Properties of NiO/MgO Heterostructured Nanowires. *Applied Physics Letters* **2009,** *95* (13), 133110.

151. Hong, D. S.; Chen, Y. S.; Sun, J. R.; Shen, B. G., Ternary Synaptic Plasticity Arising from Memdiode Behavior of TiO_x Single Nanowires. *Advanced Electronic Materials* **2016,** *2* (4), 1500359.

152. Nagashima, K.; Yanagida, T.; Kanai, M.; Oka, K.; Klamchuen, A.; Rahong, S.; Meng, G.; Horprathum, M.; Xu, B.; Zhuge, F. W.; He, Y.; Kawai, T., Switching Properties of Titanium Dioxide Nanowire Memristor. *Japanese Journal of Applied Physics* **2012,** *51* (11).

153. Wang, B.; Ren, T. S.; Chen, S.; Zhang, B. S.; Zhang, R. F.; Qi, J.; Chu, S.; Huang, J.; Liu, J. L., Resistive Switching in Ga- and Sb-Doped ZnO Single Nanowire Devices. *Journal of Materials Chemistry C* **2015,** *3* (45), 11881-11885.

154. Qi, J.; Huang, J.; Paul, D.; Ren, J. J.; Chu, S.; Liu, J. L., Current Self-Complianced and Self-Rectifying Resistive Switching in Ag-Electroded Single Na-Doped ZnO Nanowires. *Nanoscale* **2013,** *5* (7), 2651-2654.

155. Huang, C. W.; Chen, J. Y.; Chiu, C. H.; Wu, W. W., Revealing Controllable Nanowire Transformation through Cationic Exchange for RRAM Application. *Nano Letters* **2014,** *14* (5), 2759-2763.

156. Bellew, A. T.; Bell, A. P.; McCarthy, E. K.; Fairfield, J. A.; Boland, J. J., Programmability of Nanowire Networks. *Nanoscale* **2014,** *6* (16), 9632-9639.

157. Liang, K. D.; Huang, C. H.; Lai, C. C.; Huang, J. S.; Tsai, H. W.; Wang, Y. C.; Shih, Y. C.; Chang, M. T.; Lo, S. C.; Chueh, Y. L., Single CuO_x Nanowire Memristor: Forming-Free Resistive Switching Behavior. *ACS Applied Materials & Interfaces* **2014,** *6* (19), 16537-16544.

158. Fan, Z.; Fan, X. D.; Li, A.; Dong, L. X., In Situ Forming, Characterization, and Transduction of Nanowire Memristors. *Nanoscale* **2013,** *5* (24), 12310-12315.

159. Bae, S. H.; Lee, S.; Koo, H.; Lin, L.; Jo, B. H.; Park, C.; Wang, Z. L., The Memristive Properties of a Single VO_2 Nanowire with Switching Controlled by Self-Heating. *Advanced Materials* **2013,** *25* (36), 5098-5103.

160. Guo, J.; Zhou, Y.; Yuan, H. J.; Zhao, D.; Yin, Y. L.; Hai, K.; Peng, Y. H.; Zhou, W. C.; Tang, D. S., Reconfigurable Resistive Switching Devices Based on Individual Tungsten Trioxide Nanowires. *Aip Advances* **2013,** *3* (4), 042137.

161. He, X. W.; Yin, Y. L.; Guo, J.; Yuan, H. J.; Peng, Y. H.; Zhou, Y.; Zhao, D.; Hai, K.; Zhou, W. C.; Tang, D. S., Memristive Properties of Hexagonal WO_3 Nanowires Induced by Oxygen Vacancy Migration. *Nanoscale Research Letters* **2013,** *8* (50), 1-8.

162. Liao, Z. M.; Hou, C.; Zhang, H. Z.; Wang, D. S.; Yu, D. P., Evolution of Resistive Switching Over Bias Duration of Single Ag_2S Nanowires. *Applied Physics Letters* **2010,** *96* (20), 203109.

163. Liao, Z. M.; Hou, C.; Zhao, Q.; Wang, D. S.; Li, Y. D.; Yu, D. P., Resistive Switching and Metallic-Filament Formation in Ag_2S Nanowire Transistors. *Small* **2009,** *5* (21), 2377-2381.

164. Hwang, S. K.; Lee, J. M.; Kim, S.; Park, J. S.; Park, H. I.; Ahn, C. W.; Lee, K. J.; Lee, T.; Kim, S. O., Flexible Multilevel Resistive Memory with Controlled Charge Trap B-and N-Doped Carbon Nanotubes. *Nano Letters* **2012,** *12* (5), 2217-2221.

165. Chu, D.; Younis, A.; Li, S., Direct Growth of TiO_2 Nanotubes on Transparent Substrates and Their Resistive Switching Characteristics. *Journal of Physics D: Applied Physics* **2012,** *45* (35), 355306.

166. Yu, Z.; Qu, X.; Yang, W.; Peng, J.; Xu, Z., A Facile Hydrothermal Synthesis and Memristive Switching Performance of Rutile TiO_2 Nanowire Arrays. *Journal of Alloys and Compounds* **2016,** *688*, 37-43.

167. Yu, Z.; Qu, X.; Yang, W.; Peng, J.; Xu, Z., Hydrothermal Synthesis and Memristive Switching Behaviors of Single-Crystalline Anatase TiO_2 Nanowire Arrays. *Journal of Alloys and Compounds* **2016,** *688*, 294-300.

168. Zhang, F.; Gan, X.; Li, X.; Wu, L.; Gao, X.; Zheng, R.; He, Y.; Liu, X.; Yang, R., Realization of Rectifying and Resistive Switching Behaviors of TiO_2 Nanorod Arrays for Nonvolatile Memory. *Electrochemical and Solid-State Letters* **2011,** *14* (10), H422-H425.

169. Tang, M.; Sun, B.; Huang, J.; Gao, J.; Li, C. M., High Performance White-Light-Controlled Resistance Switching Memory of an Ag/alpha-Fe_2O_3/FTO Thin Film. *Rsc Advances* **2016,** *6* (30), 25028-25033.

170. Sun, Y.; Yan, X.; Zheng, X.; Liu, Y.; Zhao, Y.; Shen, Y.; Liao, Q.; Zhang, Y., High On-Off Ratio Improvement of ZnO-Based Forming-Free Memristor by Surface Hydrogen Annealing. *ACS Applied Materials & Interfaces* **2015,** *7* (13), 7382-7388.

171. Huang, C.-H.; Huang, J.-S.; Lin, S.-M.; Chang, W.-Y.; He, J.-H.; Chueh, Y.-L., ZnO_{1-x} Nanorod Arrays/ZnO Thin Film Bilayer Structure: From Homojunction Diode and High-Performance Memristor to Complementary 1D1R Application. *ACS Nano* **2012,** *6* (9), 8407-8414.

172. Sun, B.; Li, C. M., Light-Controlled Resistive Switching Memory of Multiferroic $BiMnO_3$ Nanowire Arrays. *Physical Chemistry Chemical Physics* **2015,** *17* (10), 6718-6721.

173. Deng, X. L.; Hong, S.; Hwang, I.; Kim, J.-S.; Jeon, J. H.; Park, Y. C.; Lee, J.; Kang, S.-O.; Kawai, T.; Park, B. H., Confining Grains of Textured Cu_2O Films to Single-Crystal Nanowires and Resultant Change in Resistive Switching Characteristics. *Nanoscale* **2012,** *4* (6), 2029-2033.

174. Pi, C.; Ren, Y.; Chim, W. K., Investigation of Bipolar Resistive Switching and the Time-Dependent SET Process in Silver Sulfide/Silver Thin Films and Nanowire Array Structures. *Nanotechnology* **2010,** *21* (8), 85709.

175. Sun, B.; Zhao, W.; Liu, Y.; Chen, P., White-Light-Controlled Resistive Switching and Photovoltaic Effects in TiO_2/ZnO Composite Nanorods Array at Room Temperature. *Journal of Materials Science: Materials in Electronics* **2014,** *25* (10), 4306-4311.

176. Raffone, F.; Risplendi, F.; Cicero, G., A New Theoretical Insight Into ZnO NWs Memristive Behavior. *Nano Letters* **2016,** *16* (4), 2543-2547.

177. Yang, Y.; Zhang, X.; Gao, M.; Zeng, F.; Zhou, W.; Xie, S.; Pan, F., Nonvolatile Resistive Switching in Single Crystalline ZnO Nanowires. *Nanoscale* **2011,** *3* (4), 1917-1921.

178. Dong, H.; Zhang, X.; Zhao, D.; Niu, Z.; Zeng, Q.; Li, J.; Cai, L.; Wang, Y.; Zhou, W.; Gao, M.; Xie, S., High Performance Bipolar Resistive Switching Memory Devices based on Zn_2SnO_4 Nanowires. *Nanoscale* **2012,** *4* (8), 2571-2574.

179. Hsu, C. W.; Chou, L. J., Bipolar Resistive Switching of Single Gold-in-Ga_2O_3 Nanowire. *Nano Letters* **2012,** *12* (8), 4247-4753.

180. Bae, Y. C.; Lee, A. R.; Lee, J. B.; Koo, J. H.; Kwon, K. C.; Park, J. G.; Im, H. S.; Hong, J. P., Oxygen Ion Drift-Induced Complementary Resistive Switching in Homo TiO_x/TiO_y/TiO_x and Hetero TiO_x/TiON/TiO_x Triple Multilayer Frameworks. *Advanced Functional Materials* **2012,** *22* (4), 709-716.

181. Kwon, J.; Sharma, A. A.; Bain, J. A.; Picard, Y. N.; Skowronski, M., Oxygen Vacancy Creation, Drift, and Aggregation in TiO_2-Based Resistive Switches at Low Temperature and Voltage. *Advanced Functional Materials* **2015,** *25* (19), 2876-2883.

182. Regoutz, A.; Gupta, I.; Serb, A.; Khiat, A.; Borgatti, F.; Lee, T.-L.; Schlueter, C.; Torelli, P.; Gobaut, B.; Light, M.; Carta, D.; Pearce, S.; Panaccione, G.; Prodromakis, T., Role and Optimization of the Active Oxide Layer in TiO_2-Based RRAM. *Advanced Functional Materials* **2016,** *26* (4), 507-513.

183. Abunahla, H.; Homouz, D.; Halawani, Y.; Mohammad, B., Modeling and Device Parameter Design to Improve Reset Time in Binary-Oxide Memristors. *Applied Physics a-Materials Science & Processing* **2014,** *117* (3), 1019-1023.

184. Salaoru, I.; Prodromakis, T.; Khiat, A.; Toumazou, C., Resistive switching of oxygen enhanced TiO_2 thin-film devices. *Applied Physics Letters* **2013,** *102* (1), 013506.

185. Efeoglu, H.; Gullulu, S.; Karacali, T., Resistive Switching of Reactive Sputtered TiO_2 Based Memristor in Crossbar Geometry. *Applied Surface Science* **2015,** *350*, 10-13.

186. Trapatseli, M.; Khiat, A.; Cortese, S.; Serb, A.; Carta, D.; Prodromakis, T., Engineering the Switching Dynamics of TiO_x-based RRAM with Al doping. *Journal of Applied Physics* **2016,** *120* (2), 025108.

187. Gergel-Hackett, N.; Hamadani, B.; Dunlap, B.; Suehle, J.; Richter, C.; Hacker, C.; Gundlach, D., A Flexible Solution-Processed Memristor. *IEEE Electron Device Letters* **2009,** *30* (7), 706-708.

188. Jung, S.; Kong, J.; Song, S.; Lee, K.; Lee, T.; Hwang, H.; Jeon, S., Resistive Switching Characteristics of Solution-Processed TiO_x for Next-Generation Non-Volatile Memory Application; Transparency, Flexibility, and Nano-Scale Memory Feasibility. *Microelectronic Engineering* **2011,** *88* (7), 1143-1147.

189. Schmidt, D. O.; Hoffmann-Eifert, S.; Zhang, H.; La Torre, C.; Besmehn, A.; Noyong, M.; Waser, R.; Simon, U., Resistive Switching of Individual, Chemically Synthesized TiO_2 Nanoparticles. *Small* **2015,** *11* (48), 6444-6456.

190. Bera, A.; Peng, H.; Lourembam, J.; Shen, Y.; Sun, X. W.; Wu, T., A Versatile Light-Switchable Nanorod Memory: Wurtzite ZnO on Perovskite $SrTiO_3$. *Advanced Functional Materials* **2013,** *23* (39), 4977-4984.

191. Liu, B.; Aydil, E. S., Growth of Oriented Single-Crystalline Rutile TiO_2 Nanorods on Transparent Conducting Substrates for Dye-Sensitized Solar Cells. *Journal of the American Chemical Society* **2009,** *131*, 3985-3990.

192. Liu, B.; Boercker, J. E.; Aydil, E. S., Oriented Single Crystalline Titanium Dioxide Nanowires. *Nanotechnology* **2008,** *19* (50), 505604.

193. Wang, H.-E.; Chen, Z.; Leung, Y. H.; Luan, C.; Liu, C.; Tang, Y.; Yan, C.; Zhang, W.; Zapien, J. A.; Bello, I.; Lee, S.-T., Hydrothermal Synthesis of Ordered Single-Crystalline Rutile TiO_2 Nanorod Arrays on Different Substrates. *Applied Physics Letters* **2010,** *96* (26), 263104.

194. Zou, R.; Zhang, Z.; Yu, L.; Tian, Q.; Chen, Z.; Hu, J., A General Approach for the Growth of Metal Oxide Nanorod Arrays on Graphene Sheets and Their Applications. *Chemistry-a European Journal* **2011,** *17* (49), 13912-13917.

195. Xiao, M.; Musselman, K. P.; Duley, W. W.; Zhou, N. Y., Resistive Switching Memory of TiO_2 Nanowire Networks Grown on Ti Foil by a Single Hydrothermal Method. *Nano-Micro Letters* **2017,** *9* (2).

196. Oka, K.; Yanagida, T.; Nagashima, K.; Kawai, T.; Kim, J. S.; Park, B. H., Resistive-Switching Memory Effects of NiO Nanowire/Metal Junctions. *Journal of the American Chemical Society* **2010,** *132* (19), 6634-6635.

197. Oka, K.; Yanagida, T.; Nagashima, K.; Kanai, M.; Kawai, T.; Kim, J.-S.; Park, B. H., Spatial Nonuniformity in Resistive-Switching Memory Effects of NiO. *Journal of the American Chemical Society* **2011,** *133* (32), 12482-12485.

198. Liu, Z.-J.; Gan, J.-Y.; Yew, T.-R., ZnO-Based One Diode-One Resistor Device Structure for Crossbar Memory Applications. *Applied Physics Letters* **2012,** *100* (15), 153503.

199. Sasaki, T.; Ueda, H.; Kanki, T.; Tanaka, H., Electrochemical Gating-Induced Reversible and Drastic Resistance Switching in VO_2 Nanowires. *Scientific Reports* **2015**, *5*, 17080.

200. Gao, S.; Zeng, F.; Wang, M.; Wang, G.; Song, C.; Pan, F., Tuning the Switching Behavior of Binary Oxide-Based Resistive Memory Devices by Inserting an Ultra-Thin Chemically Active Metal Nanolayer: a Case Study on the Ta_2O_5-Ta System. *Physical Chemistry Chemical Physics* **2015,** *17* (19), 12849-12856.

201. Chang, T.; Jo, S.-H.; Lu, W., Short-Term Memory to Long-Term memory transition in a nanoscale memristor. *ACS Nano* **2011**, *5* (9), 7669-7676.

202. Qingjiang, L.; Khiat, A.; Salaoru, I.; Papavassiliou, C.; Hui, X.; Prodromakis, T., Memory Impedance in TiO_2 Based Metal-Insulator-Metal Devices. *Scientific Reports* **2014**, *4*, 4522.

203. Hu, Y.; Perello, D.; Yun, M.; Kwon, D.-H.; Kim, M., Variation of Switching Mechanism in TiO_2 Thin Film Resistive Random Access Memory with Ag and Graphene Electrodes. *Microelectronic Engineering* **2013**, *104*, 42-47.

204. Senthilkumar, V.; Kathalingam, A.; Kannan, V.; Senthil, K.; Rhee, J.-K., Reproducible Resistive Switching in Hydrothermal Processed TiO_2 Nanorod Film for Non-Volatile Memory Applications. *Sensors and Actuators a-Physical* **2013**, *194*, 135-139.

205. Liao, J.-Y.; Lei, B.-X.; Chen, H.-Y.; Kuang, D.-B.; Su, C.-Y., Oriented Hierarchical Single Crystalline Anatase TiO_2 Nanowire Arrays on Ti-Foil Substrate for Efficient Flexible Dye-Sensitized Solar Cells. *Energy & Environmental Science* **2012,** *5* (2), 5750-5757.

206. Wu, W. Q.; Rao, H. S.; Xu, Y. F.; Wang, Y. F.; Su, C. Y.; Kuang, D. B., Hierarchical Oriented Anatase TiO_2 Nanostructure Arrays on Flexible Substrate for Efficient Dye-Sensitized Solar Cells. *Scientific Reports* **2013**, *3*, 1892.

207. Huo, K.; Zhang, X.; Fu, J.; Qian, G.; Xin, Y.; Zhu, B.; Ni, H.; Chu, P. K., Synthesis and Field Emission Properties of Rutile TiO_2 Nanowires Arrays Grown Directly on a Ti Metal Self-Source Substrate. *Journal of Nanoscience and Nanotechnology* **2009,** *9* (5), 3341-3346.

208. Wu, Y.; Long, M.; Cai, W.; Dai, S.; Chen, C.; Wu, D.; Bai, J., Preparation of Photocatalytic Anatase Nanowire Films by in Situ Oxidation of Titanium Plate. *Nanotechnology* **2009,** *20* (18), 185703.

209. Ohsaka, T.; Izumi, F.; Fujiki, Y., Raman spectrum of Anatase, TiO_2. *Journal of Raman Spectroscopy* **1978,** *7* (6), 321-324.

210. Kim, K. M.; Choi, B. J.; Shin, Y. C.; Choi, S.; Hwang, C. S., Anode-interface localized filamentary mechanism in resistive switching of TiO_2 thin films. *Applied Physics Letters* **2007,** *91* (1), 012907.

211. Wang, P. C.; Li, P. G.; Zhi, Y. S.; Guo, D. Y.; Pan, A. Q.; Zhan, J. M.; Liu, H.; Shen, J. Q.; Tang, W. H., Bias Tuning Charge-Releasing Leading to Negative Differential Resistance in Amorphous Gallium Oxide/Nb:$SrTiO_3$ Heterostructure. *Applied Physics Letters* **2015,** *107* (26), 262110.

212. Hota, M. K.; Nagaraju, D. H.; Hedhili, M. N.; Alshareef, H. N., Electroforming Free Resistive Switching Memory in Two-Dimensional VO_x Nanosheets. *Applied Physics Letters* **2015,** *107* (16), 163106.

213. Barman, A.; Saini, C. P.; Sarkar, P. K.; Roy, A.; Satpati, B.; Kanjilal, D.; Ghosh, S. K.; Dhar, S.; Kanjilal, A., Probing Electron Density Across Ar^+ Irradiation-Induced Self-Organized TiO_{2-x} Nanochannels for Memory Application. *Applied Physics Letters* **2016,** *108* (24), 244104.

214. Lin, C.-Y.; Wu, C.-Y.; Wu, C.-Y.; Tseng, T.-Y.; Hu, C., Modified Resistive Switching Behavior of ZrO_2 Memory Films Based on the Interface Layer Formed by Using Ti Top Electrode. *Journal of Applied Physics* **2007,** *102* (9), 094101.

215. Weibel, A.; Bouchet, R.; Knauth, P., Electrical Properties and Defect Chemistry of Anatase (TiO_2). *Solid State Ionics* **2006,** *177* (3-4), 229-236.

216. Choi, B. J.; Jeong, D. S.; Kim, S. K.; Rohde, C.; Choi, S.; Oh, J. H.; Kim, H. J.; Hwang, C. S.; Szot, K.; Waser, R.; Reichenberg, B.; Tiedke, S., Resistive Switching Mechanism of TiO_2 Thin Films Grown by Atomic-Layer Deposition. *Journal of Applied Physics* **2005,** *98* (3), 033715.

217. Xiao, M.; Musselman, K. P.; Duley, W. W.; Zhou, Y. N., Reliable and Low-Power Multilevel Resistive Switching in TiO_2 Nanorod Arrays Structured with a TiO_x Seed Layer. *ACS Applied Materials & Interfaces* **2017,** *9* (5), 4808-4817.

218. Li, Y.; Qian, F.; Xiang, J.; Lieber, C. M., Nanowire Electronic and Optoelectronic Devices. *Materials Today* **2006,** *9* (10), 18-27.

219. Lieber, C. M., Semiconductor nanowires: A platform for nanoscience and nanotechnology. *MRS bulletin / Materials Research Society* **2011,** *36* (12), 1052-1063.

220. Javey, A.; Nam, S.; Friedman, R. S.; Yan, H.; Lieber, C. M., Layer-by-Layer Assembly of Nanowires for Three-Dimensional, Multifunctional Electronics. *Nano letters* **2007,** *7* (3), 773-777.

221. Lin, L.; Zou, G.; Liu, L.; Duley, W. W.; Zhou, Y. N., Plasmonic Engineering of Metal-Oxide Nanowire Heterojunctions in Integrated Nanowire Rectification Units. *Applied Physics Letters* **2016,** *108* (20), 203107.

222. Dong, Y.; Yu, G.; McAlpine, M. C.; Lu, W.; Lieber, C. M., Si/a-Si Core/Shell Nanowires as Nonvolatile Crossbar Switches. *Nano Letters* **2008,** *8* (2), 386-391.

223. Feng, X.; Shankar, K.; Varghese, O. K.; Paulose, M.; Latempa, T. J.; Grimes, C. A., Vertically Aligned Single Crystal TiO_2 Nanowire Arrays Grown Directly on Transparent Conducting Oxide Coated Glass: Synthesis Details and Applications. *Nano Letters* **2008,** *8* (11), 3781-3786.

224. Wang, J.; Zhang, T.; Wang, D.; Pan, R.; Wang, Q.; Xia, H., Improved Morphology and Photovoltaic Performance in TiO_2 Nanorod Arrays Based Dye Sensitized Solar Cells by Using a Seed Layer. *Journal of Alloys and Compounds* **2013,** *551*, 82-87.

225. Li, H.; Yu, Q.; Huang, Y.; Yu, C.; Li, R.; Wang, J.; Guo, F.; Jiao, S.; Gao, S.; Zhang, Y.; Zhang, X.; Wang, P.; Zhao, L., Ultralong Rutile TiO_2 Nanowire Arrays for Highly Efficient Dye-Sensitized Solar Cells. *ACS Applied Materials & Interfaces* **2016,** *8* (21), 13384-13391.

226. Lv, M.; Zheng, D.; Ye, M.; Xiao, J.; Guo, W.; Lai, Y.; Sun, L.; Lin, C.; Zuo, J., Optimized Porous Rutile TiO_2 Nanorod Arrays for Enhancing the Efficiency of Dye-Sensitized Solar Cells. *Energy & Environmental Science* **2013,** *6* (5), 1615-1622.

227. Berhe, S. A.; Nag, S.; Molinets, Z.; Youngblood, W. J., Influence of Seeding and Bath Conditions in Hydrothermal Growth of Very Thin (~20 nm) Single-Crystalline Rutile TiO_2 Nanorod Films. *ACS Applied Materials & Interfaces* **2013,** *5* (4), 1181-1185.

228. Tamilselvan, V.; Yuvaraj, D.; Rakesh Kumar, R.; Narasimha Rao, K., Growth of Rutile TiO_2 Nanorods on TiO_2 Seed Layer Deposited by Electron Beam Evaporation. *Applied Surface Science* **2012,** *258* (10), 4283-4287.

229. Zhong, P.; Ma, X.; Chen, X.; Zhong, R.; Liu, X.; Ma, D.; Zhang, M.; Li, Z., Morphology-Controllable Polycrystalline TiO_2 Nanorod Arrays for Efficient Charge Collection in Dye-Sensitized Solar Cells. *Nano Energy* **2015,** *16*, 99-111.

230. Yuan, W.; Yuan, J.; Xie, J.; Li, C. M., Polymer-Mediated Self-Assembly of TiO_2@Cu_2O Core-Shell Nanowire Array for Highly Efficient Photoelectrochemical Water Oxidation. *ACS Applied Materials & Interfaces* **2016,** *8* (9), 6082-6092.

231. Bang, J. H.; Kamat, P. V., Solar Cells by Design: Photoelectrochemistry of TiO_2 Nanorod Arrays Decorated with CdSe. *Advanced Functional Materials* **2010,** *20* (12), 1970-1976.

232. Su, C.; Liu, L.; Zhang, M.; Zhang, Y.; Shao, C., Fabrication of Ag/TiO2 Nanoheterostructures with Visible Light Photocatalytic Function via a Solvothermal Approach. *Crystengcomm* **2012,** *14* (11), 3989-3999.

233. Li, W.; Liang, R.; Hu, A.; Huang, Z.; Zhou, Y. N., Generation of Oxygen Vacancies in Visible Light Activated One-Dimensional Iodine TiO_2 Photocatalysts. *RSC Advances* **2014,** *4* (70), 36959-36966.

234. Zhu, Y.; Li, M.; Zhou, H.; Hu, Z.; Liu, X.; Fang, X.; Sebo, B.; Fang, G.; Zhao, X., Nonvolatile Bipolar Resistive Switching in an Ag/TiO_2/Nb : $SrTiO_3$/In Device. *Journal of Physics D: Applied Physics* **2012,** *45* (37), 375303.

235. Yu, Y.; Lan, X.; Jiang, Y.; Zhang, Y.; Zhang, Y.; Zhu, Z.; Wang, L.; Wu, C.; Jie, J., Interfacially Engineered High-Speed Nonvolatile Memories Employing p-Type Nanoribbons. *Advanced Materials Interfaces* **2014,** *1* (8), 1400130.

236. Lee, M. H.; Kim, K. M.; Kim, G. H.; Seok, J. Y.; Song, S. J.; Yoon, J. H.; Hwang, C. S., Study on the Electrical Conduction Mechanism of Bipolar Resistive Switching TiO_2 Thin Films Using Impedance Spectroscopy. *Applied Physics Letters* **2010,** *96* (15), 152909.

237. Jeon, D. S.; Park, J. H.; Kim, M. J.; Kim, T. G., Low Power NiN-based Resistive Switching Memory Device Using Ti Doping. *Applied Physics Letters* **2016,** *109* (18), 183507.

238. Mora-Sero, I.; Bertoluzzi, L.; Gonzalez-Pedro, V.; Gimenez, S.; Fabregat-Santiago, F.; Kemp, K. W.; Sargent, E. H.; Bisquert, J., Selective Contacts Drive Charge Extraction in Quantum Dot Solids via Asymmetry in Carrier Transfer Kinetics. *Nature Communications* **2013,** *4*, 2272.

239. Valentin, C. D.; Pacchioni, G.; Selloni, A., Reduced and n-Type Doped TiO_2: Nature of Ti^{3+} Species. *J. Phys. Chem. C* **2009,** (113) 20543-20552.

240. Mattioli, G.; Filippone, F.; Alippi, P.; Amore Bonapasta, A., Ab *initio* Study of the Electronic States Induced by Oxygen Vacancies in Rutile and Anatase TiO_2. *Physical Review B* **2008,** *78* (24), 241201.

241. Yu, X.; Kim, B.; Kim, Y. K., Highly Enhanced Photoactivity of Anatase TiO_2 Nanocrystals by Controlled Hydrogenation-Induced Surface Defects. *ACS Catalysis* **2013,** *3* (11), 2479-2486.

242. Kushwaha, A.; Aslam, M., Defect Induced High Photocurrent in Solution Grown Vertically Aligned ZnO Nanowire Array Films. *Journal of Applied Physics* **2012,** *112* (5), 054316.

243. Sharma, Y.; Misra, P.; Pavunny, S. P.; Katiyar, R. S., Multilevel Unipolar Resistive Memory Switching in Amorphous $SmGdO_3$ Thin Film. *Applied Physics Letters* **2014,** *104* (7), 073501.

244. Nili, H.; Walia, S.; Kandjani, A. E.; Ramanathan, R.; Gutruf, P.; Ahmed, T.; Balendhran, S.; Bansal, V.; Strukov, D. B.; Kavehei, O.; Bhaskaran, M.; Sriram, S., Donor-Induced Performance Tuning of Amorphous $SrTiO_3$ Memristive Nanodevices: Multistate Resistive Switching and Mechanical Tunability. *Advanced Functional Materials* **2015,** *25* (21), 3172-3182.

245. Lampert, M. A., Simplified Theory of Space-Charge-Limited Currents in an Insulator with Traps. *Physical Review* **1956,** *103* (6), 1648-1656.

246. Xiao, M.; Shen, D.; Musselman, K. P.; Duley, W. W.; Zhou, Y. N., Oxygen Vacancy Migration/Diffusion Induced Synaptic Plasticity In A Single Titanate Nanobelt. *Nanoscale* **2018,** *10* (13), 6069-6079.

247. Strukov, D. B., Nanotechnology: Smart Connections. *Nature* **2011,** *476* (7361), 403-405.

248. Ho, V. M.; Lee, J. A.; Martin, K. C., The Cell Biology Of Synaptic Plasticity. *Science* **2011,** *334* (6056), 623-628.

249. Zucker, R. S.; Regehr, W. G., Short-term Synaptic Plasticity. *Annual Review Physiology* **2002,** *64*, 355-405.

250. Wang, J.; Li, Y.; Liang, R.; Zhang, Y.; Mao, W.; Yang, Y.; Ren, T.-L., Synaptic Computation Demonstrated in a Two-Synapse Network Based on Top-Gate Electric-Double-Layer Synaptic Transistors. *IEEE Electron Device Letters* **2017,** *38* (10), 1496-1499.

251. Tian, H.; Mi, W.; Wang, X. F.; Zhao, H.; Xie, Q. Y.; Li, C.; Li, Y. X.; Yang, Y.; Ren, T. L., Graphene Dynamic Synapse with Modulatable Plasticity. *Nano Letters* **2015,** *15* (12), 8013-8019.

252. van de Burgt, Y.; Lubberman, E.; Fuller, E. J.; Keene, S. T.; Faria, G. C.; Agarwal, S.; Marinella, M. J.; Alec Talin, A.; Salleo, A., A Non-volatile Organic Electrochemical Device as a Low-voltage Artificial Synapse For Neuromorphic Computing. *Nature Materials* **2017,** *16* (4), 414-418.

253. Xu, W.; Cho, H.; Kim, Y. H.; Kim, Y. T.; Wolf, C.; Park, C. G.; Lee, T. W., Organometal Halide Perovskite Artificial Synapses. *Advanced Materials* **2016,** *28* (28), 5916-5922.

254. John, R. A.; Ko, J.; Kulkarni, M. R.; Tiwari, N.; Chien, N. A.; Ing, N. G.; Leong, W. L.; Mathews, N., Flexible Ionic-Electronic Hybrid Oxide Synaptic TFTs with Programmable Dynamic Plasticity for Brain-Inspired Neuromorphic Computing. *Small* **2017,** *13* (32), 1701193.

255. Arnold, A. J.; Razavieh, A.; Nasr, J. R.; Schulman, D. S.; Eichfeld, C. M.; Das, S., Mimicking Neurotransmitter Release in Chemical Synapses via Hysteresis Engineering in MoS_2 Transistors. *ACS Nano* **2017,** *11* (3), 3110-3118.

256. Kim, S.; Choi, B.; Lim, M.; Yoon, J.; Lee, J.; Kim, H. D.; Choi, S. J., Pattern Recognition Using Carbon Nanotube Synaptic Transistors with an Adjustable Weight Update Protocol. *ACS Nano* **2017,** *11* (3), 2814-2822.

257. Wang, Y. F.; Lin, Y. C.; Wang, I. T.; Lin, T. P.; Hou, T. H., Characterization and Modeling of Nonfilamentary Ta/TaO_x/TiO_2/Ti Analog Synaptic Device. *Scientific Reports* **2015,** *5*, 10150.

258. Du, C.; Ma, W.; Chang, T.; Sheridan, P.; Lu, W. D., Biorealistic Implementation of Synaptic Functions with Oxide Memristors through Internal Ionic Dynamics. *Advanced Functional Materials* **2015,** *25* (27), 4290-4299.

259. Yang, R.; Huang, H.-M.; Hong, Q.-H.; Yin, X.-B.; Tan, Z.-H.; Shi, T.; Zhou, Y.-X.; Miao, X.-S.; Wang, X.-P.; Mi, S.-B.; Jia, C.-L.; Guo, X., Synaptic Suppression Triplet-STDP Learning Rule Realized in Second-Order Memristors. *Advanced Functional Materials* **2018,** *28* (5), 1704455.

260. Tian, H.; Mi, W.; Zhao, H.; Mohammad, M. A.; Yang, Y.; Chiu, P. W.; Ren, T. L., A novel Artificial Synapse With Dual Modes Using Bilayer Graphene as The Bottom Electrode. *Nanoscale* **2017,** *9* (27), 9275-9283.

261. O'Kelly, C. J.; Fairfield, J. A.; McCloskey, D.; Manning, H. G.; Donegan, J. F.; Boland, J. J., Associative Enhancement of Time Correlated Response to Heterogeneous Stimuli in a Neuromorphic Nanowire Device. *Advanced Electronic Materials* **2016,** *2* (6), 1500458.

262. Wang, Y. M.; Du, G. J.; Liu, H.; Liu, D.; Qin, S. B.; Wang, N.; Hu, C. G.; Tao, X. T.; Jiao, J.; Wang, J. Y.; Wang, Z. L., Nanostructured sheets of Ti-O Nanobelts for Gas Sensing and Antibacterial Applications. *Advanced Functional Materials* **2008,** *18* (7), 1131-1137.

263. Liang, R.; Hu, A. M.; Li, W. J.; Zhou, Y. N., Enhanced Degradation Of Persistent Pharmaceuticals Found In Wastewater Treatment Effluents using TiO_2 Nanobelt Photocatalysts. *Journal of Nanoparticle Research* **2013,** *15* (10), 1990.

264. Zhao, Z.; Tian, J.; Sang, Y.; Cabot, A.; Liu, H., Structure, Synthesis, and Applications of TiO_2 Nanobelts. *Advanced materials* **2015,** *27* (16), 2557-2582.

265. Eguia-Barrio, A.; Castillo-Martinez, E.; Zarrabeitia, M.; Munoz-Marquez, M. A.; Casas-Cabanas, M.; Rojo, T., Structure of $H_2Ti_3O_7$and its Evolution During Sodium Insertion as Anode for Na Ion Batteries. *Physical Chemistry Chemical Physics: PCCP* **2015,** *17* (10), 6988-6994.

266. Liao, J. Y.; Higgins, D.; Lui, G.; Chabot, V.; Xiao, X.; Chen, Z., Multifunctional TiO_2-C/MnO_2 Core-double-shell Nanowire Arrays as High-performance 3D Electrodes for Lithium Ion Batteries. *Nano Letters* **2013,** *13* (11), 5467-5473.

267. Sarkar, A.; Karmakar, K.; Singh, A. K.; Mandal, K.; Khan, G. G., Surface Functionalized $H_2Ti_3O_7$ Nanowires Engineered for Visible-Light Photoswitching, Electrochemical Water

Splitting, and Photocatalysis. *Physical chemistry chemical physics:PCCP* **2016,** *18* (38), 26900-26912.

268. Chakraborty, I.; Chatterjee, S.; Ayyub, P., Field Emission from Hydrogen Titanate Nanotubes. *Applied Physics Letters* **2011,** *99* (14), 143106.

269. Xu, X.; Tang, C.; Zeng, H.; Zhai, T.; Zhang, S.; Zhao, H.; Bando, Y.; Golberg, D., Structural Transformation, Photocatalytic, and Field-Emission Properties of Ridged TiO_2 Nanotubes. *ACS Applied Materials & Interfaces* **2011,** *3* (4), 1352-1358.

270. Saini, C. P.; Barman, A.; Das, D.; Satpati, B.; Bhattacharyya, S. R.; Kanjilal, D.; Ponomaryov, A.; Zvyagin, S.; Kanjilal, A., Role of Oxygen Vacancy on the Hydrophobic Behavior of TiO_2 Nanorods on Chemically Etched Si Pyramids. *The Journal of Physical Chemistry C* **2016,** *121* (1), 278-283.

271. Du, Q.; Lu, G., Controllable Synthesis and Photocatalytic Properties Study of $Na_2Ti_3O_7$ and $H_2Ti_3O_7$ Nanotubes with High Exposed Facet (010). *Journal of Nanoscience and Nanotechnology* **2015,** *15* (6), 4385-4391.

272. Liu, G.; Wang, C.; Zhang, W. B.; Pan, L.; Zhang, C. C.; Yang, X.; Fan, F.; Chen, Y.; Li, R. W., Organic Biomimicking Memristor for Information Storage and Processing Applications. *Advanced Electronic Materials* **2016,** *2* (2), 1500298.

273. Kim, S.; Choi, S.; Lu, W., Comprehensive Physical Model of Dynamic Resistive Switching in an Oxide Memristor. *ACS Nano* **2014,** *8* (3), 2369-2376.

274. Yin, X. B.; Yang, R.; Xue, K. H.; Tan, Z. H.; Zhang, X. D.; Miao, X. S.; Guo, X., Mimicking the Brain Functions of Learning, Forgetting and Explicit/Implicit Memories with $SrTiO_3$-based Memristive Devices. *Physical Chemistry Chemical Physics:PCCP* **2016,** *18* (46), 31796-31802.

275. Murdoch, B. J.; McCulloch, D. G.; Ganesan, R.; McKenzie, D. R.; Bilek, M. M. M.; Partridge, J. G., Memristor and Selector Devices Fabricated From $HfO_{2-x}N_x$. *Applied Physics Letters* **2016,** *108* (14), 143504.

276. Lin, Y. F.; Jian, W. B., The Impact of Nanocontact on Nanowire Based Nanoelectronics. *Nano Letters* **2008,** *8* (10), 3146-3150.

277. Zhang, Z. Y.; Jin, C. H.; Liang, X. L.; Chen, Q.; Peng, L. M., Current-voltage Characteristics and Parameter Retrieval of Semiconducting Nanowires. *Applied Physics Letters* **2006,** *88* (7), 073102.

278. Deng, B.; Luisa da Rosa, A.; Frauenheim, T.; Xiao, J. P.; Shi, X. Q.; Zhang, R. Q.; Van Hove, M. A., Oxygen Vacancy Diffusion in bare ZnO Nanowires. *Nanoscale* **2014,** *6* (20), 11882-11886.

279. Marmitt, G. G.; Nandi, S. K.; Venkatachalam, D. K.; Elliman, R. G.; Vos, M.; Grande, P. L., Oxygen Diffusion in TiO_2 Films Studied by Electron and Ion Rutherford Backscattering. *Thin Solid Films* **2017,** *629*, 97-102.

280. Iddir, H.; Öğüt, S.; Zapol, P.; Browning, N. D., Diffusion Mechanisms of native point defects in rutile TiO_2: Ab initiototal-energy calculations. *Physical Review B* **2007,** *75* (7), 073203.

281. Shannon, J. M., Control of Schottky-Barrier Height Using Highly Doped Surface-Layers. *Solid-State Electronics* **1976,** *19* (6), 537-543.

282. Zidan, M. A.; Strachan, J. P.; Lu, W. D., The Future of Electronics based on Memristive Systems. *Nature Electronics* **2018,** *1* (1), 22-29.

283. Diorio, C.; Hasler, P.; Minch, A.; Mead, C. A., A Single-transistor Silicon Synapse. *IEEE Transactions on Electron Devices* **1996,** *43* (11), 1972-1980.

284. Mead, C., Neuromorphic Electronic Systems. *Proceedings of the IEEE* **1990,** *78* (10), 1629-1636.

285. Najem, J. S.; Taylor, G. J.; Weiss, R. J.; Hasan, M. S.; Rose, G.; Schuman, C. D.; Belianinov, A.; Collier, C. P.; Sarles, S. A., Memristive Ion Channel-Doped Biomembranes as Synaptic Mimics. *ACS Nano* **2018,** *12* (5), 4702-4711.

286. Park, Y.; Han, U. B.; Kim, M. K.; Lee, J. S., Solution-Processed Flexible Threshold Switch Devices. *Advanced Electronic Materials* **2018,** *4* (4), 1700521.

287. Wang, Z. R.; Rao, M. Y.; Midya, R.; Joshi, S.; Jiang, H.; Lin, P.; Song, W. H.; Asapu, S.; Zhuo, Y.; Li, C.; Wu, H. Q.; Xia, Q. F.; Yang, J. J., Threshold Switching of Ag or Cu in Dielectrics: Materials, Mechanism, and Applications. *Advanced Functional Materials* **2018,** *28* (6), 1704862.

288. Midya, R.; Wang, Z.; Asapu, S.; Joshi, S.; Li, Y.; Zhuo, Y.; Song, W.; Jiang, H.; Upadhay, N.; Rao, M.; Lin, P.; Li, C.; Xia, Q.; Yang, J. J., Artificial Neural Network (ANN) to Spiking Neural Network (SNN) Converters Based on Diffusive Memristors. *Advanced Electronic Materials* **2019**, 1900060.

289. Yan, X. B.; Zhou, Z. Y.; Zhao, J. H.; Liu, Q.; Wang, H.; Yuan, G. L.; Chen, J. S., Flexible Memristors as Electronic Synapses for Neuro-inspired Computation based on Scotch Tape-exfoliated Mica Substrates. *Nano Research* **2018,** *11* (3), 1183-1192.

290. Kalita, H.; Krishnaprasad, A.; Choudhary, N.; Das, S.; Dev, D.; Ding, Y.; Tetard, L.; Chung, H. S.; Jung, Y.; Roy, T., Artificial Neuron using Vertical MoS_2/Graphene Threshold Switching Memristors. *Scientific Reports* **2019,** *9* (1), 53.

291. Evans, D. A.; Stempel, A. V.; Vale, R.; Ruehle, S.; Lefler, Y.; Branco, T., A Synaptic Threshold Mechanism for Computing Escape Decisions. *Nature* **2018,** *558* (7711), 590-594.

292. Lee, D.; Kwak, M.; Moon, K.; Choi, W.; Park, J.; Yoo, J.; Song, J.; Lim, S.; Sung, C.; Banerjee, W.; Hwang, H., Various Threshold Switching Devices for Integrate and Fire Neuron Applications. *Advanced Electronic Materials* **2019**, 1800866.

293. Yoon, J. H.; Wang, Z.; Kim, K. M.; Wu, H.; Ravichandran, V.; Xia, Q.; Hwang, C. S.; Yang, J. J., An Artificial Nociceptor based on a Diffusive Memristor. *Nature Communications* **2018,** *9* (1), 417.

294. Ge, J.; Zhang, S.; Liu, Z.; Xie, Z.; Pan, S., Flexible Artificial Nociceptor Using a Biopolymer-based Forming-free Memristor. *Nanoscale* **2019,** *11* (14), 6591-6601.

295. Kim, Y.; Kwon, Y. J.; Kwon, D. E.; Yoon, K. J.; Yoon, J. H.; Yoo, S.; Kim, H. J.; Park, T. H.; Han, J. W.; Kim, K. M.; Hwang, C. S., Nociceptive Memristor. *Advanced Materials* **2018,** *30* (8).

296. Sun, H. T.; Liu, Q.; Li, C. F.; Long, S. B.; Lv, H. B.; Bi, C.; Huo, Z. L.; Li, L.; Liu, M., Direct Observation of Conversion Between Threshold Switching and Memory Switching Induced by Conductive Filament Morphology. *Advanced Functional Materials* **2014,** *24* (36), 5679-5686.

297. Du, G.; Wang, C.; Li, H. X.; Mao, Q. A.; Ji, Z. G., Bidirectional Threshold Switching Characteristics in Ag/ZrO_2/Pt Electrochemical Metallization Cells. *Aip Advance* **2016,** *6* (8), 085316.

298. Hino, T.; Hasegawa, T.; Tanaka, H.; Tsuruoka, T.; Terabe, K.; Ogawa, T.; Aono, M., Volatile and Nonvolatile Selective Switching of a Photo-assisted Initialized Atomic Switch. *Nanotechnology* **2013,** *24* (38), 384006.

299. Du, H.; Wan, T.; Qu, B.; Cao, F.; Lin, Q.; Chen, N.; Lin, X.; Chu, D., Engineering Silver Nanowire Networks: From Transparent Electrodes to Resistive Switching Devices. *ACS Applied Materials & Interfaces* **2017,** *9* (24), 20762-20770.

300. Wan, T.; Pan, Y.; Du, H.; Qu, B.; Yi, J.; Chu, D., Threshold Switching Induced by Controllable Fragmentation in Silver Nanowire Networks. *ACS Applied Materials & Interfaces* **2018,** *10* (3), 2716-2724.

301. Zhang, X. M.; Wang, W.; Liu, Q.; Zhao, X. L.; Wei, J. S.; Cao, R. R.; Yao, Z. H.; Zhu, X. L.; Zhang, F.; Lv, H. B.; Long, S. B.; Liu, M., An Artificial Neuron Based on a Threshold Switching Memristor. *IEEE Electron Device Letters* **2018,** *39* (2), 308-311.

302. Peng, H. Y.; Li, Y. F.; Lin, W. N.; Wang, Y. Z.; Gao, X. Y.; Wu, T., Deterministic Conversion Between Memory and Threshold Resistive Switching via Tuning the Strong Electron Correlation. *Scientific Reports* **2012,** *2*, 442.

303. Chang, S. H.; Lee, J. S.; Chae, S. C.; Lee, S. B.; Liu, C.; Kahng, B.; Kim, D. W.; Noh, T. W., Occurrence of Both Unipolar Memory and Threshold Resistance Switching in a NiO Film. *Physcial Review Letters* **2009,** *102* (2), 026801.

304. He, L.; Liao, Z. M.; Wu, H. C.; Tian, X. X.; Xu, D. S.; Cross, G. L.; Duesberg, G. S.; Shvets, I. V.; Yu, D. P., Memory and Threshold Resistance Switching in Ni/NiO Core-shell Nanowires. *Nano Letters* **2011,** *11* (11), 4601-4606.

305. Wang, H.; Du, Y. M.; Li, Y. T.; Zhu, B. W.; Leow, W. R.; Li, Y. G.; Pan, J. S.; Wu, T.; Chen, X. D., Configurable Resistive Switching between Memory and Threshold Characteristics for Protein-Based Devices. *Advanced Functional Materials* **2015,** *25* (25), 3825-3831.

306. Chae, B. G.; Seol, J. B.; Song, J. H.; Baek, K.; Oh, S. H.; Hwang, H.; Park, C. G., Nanometer-Scale Phase Transformation Determines Threshold and Memory Switching Mechanism. *Advanced materials* **2017,** *29* (30), 1701752.

307. Woo, J.; Lee, D.; Koo, Y.; Hwang, H., Dual Functionality Of Threshold And Multilevel Resistive Switching Characteristics In Nanoscale HfO_2-based RRAM Devices for Artificial Neuron and Synapse Elements. *Microelectronic Engineering* **2017,** *182*, 42-45.

308. Liu, J.; Yang, H.; Ji, Y.; Ma, Z.; Chen, K.; Zhang, X.; Zhang, H.; Sun, Y.; Huang, X.; Oda, S., An Electronic Synaptic Device Based on HfO_2/TiO_x Bilayer Structure Memristor With Self-Compliance and Deep-RESET Characteristics. *Nanotechnology* **2018,** *29* (41), 415205.

309. Messerschmitt, F.; Kubicek, M.; Rupp, J. L. M., How Does Moisture Affect the Physical Property of Memristance for Anionic-Electronic Resistive Switching Memories? *Advanced Functional Materials* **2015,** *25* (32), 5117-5125.

310. Lynall, D.; Nair, S. V.; Gutstein, D.; Shik, A.; Savelyev, I. G.; Blumin, M.; Ruda, H. E., Surface State Dynamics Dictating Transport in InAs Nanowires. *Nano Letters* **2018,** *18* (2), 1387-1395.

311. Speckbacher, M.; Treu, J.; Whittles, T. J.; Linhart, W. M.; Xu, X.; Saller, K.; Dhanak, V. R.; Abstreiter, G.; Finley, J. J.; Veal, T. D.; Koblmuller, G., Direct Measurements of Fermi Level Pinning at the Surface of Intrinsically n-Type InGaAs Nanowires. *Nano Letters* **2016,** *16* (8), 5135-42.

312. Tao, R.; Mouis, M.; Ardila, G., Unveiling the Influence of Surface Fermi Level Pinning on the Piezoelectric Response of Semiconducting Nanowires. *Advanced Electronic Materials* **2017**, 1700299.

313. Merino-Diez, N.; Garcia-Lekue, A.; Carbonell-Sanroma, E.; Li, J.; Corso, M.; Colazzo, L.; Sedona, F.; Sanchez-Portal, D.; Pascual, J. I.; de Oteyza, D. G., Width-Dependent Band Gap in Armchair Graphene Nanoribbons Reveals Fermi Level Pinning on Au(111). *ACS Nano* **2017,** *11* (11), 11661-11668.

314. Kim, G. S.; Kim, S. H.; Lee, T. I.; Cho, B. J.; Choi, C.; Shin, C.; Shim, J. H.; Kim, J.; Yu, H. Y., Fermi-Level Unpinning Technique with Excellent Thermal Stability for n-Type Germanium. *ACS Applied Materials & Interfaces* **2017,** *9* (41), 35988-35997.

315. Bampoulis, P.; van Bremen, R.; Yao, Q.; Poelsema, B.; Zandvliet, H. J. W.; Sotthewes, K., Defect Dominated Charge Transport and Fermi Level Pinning in MoS_2/Metal Contacts. *ACS Applied Materials & Interfaces* **2017,** *9* (22), 19278-19286.

316. Yoon, H. H.; Jung, S.; Choi, G.; Kim, J.; Jeon, Y.; Kim, Y. S.; Jeong, H. Y.; Kim, K.; Kwon, S. Y.; Park, K., Strong Fermi-Level Pinning at Metal/n-Si(001) Interface Ensured by Forming an Intact Schottky Contact with a Graphene Insertion Layer. *Nano Letters* **2017,** *17* (1), 44-49.

317. Chiu, F. C., A Review on Conduction Mechanisms in Dielectric Films. *Advances in Materials Science and Engineering* **2014,** *2014*, 1-18.

318. Hope, G. A.; Bard, A. J., Platinum Titanium-Dioxide (Rutile) Interface - Formation of Ohmic and Rectifying Junctions. *Journal of Physical Chemistry-Us* **1983,** *87* (11), 1979-1984.

319. Hu, Y. F.; Liu, Y.; Li, W. L.; Gao, M.; Liang, X. L.; Li, Q.; Peng, L. M., Observation of a 2D Electron Gas and the Tuning of the Electrical Conductance of ZnO Nanowires by Controllable Surface Band-Bending. *Advanced Functional Materials* **2009,** *19* (15), 2380-2387.

320. Jie, J. S.; Zhang, W. J.; Peng, K. Q.; Yuan, G. D.; Lee, C. S.; Lee, S. T., Surface-Dominated Transport Properties of Silicon Nanowires. *Advanced Functional Materials* **2008,** *18* (20), 3251-3257.

321. Lim, E. W.; Ismail, R., Conduction Mechanism of Valence Change Resistive Switching Memory: A Survey. *Electronics* **2015,** *4* (3), 586-613.

322. Tang, H.; Prasad, K.; Sanjines, R.; Schmid, P. E.; Levy, F., Electrical and Optical-Properties of TiO_2 Anatase Thin-Films. *Journal of Applied Physics* **1994,** *75* (4), 2042-2047.

323. Pascual, J.; Camassel, J.; Mathieu, H., Fine-Structure in the Intrinsic Absorption-Edge of TiO_2. *Physical Review B* **1978,** *18* (10), 5606-5614.

324. Futscher, M. H.; Lee, J. M.; McGovern, L.; Muscarella, L. A.; Wang, T.; Haider, M. I.; Fakharuddin, A.; Schmidt-Mende, L.; Ehrler, B., Quantification of Ion Migration in $CH_3NH_3PBI_3$ Perovskite Solar Cells By Transient Capacitance Measurements. *Materials Horizon* **2019**. DOI: 10.1039/c9mh00445a.

325. Seok, T. J.; Liu, Y.; Jung, H. J.; Kim, S. B.; Kim, D. H.; Kim, S. M.; Jang, J. H.; Cho, D. Y.; Lee, S. W.; Park, T. J., Field-Effect Device Using Quasi-Two-Dimensional Electron Gas in Mass-Producible Atomic-Layer-Deposited Al_2O_3/TiO_2 Ultrathin (<10 nm) Film Heterostructures. *ACS Nano* **2018,** *12* (10), 10403-10409.

326. Sarkar, T.; Gopinadhan, K.; Zhou, J.; Saha, S.; Coey, J. M.; Feng, Y. P.; Ariando; Venkatesan, T., Electron Transport at the TiO_2 Surfaces of Rutile, Anatase, and Strontium Titanate: The Influence of Orbital Corrugation. *ACS Applied Materials & Interfaces* **2015,** *7* (44), 24616-24621.

327. Chen, X.; Liu, L.; Yu, P. Y.; Mao, S. S., Increasing Solar Absorption for Photocatalysis with Black Hydrogenated Titanium Dioxide Nanocrystals. *Science* **2011,** *331*, 746-750.

328. Kumar, M.; Kim, H. S.; Kim, J., A Highly Transparent Artificial Photonic Nociceptor. *Advanced Materials* **2019,** *31* (19), e1900021.

329. Raouf, R.; Quick, K.; Wood, J. N., Pain as a Channelopathy. *Journal of Clinical Investigation* **2010,** *120* (11), 3745-3752.

330. Julius, D.; Basbaum, A. I., Molecular Mechanisms of Nociception. *Nature* **2001,** *413* (6852), 203-210.